Forschungszentrum Karlsruhe
Technik und Umwelt

Wissenschaftliche Berichte
FZKA 6208
INV-COBE(98)-D018

Quench Behavior of Zircaloy Fuel Rod Cladding Tubes. Small-Scale Experiments and Modeling of the Quench Phenomena

P. Hofmann, A. Miassoedov, L. Steinbock, M. Steinbrück, A. V. Berdyshev, A. V. Boldyrev, A. V. Palagin, V. E. Shestak, M. S. Veshchunov

Institut für Materialforschung
Projekt Nukleare Sicherheitsforschung

März 1999

Forschungszentrum Karlsruhe
Technik und Umwelt
Wissenschaftliche Berichte
FZKA 6208
INV-COBE(98)-D018

Quench Behavior of Zircaloy Fuel Rod Cladding Tubes. Small-Scale Experiments and Modeling of the Quench Phenomena

P. Hofmann, A. Miassoedov, L. Steinbock, M. Steinbrück,
A.V. Berdyshev*, A.V. Boldyrev*, A.V. Palagin*, V.E. Shestak*, M.S. Veshchunov*

Institut für Materialforschung
Projekt Nukleare Sicherheitsforschung

*Nuclear Safety Institute (IBRAE), Russian Academy of Sciences, Moscow

Forschungszentrum Karlsruhe GmbH, Karlsruhe
1999

Als Manuskript gedruckt

Forschungszentrum Karlsruhe GmbH
Postfach 3640, 76021 Karlsruhe

Mitglied der Hermann von Helmholtz-Gemeinschaft
Deutscher Forschungszentren (HGF)

ISSN 0947-8620

Summary

In all severe accidents scenarios the main goal of operator actions (AMM, accident management measure) will be the injection of water into the core region as soon as possible and as much as possible, in order to reestablish adequate core cooling for termination of the accident. Flooding of the uncovered core is the accident management measure with top priority. The quenching can cause renewed oxidation of the Zircaloy fuel rod cladding, resulting in a temporary temperature increase of the rods before cool-down occurs, a sharp increase in hydrogen production and the release of additional fission products. Especially a very high hydrogen production rate is of concern because any effective hydrogen mitigation system (catalytic recombiners, controlled deflagration) must be able to cope with such rates.

A series of separate-effects tests is being carried out on Zircaloy PWR fuel rod cladding to study the enhanced oxidation which can occur on quenching. In these tests single tube specimens are heated by induction to a high temperature and then rapidly cooled down by injection of a cold steam. The principal experimental parameters investigated are the extent of pre-oxidation and the temperature of the tube before cooldown. In particular, the main objectives of the experimental program are:

- to provide an extensive experimental database for the development of detailed mechanistic quench models;
- to investigate the physico-chemical behavior of the overheated fuel elements under different flooding conditions;
- to determine the cladding failure criteria, cracking of the oxide layer which results in oxidation of the new metallic surfaces and additional hydrogen production.

A total of 24 experiments has been performed with specimens with oxide layer thicknesses varying from 100 µm to 350 µm which were rapidly cooled by steam from 1100 °C, 1200 °C, 1400 °C and 1600 °C.

The experiments are supported by theoretical work at the Nuclear Safety Institute (IBRAE) (Russian Academy of Sciences), where modeling of the main processes taking place during reflooding is carried out. The following models were developed: a) thermal-hydraulic model QBOIL, b) heat conduction model QTEM, c) oxidation model QOXI (based on the partial derivatives solution) with a steam starvation model implemented, and d) improved mechanical deformation model QDEF. The various models are implemented in the code SVECHA and verified by experimental results. The new version of the SVECHA/QUENCH code provides a satisfactory reproduction of the experimentally observed temperature evolution curves over the full range of the single rod experimental conditions and correctly predicts the rod specimen failure modes (cracking, spalling, breaching) under the quench test conditions. The implementation of the steam starvation model makes it possible to describe the corresponding effect in the case of high temperature water quench tests.

Abschreckverhalten von Zirkaloy-Brennstabhüllrohren. Einzeleffektexperimente und Modellierung der Abschreckphänomene

Zusammenfassung

Bei einem schweren Unfall in einem Kernkraftwerk wird es das oberste Ziel der Betriebsmannschaft sein, den überhitzten und freistehenden Kern wieder mit Wasser zu bedecken, um damit eine ausreichende Kühlung und die Beendigung des Unfalls zu erreichen. Der Flutvorgang kann zu einer erneuten Oxidation der Zircaloy-Hüllrohre führen, die mit einer starken temporären Temperaturerhöhung der Brennstäbe sowie mit einer erhöhten Wasserstoffproduktion und Spaltproduktfreisetzung verbunden ist. Zur Auslegung von effektiven H_2-Abbausystemen (Rekombinatoren, kontrollierte Deflagration) bei bestehenden und zukünftigen Reaktoren müssen insbesondere die Wasserstoffproduktionsraten bei solchen Szenarien bekannt sein.

Im Rahmen des QUENCH-Programms am FZK werden Einzeleffektuntersuchungen zum Oxidationsverhalten von DWR- Brennelementhüllrohren beim Fluten durchgeführt. In diesen Experimenten werden 15 cm lange Brennstabsimulatoren mittels direkter induktiver Heizung auf eine vorbestimmte Temperatur aufgeheizt und anschließend in einem kalten Dampfstrom schnell abgekühlt. Die hauptsächlichen Parameter bei diesen Versuchen sind der Grad der Voroxidation und die Abschrecktemperatur. Die wesentlichen Ziele des Programms sind:

- die Gewinnung einer experimentellen Datenbasis für die Entwicklung von detaillierten mechanistischen Modellen zur Beschreibung des Abschreckverhaltens;
- die Untersuchung des physikalisch-chemischen Verhaltens von überhitzten Brennelementen unter verschiedenen Flutbedingungen;
- die Bestimmung eines Versagenskriteriums für die oxidierten Hüllrohre und Untersuchung der Rissbildung in den Oxidschichten, die zur Oxidation der dabei gebildeten metallischen Oberflächen und somit zu einer zusätzlichen Wasserstoffproduktion führen können.

Insgesamt wurden 24 Experimente durchgeführt. Die mit 100–350 µm Oxidschichtdicken voroxidierten Proben wurden bei Temperaturen von 1100 °C, 1200 °C, 1400 °C und 1600 °C abgeschreckt.

Die Experimente werden durch theoretische Arbeiten am Institut für Nukleare Sicherheit (IBRAE) der Russischen Akademie der Wissenschaften unterstützt, wo die Modellierung der maßgeblichen Prozesse beim Abschrecken durchgeführt wird. Die folgenden Modelle wurden im Rahmen dieser Arbeiten entwickelt: a) das thermohydraulische Modell QBOIL, b) das Wärmeleitungsmodell QTEM, c) das Oxidationsmodell QOXI, welches ein Dampfmangelmodell einschließt, und d) das verbesserte mechanische Deformationsmodell QDEF. Alle Modelle wurden in das Rechenprogramm SVECHA implementiert und mit den experimentellen Daten validiert. Die neue Version des Programmpakets SVECHA/QUENCH liefert eine sehr gute Übereinstimmung der experimentell ermittelten Temperaturverläufe mit den berechneten für die gesamte Testmatrix der Einzelstabversuche. Darüber hinaus werden die Versagensmechanismen der Hüllrohre (Rißbildung, Abplatzen von Oxidschichten, Bruch) unter Abschreckbedingungen von der Modellen richtig vorausgesagt. Die Einführung des Dampfmangelmodells erlaubt nun auch eine Beschreibung der Effekte beim Abschrecken von hohen Temperaturen mit Wasser.

Contents

1. Introduction

1.1 The hydrogen problem in Light Water Reactor safety

Light Water Reactor (LWR) safety studies have shown [1, 2] that in the very rare event of loss of coolant accidents (LOCA) or plant transients, combined with complete failure of the multiple safety injection systems, the reactor core will heatup and can be damaged severely. At temperatures above 1300 K metallic components of the core and the fuel can react with steam to produce hydrogen according to the following reactions:

$$Zr + 2H_2O \rightarrow ZrO_2 + 2H_2 + 576 \text{ kJ/mole Zr}, \tag{1.1}$$

$$2Cr + 3H_2O \rightarrow Cr_2O_3 + 3H_2 + 2 \cdot 186 \text{ kJ/mole Cr}, \tag{1.2}$$

$$Fe + H_2O \rightarrow FeO + H_2 + 3 \text{ kJ/mole Fe}, \tag{1.3}$$

$$UO_2 + xH_2O \rightarrow UO_{2+x} + xH_2. \tag{1.4}$$

Oxidation of the Zircaloy cladding is accompanied by a very significant energy release, whereas on the other hand Fe oxidation is energetically nearly neutral and the fuel oxidation by steam is negligible.

In large Pressurized Water Reactors (PWRs) of the 1000 to 1500 MW_e class the mass of hydrogen produced by the above reactions in case of a severe accident can be in the range of about 500 to 1500 kg. This hydrogen will be released at the break location of the primary coolant system into the containment atmosphere. Mixing with air and simultaneous steam condensation on the cold containment walls can lead to quite reactive H_2-air-steam mixtures, depending on details of the accident sequence.

Ignition of such mixtures would then create significant pressure loads on the containment walls and endanger the containment leak tightness.[†] Containment failure in the early accident phase, during which the atmosphere still contains high concentrations of volatile fission products and radioactive aerosols, would result in large contaminations of the environment, comparable to the Chernobyl accident. This can not be accepted.

[†]The energy released by combustion of 1 kg of hydrogen (120 MJ/kg) corresponds to that of 30 kg of TNT.

There is increasing consensus among licensing, regulatory, industrial and research organizations that such events must be avoided by introducing hydrogen control measurements and removal (recombiners) or conversion (ignitors) measures in existing as well as in future nuclear power plants. The recent amendment to the German Atomic Law requires exclusion of significant radiological consequences outside the plant, even in case of severe accidents [3].

1.2 Hydrogen generation during reflood

In all severe accidents scenarios the main goal of operator actions (AMM, accident management measure) will be the injection of water into the core region as soon as possible and as much as possible, in order to reestablish adequate core cooling for termination of the accident. Flooding of the uncovered core is the accident management measure with top priority. Reflood and quenching of an uncovered core can also be initiated automatically, e.g. by return of electric power in case of a station blackout scenario.

Quenching can be defined as the injection of water to cool the degrading core. It is postulated that the core is uncovered and continuously heats up due to decay heat from the radioactive fission products and the energy stored prior to the LOCA. In PWRs, the core is recovered by flooding from below, the overheated rods are quenched and adequate heat transfer is re-established. In certain types of PWRs emergency core cooling (ECC) injection occures at the top of the core, or combined top and bottom injections are also practiced. In Boiling Water Reactors (BWRs), the hot fuel rods may be quenched by a spray that forms a liquid film flowing down and cooling the rods together with bottom reflooding. Emergency coolant injection by bottom reflooding creates a rising quench front and upper water injection or core spray creates a falling film sputtering front. It is not yet clear which water injection mode (top or bottom or both) is most effective to cool the overheated core.

As a result of the high temperatures attained by the cladding ($\geq 1300\,K$) before the emergency coolant arrives, water does not initially wet the hot cladding surface (Leidenfrost phenomena). Quenching of hot surfaces occurs when the coolant reestablishes contact with the dry surface. The temperatures of the fuel pellets and fuel cladding are reduced by heat conduction and convection to the coolant. As the coolant rises in a hot channel or in the overheated nuclear fuel rod bundle, complex heat transfer and two-phase flow phenomena take place.

The quenching can cause renewed oxidation of the Zircaloy fuel rod cladding, resulting in a temporary temperature increase of the rods before cooldown occurs, a sharp increase in

hydrogen production and the release of additional fission products. The additional quench-related hydrogen might threaten the containment, and the increased fission product release increases the source term. Evidence for these effects has been obtained from the analysis of the TMI-2 accident [4], and in the bundle melt-down in-pile experiments LOFT LP-FP-2 [5], PBF SFD-ST [6] as well as in the CORA out-of-pile experiments CORA-12, CORA-13, CORA-17 [7, 8]. Additional evidence concerning the behavior of degraded cores on rapid cooling came from the PHEBUS B9R test [9], where oxidized and degraded rods were cooled by injected cold steam. Especially a very high hydrogen production rate is of concern because any effective hydrogen mitigation system must be able to cope with such rates. The ability to understand and model the underlying physical and chemical processes is necessary for the design of any meaningful hydrogen control and mitigation system.

Two explanations are currently put forward to explain the observed rapid increased hydrogen production during flooding:

- Formation of cracks in the oxide layer due to rapid cooling of the fuel rods which results in high mechanical stresses. The cracks create new surfaces of unoxidized metallic Zircaloy substrate. Another type of stress which may result in the formation of the cracks in the oxidized cladding are phase transitions in the materials during cooldown. Reaction of steam with the metallic components of the newly-formed surfaces leads to a local temperature escalation because of the exothermic Zircaloy/steam reaction and results in an additional rapid hydrogen generation.

- Uptake of hydrogen in Zircaloy during oxidation of the metal and its later release during quenching may possibly influence the source term [10, 11, 12]. Zirconium and Zircaloy can dissolve large amounts of hydrogen even at high temperatures. Therefore, Zircaloy can act as a sink or source of hydrogen, depending on the environmental conditions. In this way the hydrogen solubility of the cladding material can alter the hydrogen source term. The absorption of hydrogen by zirconium is a well-established phenomenon, its relative importance during reflood requires further investigation.

Attempts to model the hydrogen generation under reflood conditions were not successful so far, using the existing system codes like SCDAP/RELAP5, ICARE2, MELCOR, KESS or others. In the State of the Art Report (SOAR) [13] of the Committee on the Safety of Nuclear Installations (CSNI) it was concluded that the phenomena in quenching degraded core bundles by water injection were poorly understood and modeled by severe accident codes, and that codes need further detailed models to describe the particular physico-chemical reflood processes.

In this situation it appears necessary to undertake a detailed analysis of mechanisms governing the generation of new metallic surfaces during reflood by cracking and fragmentation of the oxygen-embrittled cladding and the resulting hydrogen production. A series of separate-effects tests has been conducted at Forschungszentrum Karlsruhe in which partially oxidized Zircaloy tube specimens have been rapidly cooled by water or by high-velocity cold steam, simulating conditions above the quench front where water has been completely evaporated. The tests provide the most detailed database on all important physico-chemical parameters needed for development of physically-based models describing generation of new metallic surfaces during quenching and their impact on the hydrogen source term.

1.3 Status of the modeling of quench phenomena

For the adequate evaluation of the hydrogen source term it is necessary to develop detailed physical models of the main processes and couple them self-consistently in a mechanistic code. Such a code named SVECHA/QUENCH (SQ) is being elaborated in the Nuclear Safety Institute (IBRAE) of the Russian Academy of Sciences (Moscow) on the basis of the FZK quench tests in close cooperation with the FZK experimentalists. The SQ code considers the following phenomena taking place during fuel rod bundle reflooding:

- heat exchange (heat conduction inside the multi-layered oxidizing fuel rod and heat convection in the surrounding water-steam media),
- oxidation of Zircaloy (Zry) cladding (heat and hydrogen release),
- mechanical behavior of the cladding (crack formation, oxide shell spalling, breaching),
- hydrogen absorption and desorption in the Zry/ZrO_2 cladding.

In its present state, the SVECHA/QUENCH code consists of the thermal-hydraulic module QBOIL, heat conduction module QTEM, oxidation module QOXI and mechanical deformation module QDEF. The hydrogen absorption/desorption module is developed as an internal part of the oxidation module.

The SQ code uses dense adaptive grids and small time steps and gives a detailed description of the single rod reflooding process. The accuracy of the SQ code predictions was confirmed by the comparison with FZK experimental results (see below).

There exist several possible ways for the application and further improvement of the single rod mechanistic SQ code:

- First, the SQ code may be used for the validation of the existing system codes: ICARE2, KESS, SCDAP/RELAP5, MELCOR, etc.
- After intensive verification against FZK separate-effects test results the SQ code models such as oxidation, hydrogen absorption, thermal-hydraulic or mechanical deformation models may be implemented in the existing system codes to improve the accuracy of the calculations.
- The other possibility is the implementation of the whole SQ code in the system code like ICARE2 or SCDAP/RELAP5. The important advantage of such implementation lies in the fact that in this case all modules relevant to quench phenomena will be coupled self-consistently and the code will be much less dependent on the meshing and global time step.
- The SQ code may be further developed and extended to the adequate description of the fuel rod bundle behavior during reflood.

The present report describes the current status of quench phenomena modeling by the SQ code as at the end of 1997. It is the continuation of the previous work [14] in which the description of the basic models was given.

In Section 3.1 a set of verification calculations against the full range of FZK single rod quench experiments (performed in 1995-1996) is described. A satisfactory reproduction of the measured rod surface temperature evolution at three axial elevations of each rod in the FZK tests (22 water and 6 steam quench experiments with various initial quench temperatures and different oxide layer thicknesses) was obtained by self-consistent operation of the SQ code numerical modules without additional adjusting of the code parameters. Implementation of the steam starvation model and its self-consistent operation with oxidation and heat exchange modules allowed the correct description of the oxidation kinetics and temperature escalation observed in the initial stage of the high temperature water quench experiments.

The main mechanisms of the crack formation and the influence of the cracks on the additional oxidation and hydrogen production observed in the FZK single-rod quench tests are described in Section 3.2. The possible reasons and criteria of the rod specimens failure under quench

conditions are qualitatively and quantitatively analyzed by the mechanical deformation model QDEF based on the self-consistent consideration of different physical-mechanical properties of various layers (β-Zr, α-Zr(O) and ZrO_2) of oxidizing cladding under complicated temperature transient conditions (phase transformation in the oxide and metal phases, steep temperature gradients) of the high-temperature quench tests.

In Section 3.3 a new kinetic model of hydrogen uptake and release by Zry cladding is developed and applied for modeling of the FZK separate-effects tests on hydrogen interactions with metal cladding under varying temperature and gas pressure conditions. Numerical simulations by the model confirm qualitative results of simplified analytical treatment of the problem and show a satisfactory agreement between measured kinetic curves and calculations.

In Section 3.4 the model is extended for the consideration of hydrogen absorption by Zr alloys during high temperature oxidation in steam. The consideration is based on the detailed experimental results of recent tests on the kinetics of hydrogen absorption by Zr-1%Nb cladding during steam oxidation in the temperature range from 900 to 1200 °C. The standard consideration of the steam oxidation process in the framework of the coupled anodic/cathodic reactions at the two oxide interfaces (gas/oxide and oxide/metal) is modified, taking into account that hydrogen may intrude into oxide in the form of positively charged protons. For quantitative description of the hydrogen behavior by this mechanism, mass transfer in the three layers: gas, oxide and metal, and at corresponding interfaces: gas/oxide and oxide/metal, is self-consistently considered. Numerical solution of the model generally confirms the main conclusions of simplified analytical treatment and provides a satisfactory agreement between measured kinetic curves and calculations.

2. Small-scale experiments

P. Hofmann, A. Miassoedov, L. Steinbock, M. Steinbrück
Institut für Materialforschung, Projekt Nukleare Sicherheitsforschung

A small-scale QUENCH rig was designed and build in which it is possible to quench short Zircaloy fuel rod segments by water or steam. The principal investigated experimental parameters are the extent of pre-oxidation and the temperature of the tube before cooldown. The experiments are supported by theoretical work at the Nuclear Safety Institute (Russian Academy of Sciences), where modeling of the main processes taking place during reflooding (heat exchange, oxidation of Zr, mechanical behavior of the cladding) is carried out. In particular, the main objectives of the experimental program are:

- to provide an extensive experimental database for the development of detailed mechanistic quench models;
- to investigate the physico-chemical behavior of the overheated fuel elements under different flooding conditions;
- to determine the cladding failure criteria, cracking of the oxide layer which results in oxidation of the new metallic surfaces and additional hydrogen production.

The design of the QUENCH rig is shown in Figure 2.1. The Zircaloy test specimen used in the tests is a cylindrical sample of a standard Siemens/KWU Zircaloy-4 fuel rod cladding tube with a length of 150 mm, an outer diameter of 10.75 mm and a wall thickness of 0.725 mm filled with high density ZrO_2 pellets with an outer diameter of 9.1 mm. The specimen is suspended by a thin Zircaloy capillary tube inside a quartz tube. Heating is provided by an induction coil around the section of the quartz tube enclosing the specimen. Power is supplied to the coil from a 20 kW oscillator, at a frequency of up to 700 kHz, which induces surface currents in the metal with consequent Joule heating. The QUENCH rig allows quenching by water or rapid cooldown by steam. The quench water is contained in a quartz cylinder which can be moved inside the outer quartz tube at a predetermined rate (0.3 – 3 cm/s). The heating of the specimen is terminated as soon as the water level in the quench cylinder reaches the 25 mm elevation of the specimen. The water level in the quench tube is kept constant by simultaneously raising a large balance water storage tank, which is connected to the quench tube. The water in the tank can be heated and is continuously circulated through the quench

cylinder. The tube specimen can also be cooled down by steam of about 150 °C which is injected into the test section simulating the conditions above the quench-water front. A steam flow rate of 1 g/s is used in the experiments with rapid steam cooling. The inductive heating of the specimen is terminated at the onset of cooldown by steam.

The scheme of the test conduct is presented in Figure 2.2. In the small-scale experiments the following phases for the test sequence are generally distinguished:

1. **initial phase**
   In the initial phase of the experiment the facility is prepared for the actual test. The specimen is heated up to 1000 °C under constant argon flow of about 90 l/h. After reaching the thermal equilibrium the steam from the steam generator is injected into the test section with a constant rate of 0.08 g/s.

2. **enhanced pre-oxidation period**
   During the pre-oxidation phase the specimen is heated up to 1400 °C under a constant flow of argon (90 l/h) and steam (0.08 g/s) through the test section. The specimen is then kept at this temperature until the desired oxide layer thickness is reached.

3. **cooldown**
   After reaching the needed oxide scale thickness the specimen is heated or cooled to the desired initial temperature at onset of cooldown (quenching). The test is then terminated by turning off the electric power. There are two possibilities to cool down the specimen after turning off the electric power: quenching by water (by raising the quench cylinder from below) or cooldown by injected steam (the argon flow is kept the same and steam flow is increased to 1 g/s).

During the experiment measurements of the temperatures, steam, argon and hydrogen flow rates and other facility parameters are performed. Gas analysis is conducted by means of two systems that are connected to the test section at two different positions by capillary tubes. One system (Caldos device) determines the hydrogen concentration in the outlet argon/hydrogen mixture by measuring the thermal conductivity of the dry gas after it has passed the condenser. The additional condenser volume is responsible then for the delay and smoothing of the hydrogen generation rate recordings, therefore, the Caldos device is used only as a redundant system. The other system (mass spectrometer) measures the gas above the test section before the condenser and gives a much better representation of the hydrogen generation rates.

Temperatures at the outer surface of the cladding are recorded at three elevations: 30 mm,

75 mm and 120 mm (referred to the lower end of the specimen). The temperature of the specimen has a substantial impact on the generation of the mechanical stresses in the material and on the oxidation kinetics. The accuracy of the temperature measurements has to be taken into account when interpreting the experimental results and using them for model development. Two different methods were used in the experiments performed earlier [14]. In the tests in a non-oxidizing atmosphere with pre-oxidized tube specimen, the legs of the Pt/Rh thermocouples were connected to the outer tube surface by a small pearl formed by welding, therefore the temperature curves always represent primarily the temperature of the hot thermocouple junction (pearl). In tests without pre-oxidation of the tube specimen a rhenium foil with a thickness of 150 µm and an area of 3x3 mm is spot-welded on the outer surface of the specimen (Fig. 2.3 a). The thermocouple pearl is then welded onto the foil (rhenium prevents the eutectic interaction of Zircaloy with the thermocouple materials). This arrangement guarantees a close contact between thermocouple and the specimen, but it cannot be used in an oxidizing atmosphere. In that case a pre-oxidized Zircaloy ring (outer diameter 11.8 mm, 0.8 mm thick) is used to fix the thermocouple pearl on the outer surface of the slightly pre-oxidized ($\leq$ 10µm ZrO_2) specimen (Fig. 2.3 b). The ring has a conical slope on its inner side to press the thermocouple onto the tube surface. The thin oxide layer prevents the chemical interaction between the cladding and the thermocouple. A small gap between the ring and the tube specimen forms at the position, where the thermocouple is pressed on the specimen. Though the two methods described above gave a good representation of the cladding temperatures, some difficulties occurred evaluating the experimental results, as indicated in [14]. The procedure of mounting the thermocouple onto the cladding surface was relatively complicated too. Therefore a new method was used in the experiments performed recently. The Pt/Rh thermocouples were tightly fastened on the cladding tube surface with a Pt/Rh wire (Fig. 2.3 c) and Fig. 2.4). A number of tests was performed to determine the reliability of the applied method of temperature measurements. In the tests with slightly oxidized cladding the temperature measured by the wire-attached thermocouple was about 40 °C lower than by the ring-pressed thermocouple because of the worse contact. With growing oxide layer thickness the contact becomes better and no difference between the two thermocouples attachments was observed. The advantages of the proposed method are reliable temperature measurements and easy handling, therefore it (Fig. 2.3 c) will be used in the future tests.

The thermocouple readings, the hydrogen generation rates detected both by Caldos device and mass spectrometer and the system overpressure for the whole test sequence are demonstrated in Figure 2.5 on the basis of the experiment with 216 µm ZrO_2 pre-oxidation and 1200 °C temperature at onset of rapid cooldown by steam. The two pressure peaks correspond to

the injection of 0.08 g/s steam at the beginning of the experiment and an increased injection of 1.0 g/s steam into the test section 30 s before the power is shutt-off. The injection of 1.0 g/s steam 30 s before power shutoff causes temporary decrease of the specimen temperature in all the experiments performed because of the better cooling. This temperature drop is soon compensated by increased electrical heating (Fig. 2.6). The Caldos device detects the hydrogen generation rate with a delay of about 60 seconds because of the additional condenser volume, which delays the transport of the generated hydrogen.

A total of 24 experiments has been performed with specimens with oxide layer thicknesses varying from 100 µm to 350 µm which were rapidly cooled by steam from 1100 °C, 1200 °C, 1400 °C and 1600 °C. The results of the experiments are discussed below.

2.1 Experimental results

The results of the experiments are summarized in Table 2.1 and presented in Figures 2.6 through 2.29. The time scales are referred to the onset of the steam cooling, i.e. zero time corresponds to the termination of the inductive heating. The plots represent the temperature-time history of the upper, central and lower thermocouple and hydrogen generation rate. The experiments releasing the largest amount of hydrogen were performed at high temperatures and experienced low pre-oxidation. Due to the experiment conduct it is not possible to prove the occurrence of crack surface oxidation during cooldown on the basis of the measured hydrogen generation which was clearly demonstrated in the experiments done before (pre-oxidized in an Ar/O_2 mixture) [14]. The amount of hydrogen released in the cooldown phase is low in comparison with the total hydrogen production during the whole test, therefore there is no direct indication that the oxidation of crack surfaces contributes to the total amount of the released hydrogen. In Figures 2.11, 2.18, 2.19 and 2.20 the system overpressure is presented together with the thermocouple readings and hydrogen generation rate. The increase of temperature and associated increase of hydrogen generation rate at the end of the cooldown is resulted from the shut off the steam injection and consequently reduced cooling of the specimen (pressure peak corresponds to the injection of 1.0 g/s steam and pressure drop-down corresponds to the shutoff of the steam supply).

High radiative heat losses in the QUENCH rig prevent significant temperature excursion during quenching such as had been observed for example in the CORA tests [15]. Nevertheless, a temperature deviation from the regular cooldown curve (Fig. 2.30) during the cooldown phase

was detected in all experiments with temperatures at onset of cooldown less than 1600 °C when the ZrO_2 layer thickness was larger than 200 µm (Figures 2.8, 2.9, 2.13, 2.14, 2.15, 2.16, 2.17, 2.20, 2.21, 2.22 and 2.23). No such temperature deviation during cooldown was observed in experiments cooled from 1600 °C even for large ZrO_2 layer thicknesses. The results are summarized graphically in Figure 2.31, which shows the presence or absence of an "escalation" phenomena. This slight temperature increase is always associated with the formation of through-wall cracks and occurred when the specimen surface temperature reached 900 – 800 °C during cooldown. Figure 2.32 shows the radial temperature distribution in the specimen at the moment when the cladding surface temperature is 800 °C calculated with the SVECHA code. The metal temperature is only 20 °C higher and no significant heat release due to oxidation at this temperature can take place. A possible explanation of this phenomenon could be the process of hydrogen absorption by metallic Zircaloy which is also exothermic and significant at this temperature. Results of investigation on hydrogen absorption are discussed later in this section.

The mechanical behavior of the Zircaloy cladding tubes can be recognized after the test by the number and type of cracks which form on cooldown in the oxide layer and the oxygen-stabilized α-Zircaloy substrate. Of main interest is the formation of the through-wall cracks since these cracks contribute most to the enhanced oxidation and increased hydrogen generation during quenching. The thicker the oxide layer on the Zircaloy cladding tube surface the thicker is also the α-Zr(O) layer and the smaller is the remaining ductile β-Zircaloy layer. Zirconia changes its crystal structure at about 1500 and 1200 °C during cooldown and this phase transition is accompanied by a volume increase, thus generating mechanical stresses in the oxide layer [16]. The α-Zr(O) layer is very brittle and is not able to withstand larger deformations which occur on cooldown as a result of the tetragonal to monoclinic ZrO_2 phase transformation.

The formation of through-wall cracks could be observed in specimens cooled by steam, with ZrO_2 layer thickness greater than 200 microns (the post-test examinations showed, that these specimens are generally very brittle, some specimens fragmented during handling after the experiments). In order to check which cracks completely penetrated the cladding tube a solvent was injected into the tube specimen. Figure 2.33 shows the result of an attempt to visualize cracks penetrating the oxide layer and the remaining metallic part of the cladding by filling segments of the cladding tubes with acetone. The solvent tracks seen on the right side of the figure indicate the pattern of cracks penetrating the cladding wall. These through-wall cracks can enable double-side cladding oxidation and consequent hydrogen generation. Figures 2.34 – 2.41 show the outer surface appearance of the tested pre-oxidized Zircaloy cladding

tubes after rapid cooldown by steam from 1100 – 1600 °C for different ZrO_2 thicknesses. At oxide layer thicknesses below about 130 µm no cracks can be observed, between 130 and about 200 µm two long axially-oriented through-wall cracks appear and at ZrO_2 layer thickness greater than 200 µm long axial and a net of additional axial and circumferential through-wall cracks forms.

Crack formation is more pronounced at lower specimen temperatures at onset of cooldown. Metallographic examinations show that most of the metallic Zircaloy is converted into the brittle oxygen-stabilized α-Zr(O). The surfaces of the cracks in the remaining metallic part of the cladding tubes are partially oxidized. The extent of oxidation of crack surfaces increases with decreasing temperature of the specimen at onset of cooldown (Figures 2.42 – 2.45). Needle-shaped cracks were observed when the specimen was cooled from higher temperatures. This result coincides with the observations in the QUENCH-01 bundle test [17] (Fig. 2.46). The absence of any oxidation of the crack surfaces during cooldown from the higher temperatures is not understood and requires further investigations.

2.2 Determination of the crack pattern on cladding tube surfaces

To determine the crack pattern and crack density, as already done for earlier experiments [18], the Zircaloy cladding tubes were mounted on a positioning device under the Leica M10 stereo microscope equipped with a digitizing electronic camera, to photograph and record the tube surface by a set of separate images.

The image assembly is now done with APL-programs. APL is a matrix language and the programs are very short and easier to maintain than the ALI-macros of OPTIMAS. Some of the image corrections have been changed. The illumination correction is no longer done with an image of a white reflecting tube but with the average from all subimages of a tube surface. The mathematical gluing is now done for both directions: the azimuthal and the axial directions. The earlier sharp cutting between the subimages is replaced with a smooth transition in azimutal and axial direction. A circumference is generated from 10 subimages each covering an angle of about 45 degrees. The changing distortion of the area element at the bottom and the top would cause blurring of the transition zone between the subimages. Therefore the subimage distortion at the top and bottom is corrected before the gluing process. The axial parallax distortion is too small to cause a problem and is neglected.

Polarized light is necessary in order to suppress the specular light artefacts due to the curvature

and specular diffusivity of the tube surface. The visibility of the cracks is enhanced by injection of a solvent with red pigment. Penetrating cracks are then visible via the following physical mechanisms: firstly the solvent fills the gaps between the columnar grains of the zirconium oxide and reduces the reflectivity of the surface. Secondly the red pigment viewed with green light further decreases the reflectivity of the cracked areas.

Experiment 25028_1 was first scanned with solvent only and then a second time with red pigmented solvent and green light (Fig. 2.47). The difference between the two images is great and they seem to have different tubes as origin. Looking closer one may detect the same crack patterns in both. But many cracks visible in the colored image are not visible in the uncolored one. The tube broke apart and was glued with cyanacrylate before the second scanning took place. The glue has probably sealed the cracks on the upper edge of the circumferential crack in the center of the tube. Therefore the red solvent could not penetrate the cracks. This example shows that the visibility of the crack patterns depends strongly on the properties of penetrating liquids. Gluing of the specimens should be avoided.

2.2.1 Oxide layer thickness measurements

The oxide layer thickness is the most important parameter governing the crack behavior of the pre-oxidized cladding tubes. The oxide layer thickness after an oxidation time at a certain temperature is estimated from earlier experiments or predicted by pre-calculations with the SVECHA code. However, the thickness of the oxide layer can be measured by two methods. The direct optical measurement on a metallographic cut of the specimen gives a precise measurement of the oxide layer thickness along the tube circumference at one axial location; this method is precise but it is time-consuming. The eddy current measurement yields thickness values for many points in a short time but this method is less precise and needs for calibration metallographic measurement data. Some of the specimens were measured with the eddy current device in order to verify the predicted values. The measurements presented in Table 2.1 show a big spread in the oxide layer thickness. In order to find a reason for that discrepancy a cut of the experiment 09028_1 was digitized (Fig. 2.48) and the oxide layer thickness was measured optically. The thickness of the layer at the 92 mm elevation is about 300 µm and is in good agreement with the predicted value 315 µm. The eddy current measurements however vary from 217 to 505 µm. When looking on the cross-section, many cracks are visible in the α-Zr(O) layer. Because this layer acts as the metallic substrate for the eddy current measurement, it is evident that the results vary so strongly. Therefore the spread in eddy current results indicate a strong variation in substrate continuity and not only in the

oxide layer thickness. In some of the experiments it was found, that at some locations the α-Zr(O) is sticking to the zirconia pellets inside the tube. Thus the cracking mechanism is dependent on three very different materials: the brittle oxide grown as dense columnar grains on the outside of the Zry tube, the α-Zr(O) being strained by the growing oxide outside and the solid zirconia which sticks to some points of the α-Zr(O). If different oxide growth is induced by small azimuthal temperature variations, the thermo-mechanical behavior is no longer axisymmetric and the tube bends and cracks no longer in a homogeneous way. The following analysis will show how representative the crack patterns are and should be changed in order to make the experiments more predictable.

2.2.2 Crack patterns of cladding tube specimens

The series of experiments with rapid cooldown by steam is summarized in Table 2.1. The lowest initiating temperature for cooldown was 1100 °C and the highest 1600 °C.The initial oxide layer thickness varied between 113 µm and 350 µm. In earlier experiments with a different pre-oxidation atmosphere (Ar/O_2 mixture) the length of the crack lines were correlated with the oxide layer thickness [18]. The present series show also a correlation between initial oxide layer thickness and total crack length. The initial thickness where cracking begins is about 150 µm. But the spread of crack length for example at 250 µm initial oxide layer thickness is rather large.

The cracking progression mechanism can be deducted by comparison of patterns for increasing oxide layer thickness (Figures 2.49 – 2.65). For instance experiments 12028_1 (Fig. 2.55) and 18028_1 (Fig. 2.58) with 150 and 157 µm oxide layer thickness but different temperatures of 1200 and 1400 °C at onset of cooldown show only two cracks on opposite sides of the tube and only a few and thin cracks extending from these main cracks in the azimuthal direction. With increasing oxide layer thickness to 176 and 216 µm (experiments 11028_1 (Fig. 2.53) and 11028_2 (Fig. 2.54)) the crack pattern still shows two or three main axial cracks but many circumferential or irregular cracks. The experiment 11028_1 shows a gradual change from the thin oxide pattern with two main axial cracks in the upper portion to the irregular crack pattern for thicker oxide layers in the lower portion of the tube specimen. This asymmetrical crack pattern is due to a difference in the oxide layer thickness. The eddy current measurement of the oxide thickness yields about 180 µm for the layer in the uncracked portion and about 210 µm in the densely cracked portion. The tube shows also a bending of about 5 mm and the outer side of the bending curve is the area with the many cracks and the thicker oxide layer. Thus the asymmetrical cracking may be explained by the asymmetrical oxide growth and the

associated strain. The spread of pre-oxidation status is shown also by the two experiments 19028_1 (Fig. 2.59) and 25028_1 (Fig. 2.60). Both tubes were oxidized during 19 minutes in order to yield 246 µm oxide layer thickness. However the oxide layer measured with eddy current has a thickness of up to 300 µm in the 25028_1 case and about 260 to 280 µm in the 19028_1 case. The latter tube is still intact, whereas the 25028_1 has broken already along two circumferential cracks. This shows that identical oxidation conditions do not necessarily yield the same oxide structure. The number and length of the cracks are about the same but the crack patterns of 19028_1 look more orthogonal than 25028_1.

Experiments with 1600 °C initial temperature

The series of specimens cooled from 1600 °C shows more regular crack patterns. Even with a thick oxide layer there are only a small number of two to four axial cracks with a few interconnections at oblique angles. It seems as if the thick oxide stabilizes the tube wall at high temperatures. The experiment 27028_1 with the thinnest oxide layer of 139 µm shows only two very short cracks. The experiment 03038_1 (Fig. 2.65) with 173 µm oxide layer shows two and a half axial cracks with some short cracks in parallel. The total crack length is 291 mm. The experiment 02038_1 (Fig. 2.64) which has a 201 µm oxide layer shows 3 axial cracks and a total length of 315 mm. The experiment 26028_1 (Fig. 2.63) with a thicker layer of 240 µm shows 3 main axial cracks with some oblique connecting cracks. The total crack length increases to 582 mm. These 4 tubes show cracks only with solvent filling. Without the solvent the oxide surface seems to be intact. The experiment 16028_1 with a (Fig. 2.62) 260 µm oxide layer thickness is the first where open cracks appear on the oxide surface. However the crack length 579 mm is about the same as for the experiment 26028_1 (Fig. 2.63) with a slightly thinner oxide layer.

Experiments with 1200 °C initial temperature

The experiment 09028_2 has the thinnest oxide layer of 113 µm and shows no cracks as in the experiment 04038_1 with a slightly thicker layer of 137 µm. Two axial cracks appear in the experiment 12028_1 (Fig. 2.55) with 157 µm oxide layer thickness. The experiment 11028_1 with a slightly thicker oxide layer was already discussed above. The different cracking behaviour in the upper and lower part of the tube indicates a break-away mechanism for cracks at this oxide layer thickness. The experiment 10028_1 (Fig. 2.52) with 201 µm (which was only a 25 µm thicker) oxide layer shows already a typical crack pattern with two or three axial cracks and irregular cracks connecting these axial cracks. At 287 µm oxide layer thickness the crack patterns look alike and the total crack length stays on a high level. The experiment 09028_1 with the thickest oxide layer of 315 µm is broken at several locations. It was filled

with epoxy in order to prepare a cut. The cut and its edge is shown in Figure 2.48.

The total length of the cracks was compared as a function of the temperature at onset of cooldown (Fig. 2.66) and initial oxide layer thickness (Fig. 2.67). At about 150 µm oxide layer thickness the total visible crack length rises sharply. But the spread of the crack length is high for experiments with about the same oxide layer thickness. In earlier experiments (water quenched) a sharp increase of crack length was found for about 200 µm initial oxide layer thickness. The current analysis shows that the crack formations begins already at thinner oxide layers and is more pronounced for thicker oxide layers [14].

2.3 Hydrogen absorption by Zircaloy during cooldown

During pre-oxidation in steam as well as during the quench process the hydrogen produced by the steam oxidation of the Zircaloy can be partially absorbed by the remaining metal phase. Separate-effects tests at high temperatures have shown a remarkable capacity of the zirconium for the storage of hydrogen.

The amount of absorbed hydrogen in specimens of the test series discussed in this report was analyzed in the so-called LAVA equipment. The LAVA is an inductively heated furnace with a crucible-type tungsten susceptor which permits heating specimens to above 2000 °C. The furnace is coupled via stainless steel pipes with a quadrupole mass spectrometer (Balzers GAM 300) with 8 mm rod system.

The hydrogen absorbed by the specimen is measured by releasing it at temperatures of about 1500 °C under a well-defined argon flow rate (20 l/h). The gas mixture is transported to the mass spectrometer where its composition is measured continuously. The hydrogen flow rate is calculated by referring the measured hydrogen concentration to the known argon flow rate (Eq. 2.1) and the total amount of hydrogen released is calculated by integrating this curve.

$$\dot{m}_{H_2} = \frac{M_{H_2}}{M_{Ar}} \cdot \frac{C_{H_2}}{C_{Ar}} \cdot \dot{m}_{Ar} \qquad (2.1)$$

Calibration measurements with Zr and Ti standard specimens have shown that the experimental error of these analyses is lower than 10 %.

For the analyses about 2 cm long cladding tube segments mostly taken from the middle part of the tube were used. From three tubes further specimens from the upper and lower part were also analyzed.

The results of the measurements are summarized in Table 2.2 and are presented in Figures 2.68–2.72. In general, the analysis of the results shows that after reaching certain oxide layer thickness (about 200 μm) and crack density, the amount of hydrogen absorbed in the metallic part of the Zircaloy tube increases considerably. In the case of cooldown from 1100 °C (Fig. 2.68) the amount of hydrogen absorbed in the specimen with 175 μm pre-oxidation is of about one order of magnitude lower than in the specimen with 255 μm pre-oxidation. The hydrogen content in the specimen with 255 μm pre-oxidation was measured at two locations (Table 2.7) and the results are very close to each other.

The same tendency was observed in the experiments with 1200 °C initial temperature at onset of cooldown (Fig. 2.69). The amount of hydrogen absorbed in the specimens with pre-oxidation larger than ≈ 200 μm is about ten times larger than for the specimens with pre-oxidation lower than 200 μm. The measurements of the absorbed hydrogen in the experiments 10028_1 and 11028_1 were performed at two different locations and the results are somewhat different from what one might expect. In these two experiments the deviation from the regular cooldown temperature was registered only by the upper thermocouple (see section 2.1, Figures 2.13, 2.14) and exactly at this elevation more hydrogen was absorbed. A possible explanation is that the temperature escalation at the upper elevation was triggered by the exothermal hydrogen absorption process, and this needs to be investigated further in the future.

In the experiments with cooldown from 1400 °C initial temperature (Fig. 2.70) the amount of the absorbed hydrogen again is very low for the low pre-oxidation and increases considerably with the increase of the pre-oxidation. There is a large difference in the results for the two identical experiments 19028_1 and 25028_1. These experiments were performed under the same conditions, but different behavior of the hydrogen release was observed (compare Fig. 2.21 and Fig. 2.22). The explanation for the different hydrogen content in the two experiments is given by the comparison of the crack patterns (Fig. 2.71). The total crack length in the 19028_1 experiment (908 mm) is approximately two times lower than in the 25028_1 experiment (1689 mm), in which about two times more hydrogen was absorbed.

Quite a different behavior is observed in the experiments with 1600 °C initial temperature at onset of cooldown (Fig. 2.72). For the low pre-oxidation the amount of absorbed hydrogen is very low and increases with increasing extent of the pre-oxidation. But even for large oxide layer thickness (≈ 300 μm in the experiment 02038_1) this amount is still relatively low in comparison with similar specimens cooled from 1100, 1200 and 1400 °C. Only for very large oxide layer thickness (≈ 380 μm in the experiment 16028_1) the amount of absorbed hydrogen is significant. Again the difference in the amount of the absorbed hydrogen could be explained

by the different crack length (315 mm in 02038_1 and 579 mm in 16028_1, see also Figures 2.64 and 2.62).

It seems that the amount of the absorbed hydrogen correlates not only with the extent of the pre-oxidation at the onset of cooldown, but also with the total crack length. It is still not clear why the same conditions in the experiments 19028_1 and 25028_1 lead to different crack patterns and consequently to different content of the absorbed hydrogen. The possibility of the hydrogen absorption process to trigger the temperature escalation must be studied in detail in the future.

Test ID	Time of pre-oxidation at 1400 °C, min	Precalculated oxide thick-ness at onset of cooldown, µm	Tempera-ture peak	Total H_2 production, mg	Crack length, mm	Measured oxide layer thickness, µm
cooldown from 1100 °C: 4 experiments						
04038_2	4	135	No	114.7	0	-
05038_1	19	270	UC	244.5	203	270[1)], 255[2)]
05038_2	12	215	UC	184.4	-	210[2)]
06038_1	7	170	No	131.8	0	175[1)]
cooldown from 1200 °C: 8 experiments						
09028_1	30	315	UC	379.7	0	290[1)]
09028_2	3	113	No	120.1	0	-
10028_1	12	201	U	239.5	1095	212[1)], 210[2)]
11028_1	9	176	U	203.0	734	185[1)], 190[2)]
11028_2	14	216	UC	246.4	1368	-
12028_1	7	157	No	184.8	255	167[1)]
13028_2	25	287	UC	295.0	1362	-
04038_1	5	137	No	122.9	0	-
cooldown from 1400 °C: 6 experiments						
17028_1	26	290	UC	330.0	437	-
18028_1	7	150	No	145.8	165	160[1)]
18028_2	12	195	UC	203.7	300	-
19028_1	19	246	UC	232.3	908	260[1)]
25028_1	19	246	UC	255.1	1689	265[1)]
25028_2	4	116	No	82.0	136	-
cooldown from 1600 °C (pre-oxidation at 1400 °C, then cooldown): 3 experiments						
16028_1	5	260	No	170.8	579	380[2)]
16028_2	6	290	No	170.2	700	370[2)]
26028_1	2	240	No	129.2	582	-
cooldown from 1600 °C (pre-oxidation during heatup from 1000 °C to 1600 °C, then cooldown): 3 experiments						
27028_1	3	139	No	20.1	10	163[1)]
02038_1	7	201	No	65.1	315	296[1)]
03038_1	5	173	No	39.2	291	-

Table 2.1: Experiments with cooldown by steam. UC: Deviation from the regular cooldown curve was registered by [C]entral and/or [U]upper thermocouple. [1)]oxide thickness measured at elevation 65–85 mm; [2)]oxide thickness measured at elevation 105–125 mm.

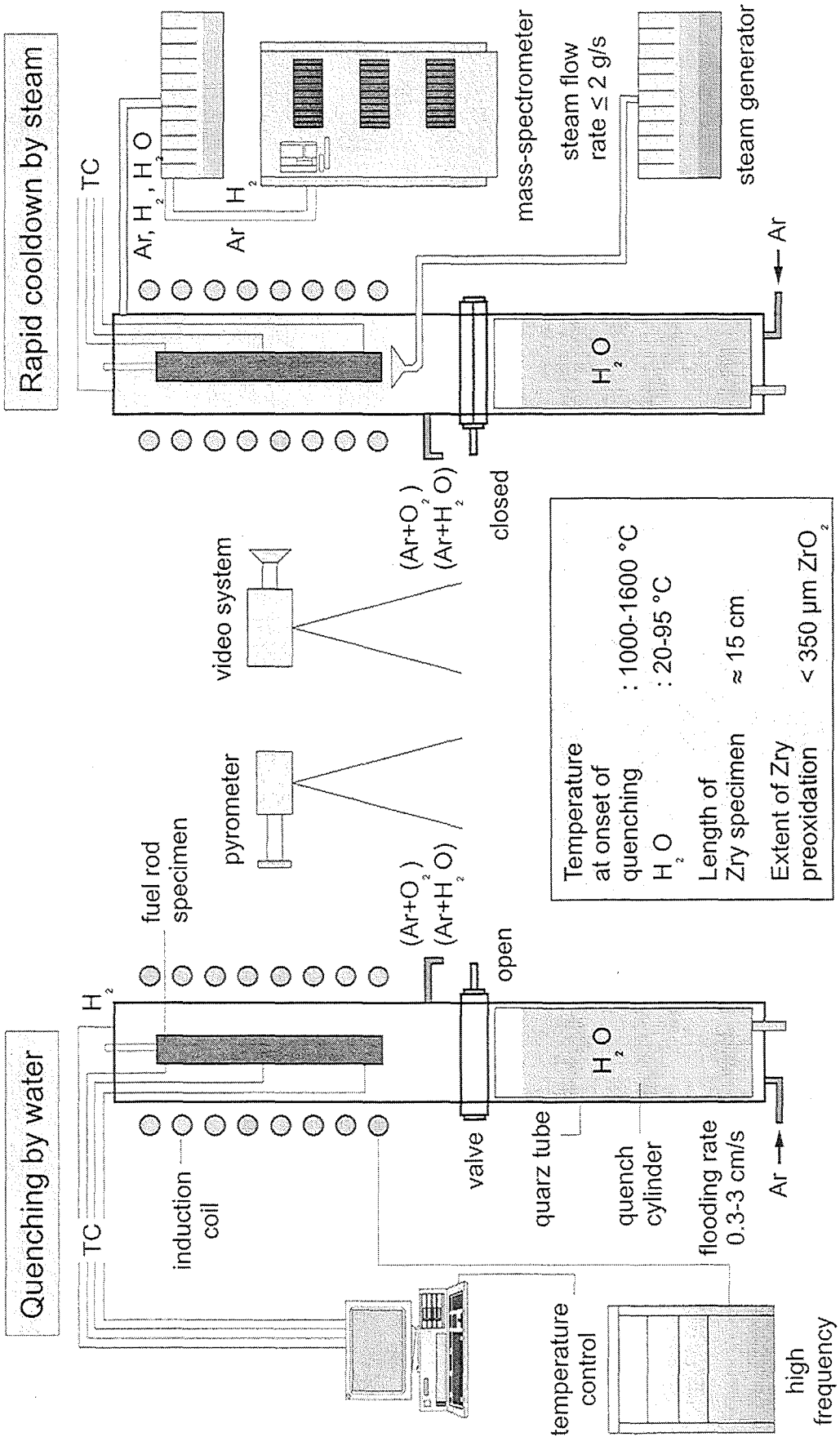

Figure 2.1: Quench apparatus simulating flooding conditions of an overheated fuel rod.

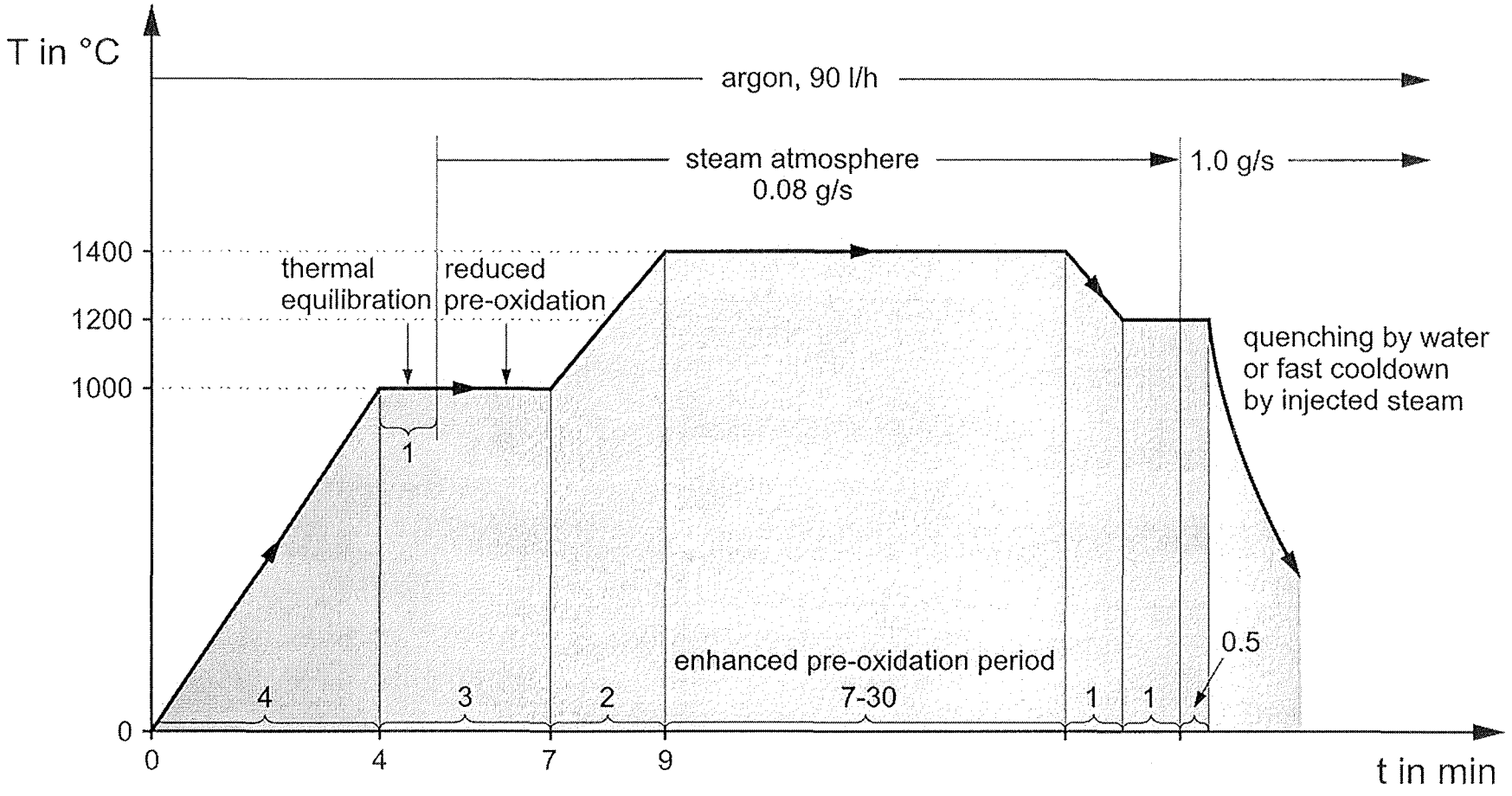

Figure 2.2: Test conduct of single rod quench experiments.

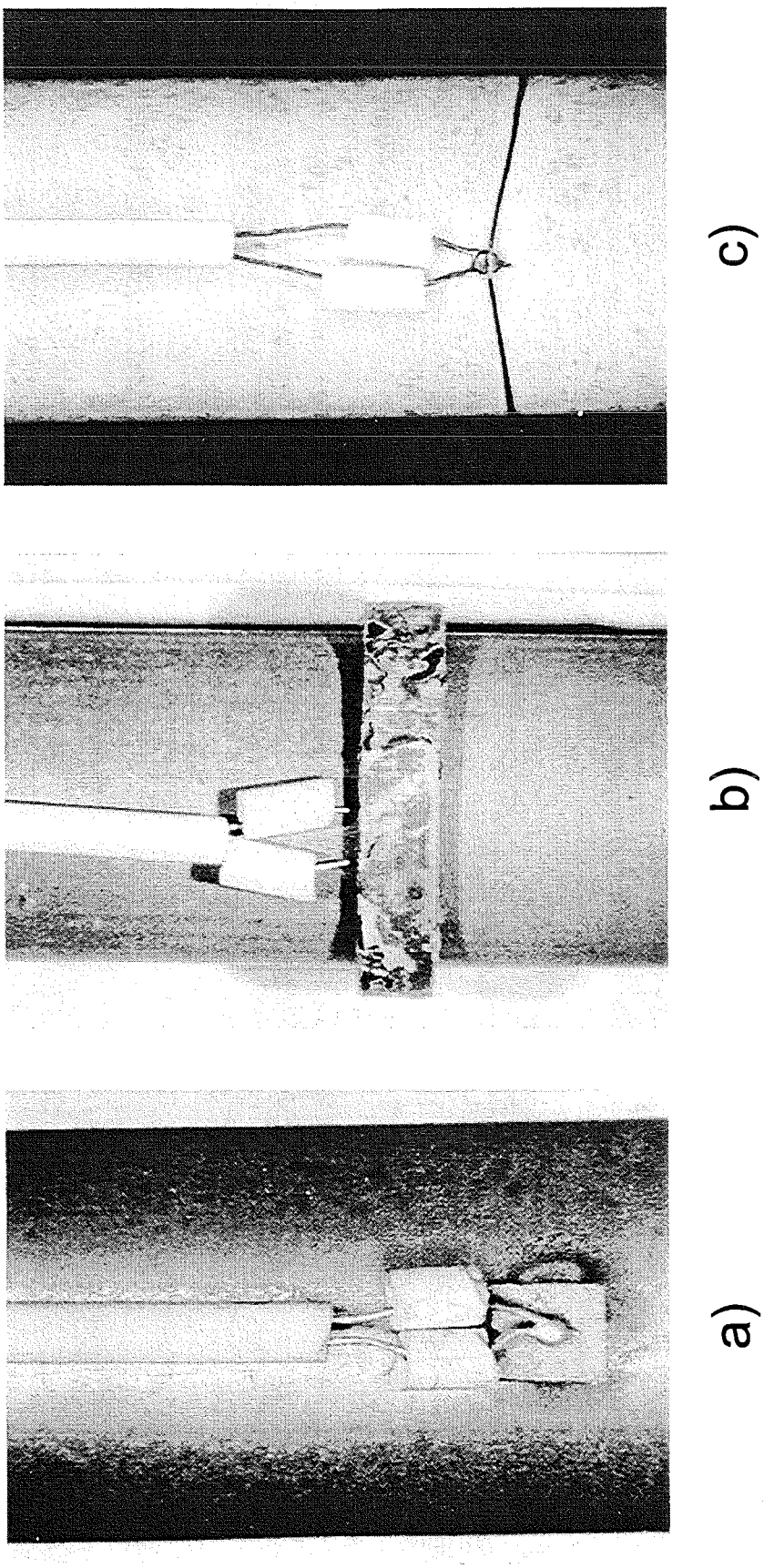

Figure 2.3: Different methods used for thermocouple attachment in the small-scale experiments: a) foil-welded TC, b) ring-pressed TC , c) wire-attached TC.

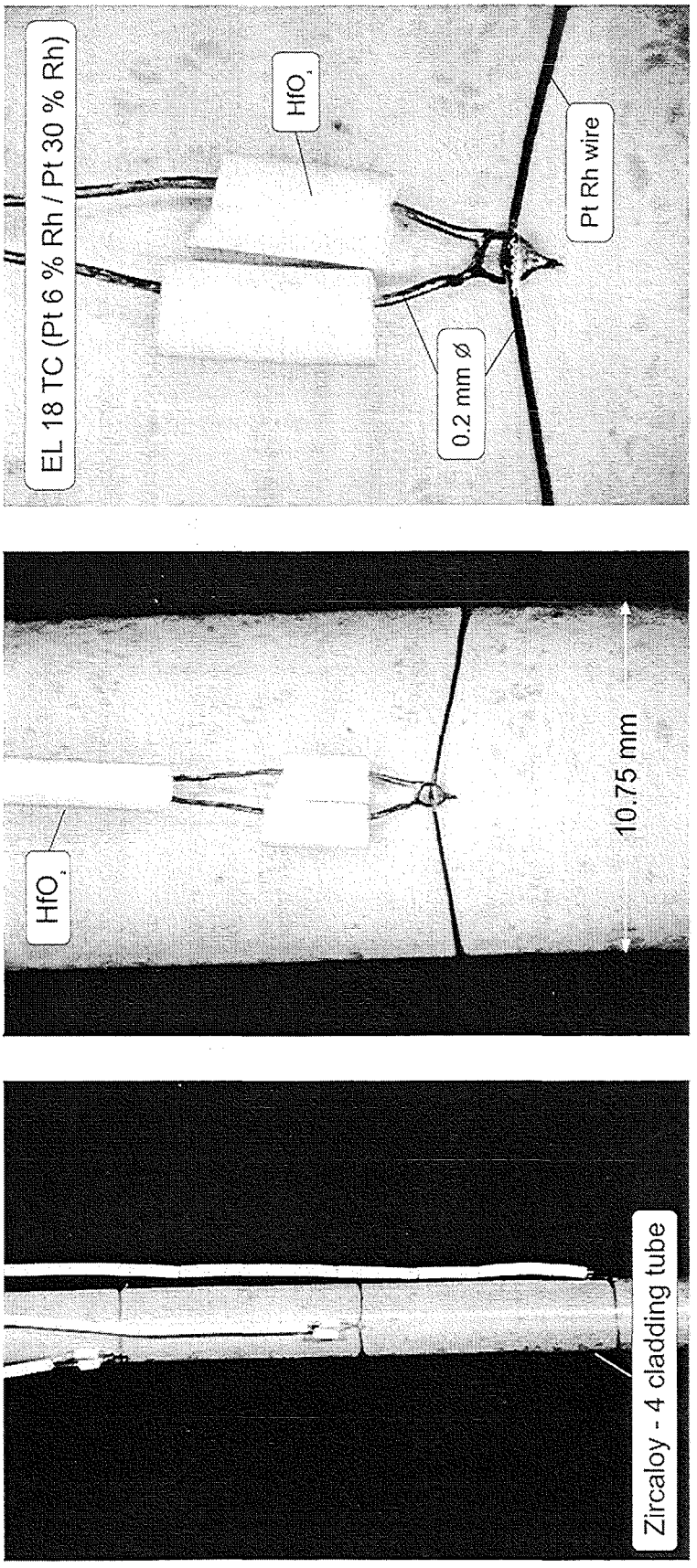

Figure 2.4: Thermocouple attached onto the Zircaloy tube surface by a Pt/Rh wire.

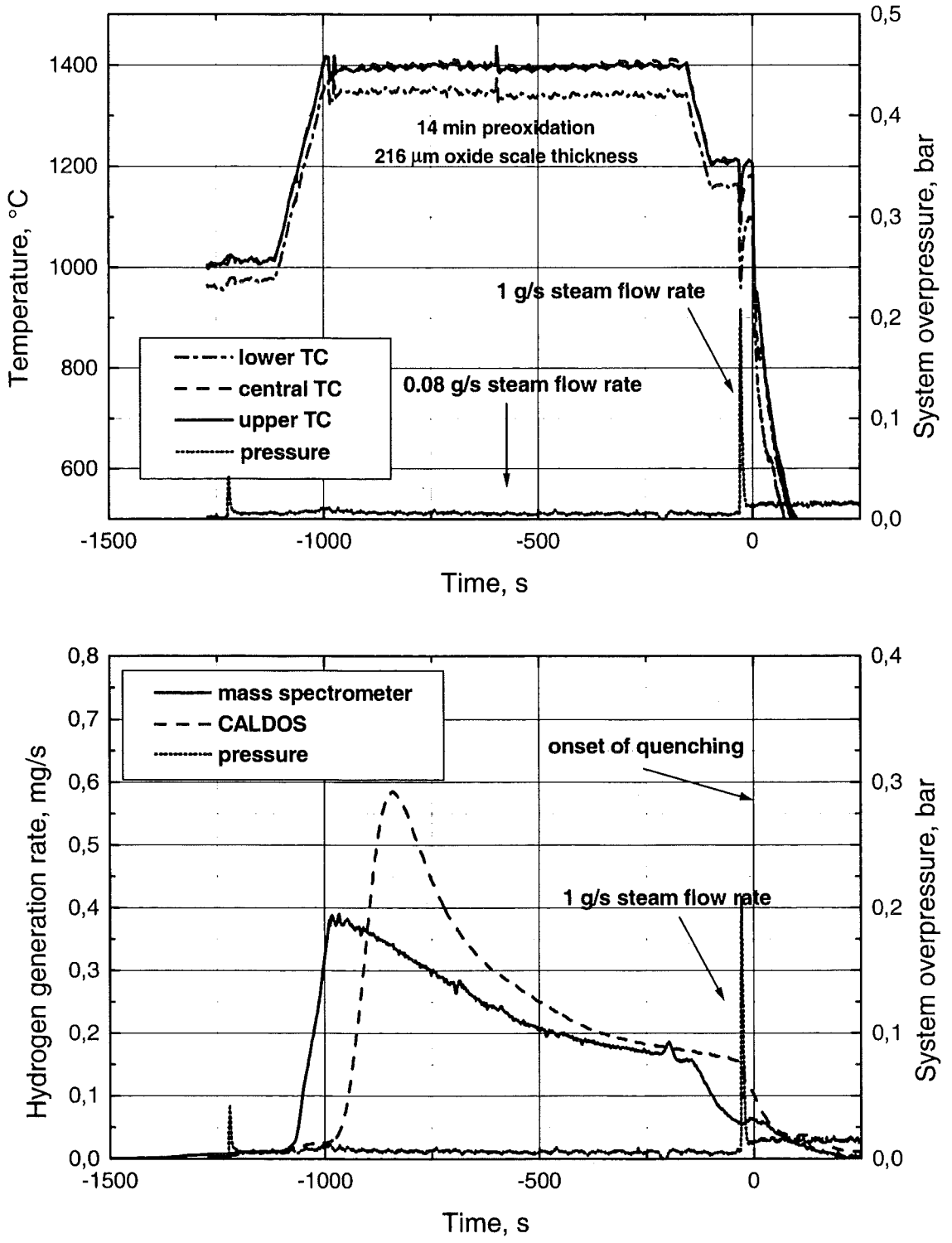

Figure 2.5: Experiment 11028_2: temperature history of the upper, central and lower thermocouple and corresponding hydrogen release rate; rapid cooldown by steam from 1200 °C; pre-calculated oxide layer thickness 216 µm.

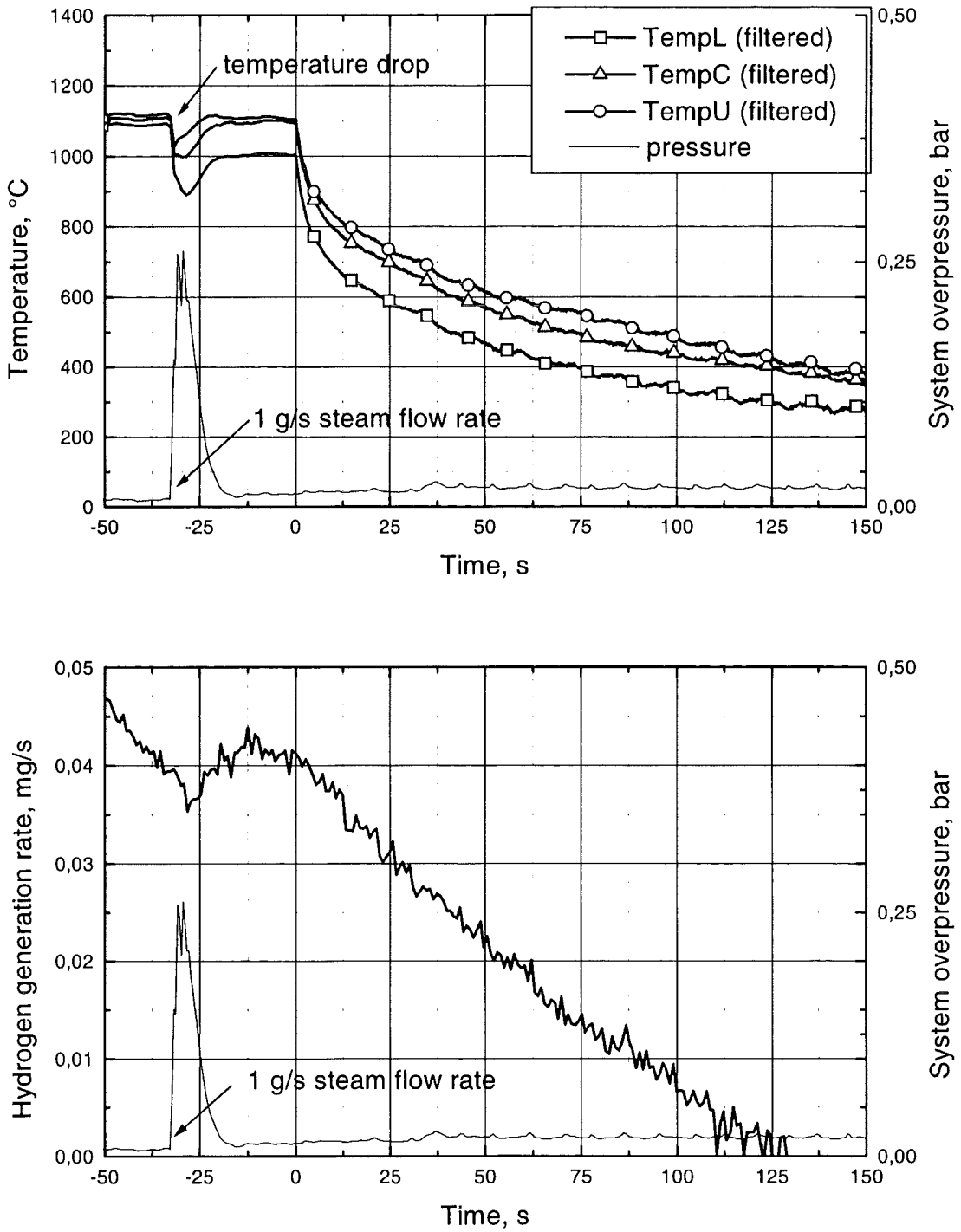

Figure 2.6: Experiment 04038_2: temperature history of the upper, central and lower thermocouple and corresponding hydrogen release rate; rapid cooldown by steam from 1100 °C; pre-calculated oxide layer thickness 135 µm.

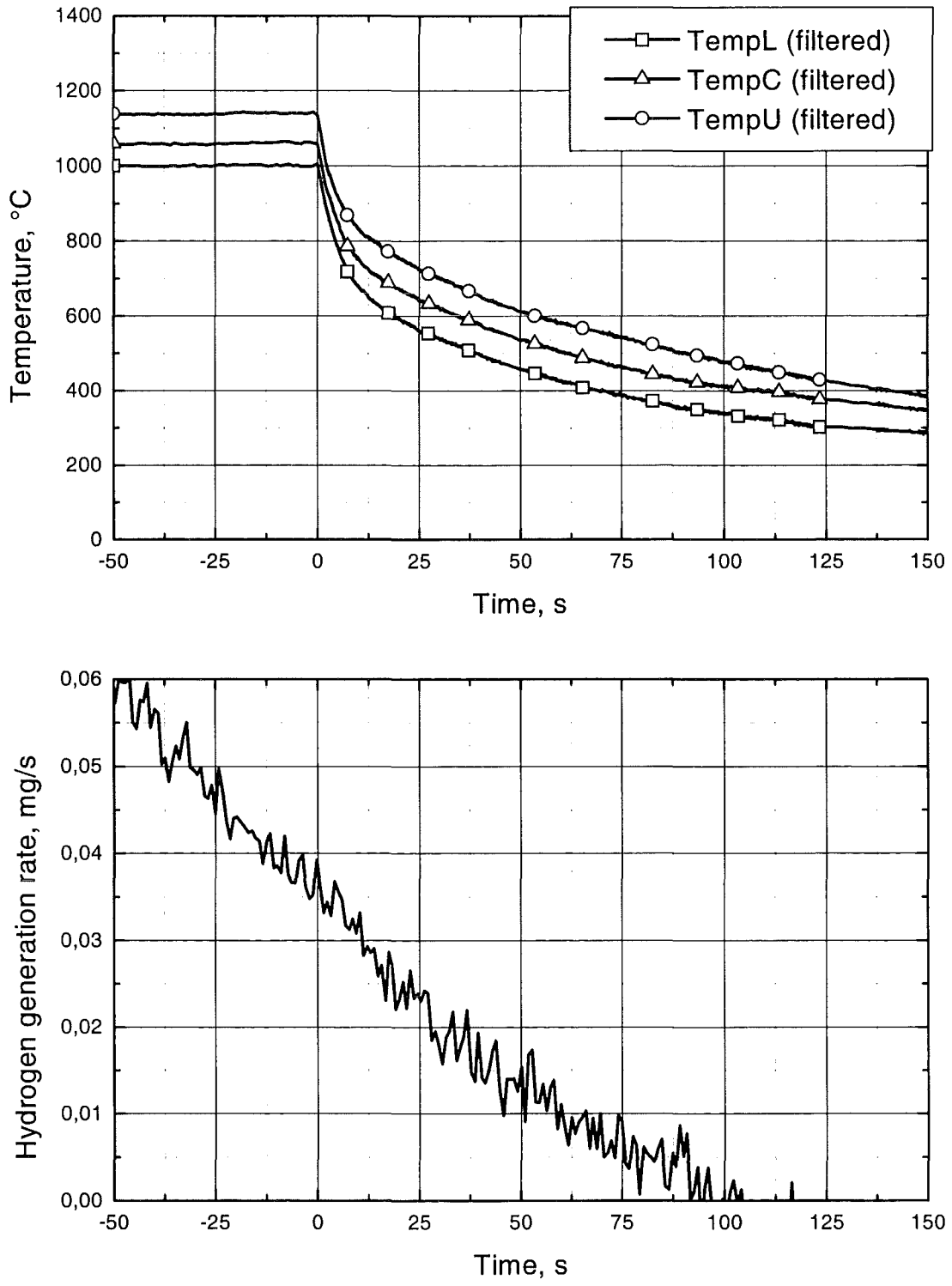

Figure 2.7: Experiment 06038_1: temperature history of the upper, central and lower thermocouple and corresponding hydrogen release rate; rapid cooldown by steam from 1100 °C; pre-calculated oxide layer thickness 170 µm.

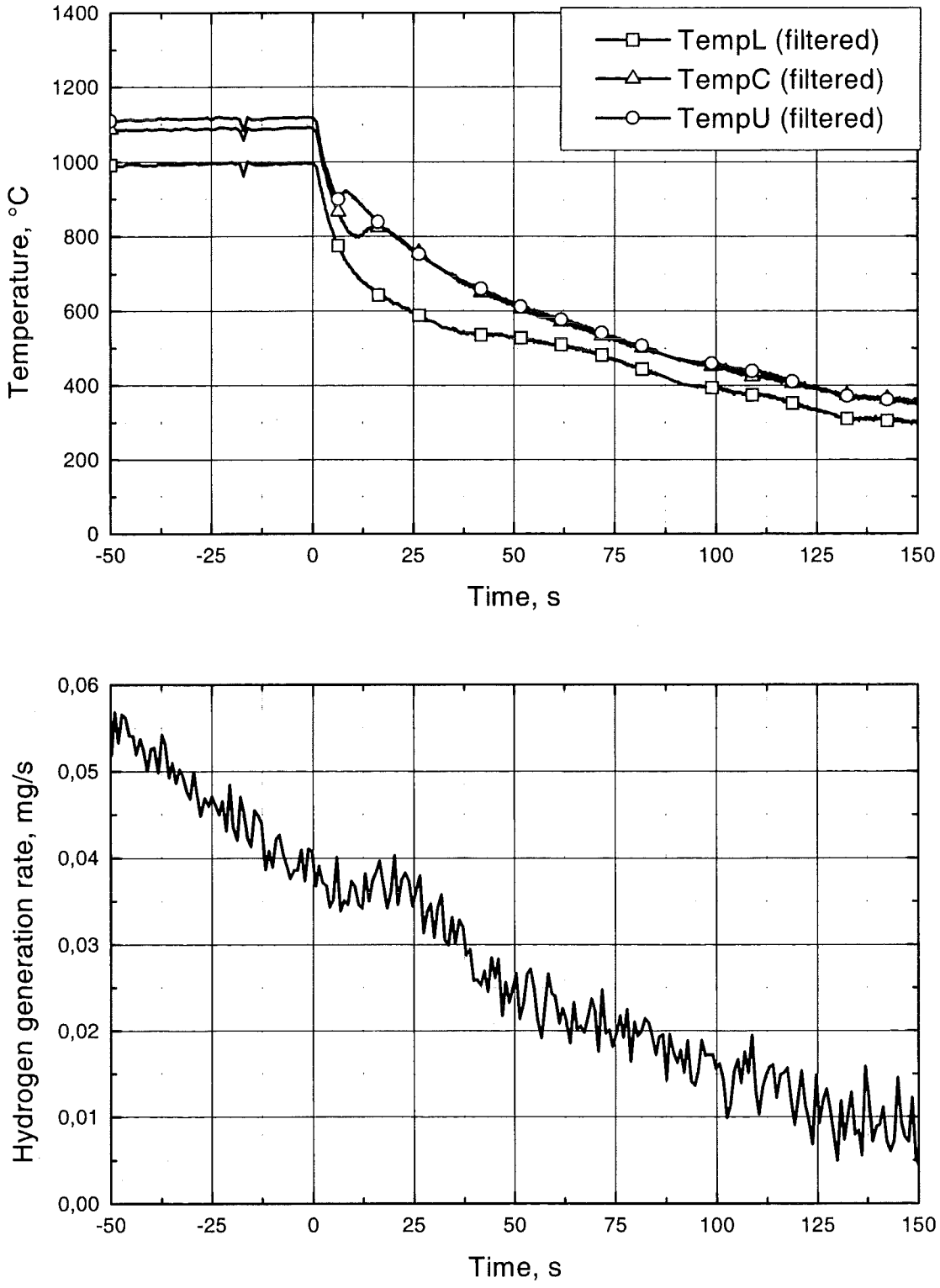

Figure 2.8: Experiment 05038_2: temperature history of the upper, central and lower thermocouple and corresponding hydrogen release rate; rapid cooldown by steam from 1100 °C; pre-calculated oxide layer thickness 215 µm.

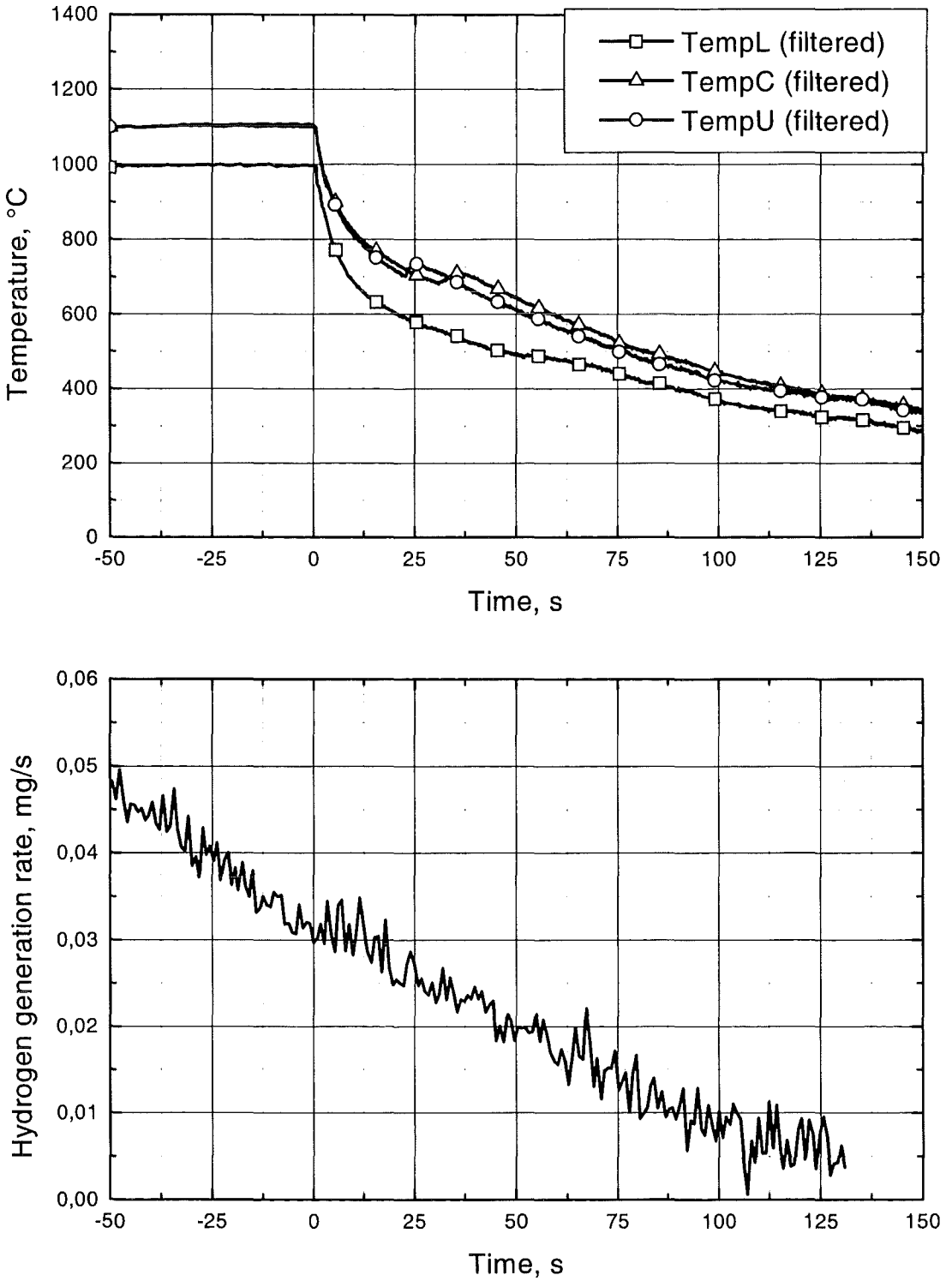

Figure 2.9: Experiment 05038_1: temperature history of the upper, central and lower thermocouple and corresponding hydrogen release rate; rapid cooldown by steam from 1100 °C; pre-calculated oxide layer thickness 270 µm.

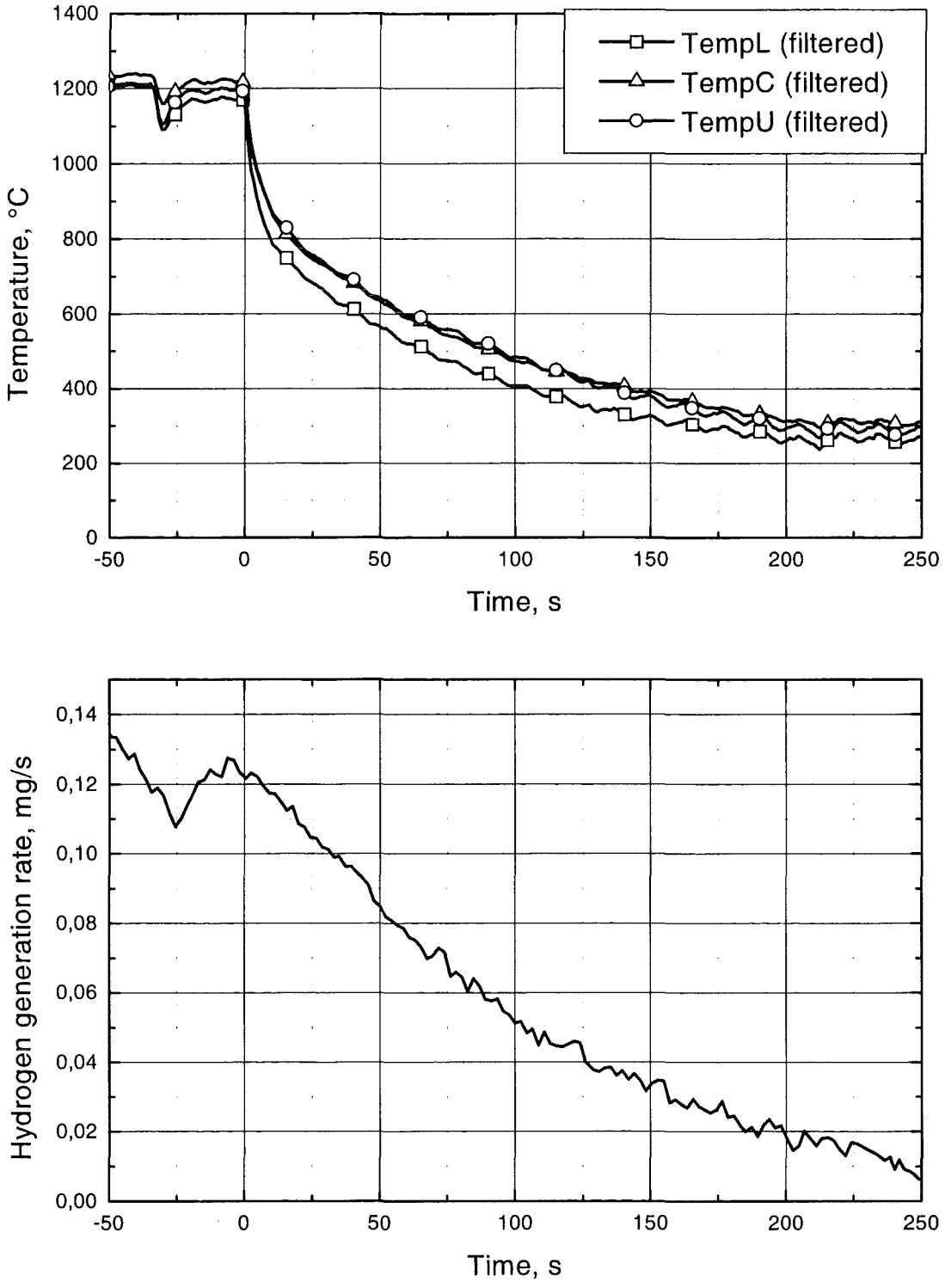

Figure 2.10: Experiment 09028_2: temperature history of the upper, central and lower thermocouple and corresponding hydrogen release rate; rapid cooldown by steam from 1200 °C; pre-calculated oxide layer thickness 113 µm.

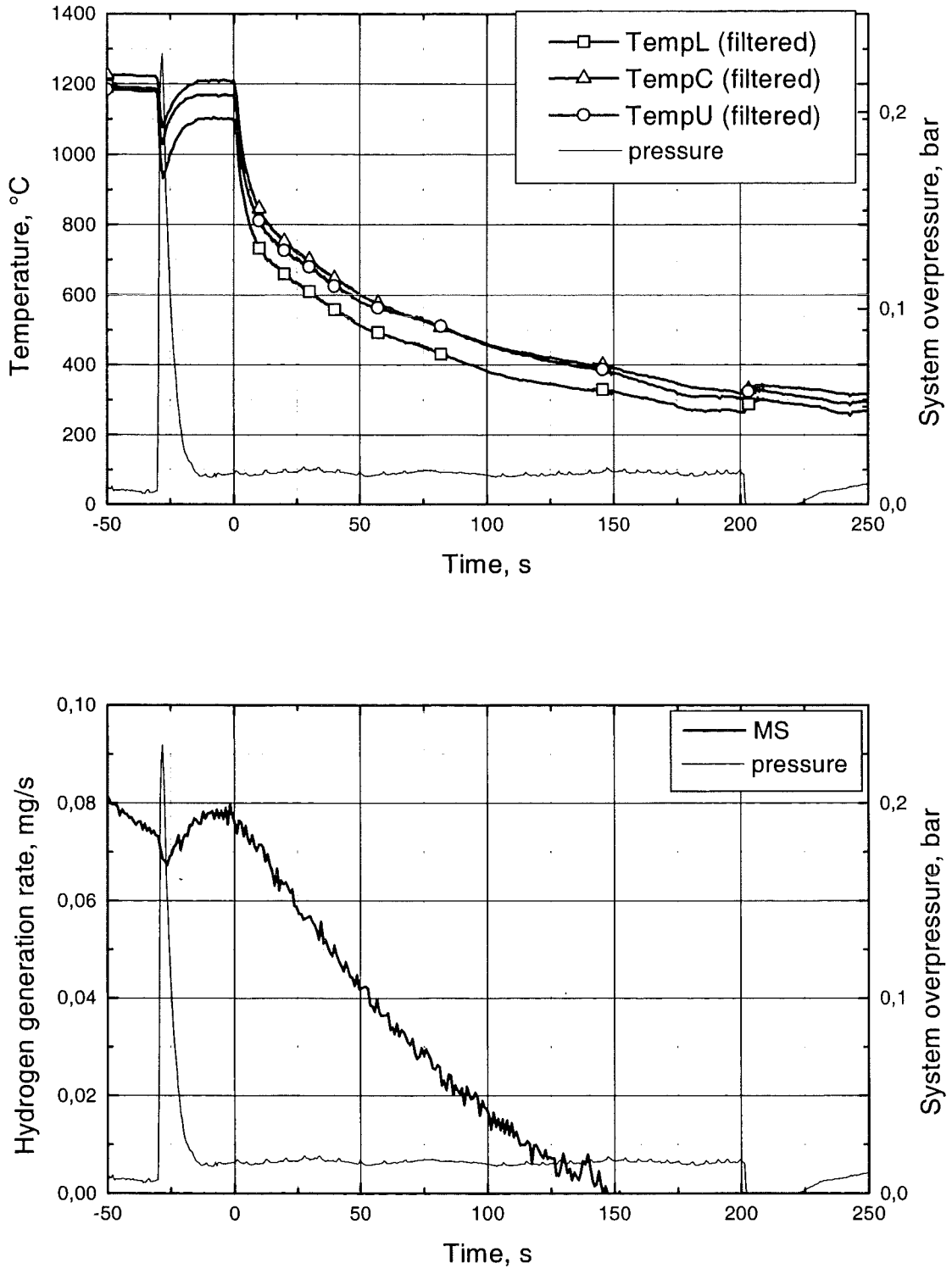

Figure 2.11: Experiment 04038_1: temperature history of the upper, central and lower thermocouple and corresponding hydrogen release rate; rapid cooldown by steam from 1200 °C; pre-calculated oxide layer thickness 137 µm.

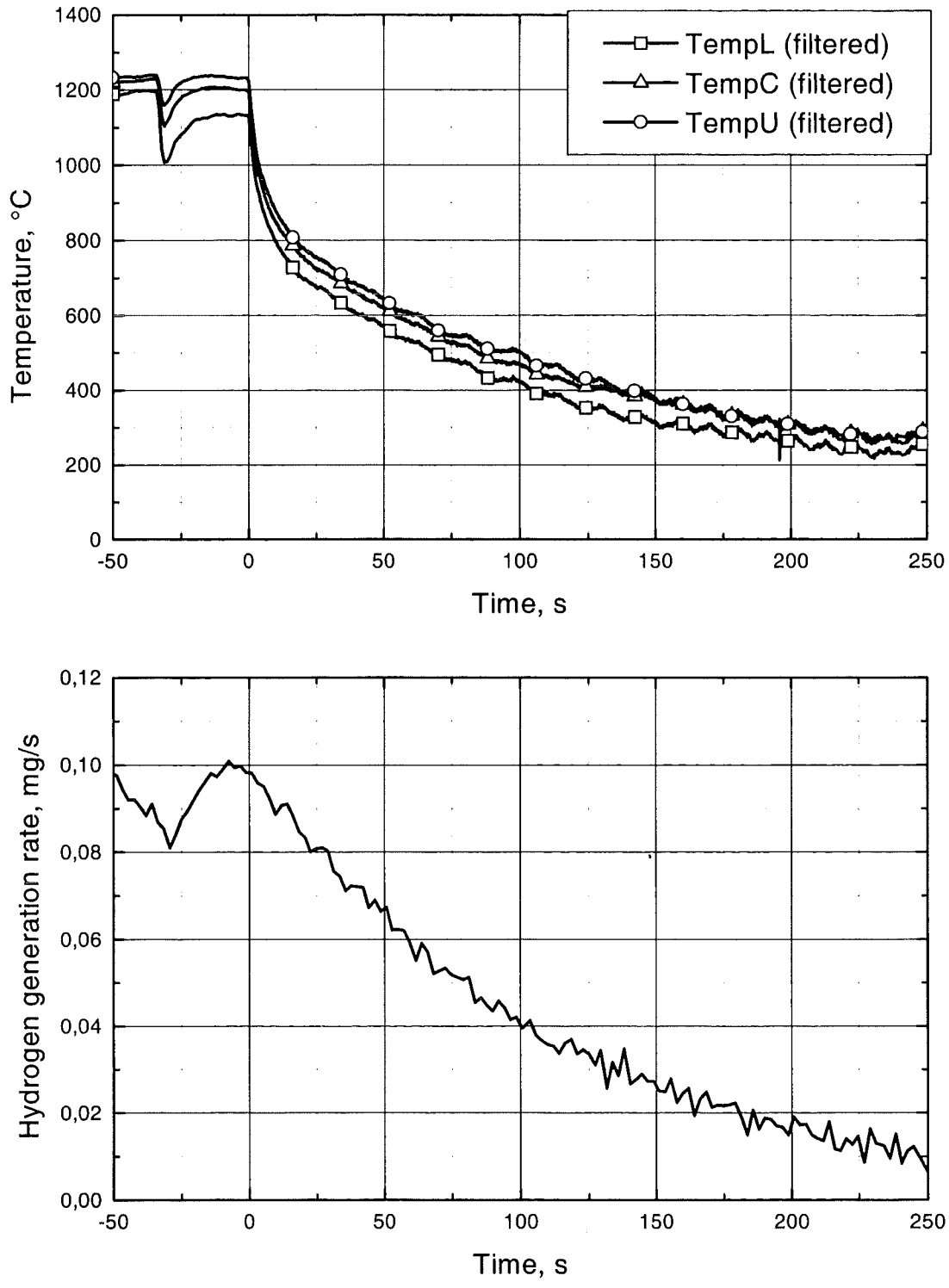

Figure 2.12: Experiment 12028_1: temperature history of the upper, central and lower thermocouple and corresponding hydrogen release rate; rapid cooldown by steam from 1200 °C; pre-calculated oxide layer thickness 157 µm.

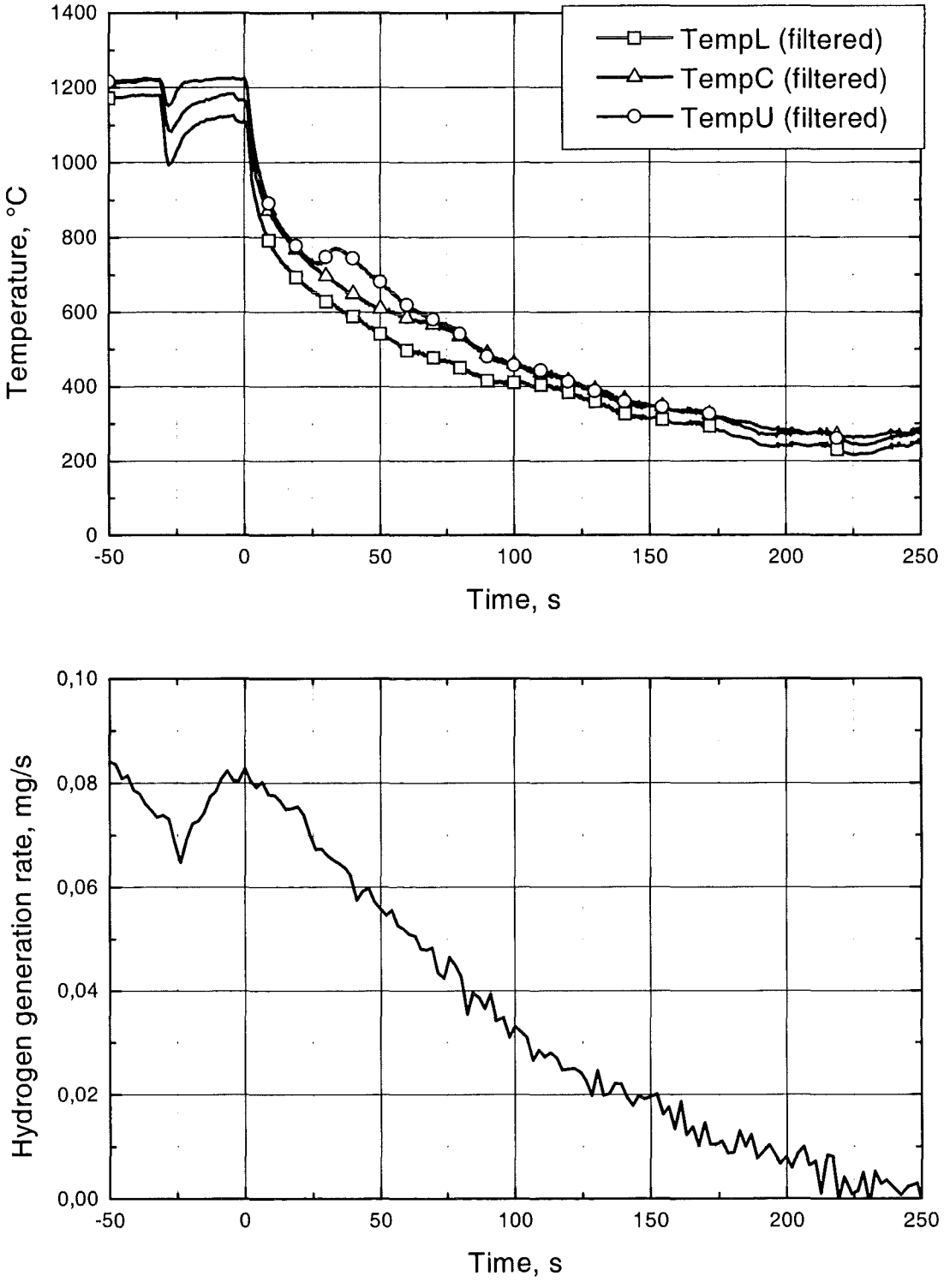

Figure 2.13: Experiment 11028_1: temperature history of the upper, central and lower thermocouple and corresponding hydrogen release rate; rapid cooldown by steam from 1200 °C; pre-calculated oxide layer thickness 176 µm.

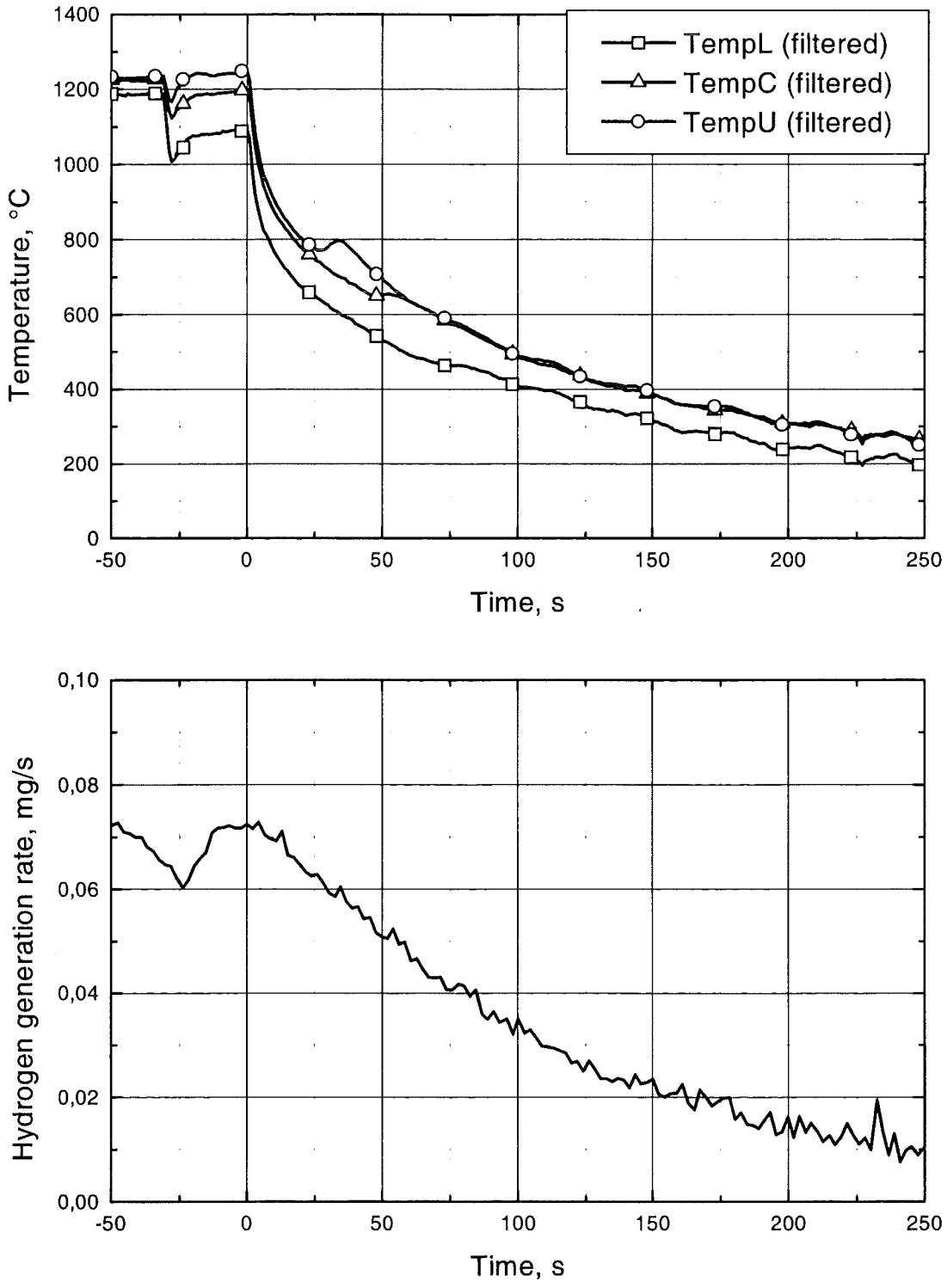

Figure 2.14: Experiment 10028_1: temperature history of the upper, central and lower thermocouple and corresponding hydrogen release rate; rapid cooldown by steam from 1200 °C; pre-calculated oxide layer thickness 201 µm.

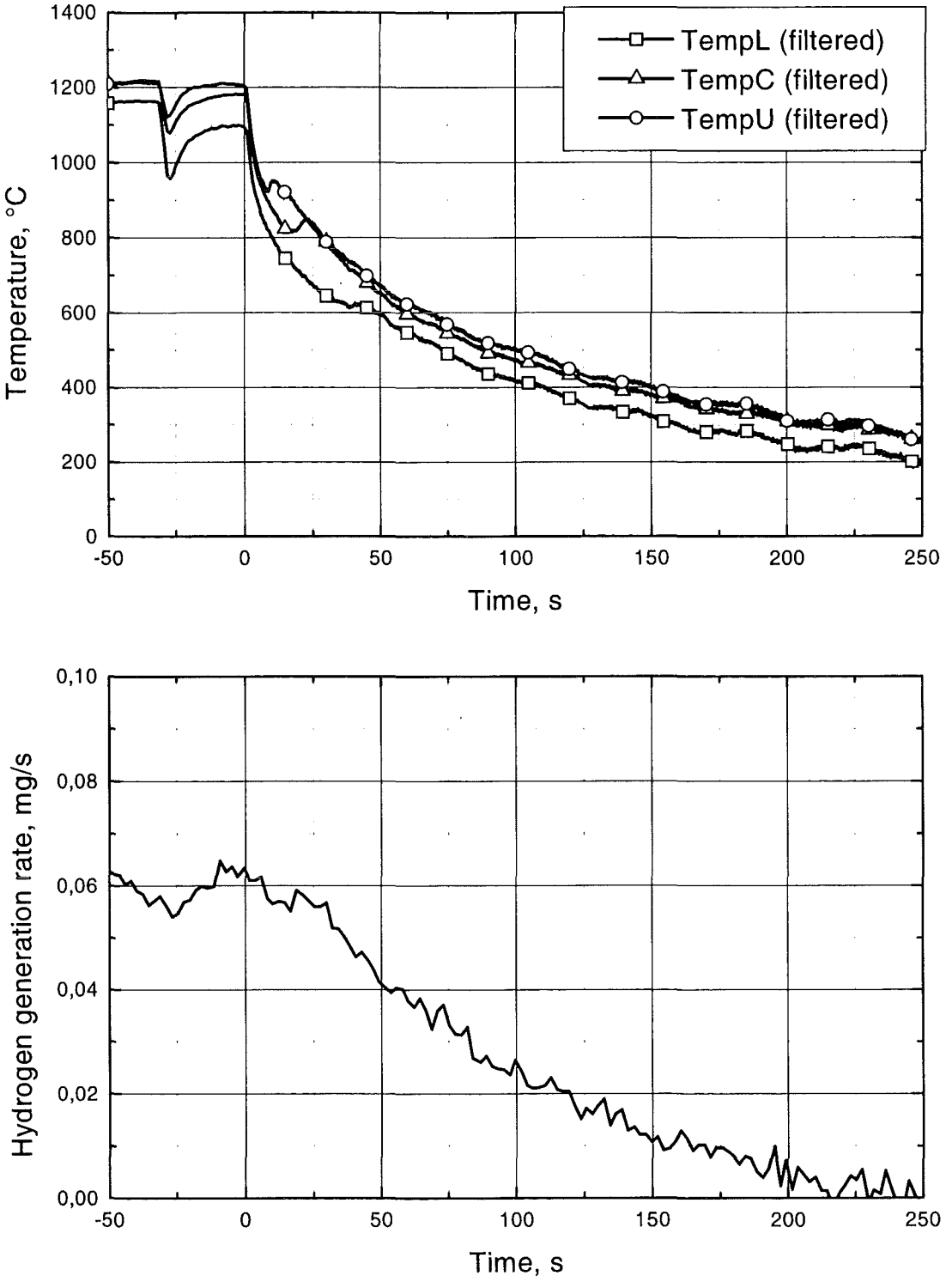

Figure 2.15: Experiment 11028_2: temperature history of the upper, central and lower thermocouple and corresponding hydrogen release rate; rapid cooldown by steam from 1200 °C; pre-calculated oxide layer thickness 216 µm.

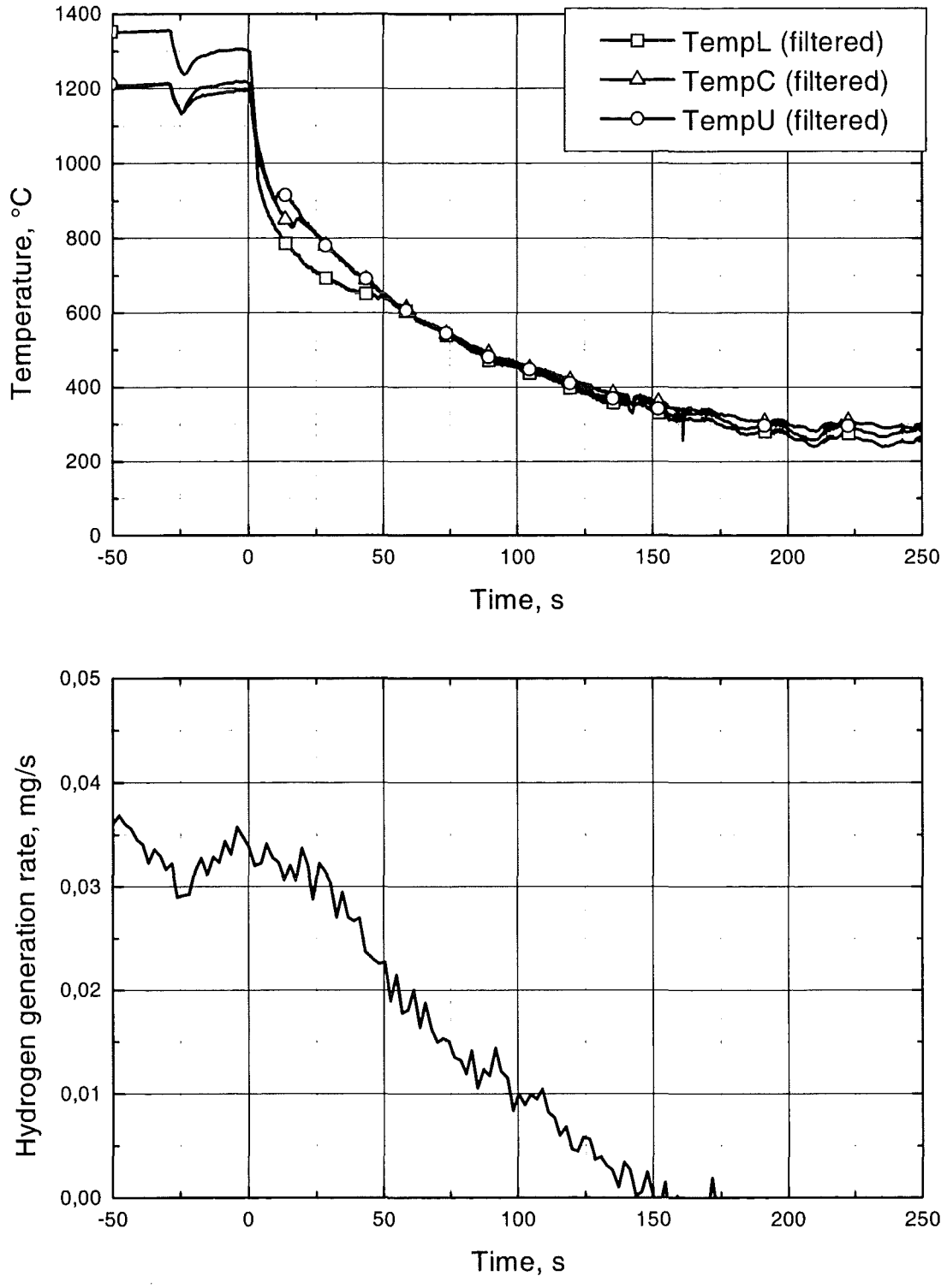

Figure 2.16: Experiment 13028_1: temperature history of the upper, central and lower thermocouple and corresponding hydrogen release rate; rapid cooldown by steam from 1200 °C; pre-calculated oxide layer thickness 287 µm.

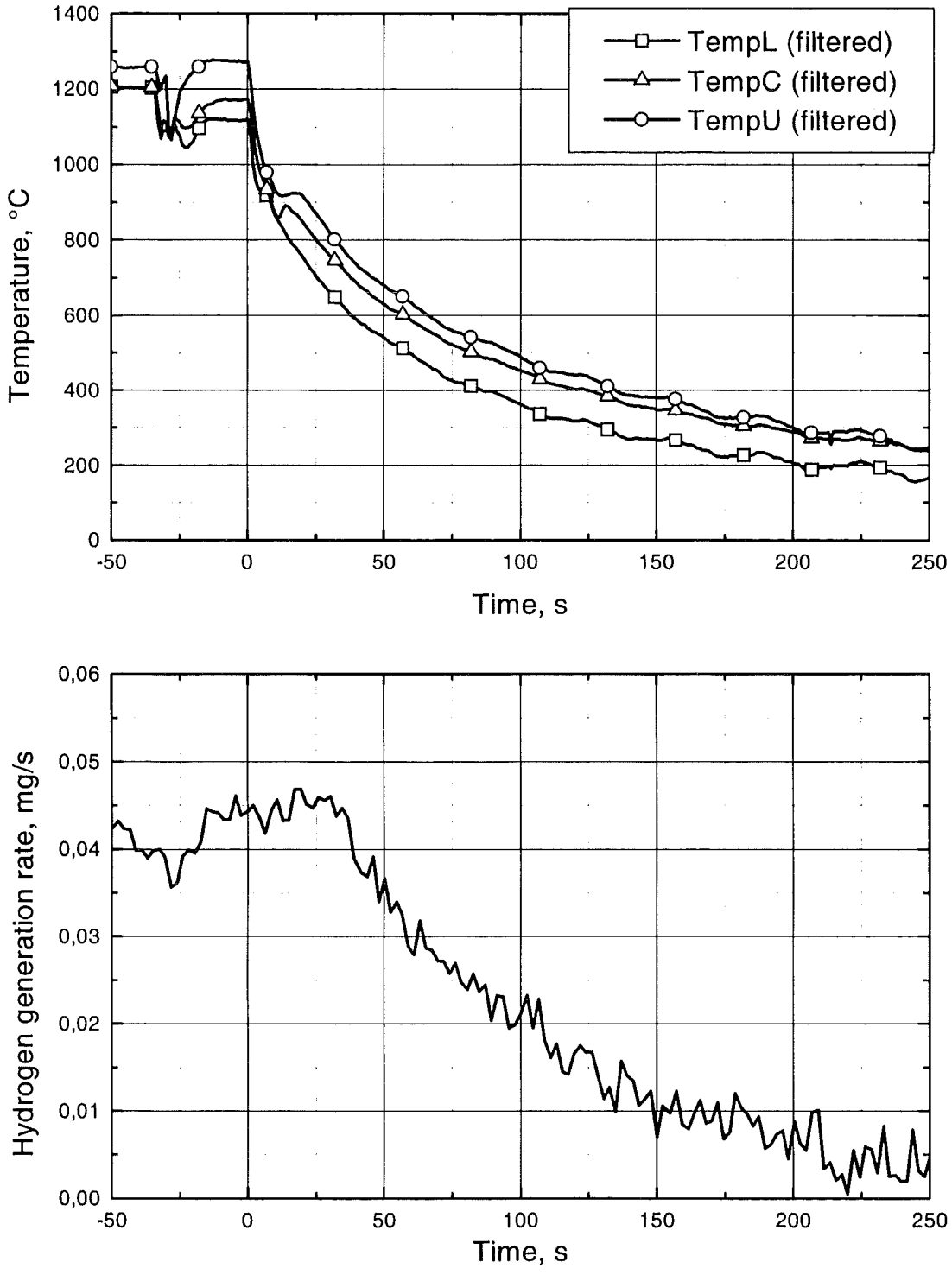

Figure 2.17: Experiment 09028_1: temperature history of the upper, central and lower thermocouple and corresponding hydrogen release rate; rapid cooldown by steam from 1200 °C; pre-calculated oxide layer thickness 315 µm.

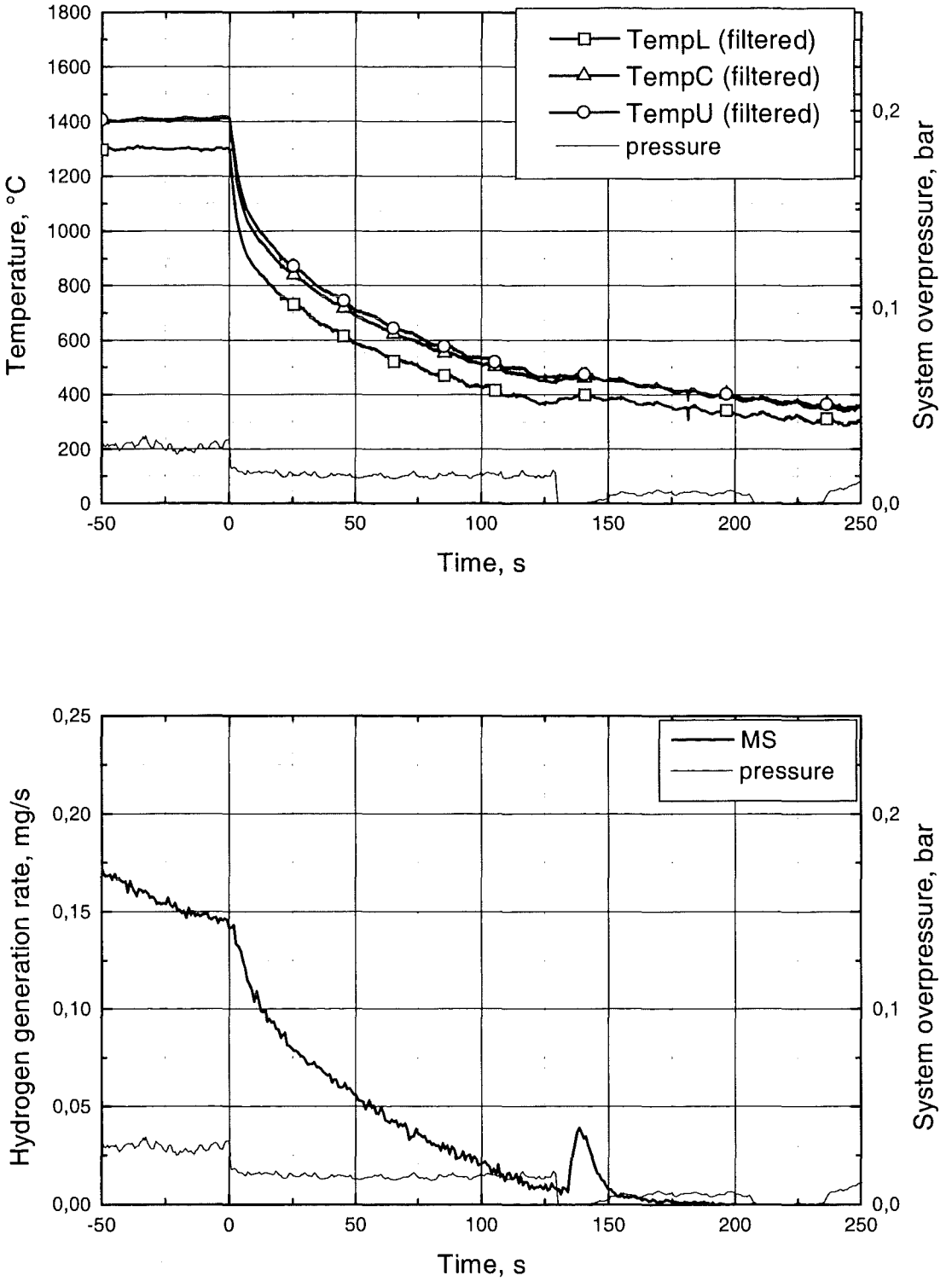

Figure 2.18: Experiment 25028_2: temperature history of the upper, central and lower thermocouple and corresponding hydrogen release rate; rapid cooldown by steam from 1400 °C; pre-calculated oxide layer thickness 116 µm.

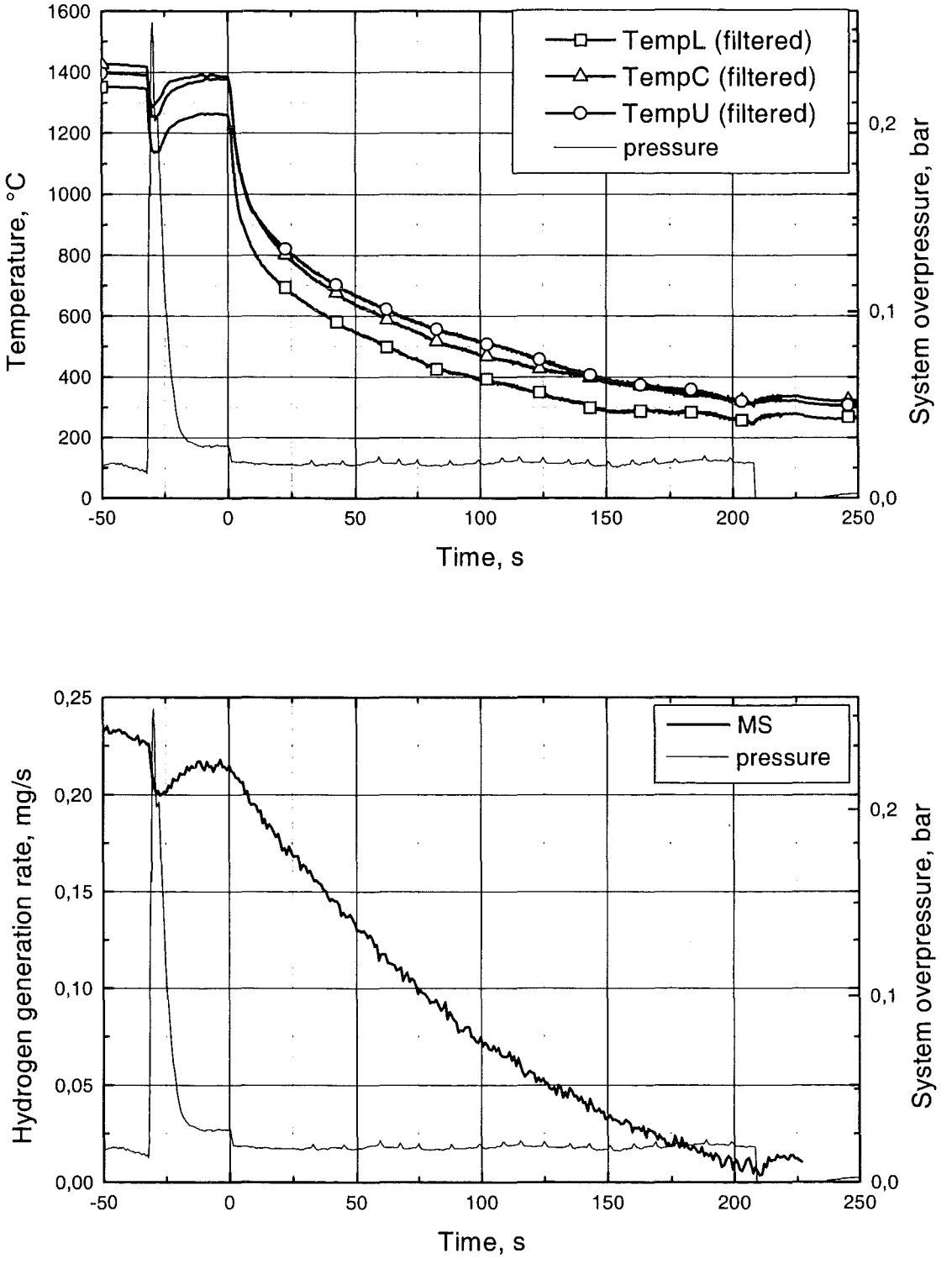

Figure 2.19: Experiment 18028_1: temperature history of the upper, central and lower thermocouple and corresponding hydrogen release rate; rapid cooldown by steam from 1400 °C; pre-calculated oxide layer thickness 150 µm.

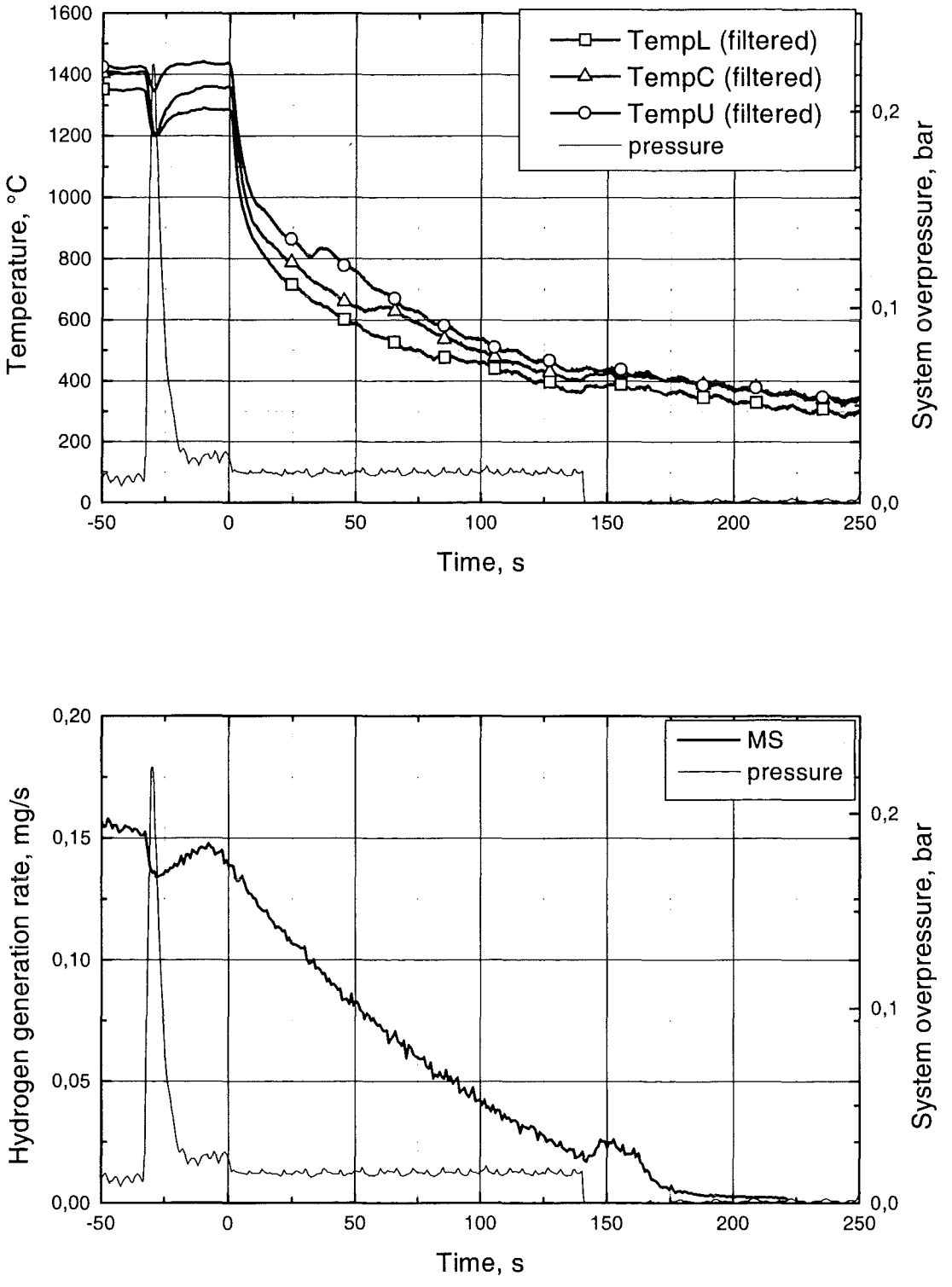

Figure 2.20: Experiment 18028_2: temperature history of the upper, central and lower thermocouple and corresponding hydrogen release rate; rapid cooldown by steam from 1400 °C; pre-calculated oxide layer thickness 195 µm.

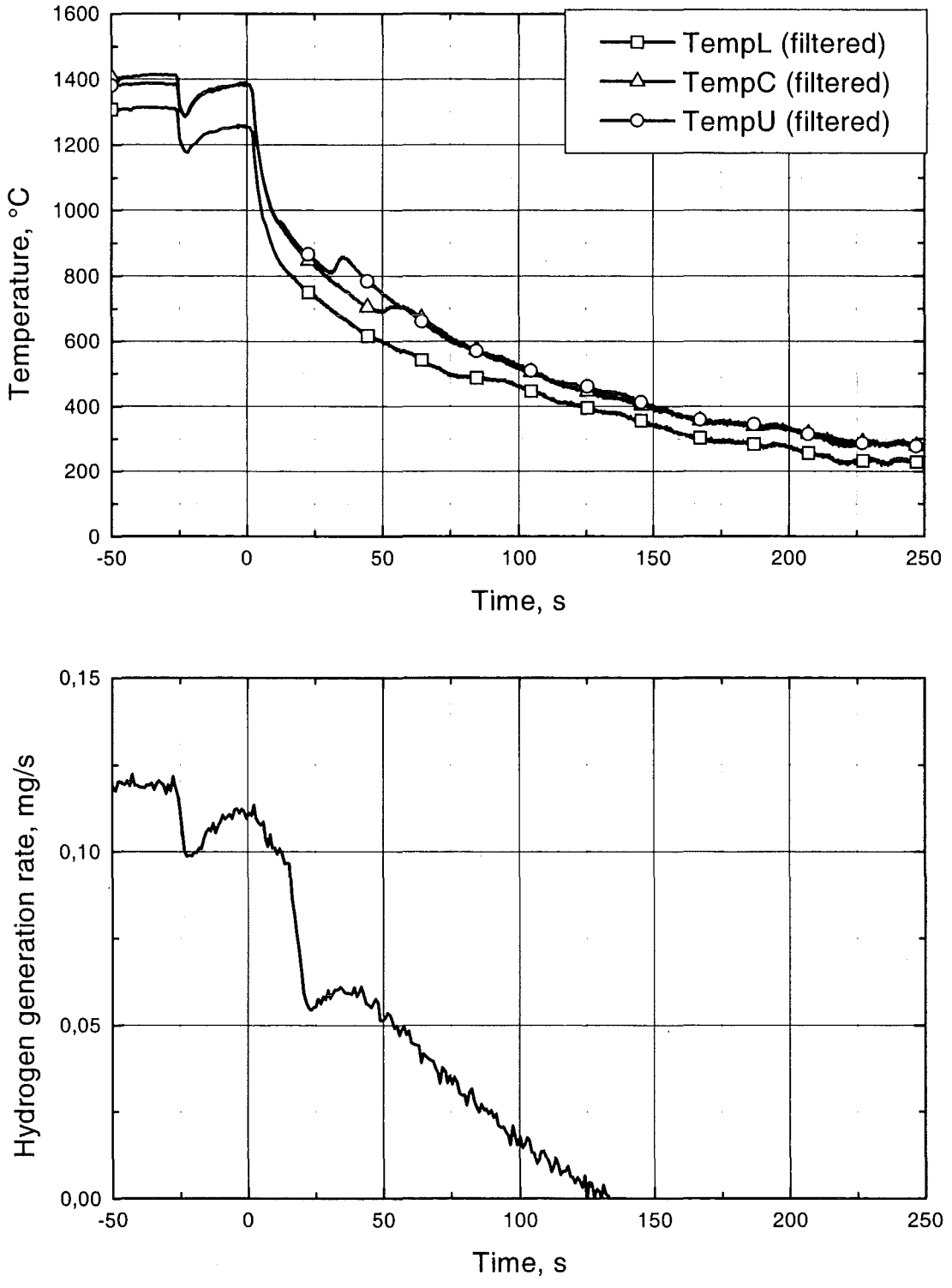

Figure 2.21: Experiment 19028_1: temperature history of the upper, central and lower thermocouple and corresponding hydrogen release rate; rapid cooldown by steam from 1400 °C; pre-calculated oxide layer thickness 246 µm.

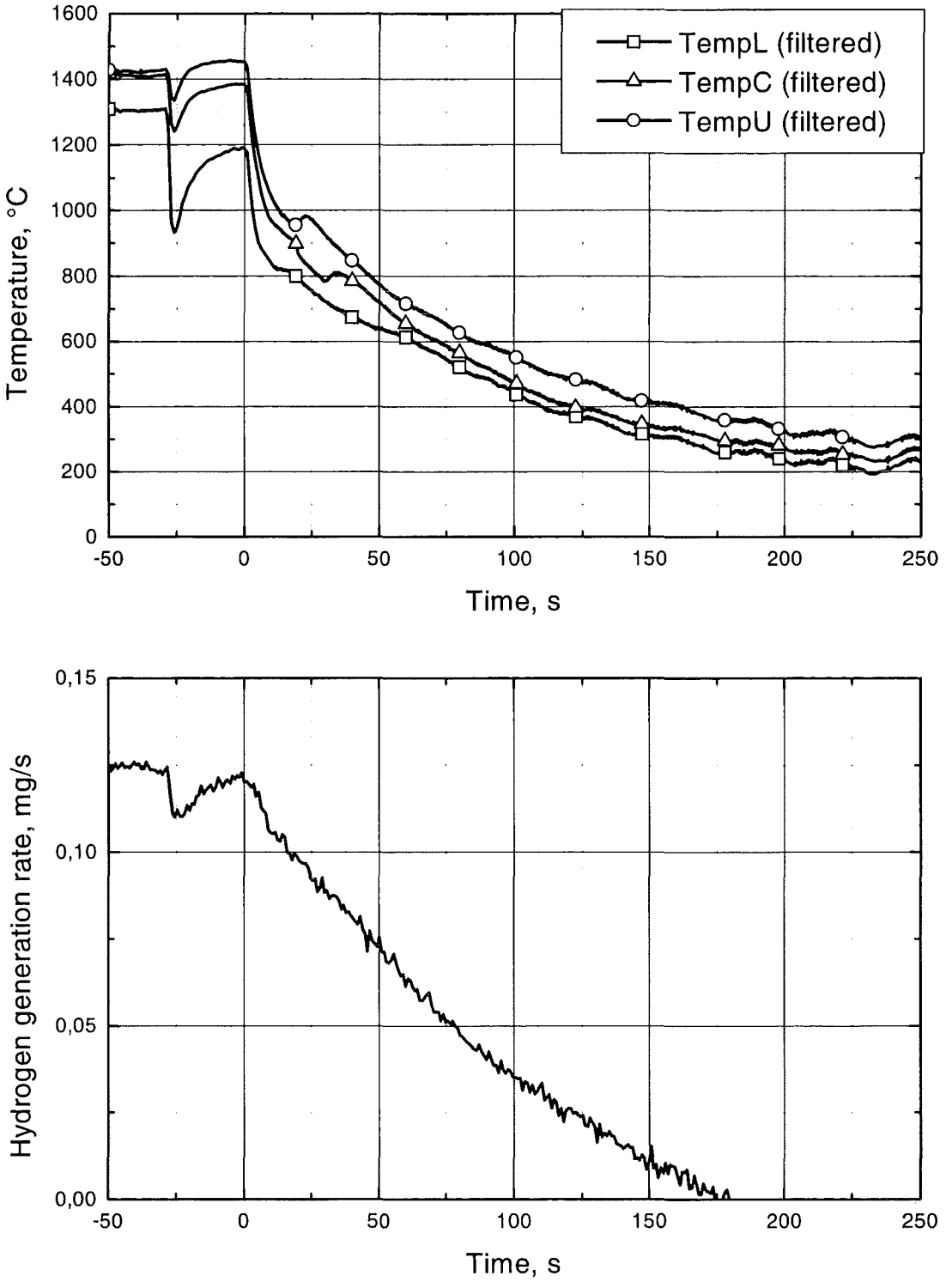

Figure 2.22: Experiment 25028_1: temperature history of the upper, central and lower thermocouple and corresponding hydrogen release rate; rapid cooldown by steam from 1400 °C; pre-calculated oxide layer thickness 246 µm.

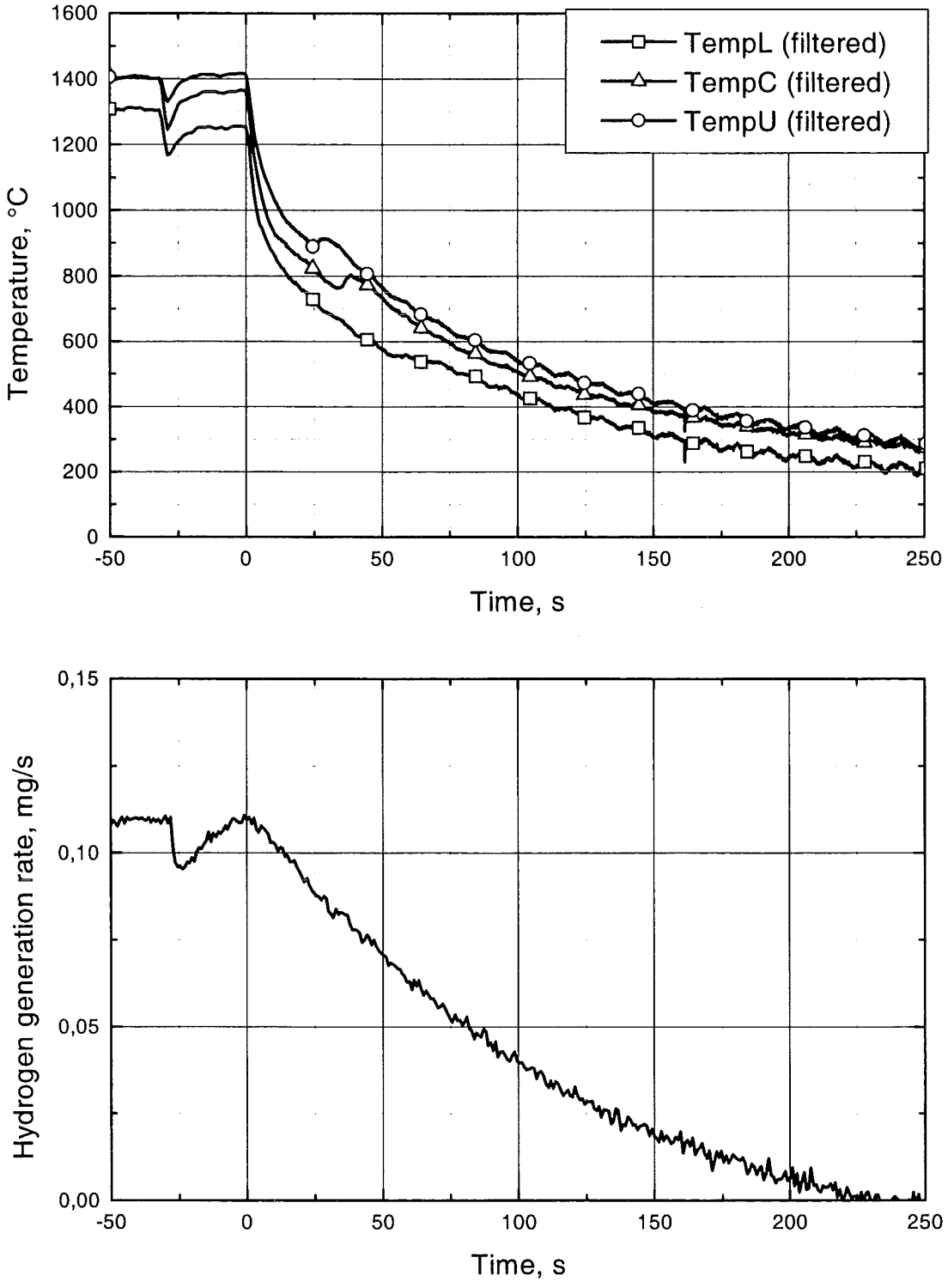

Figure 2.23: Experiment 17028_1: temperature history of the upper, central and lower thermocouple and corresponding hydrogen release rate; rapid cooldown by steam from 1400 °C; pre-calculated oxide layer thickness 290 µm.

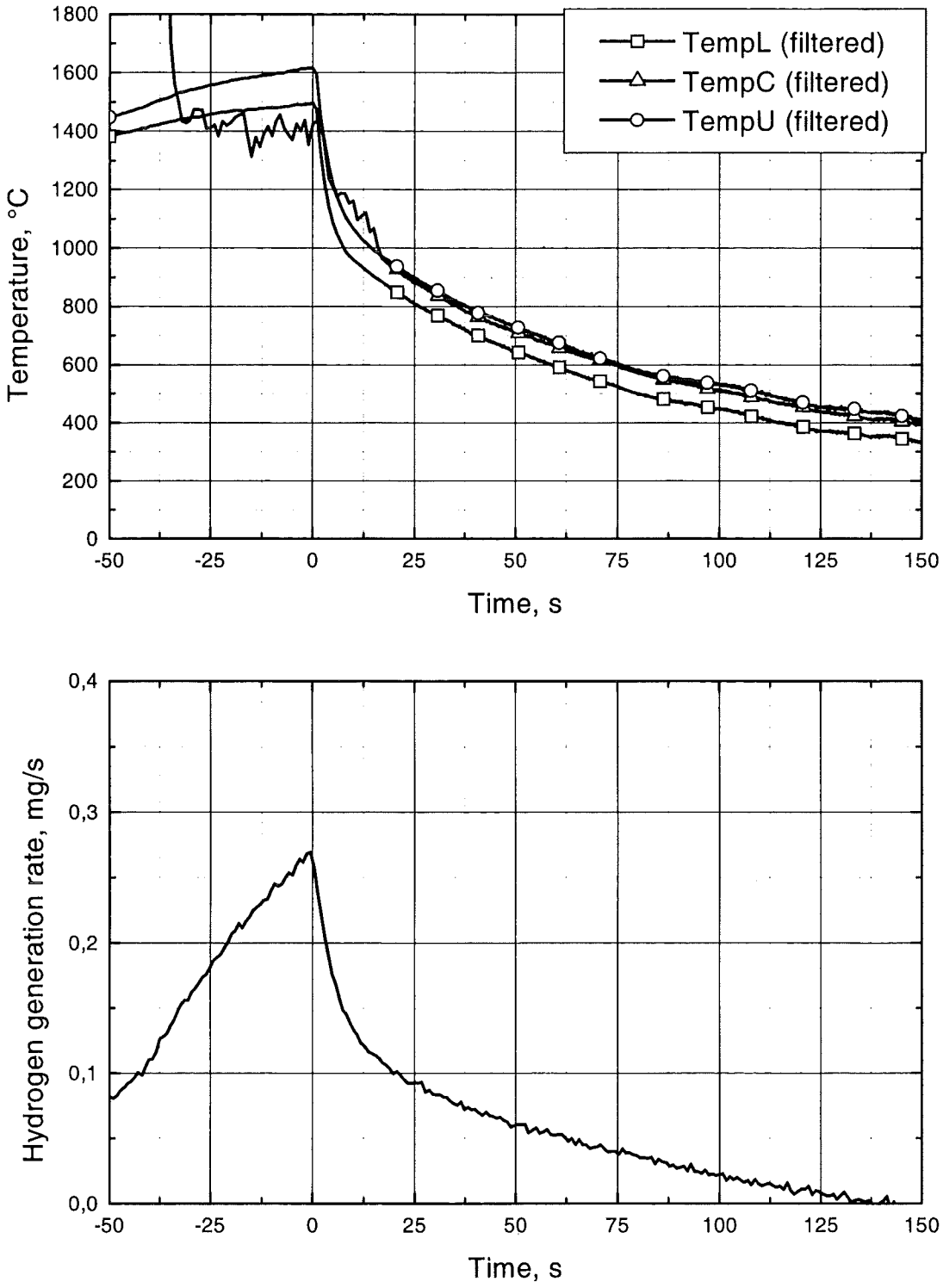

Figure 2.24: Experiment 27028_1: temperature history of the upper, central and lower thermocouple and corresponding hydrogen release rate; rapid cooldown by steam from 1600 °C; pre-calculated oxide layer thickness 139 µm.

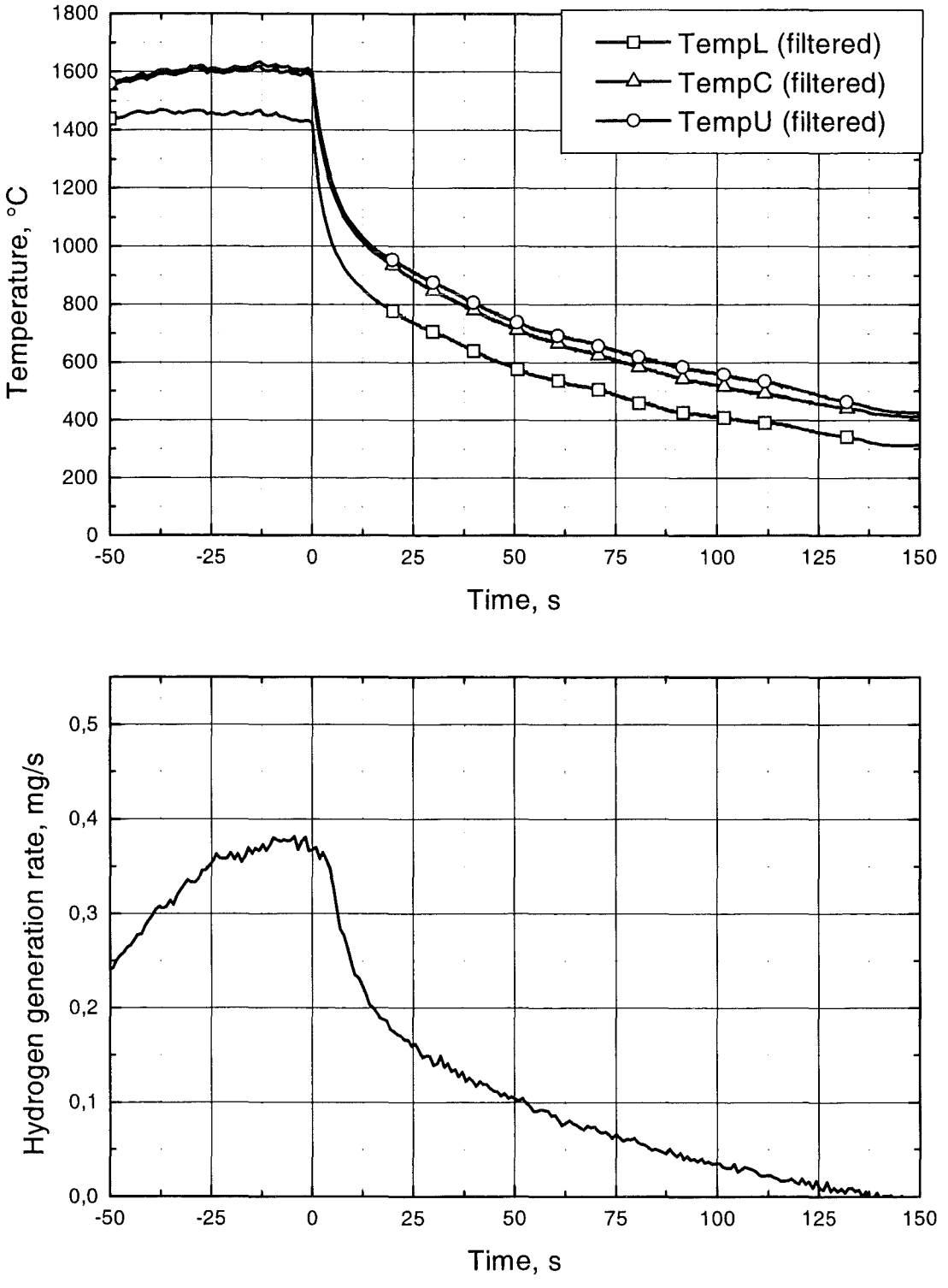

Figure 2.25: Experiment 03038_1: temperature history of the upper, central and lower thermocouple and corresponding hydrogen release rate; rapid cooldown by steam from 1600 °C; pre-calculated oxide layer thickness 173 µm.

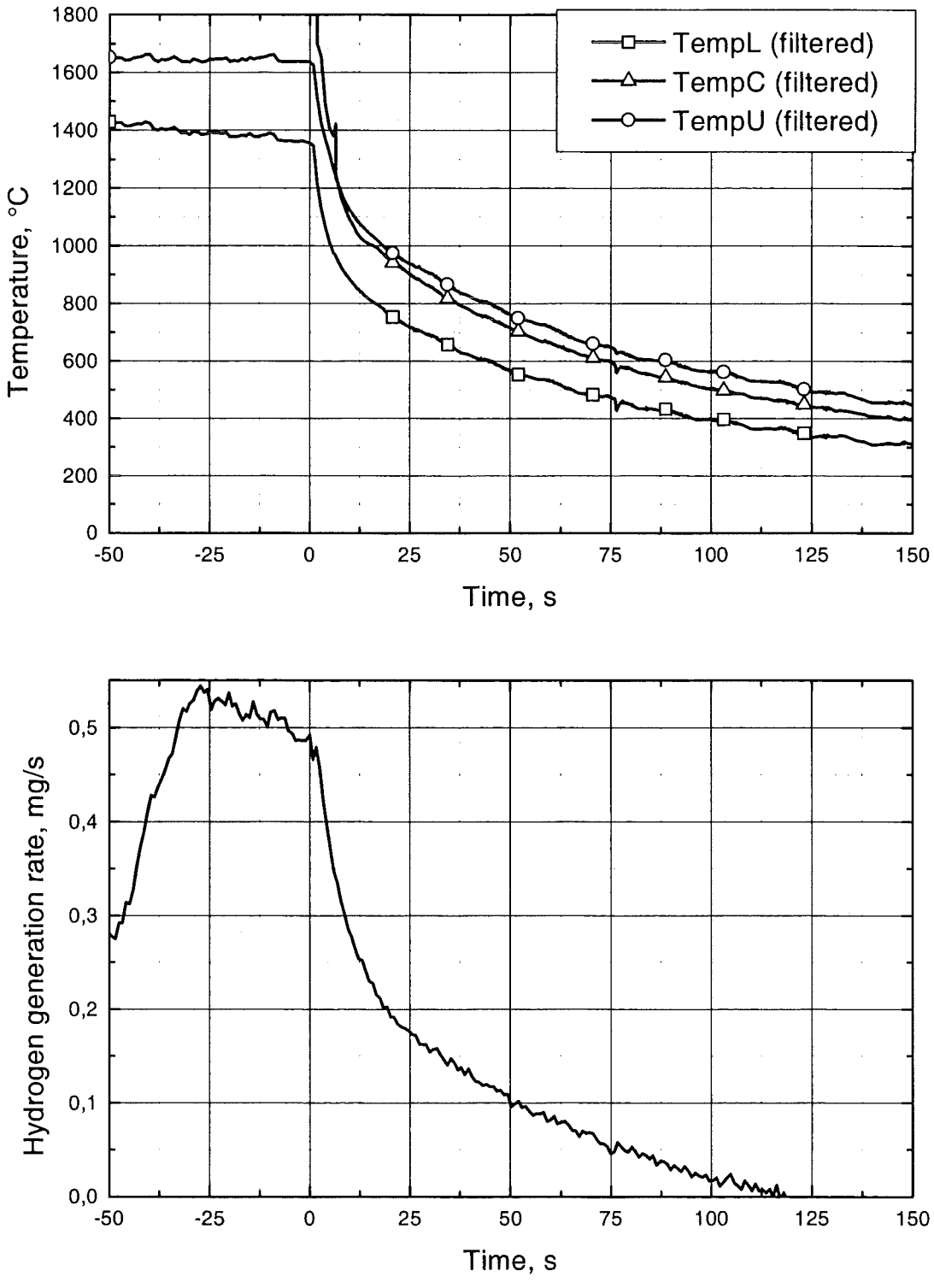

Figure 2.26: Experiment 02038_1: temperature history of the upper, central and lower thermocouple and corresponding hydrogen release rate; rapid cooldown by steam from 1600 °C; pre-calculated oxide layer thickness 201 μm.

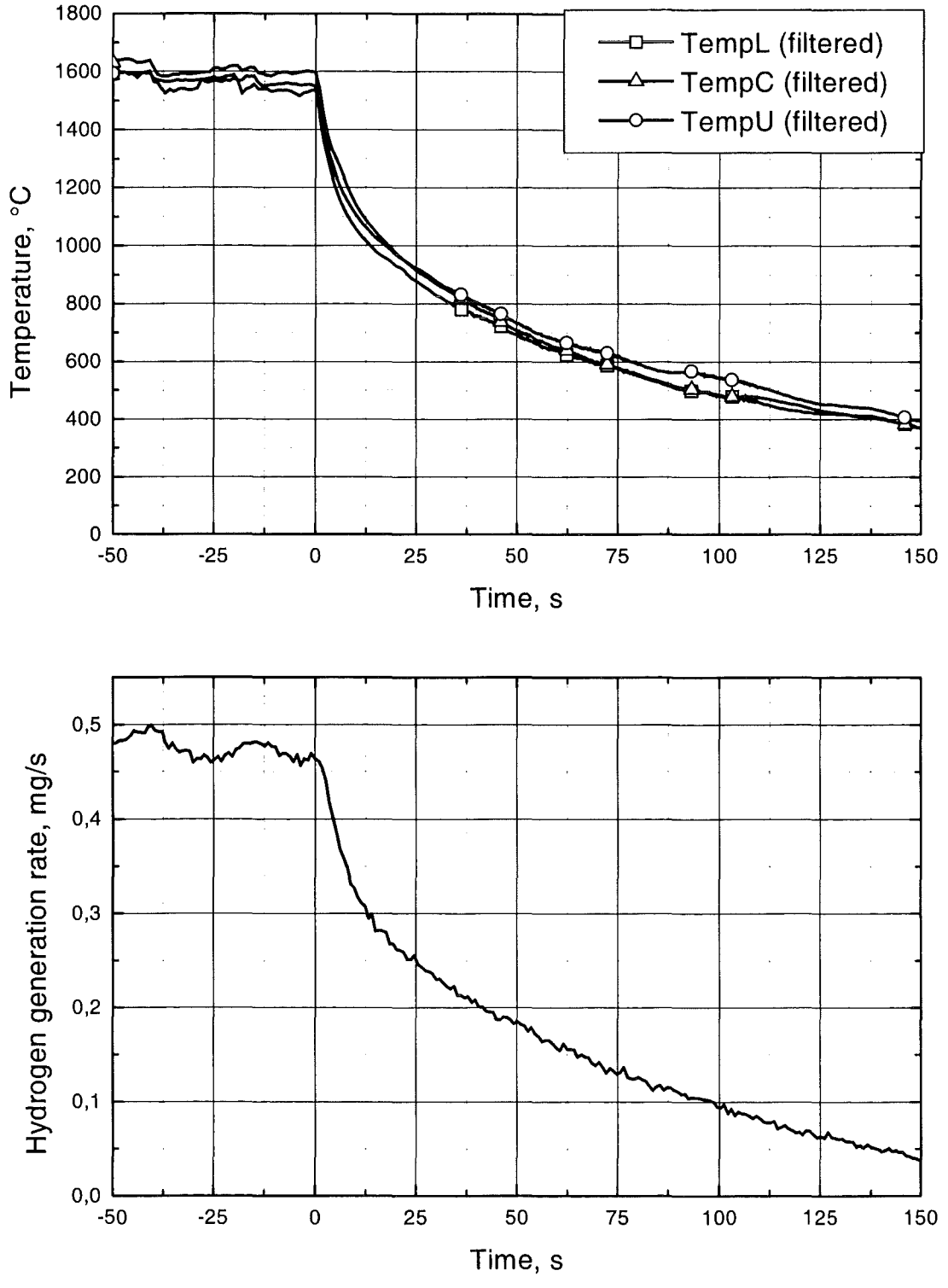

Figure 2.27: Experiment 26028_1: temperature history of the upper, central and lower thermocouple and corresponding hydrogen release rate; rapid cooldown by steam from 1600 °C; pre-calculated oxide layer thickness 240 µm.

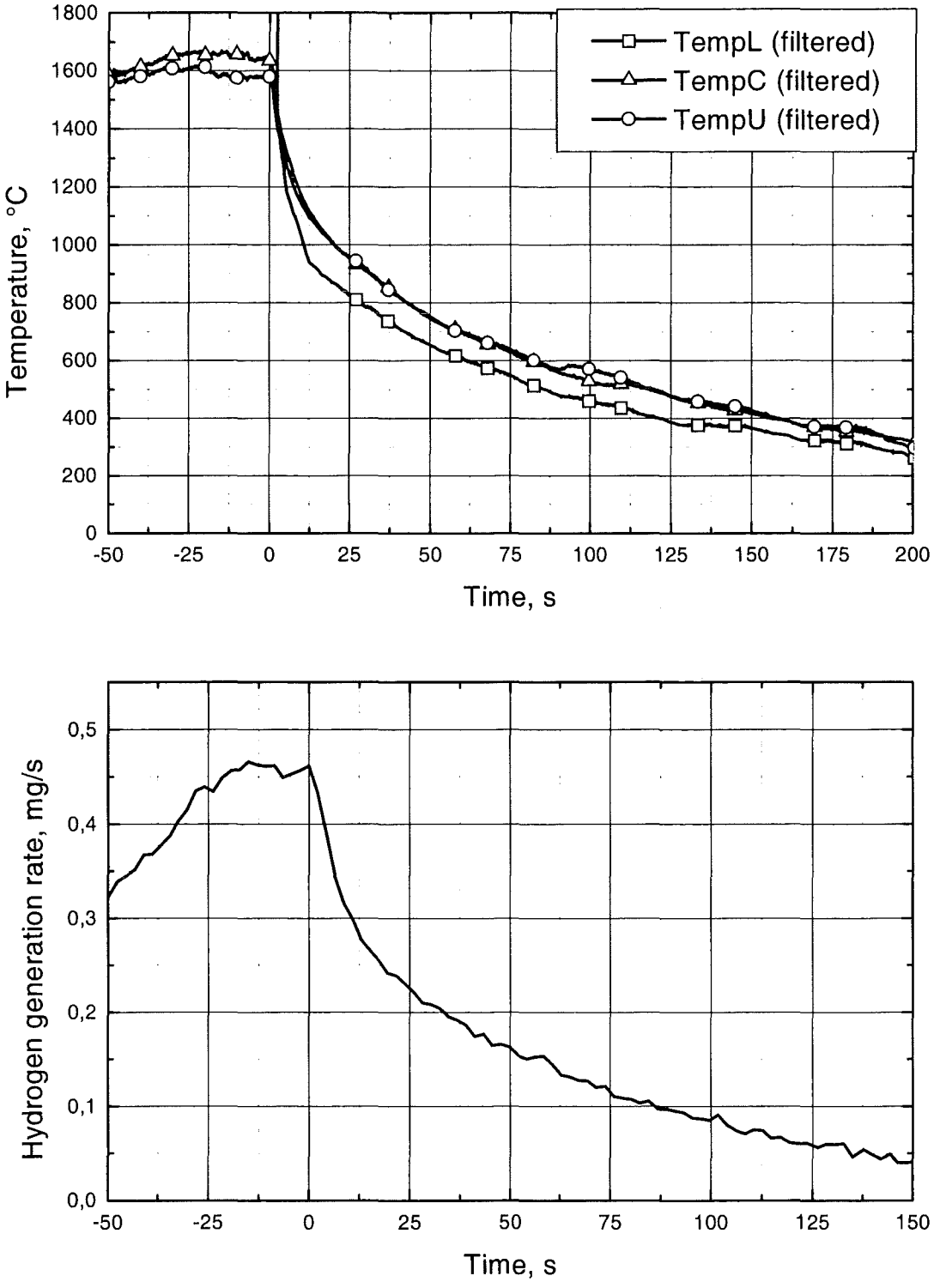

Figure 2.28: Experiment 16028_1: temperature history of the upper, central and lower thermocouple and corresponding hydrogen release rate; rapid cooldown by steam from 1600 °C; pre-calculated oxide layer thickness 260 µm.

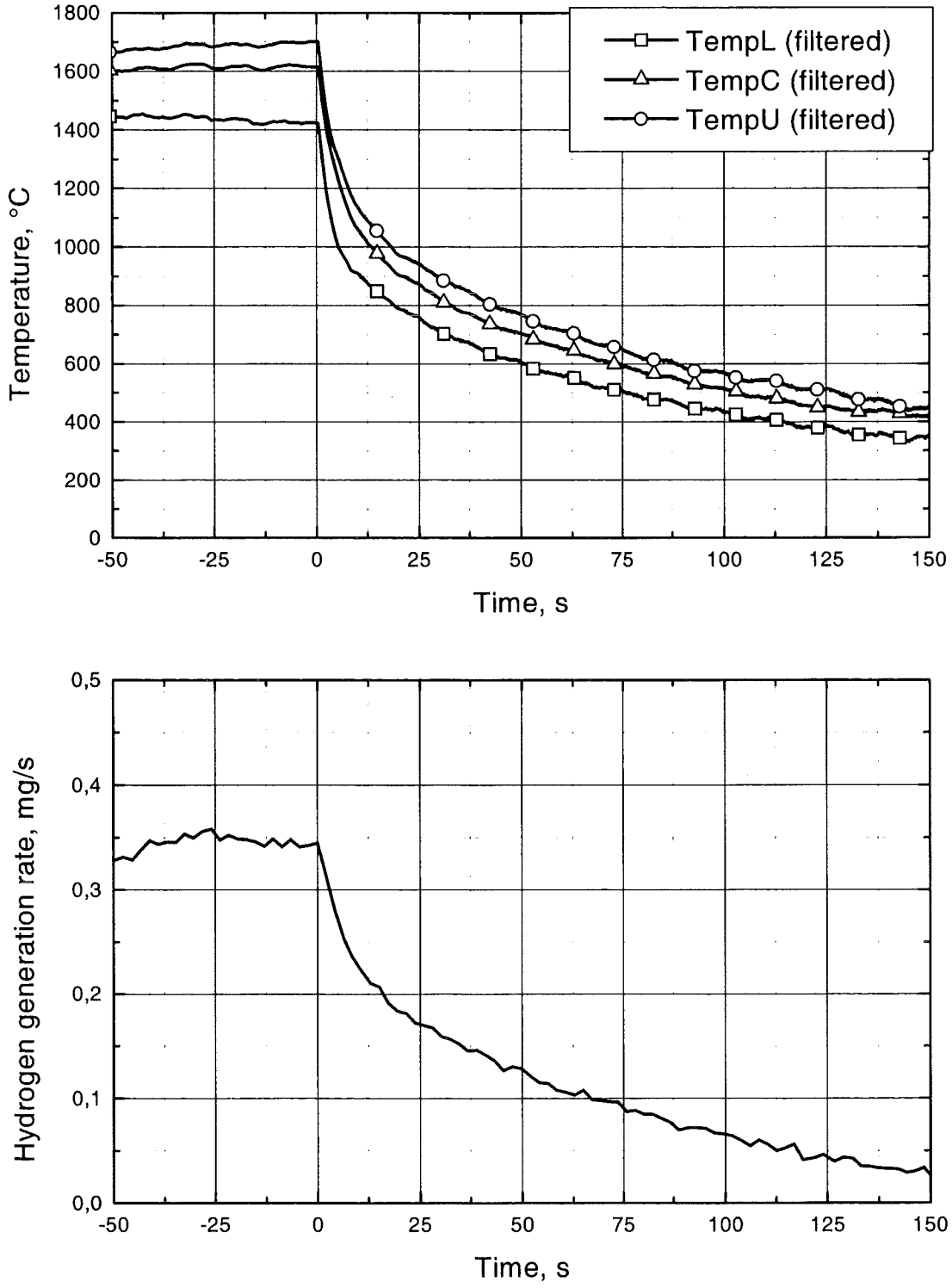

Figure 2.29: Experiment 16028_2: temperature history of the upper, central and lower thermocouple and corresponding hydrogen release rate; rapid cooldown by steam from 1600 °C; pre-calculated oxide layer thickness 290 µm.

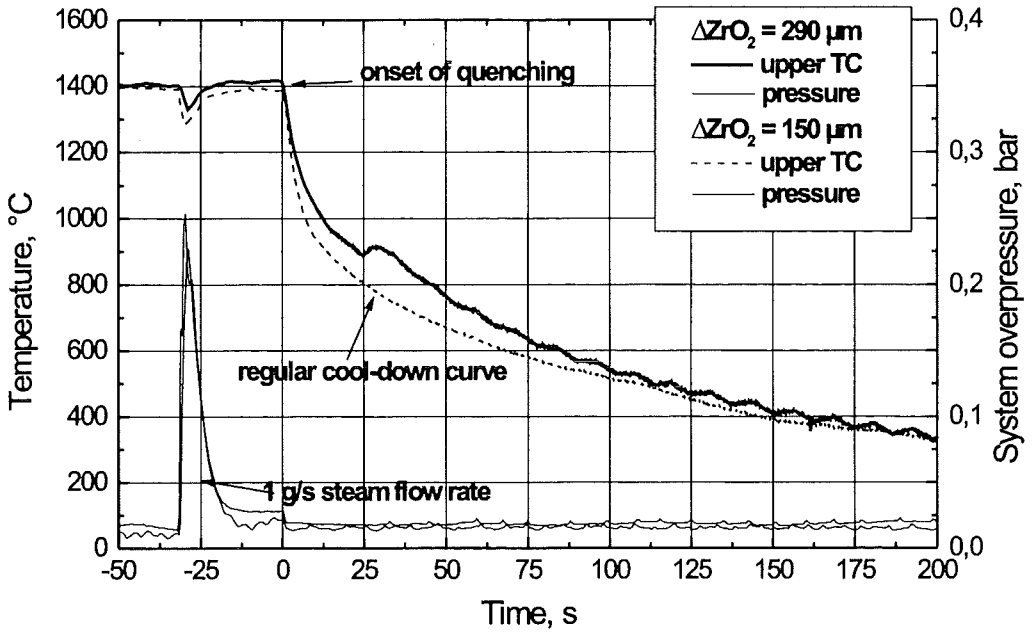

Figure 2.30: Temperature deviation from the regular cooldown curve; steam cooling from 1400 °C.

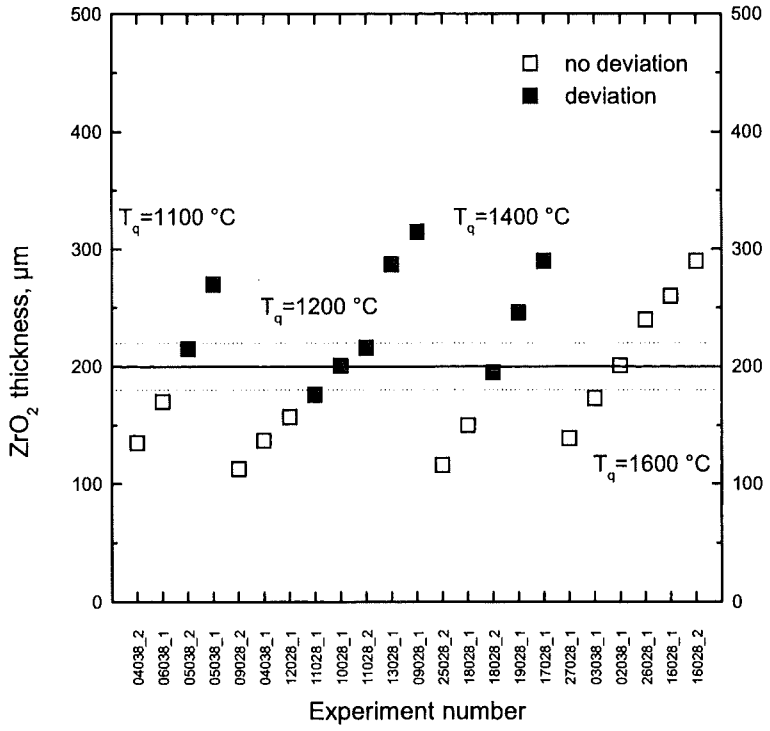

Figure 2.31: Temperature deviation from the regular cooldown curve in small-scale experiments.

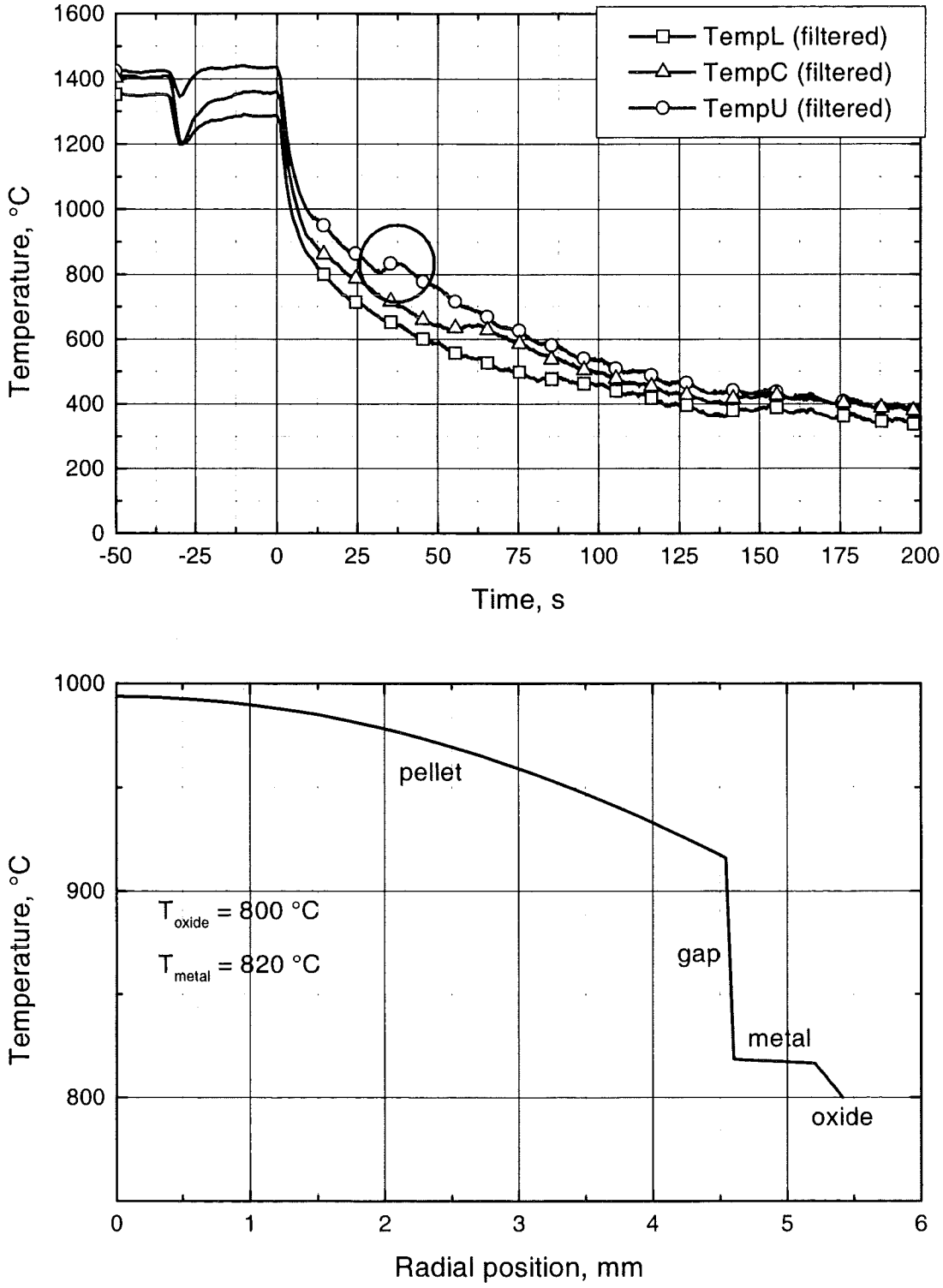

Figure 2.32: Deviation from the regular cooldown temperature observed in the experiments (upper plot) and temperature profile in rod calculted by the SVECHA code (lower plot); steam cooling from 1400 °C.

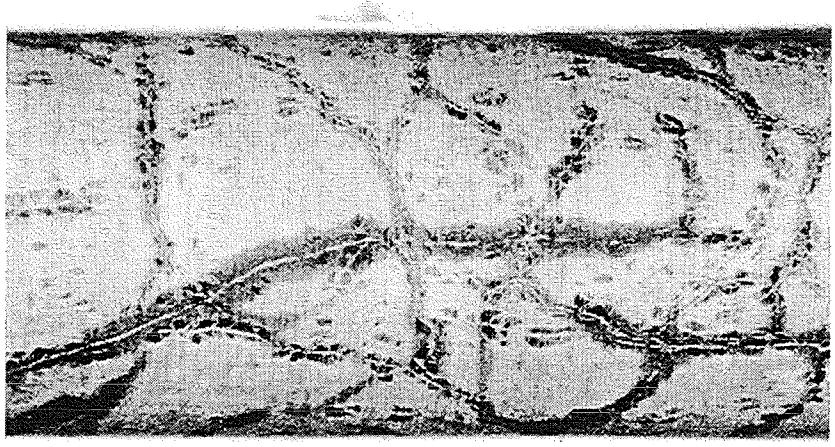

solvent penetration from the inside

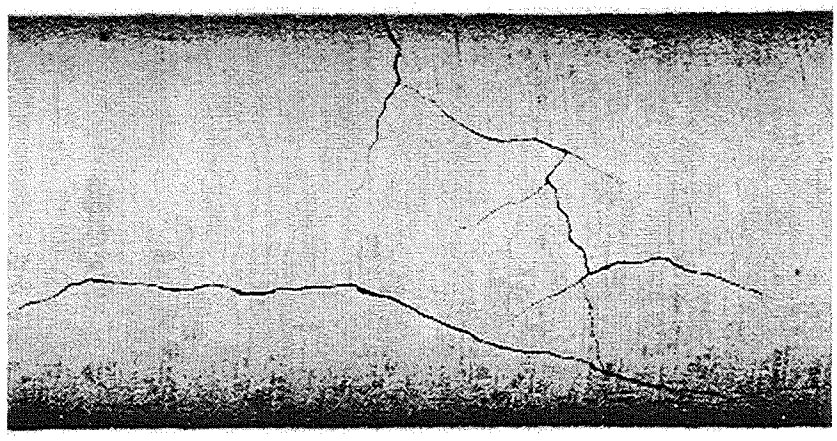

without visualization

Figure 2.33: Zircaloy cladding tube after rapid cooldown by steam. Visualization of cracks.

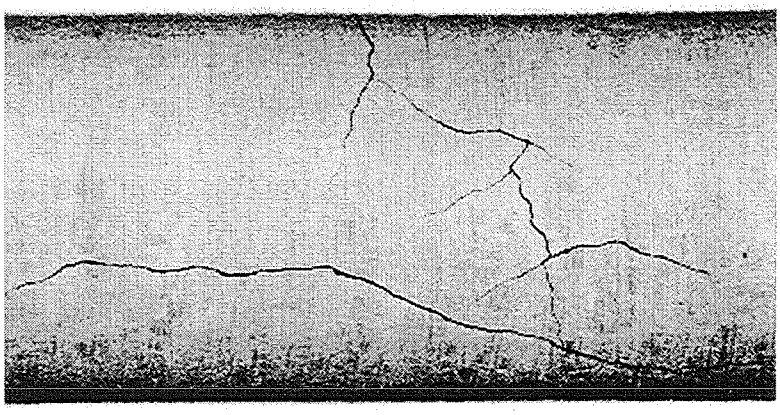

Sample 05038_1; δ_{ZrO_2} = 270 µm

Sample 05038_2; δ_{ZrO_2} = 215 µm

Figure 2.34: Crack formation in pre-oxidized Zircaloy cladding tubes after rapid cooldown by steam; temperature at onset of cooldown: 1100 °C.

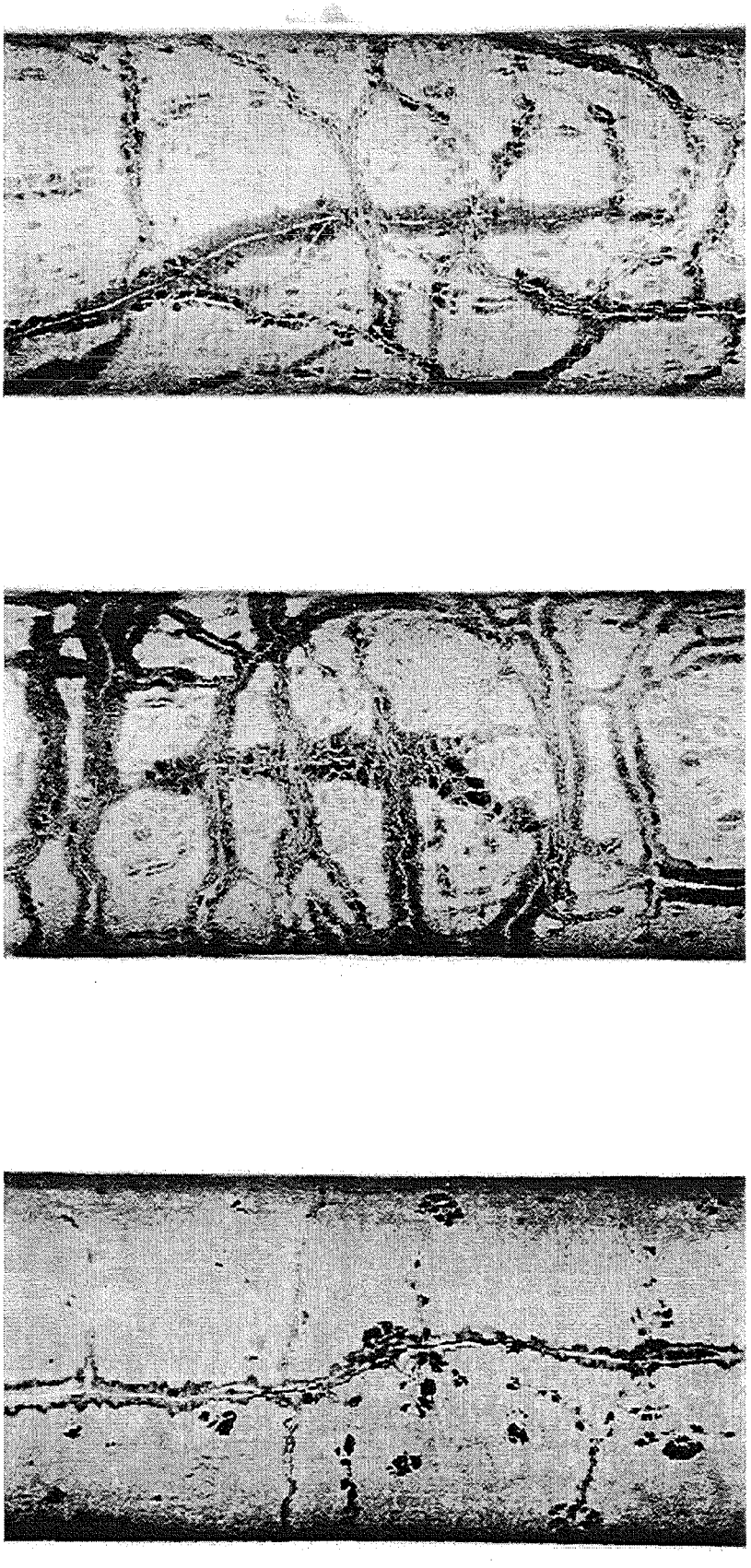

Figure 2.35: Crack formation in pre-oxidized Zircaloy cladding tubes after rapid cooldown by steam; temperature at onset of cooldown: 1200 °C.

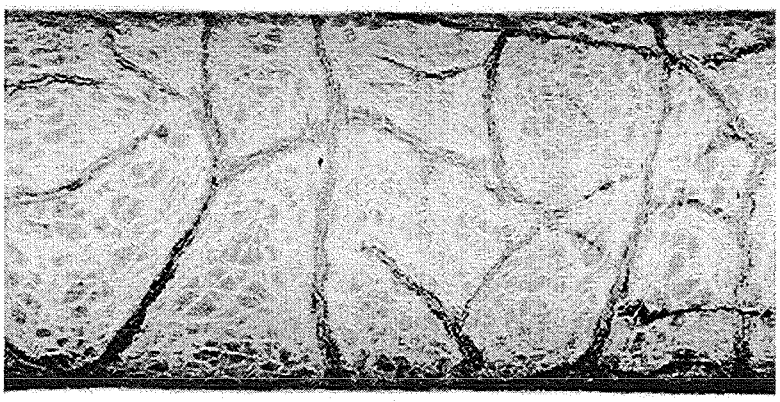

Sample 09028_1; δ_{ZrO_2} = 315 µm

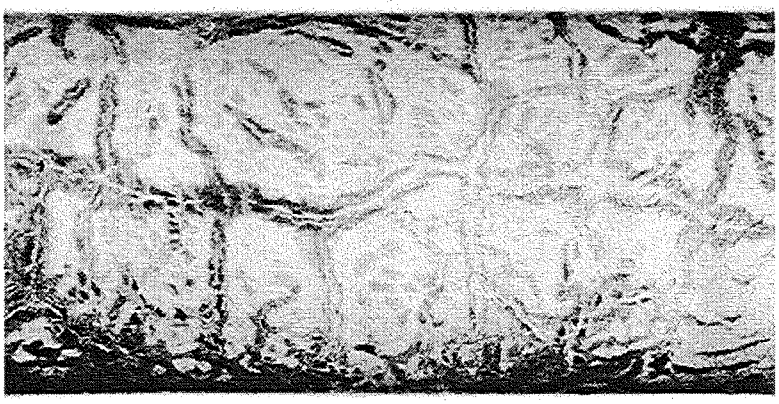

Sample 11028_2; δ_{ZrO_2} = 216 µm

Figure 2.36: Crack formation in pre-oxidized Zircaloy cladding tubes after rapid cooldown by steam; temperature at onset of cooldown: 1200 °C.

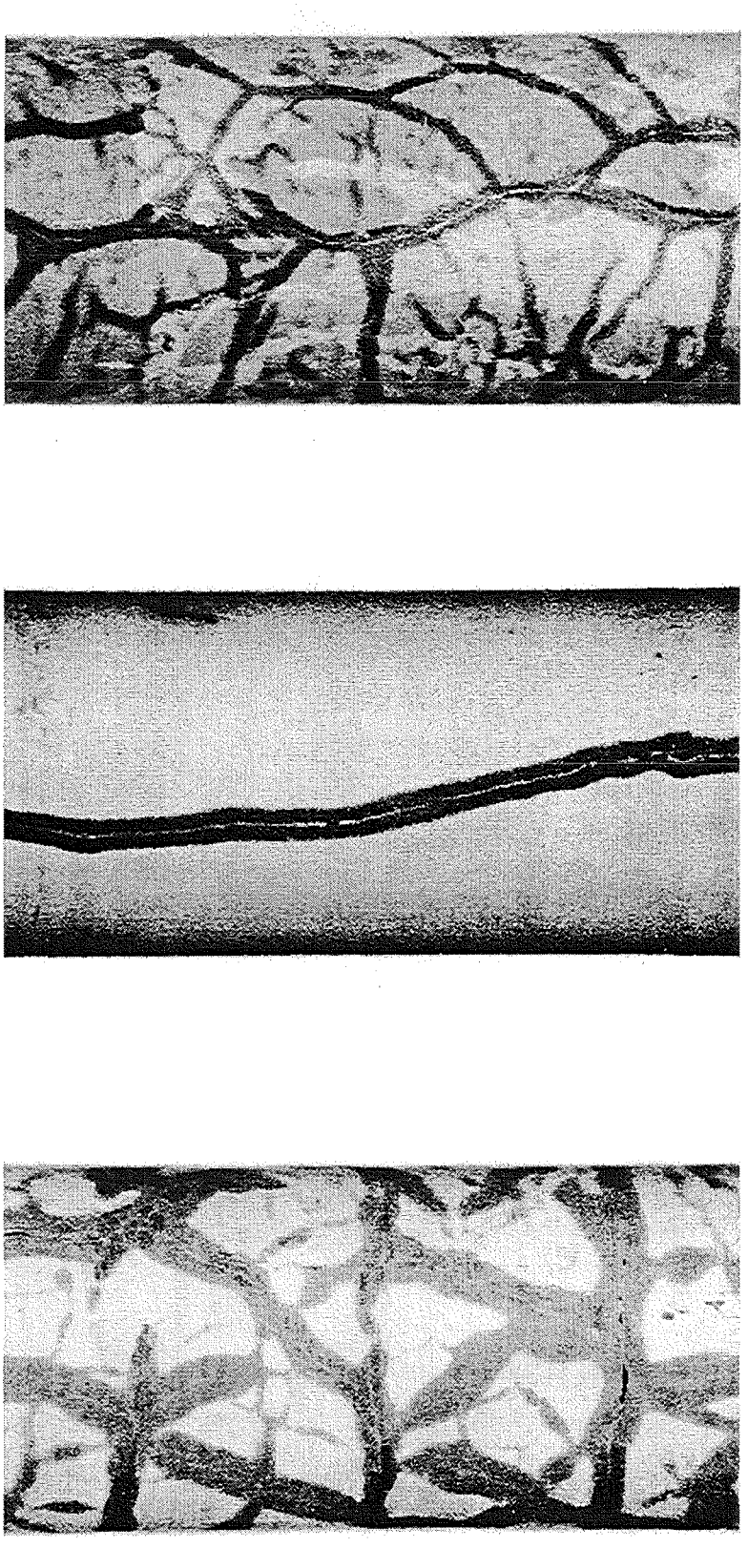

Figure 2.37: Crack formation in pre-oxidized Zircaloy cladding tubes after rapid cooldown by steam; temperature at onset of cooldown: 1400 °C.

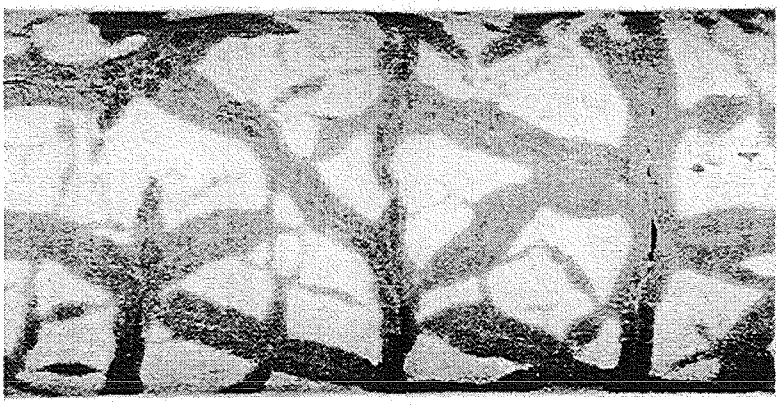

Sample 25028_1; δ_{ZrO_2} = 300 µm

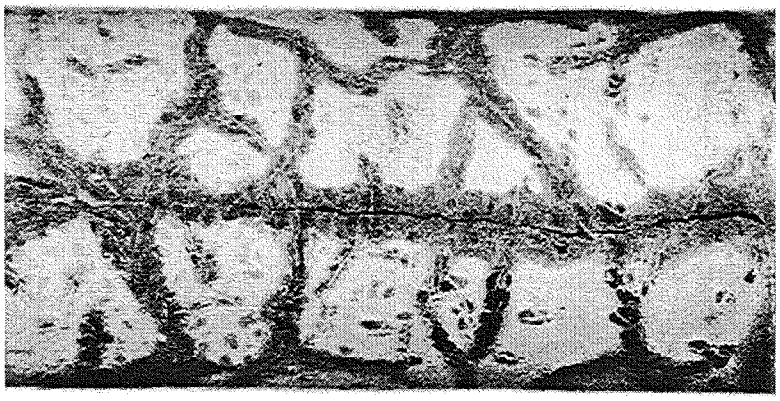

Sample 19028_1; δ_{ZrO_2} = 235 µm

Figure 2.38: Crack formation in pre-oxidized Zircaloy cladding tubes after rapid cooldown by steam; temperature at onset of cooldown: 1400 °C.

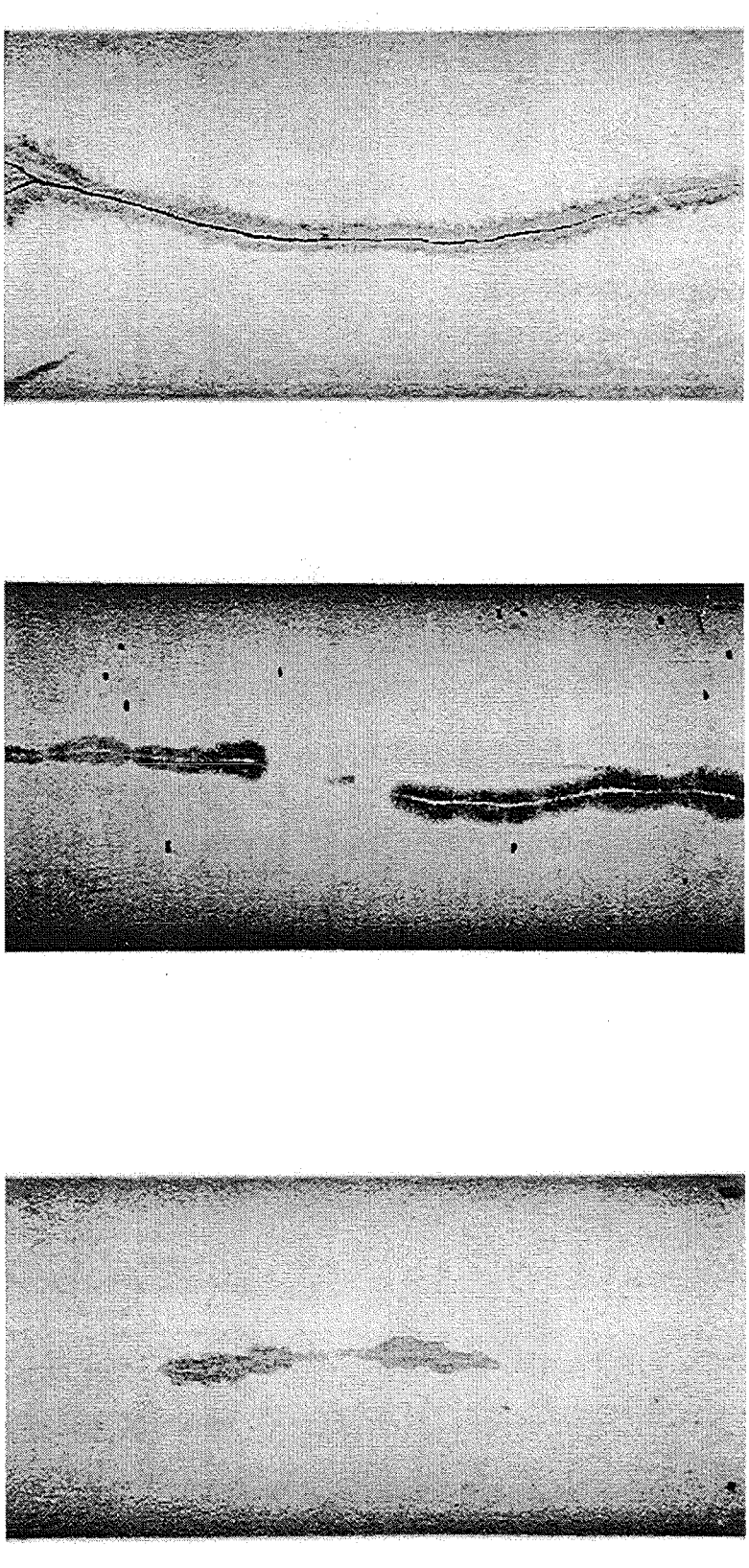

Figure 2.39: Crack formation in pre-oxidized Zircaloy cladding tubes after rapid cooldown by steam; temperature at onset of cooldown: 1600 °C.

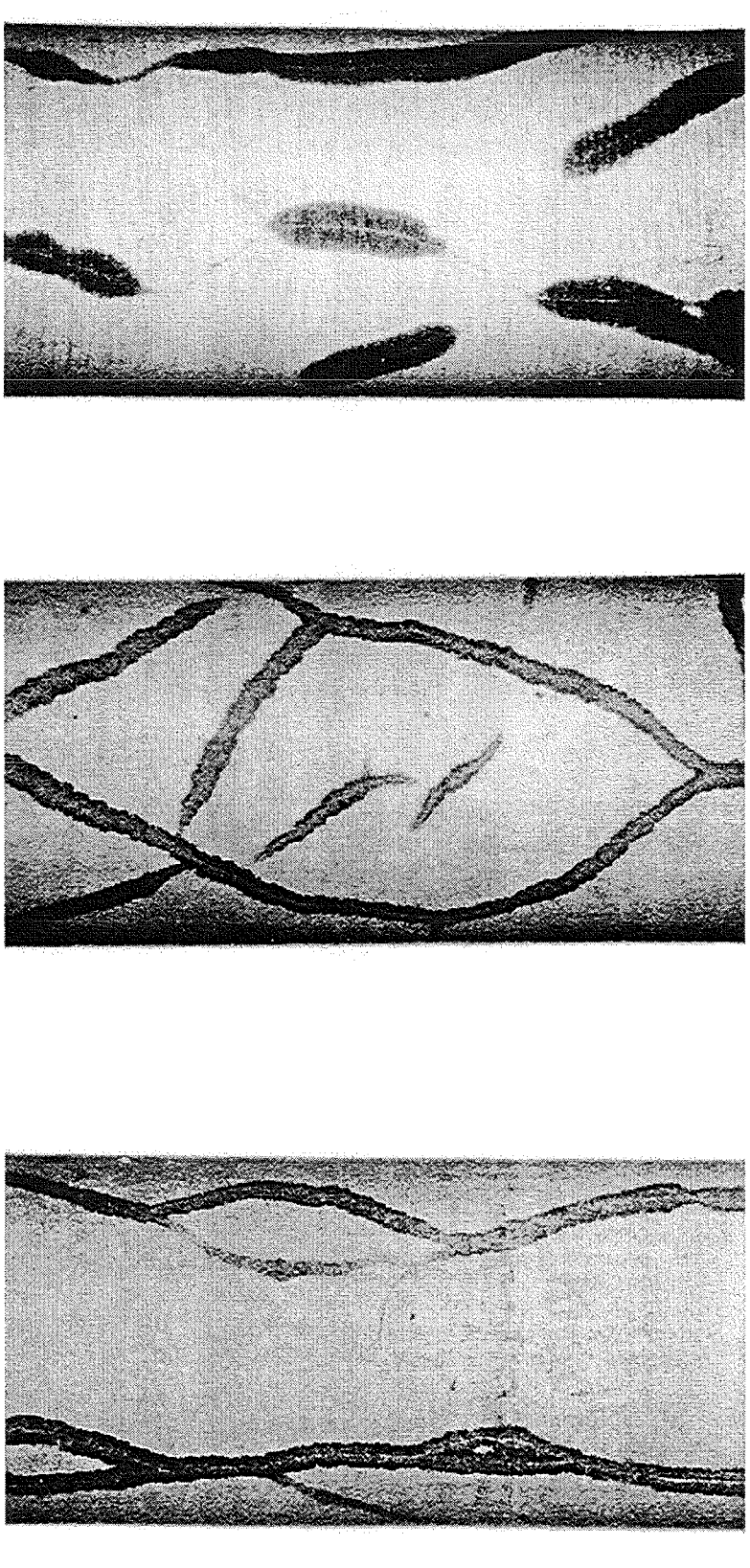

Figure 2.40: Crack formation in pre-oxidized Zircaloy cladding tubes after rapid cooldown by steam; temperature at onset of cooldown: 1600 °C.

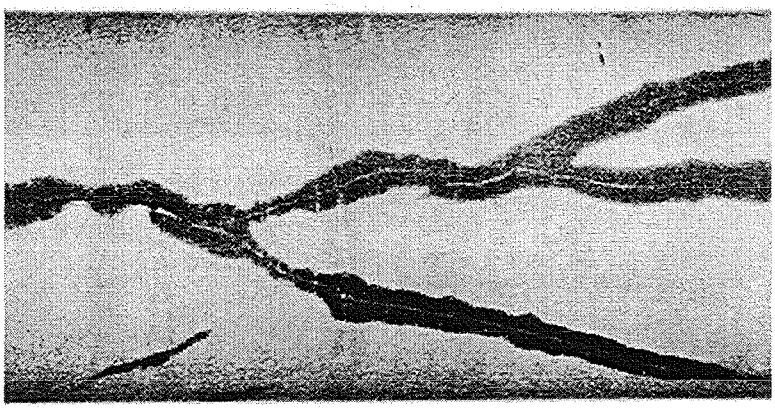

Sample 16028_2; δ_{ZrO_2} = 370 µm

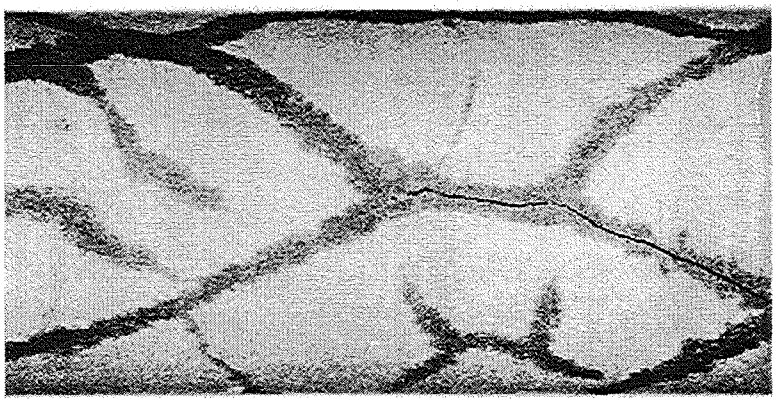

Sample 02038_1; δ_{ZrO_2} = 340 µm

Figure 2.41: Crack formation in pre-oxidized Zircaloy cladding tubes after rapid cooldown by steam; temperature at onset of cooldown: 1600 °C.

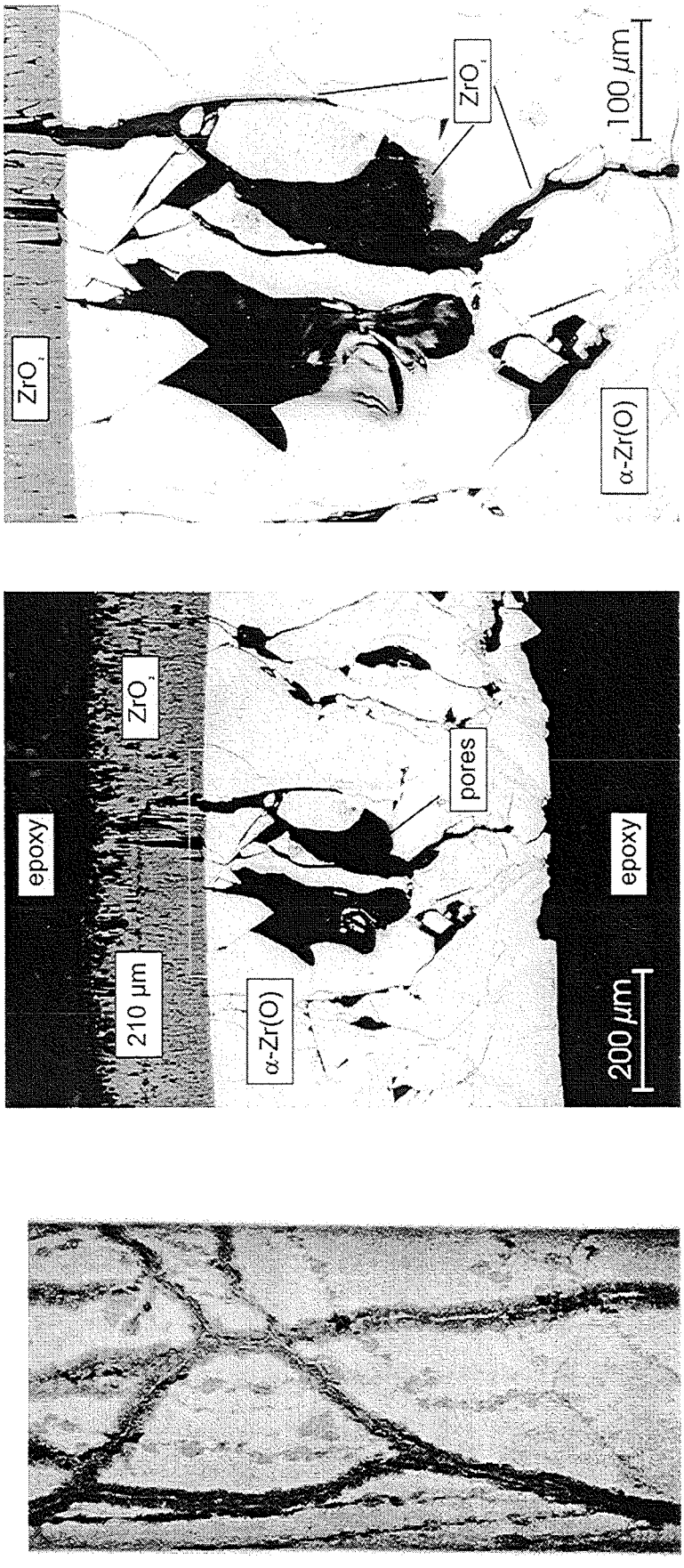

Figure 2.42: Oxidation of crack and Zircaloy tube surfaces. Test 05038_2; elevation 98 mm, temperature at onset of cooldown: 1100 °C.

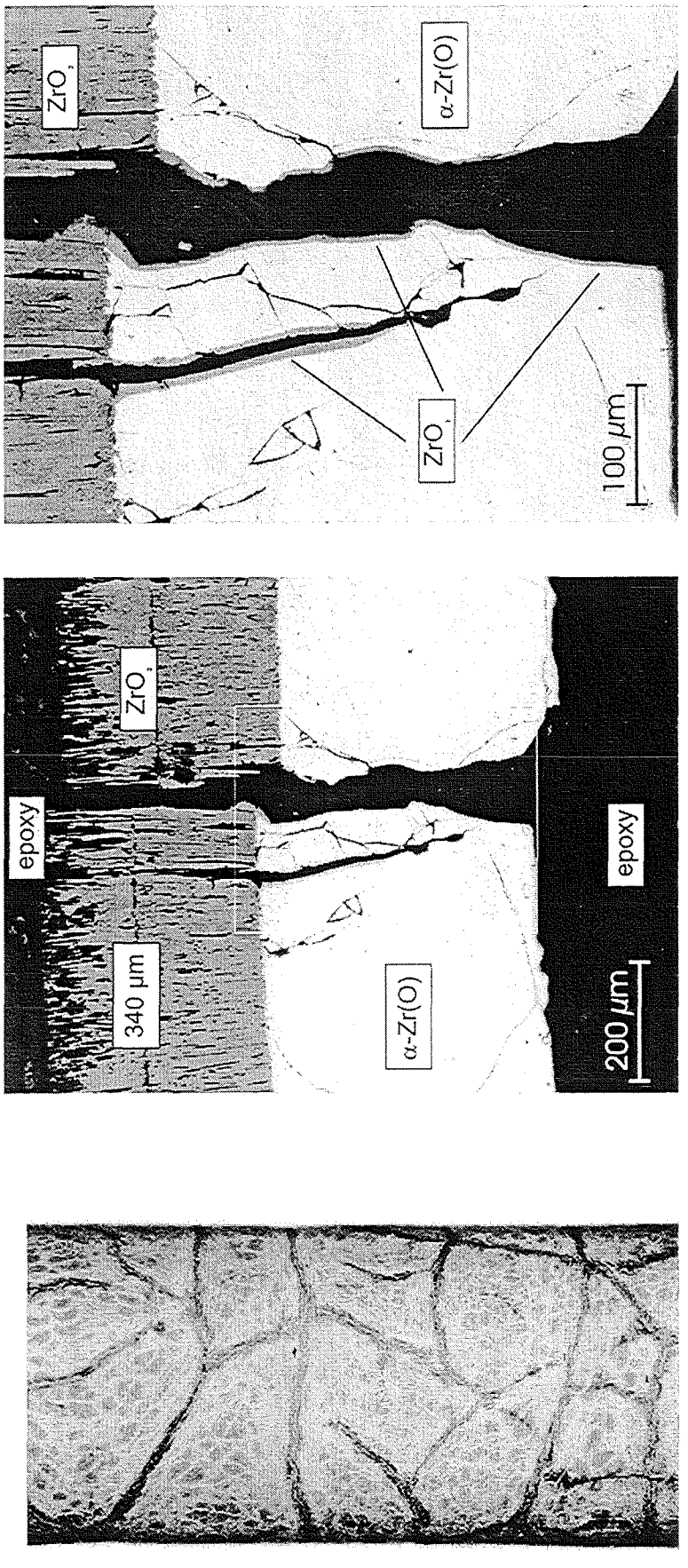

Figure 2.43: Oxidation of crack and Zircaloy tube surfaces. Test 09028_1; elevation 98 mm, temperature at onset of cooldown: 1200 °C.

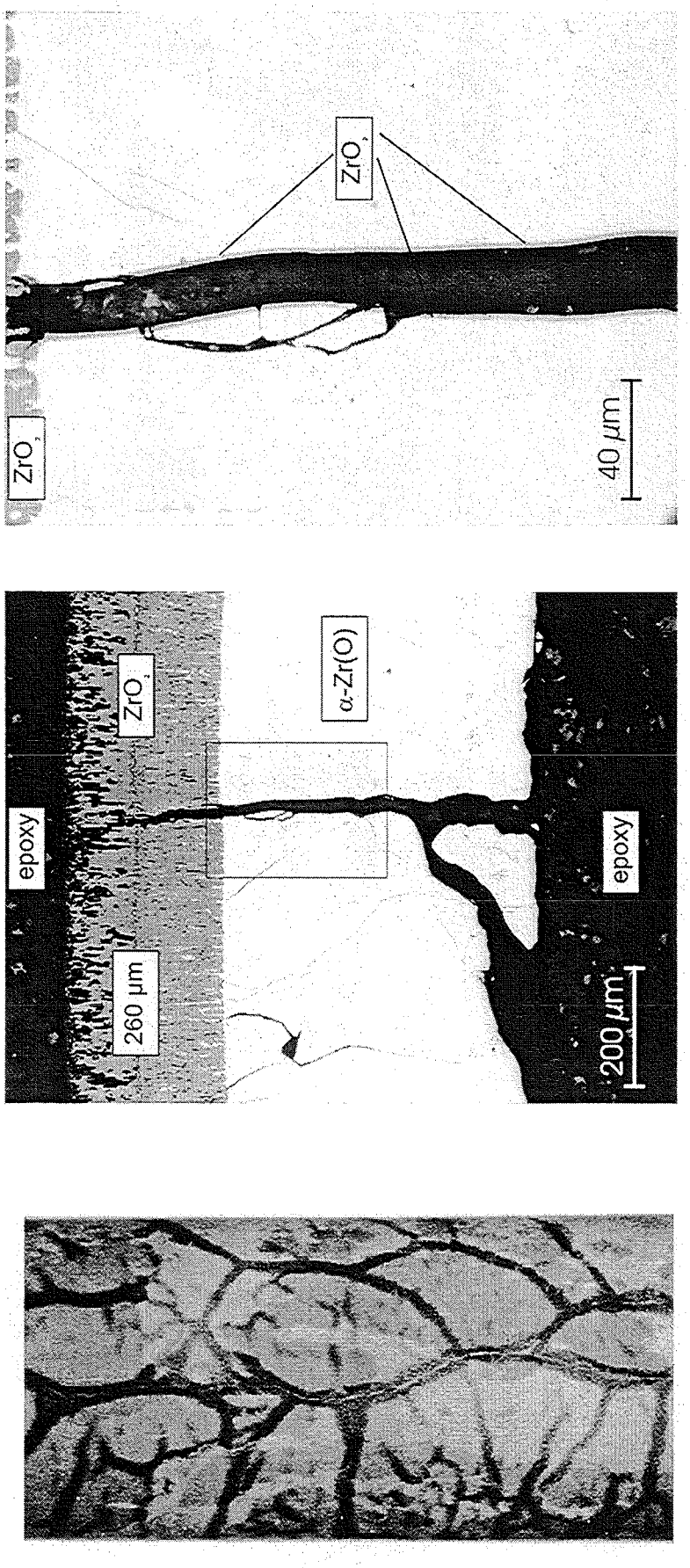

Figure 2.44: Oxidation of crack and Zircaloy tube surfaces. Test 18028_2; elevation 98 mm, temperature at onset of cooldown: 1400 °C.

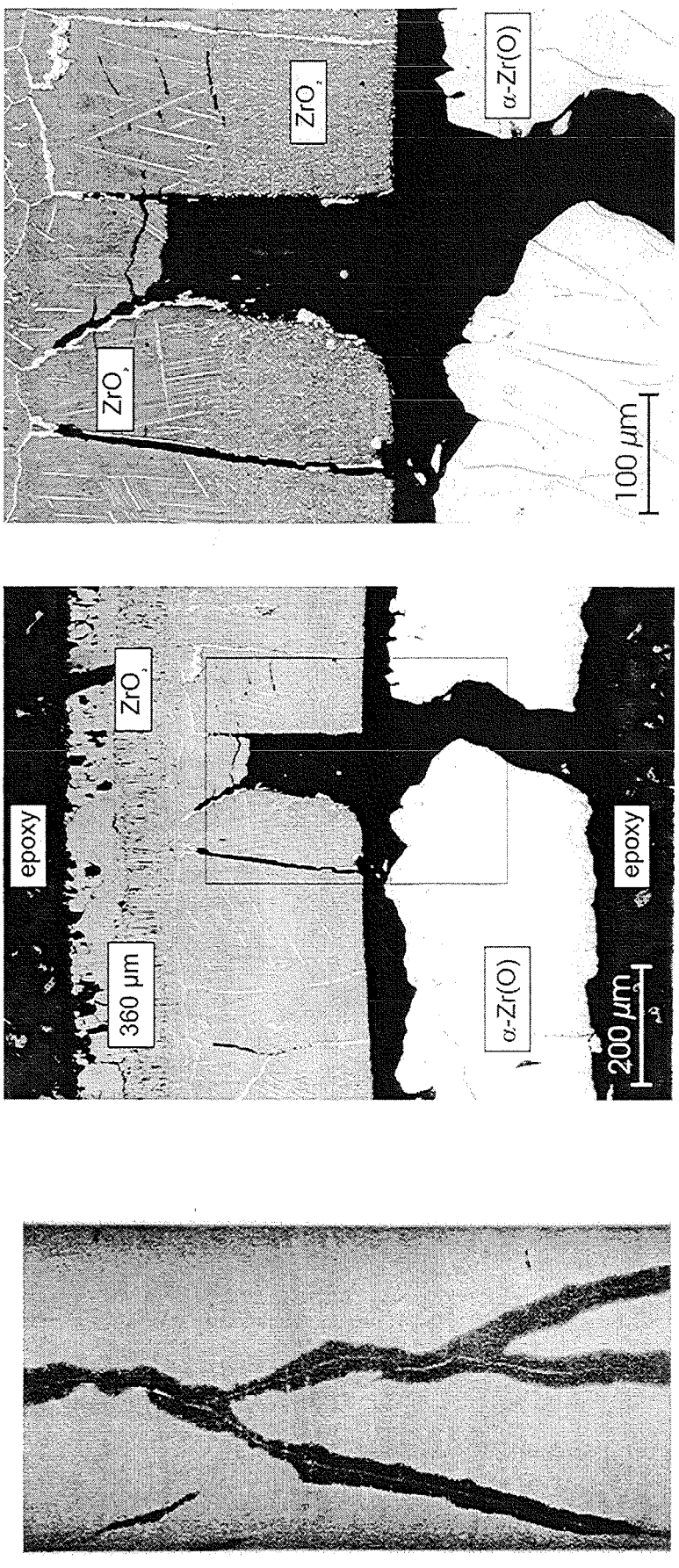

Figure 2.45: Oxidation of crack and Zircaloy tube surfaces. Test 16028_2; elevation 98 mm, temperature at onset of cooldown: 1600 °C.

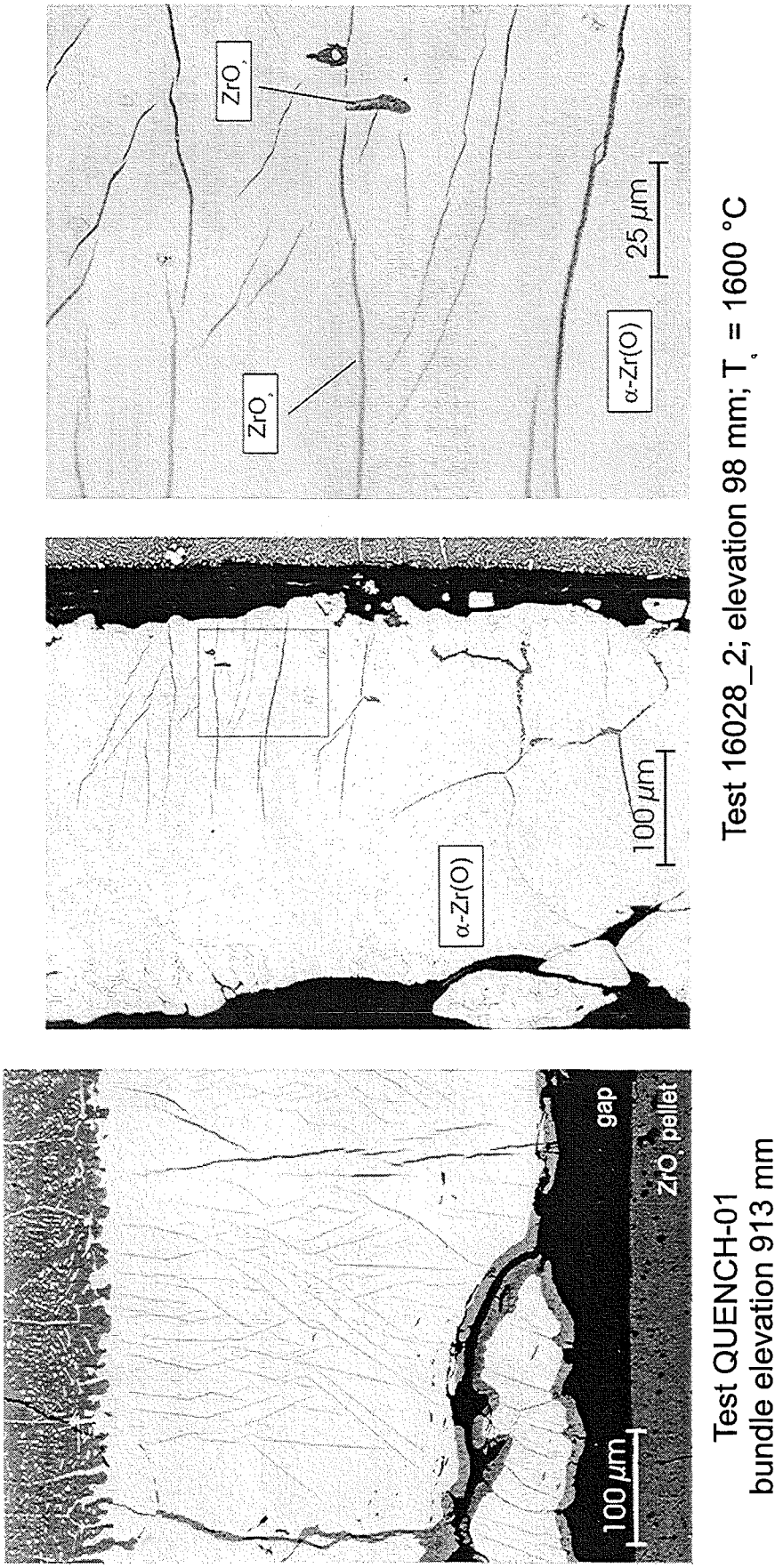

Figure 2.46: Formation of needle-shaped cracks in QUENCH-01 test and in small-scale experiments when quenched from higher temperatures.

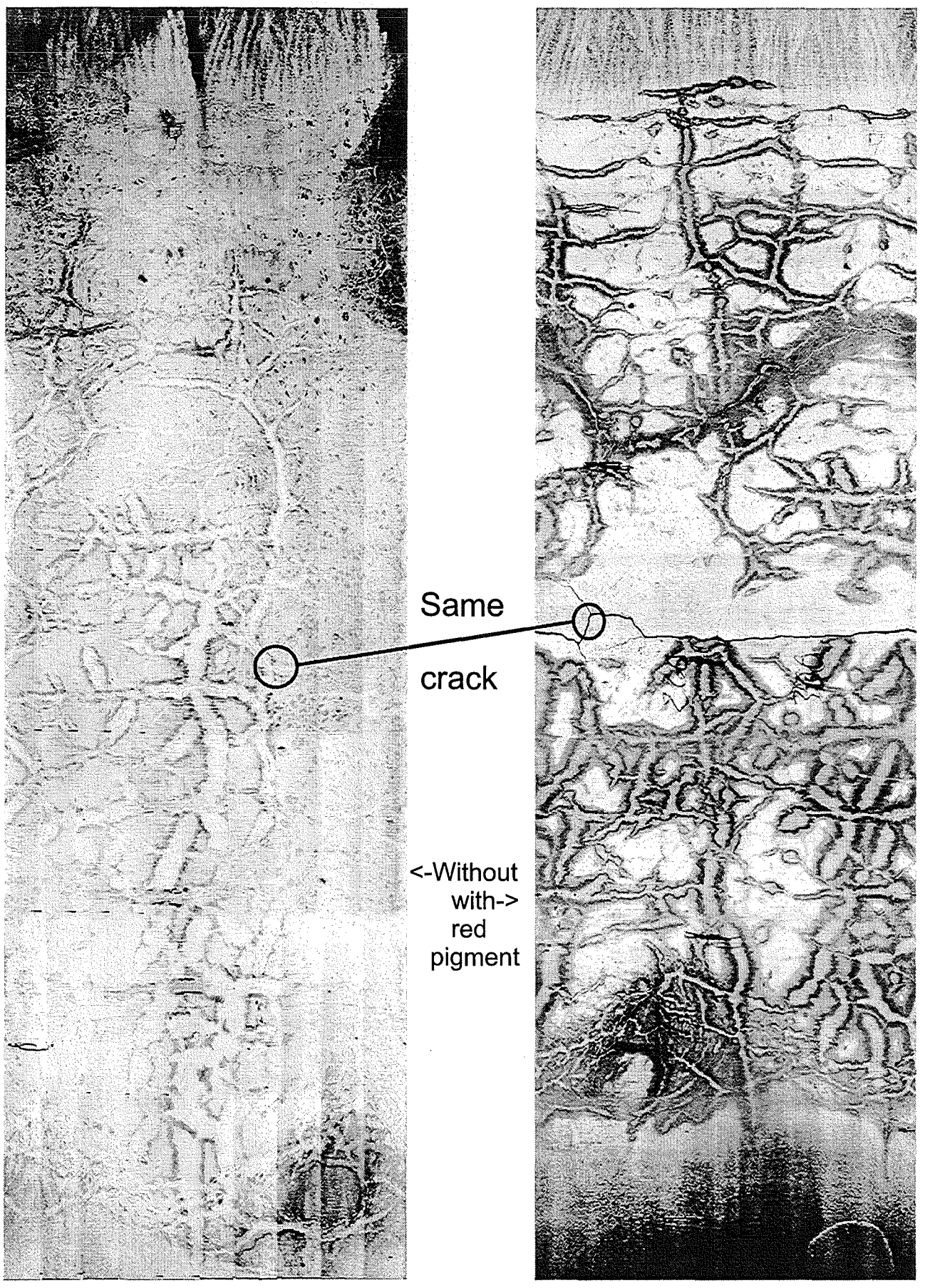

Figure 2.47: Different surface aspects as function of solvent composition (experiment 25028_1).

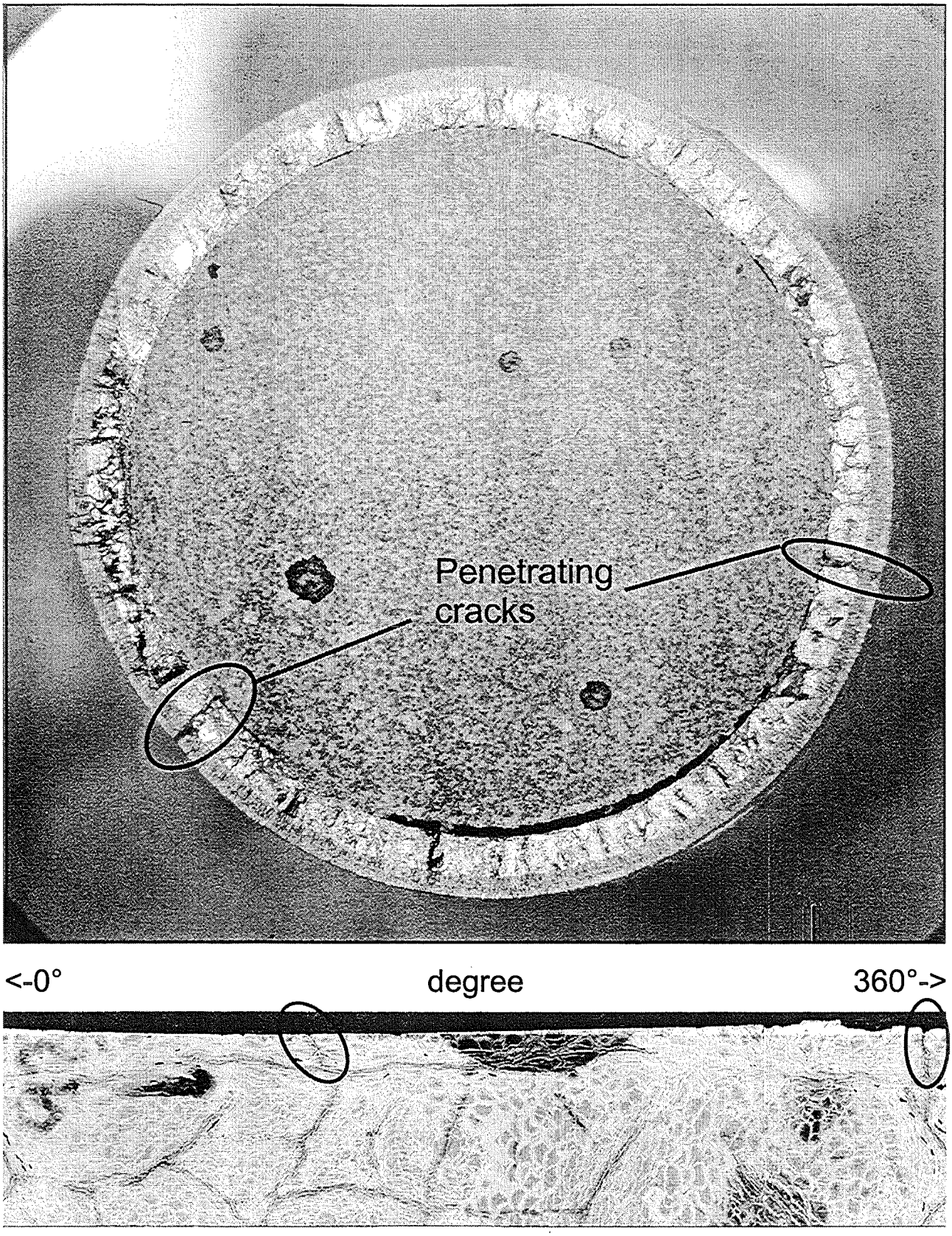

Figure 2.48: Cross section of 09028_1 at 92 mm elevation with two penetrating cracks in the zirconia and many cracks in the α-Zr(O) layer.

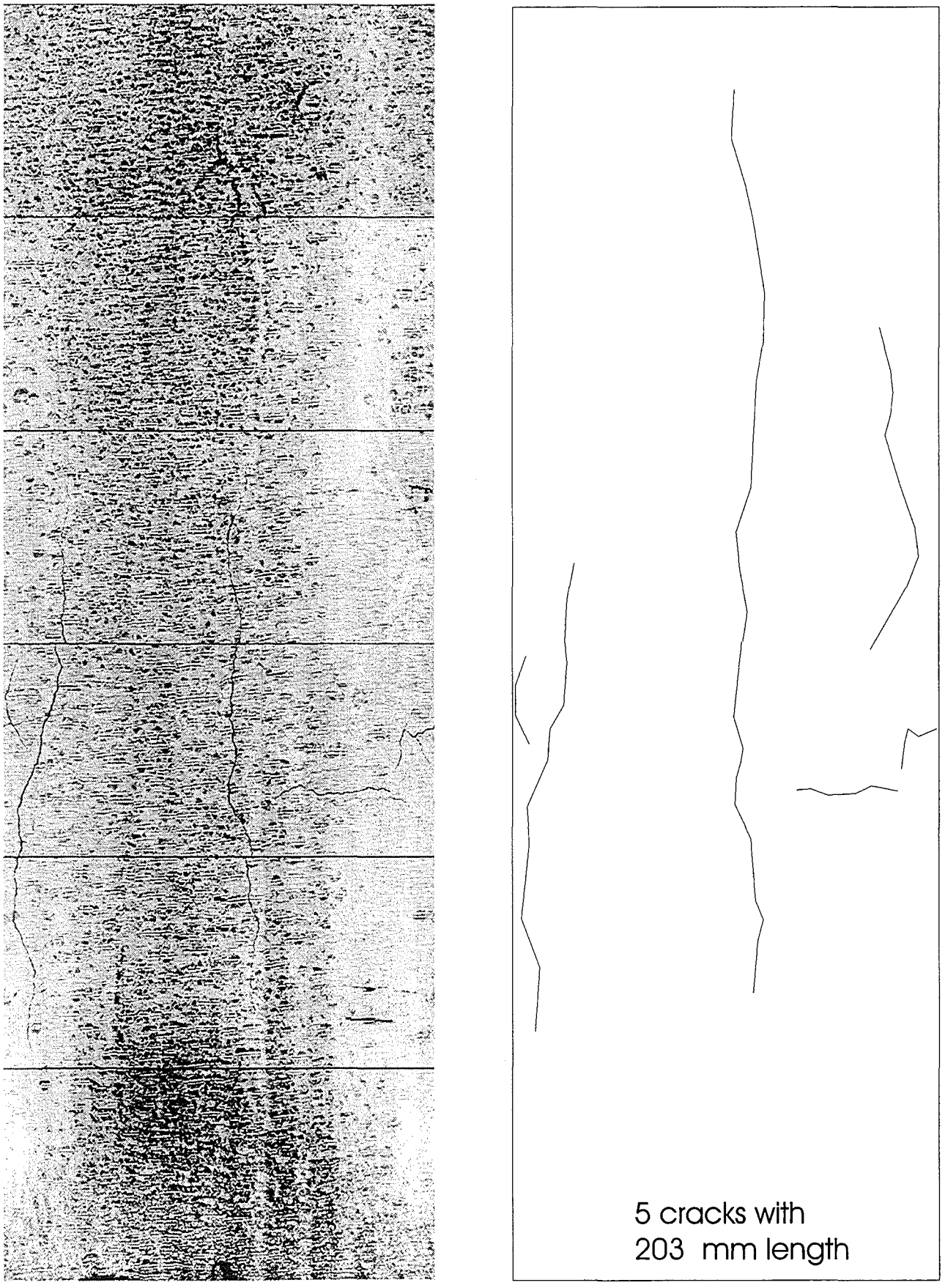

Figure 2.49: Cladding tube surface of experiment 05038_1 (1100 °C, 270 µm oxide layer thickness). Left: solvent filled cracks; right: hand traced cracks.

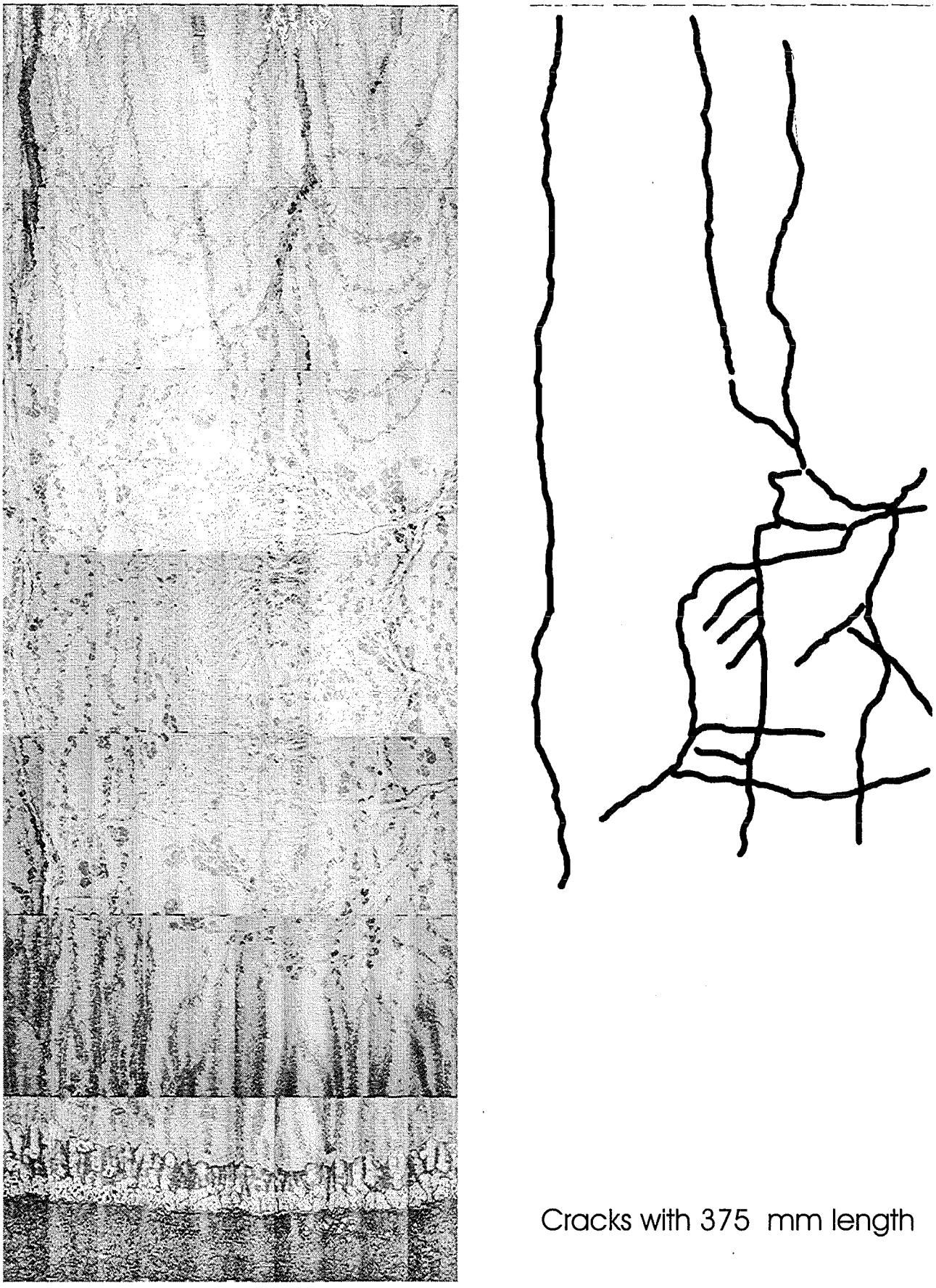

Figure 2.50: Cladding tube surface of experiment 05038_2 (1100 °C, 215 µm oxide layer thickness). Left: solvent filled cracks; right: hand traced cracks.

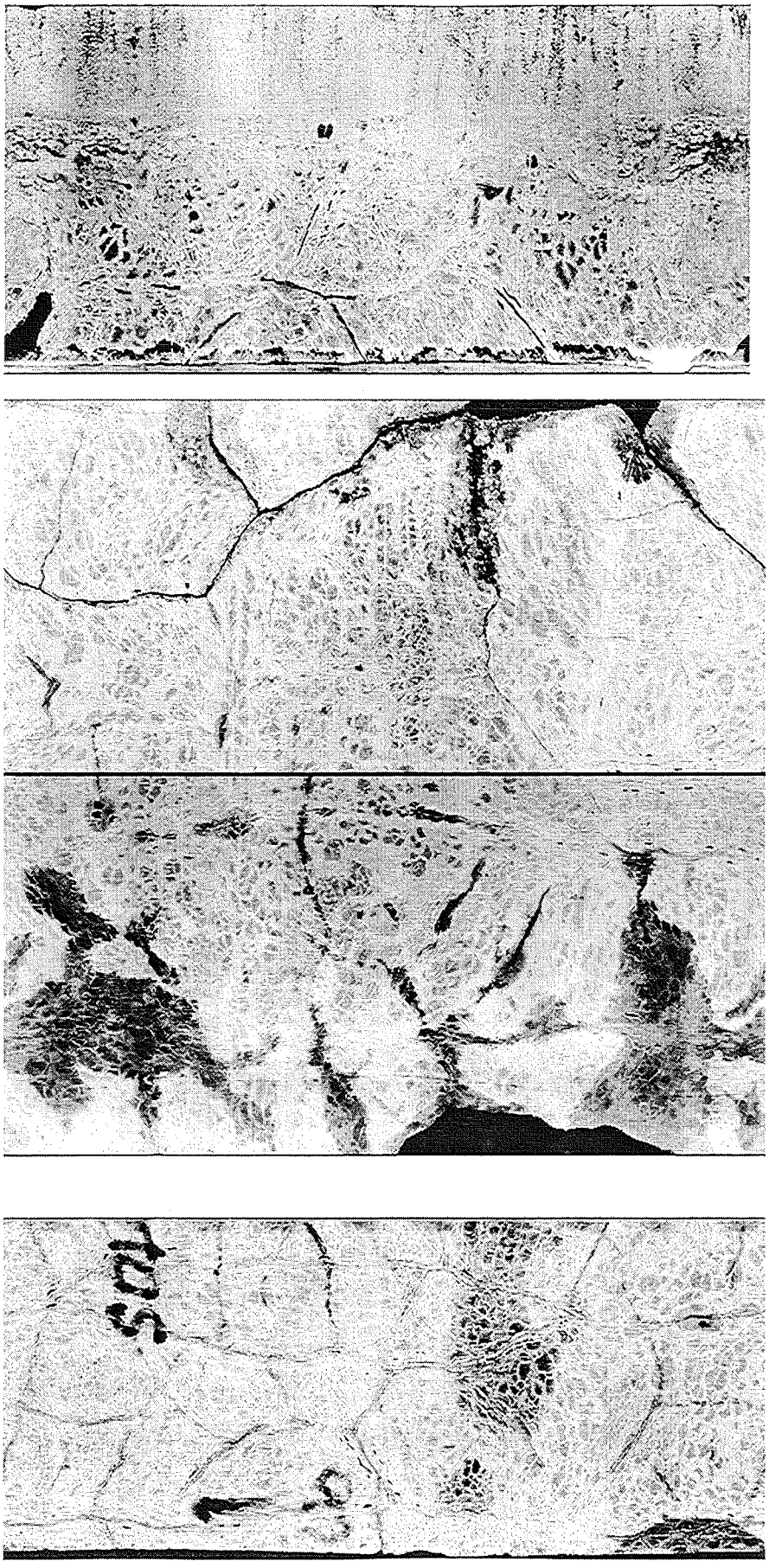

Figure 2.51: Parts of cladding tube circumference from the experiment 09028_1 (1200 °C, 315 µm oxide layer thickness); 4 different circumference images of broken tube.

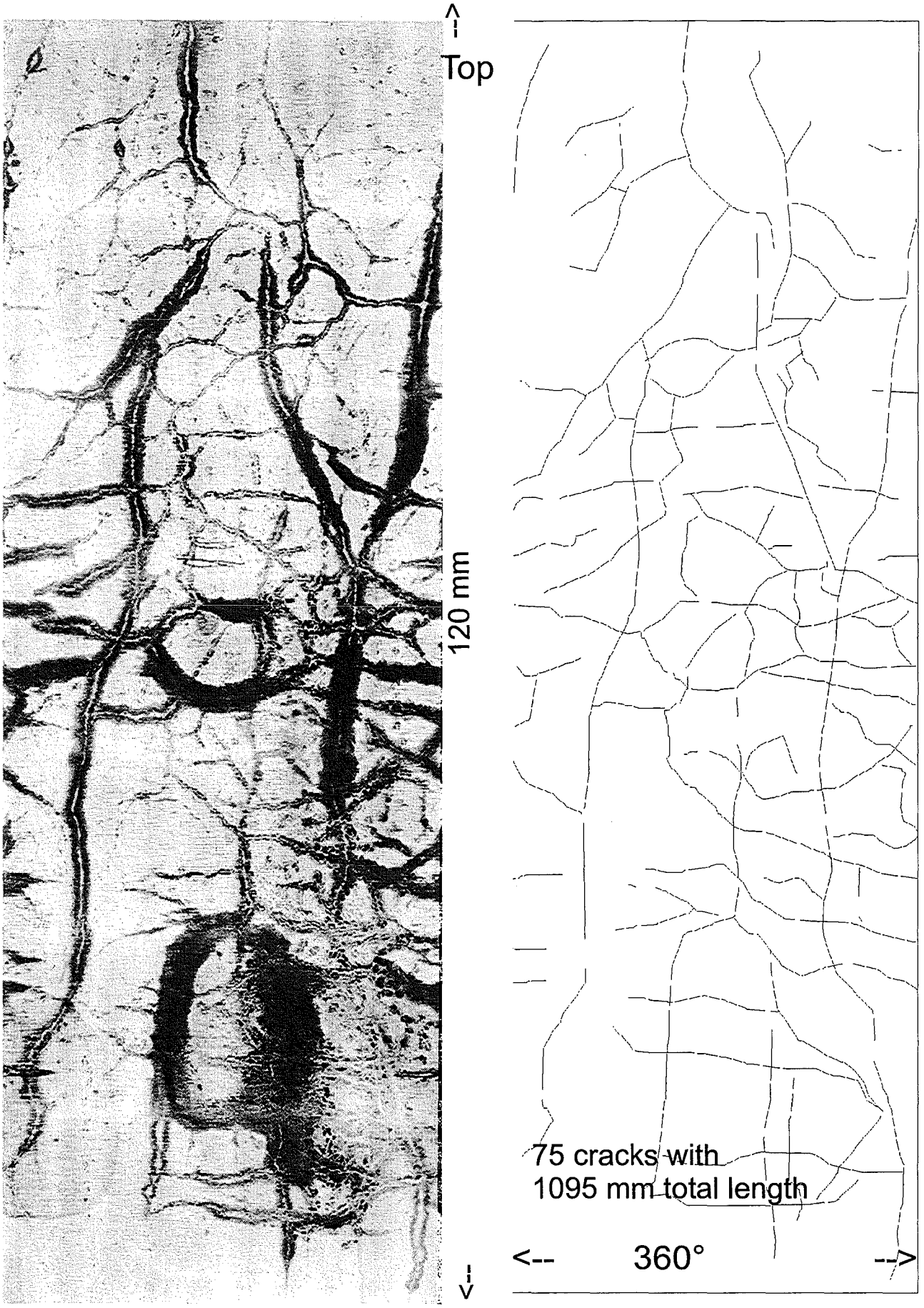

Figure 2.52: Cladding tube circumference of the experiment 10028_1 (1200 °C, 157 µm oxide layer thickness). Left: surface with red penetrant color; right: hand traced cracks.

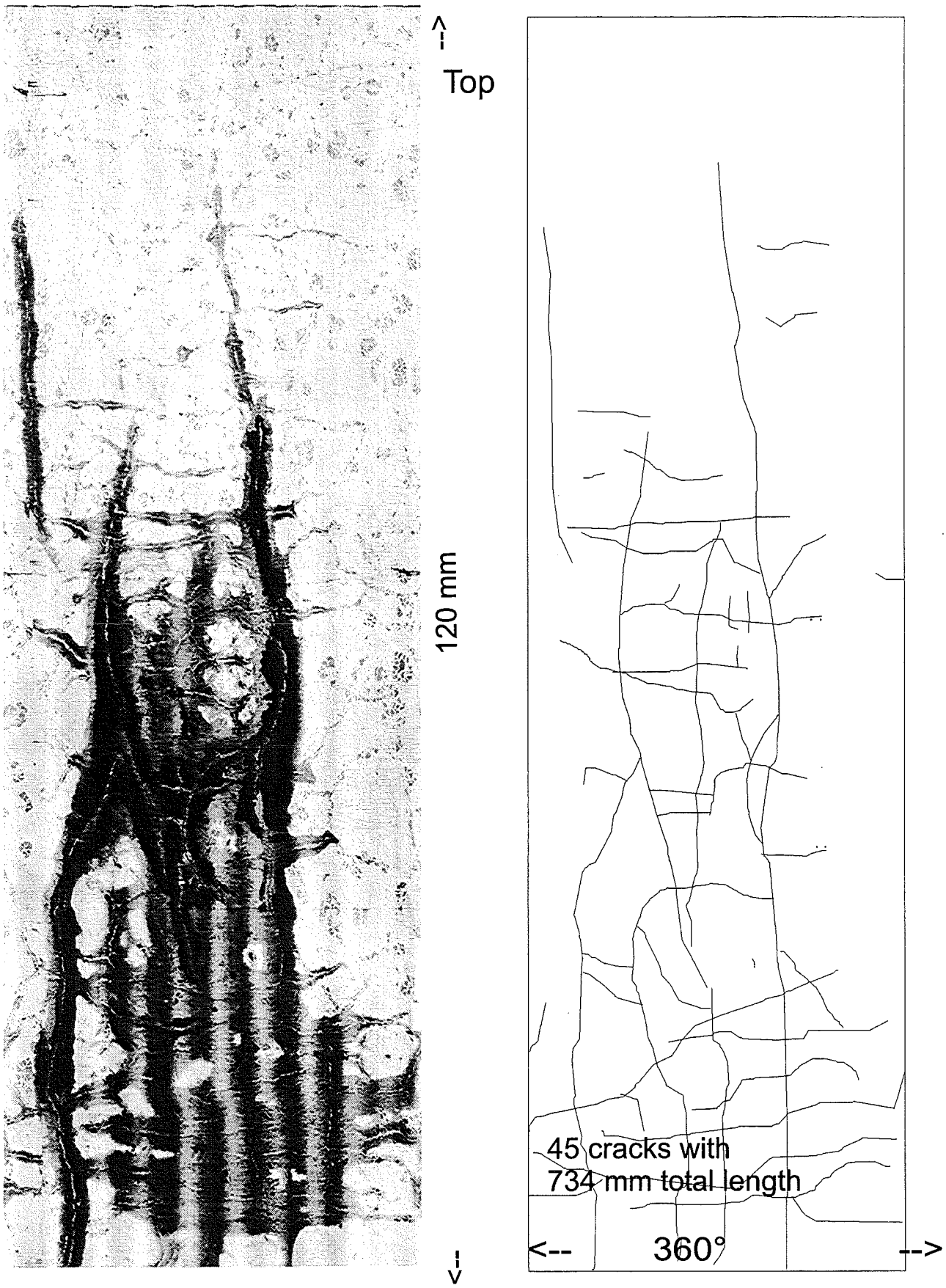

Figure 2.53: Cladding tube circumference of the experiment 11028_1 (1200 °C, 176 µm oxide layer thickness). Left: surface with red penetrant color; right: hand traced cracks.

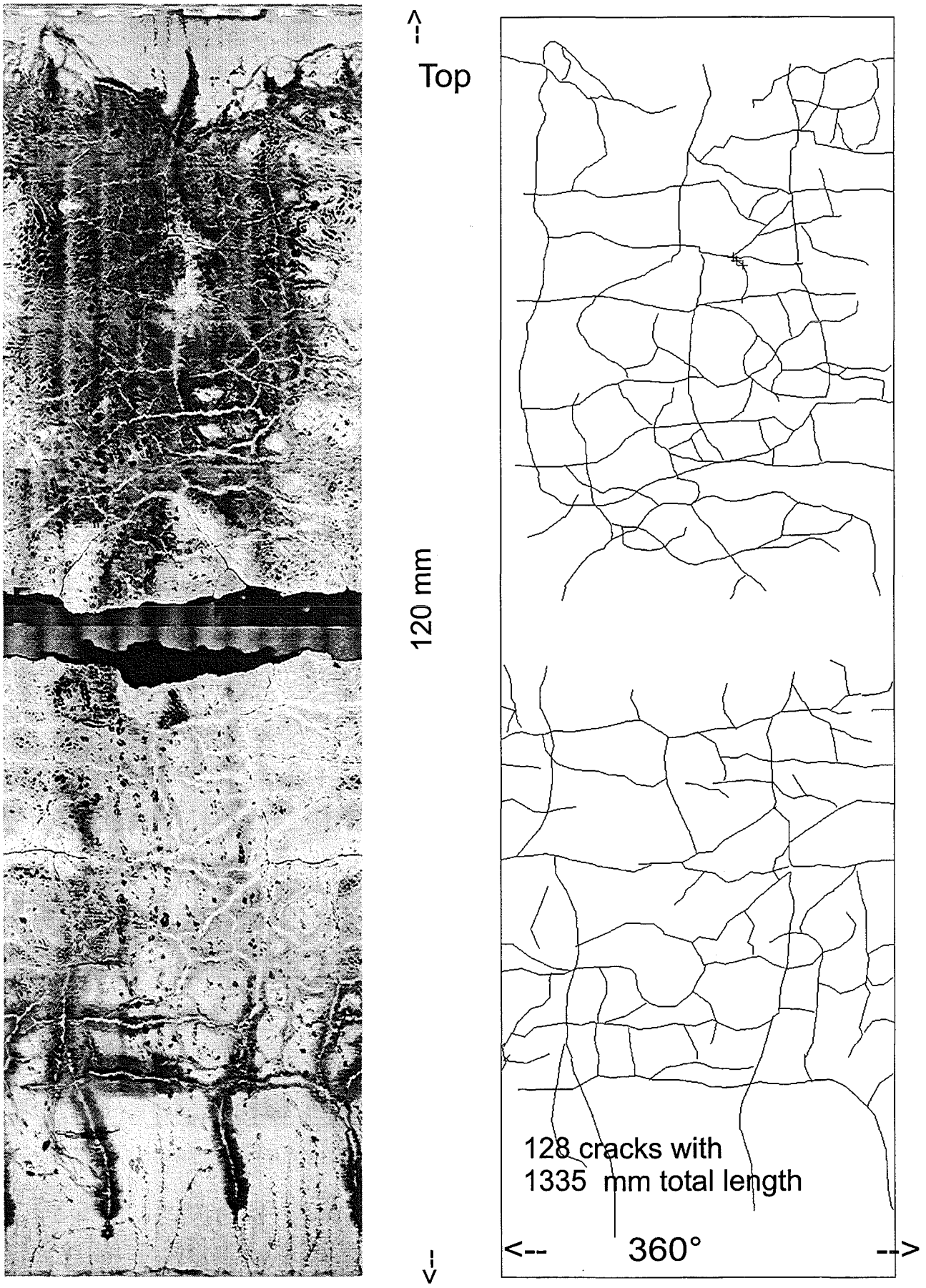

Figure 2.54: Cladding tube circumference of the experiment 11028_2 (1200 °C, 216 µm oxide layer thickness). Left: surface with red penetrant color; right: hand traced cracks.

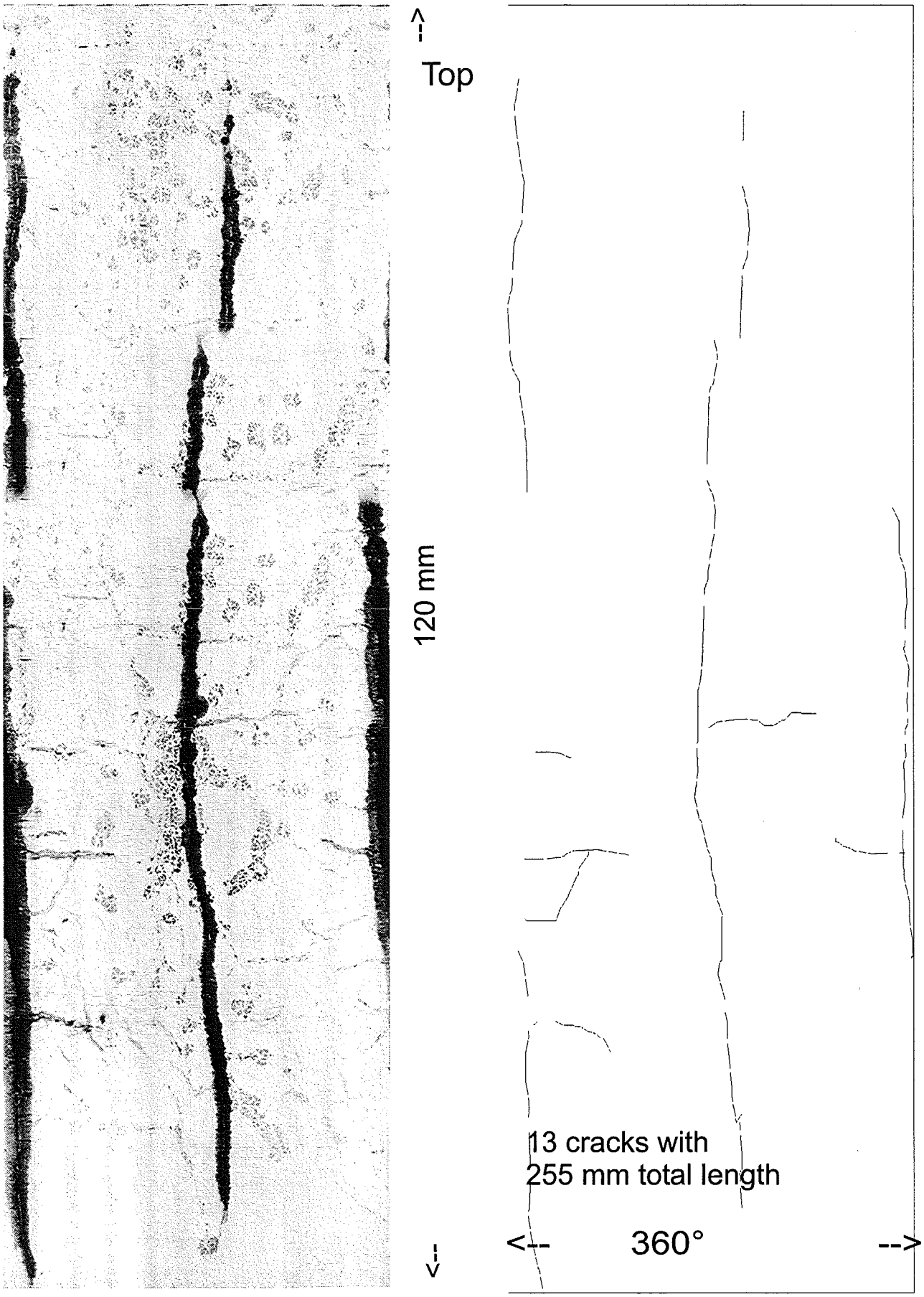

Figure 2.55: Cladding tube circumference of the experiment 12028_1 (1200 °C, 157 µm oxide layer thickness). Left: surface with red penetrant color; right: hand traced cracks.

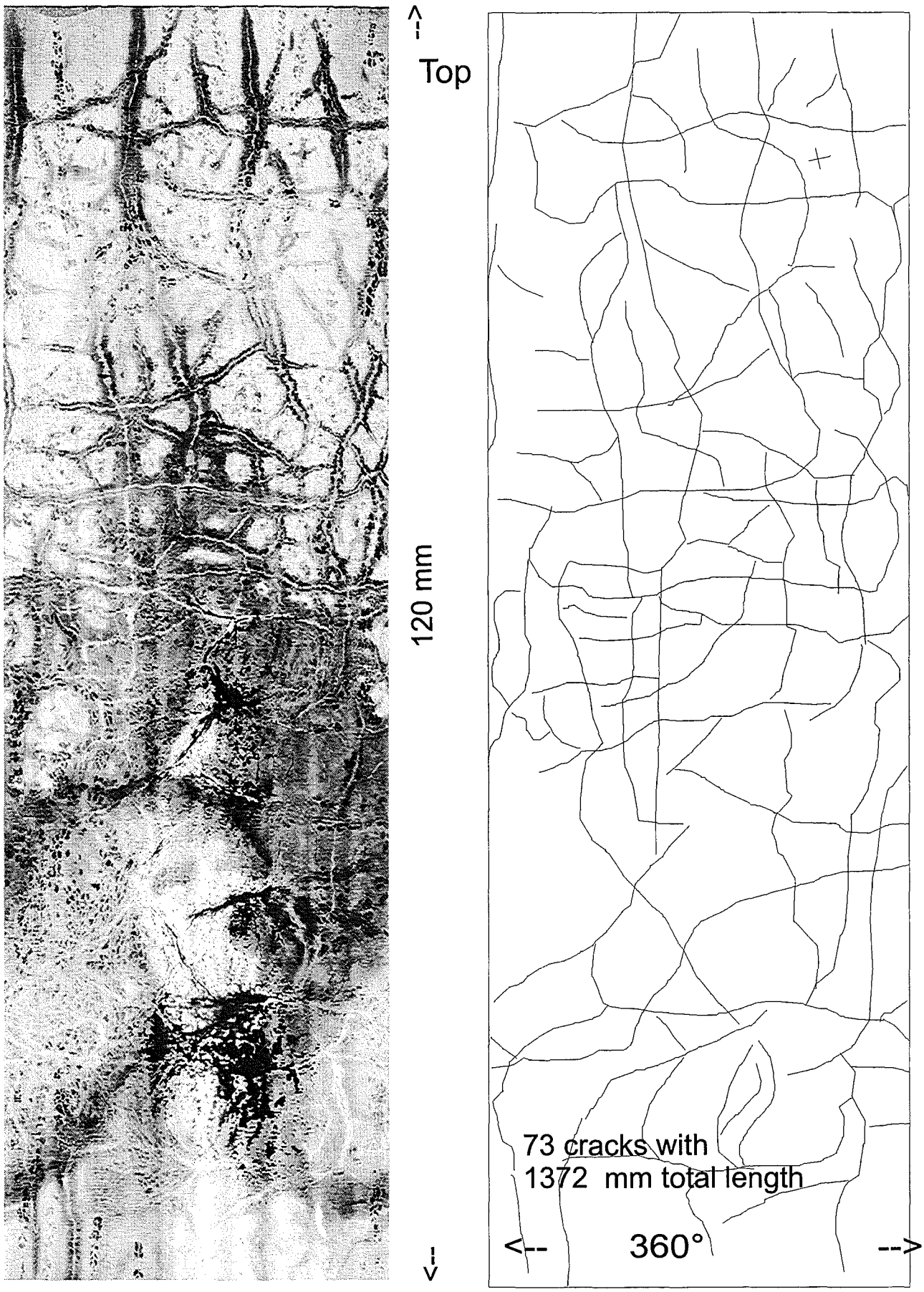

Figure 2.56: Cladding tube circumference of the experiment 13028_1 (1200 °C, 287 µm oxide layer thickness). Left: surface with red penetrant color; right: hand traced cracks.

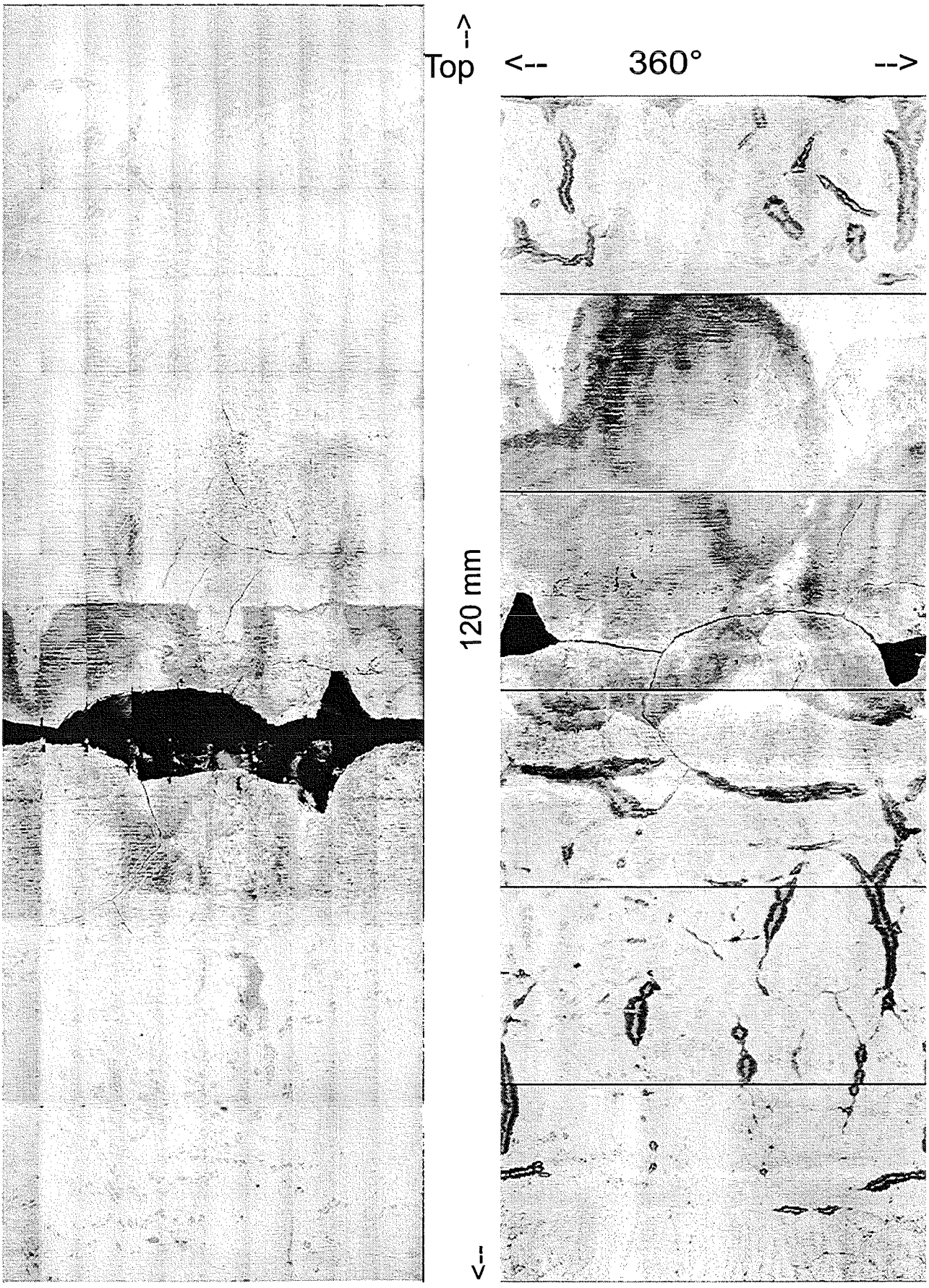

Figure 2.57: Cladding tube circumference of the experiment 17028_1 (1400 °C, 246 µm oxide layer thickness). Left: broken without color penetrant; right: glued with color penetrant.

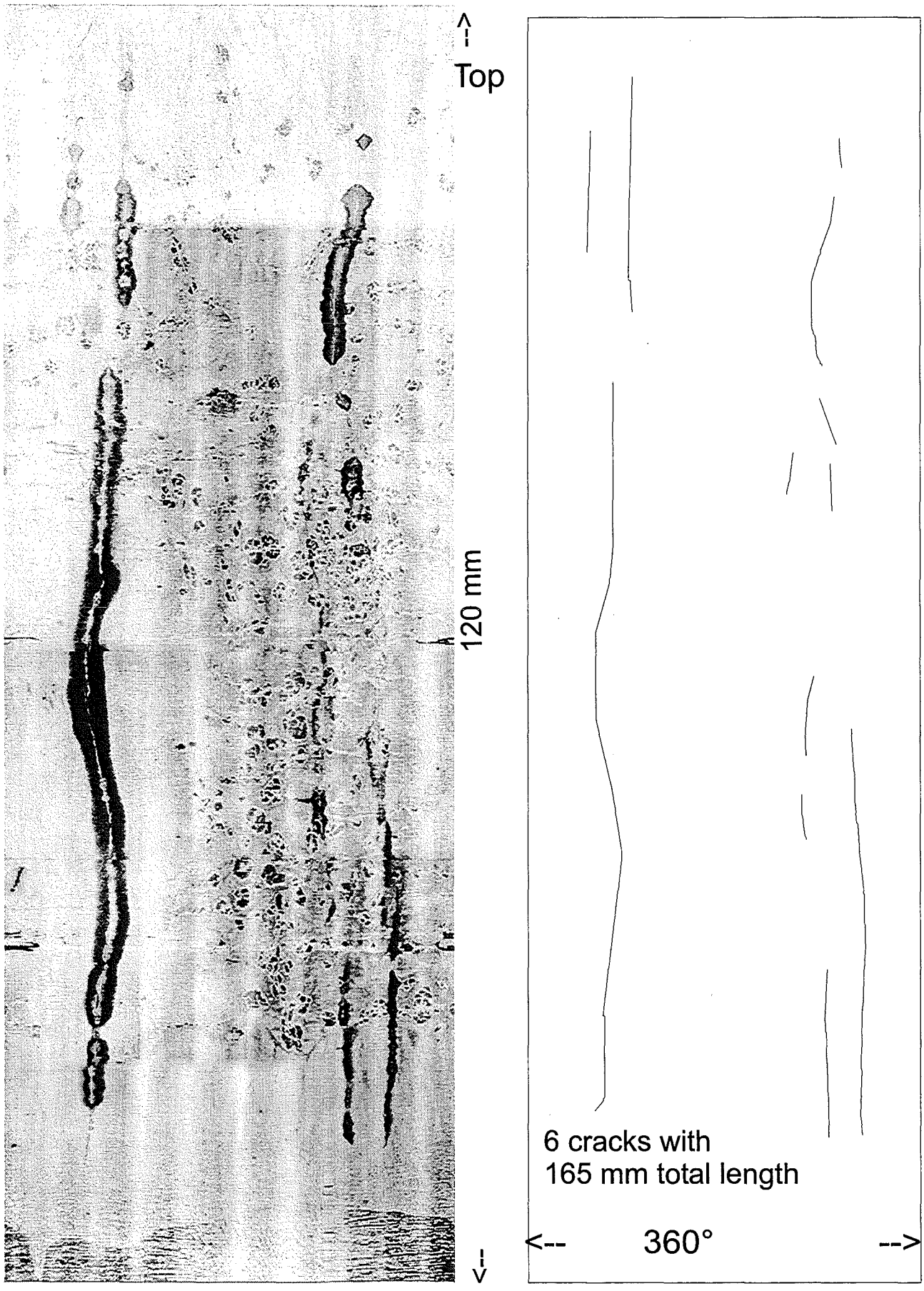

Figure 2.58: Cladding tube circumference of the experiment 18028_1 (1400 °C, 150 µm oxide layer thickness). Left: surface with red penetrant color; right: hand traced cracks.

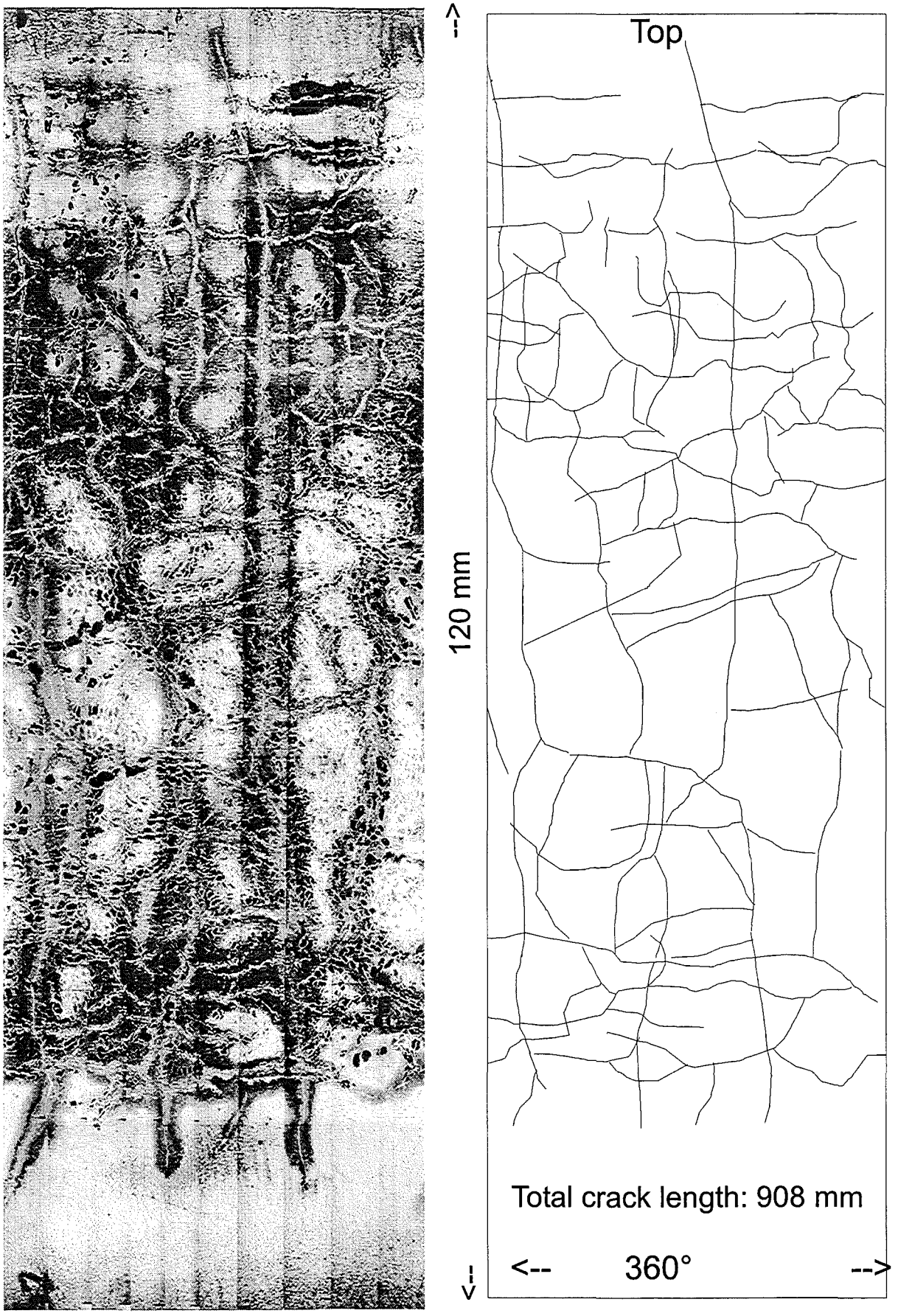

Figure 2.59: Cladding tube circumference of the experiment 19028_1 (1400 °C, 246 µm oxide layer thickness). Left: surface with red penetrant color; right: hand traced cracks.

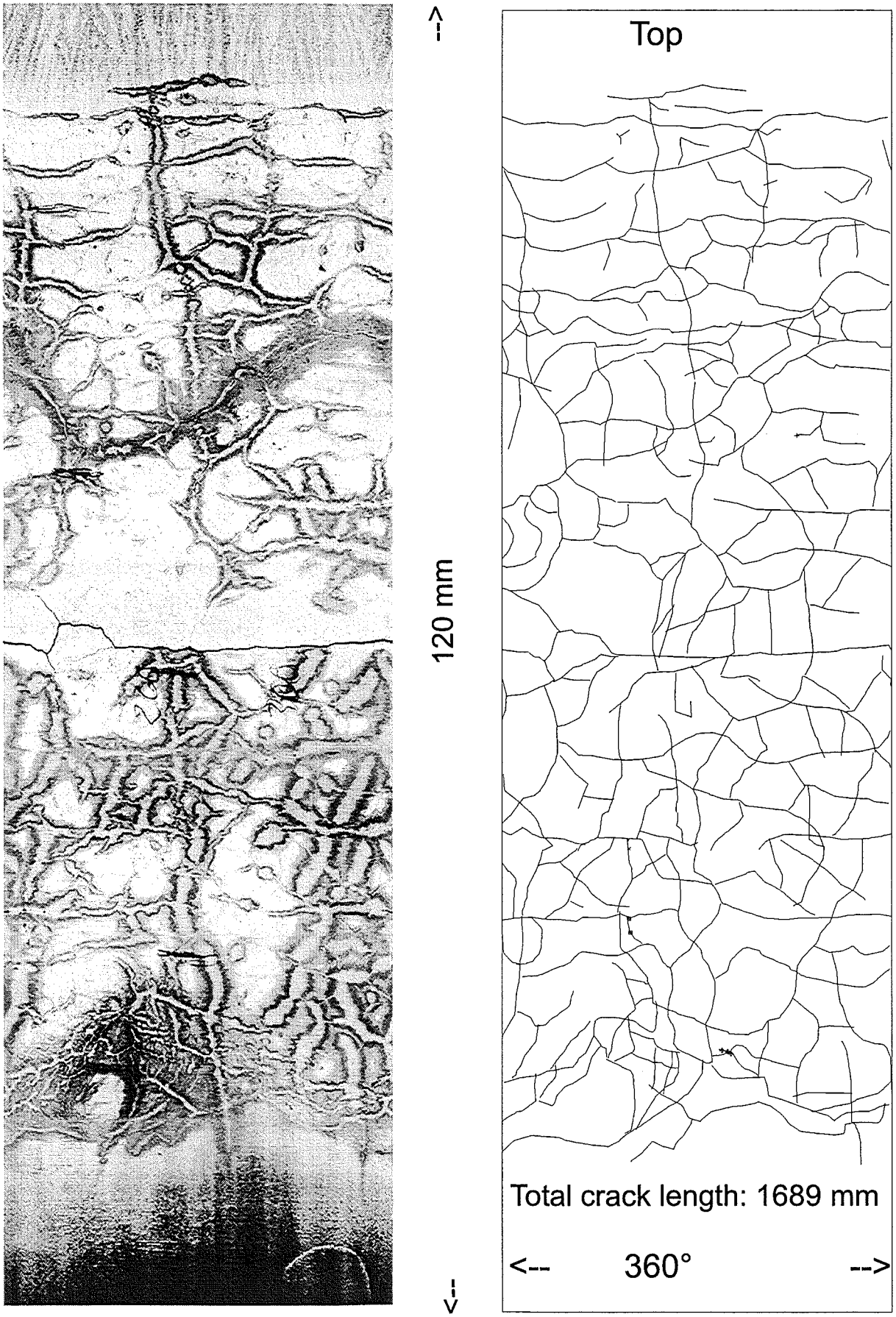

Figure 2.60: Cladding tube circumference of the experiment 25028_1 (1400 °C, 246 µm oxide layer thickness). Left: surface with red penetrant color; right: hand traced cracks.

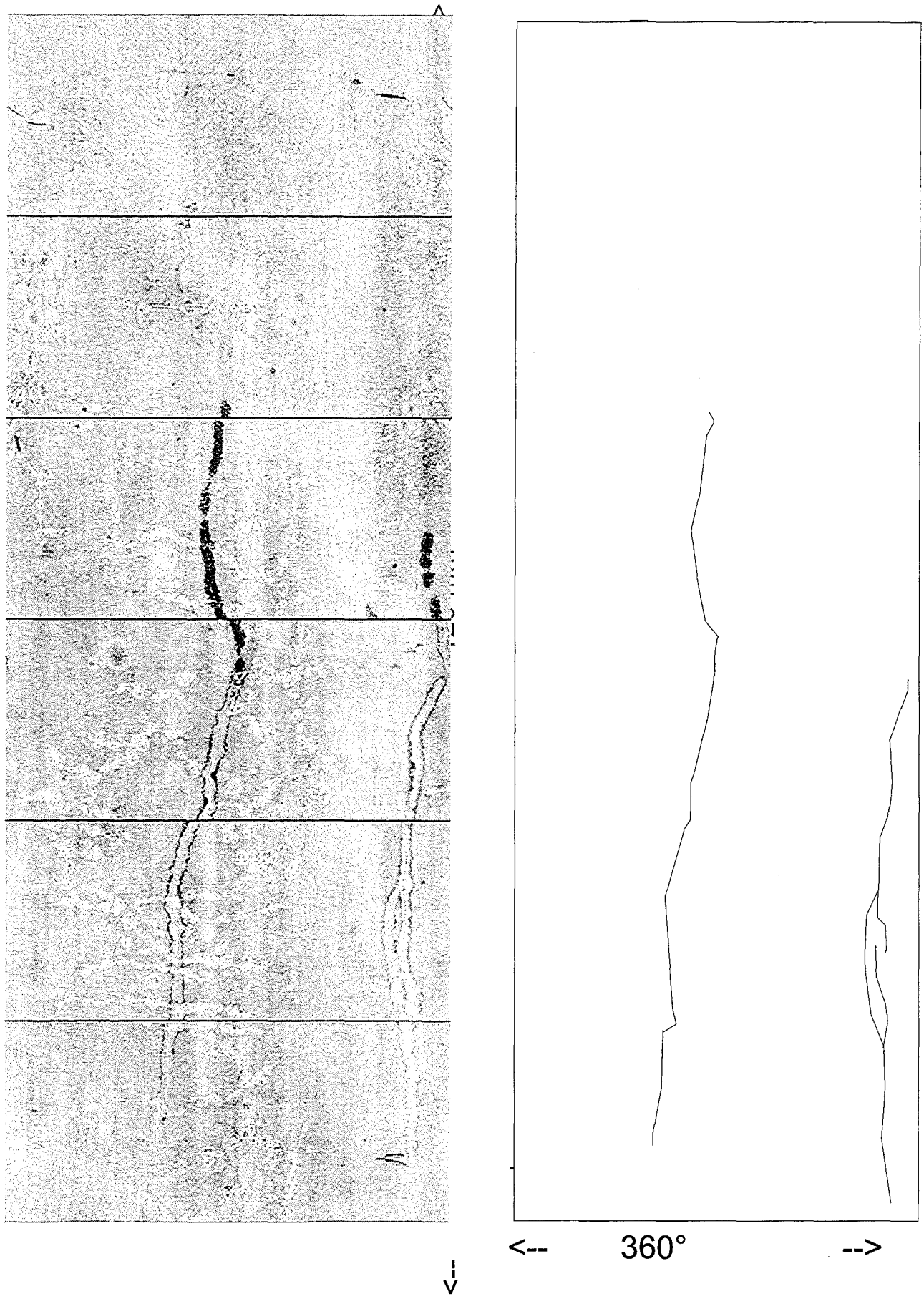

Figure 2.61: Cladding tube circumference of the experiment 25028_2 (1400 °C, 116 µm oxide layer thickness). Left: surface with red penetrant color; right: hand traced cracks.

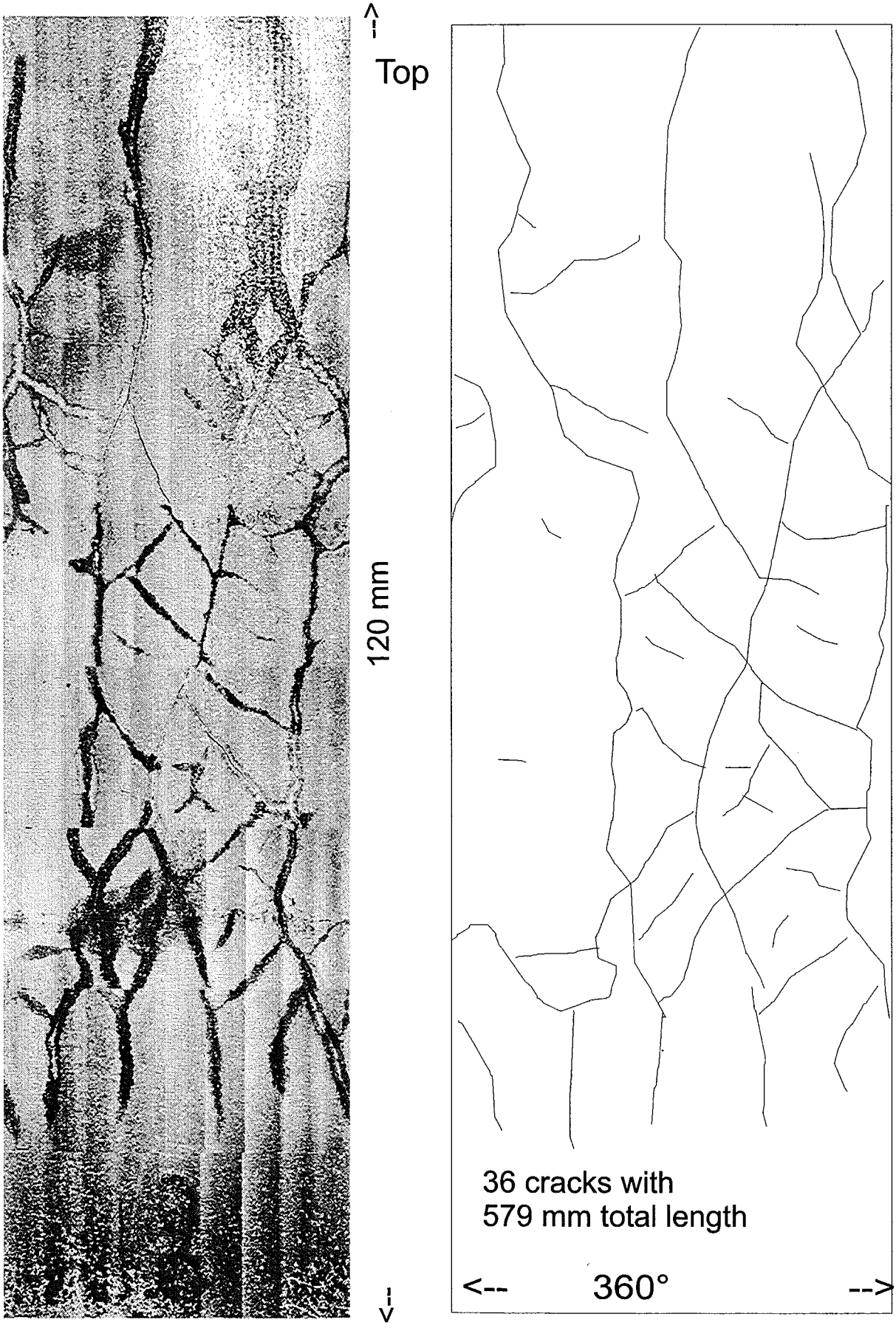

Figure 2.62: Cladding tube circumference of the experiment 16028_1 (1600 °C, 260 µm oxide layer thickness). Left: surface with red penetrant color; right: hand traced cracks.

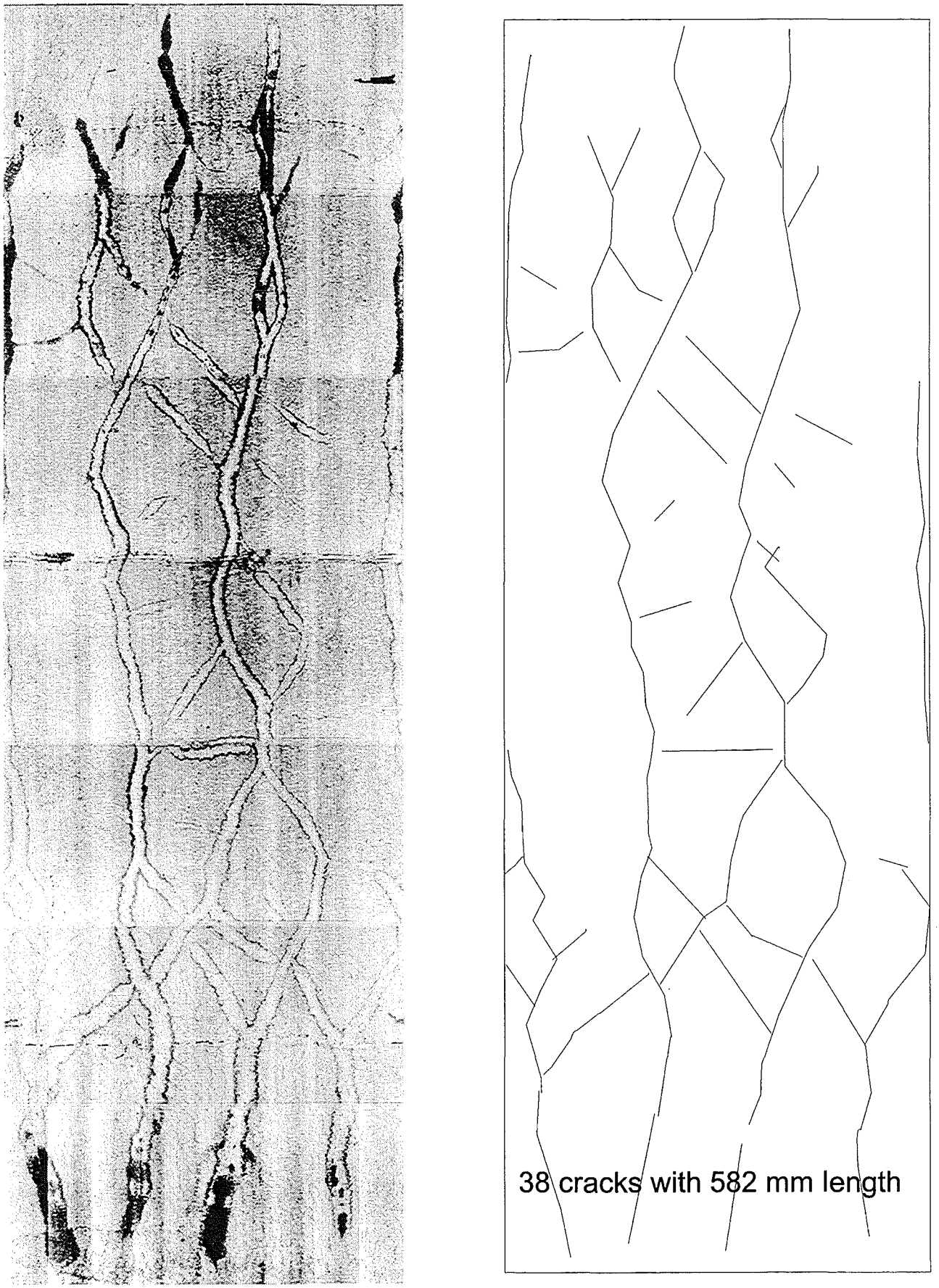

Figure 2.63: Cladding tube circumference of the experiment 26028_1 (1600 °C, 240 µm oxide layer thickness). Left: surface with red penetrant color; right: hand traced cracks.

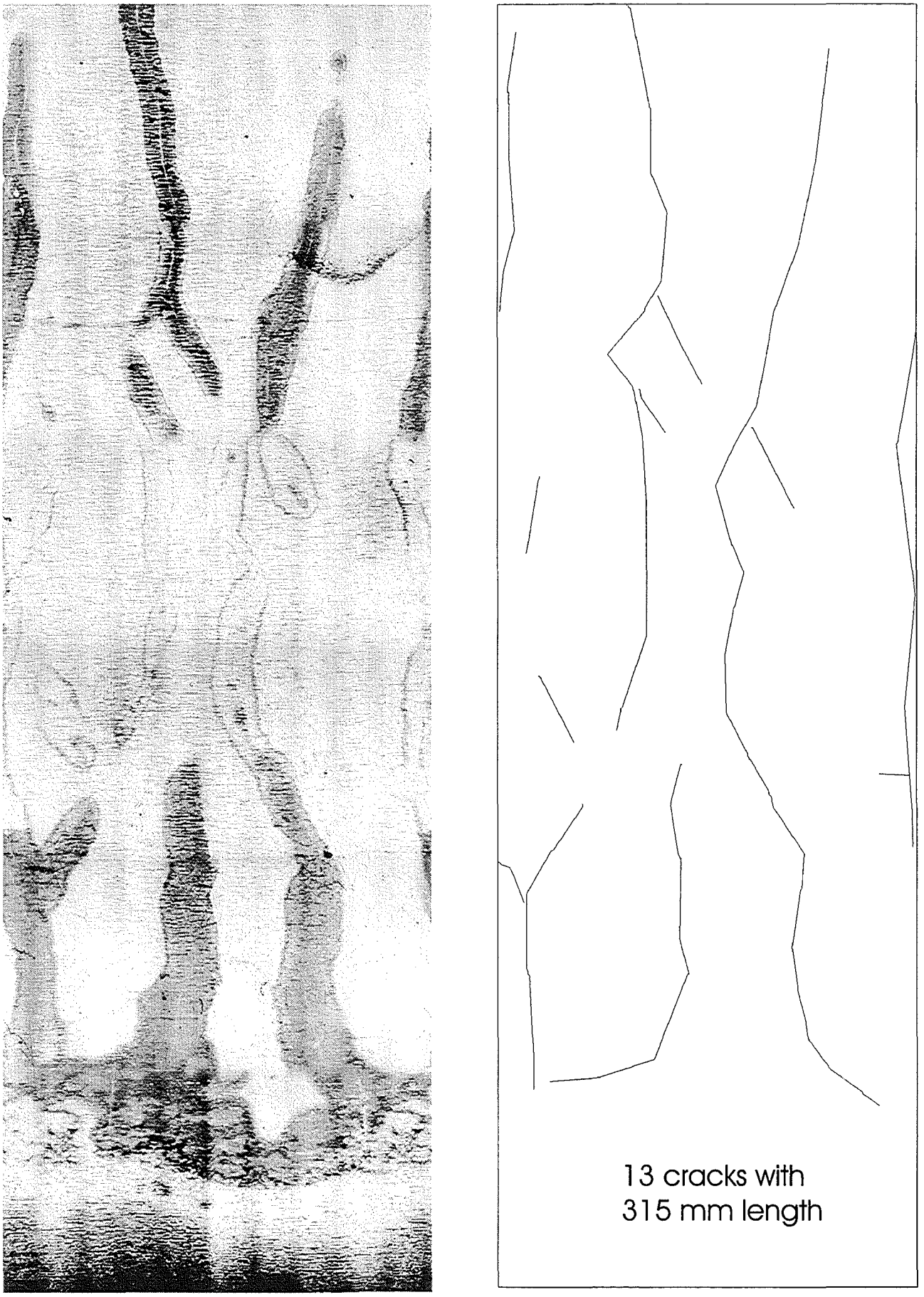

Figure 2.64: Cladding tube circumference of the experiment 02038_1 (1600 °C, 201 µm oxide layer thickness). Left: surface with red penetrant color; right: hand traced cracks.

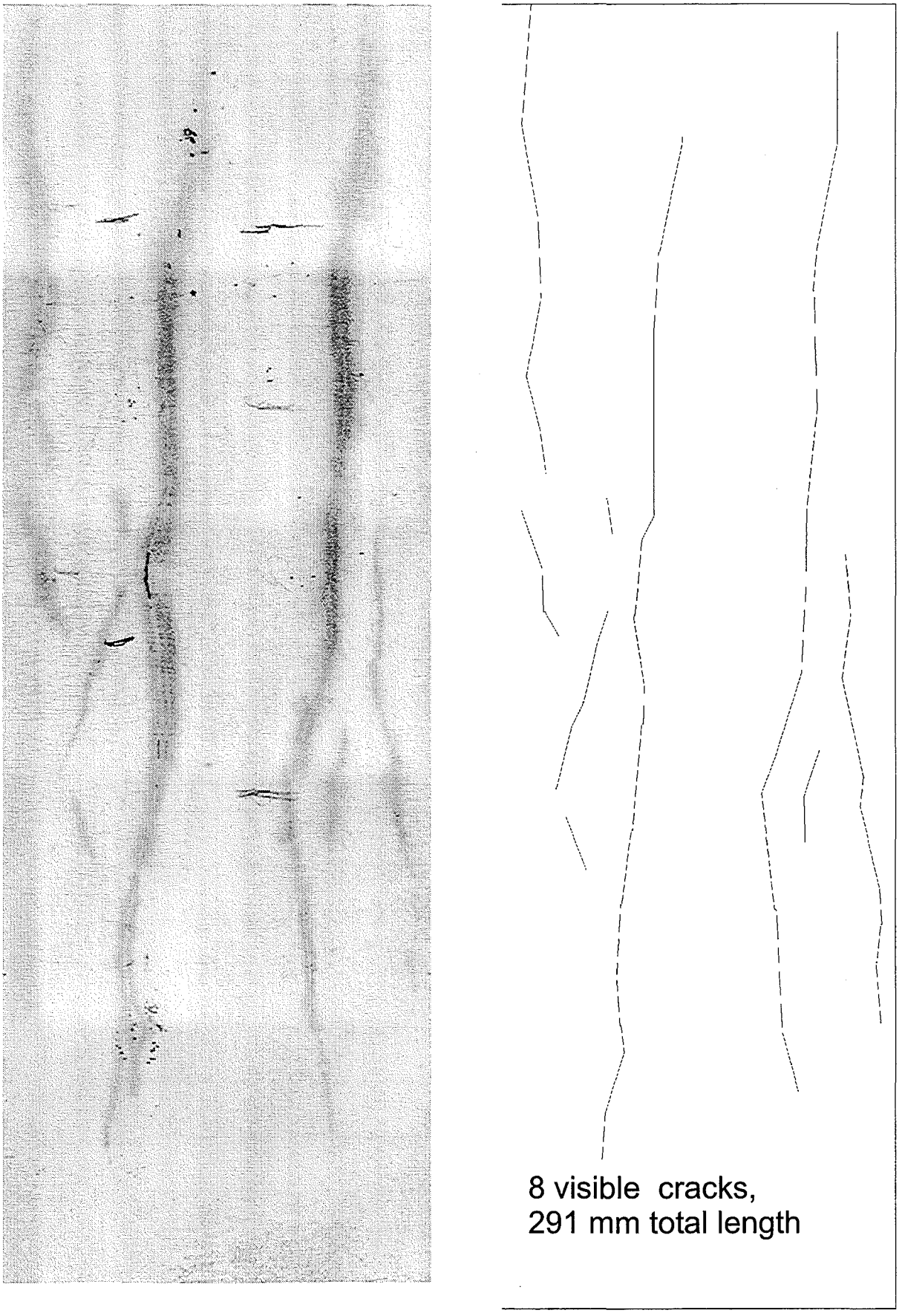

Figure 2.65: Cladding tube circumference of the experiment 03038_1 (1600 °C, 173 µm oxide layer thickness). Left: surface with red penetrant color; right: hand traced cracks.

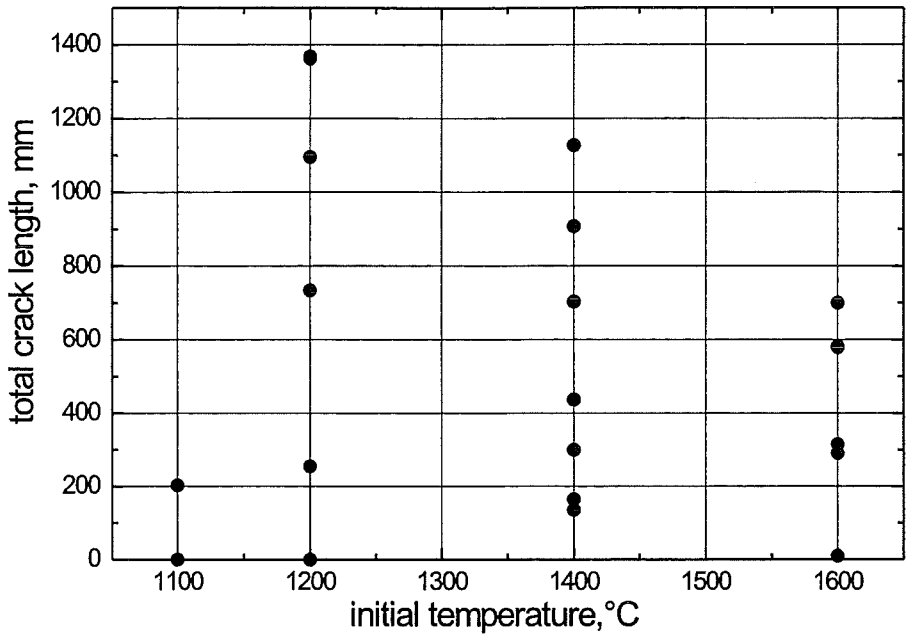

Figure 2.66: Total crack length vs. temperature.

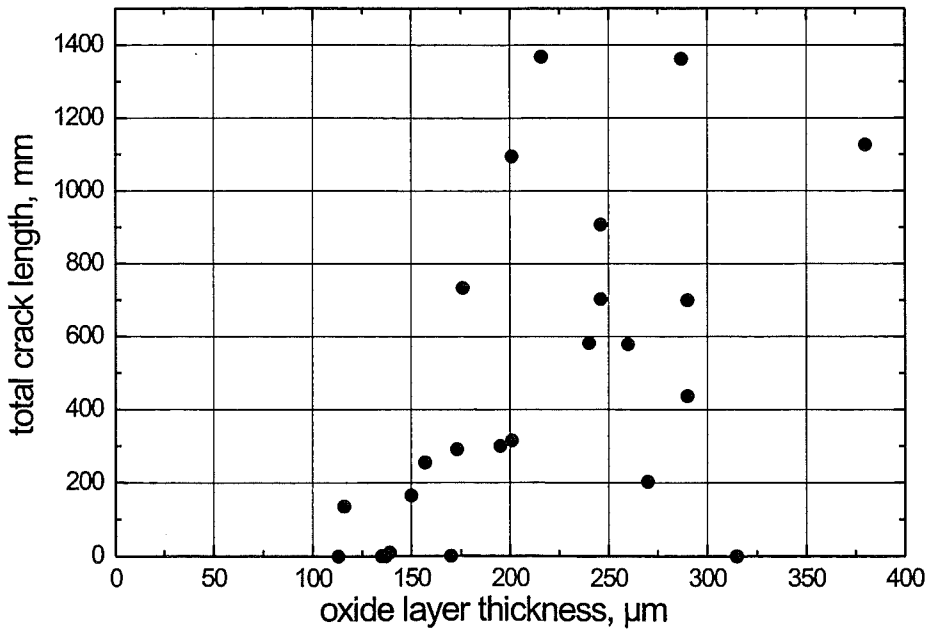

Figure 2.67: Crack length vs. initial oxide layer thickness.

Test ID	Time of pre-oxidation at 1400 °C, min	Measured oxide thick-ness at onset of cooldown, μm	H concen-tration (refer-red to metal atoms), weight %	H concen-tration (refer-red to metal atoms), mole %	Position of the probe, mm
cooldown from 1100 °C					
06038_1a	7	175	0.0018	0.16	65-85
05038_1a	19	255	0.0150	1.35	105-125
05038_1b	19	270	0.0164	1.47	65-85
cooldown from 1200 °C					
12028_1a	7	167	0.0024	0.22	65-85
10028_1a	12	210	0.0246	2.19	105-125
100281_b	12	212	0.0159	1.43	65-85
11028_1a	9	190	0.0239	2.13	105-125
11028_1b	9	185	0.0089	0.81	65-85
090281_a	30	290	0.0142	1.28	65-85
cooldown from 1400 °C					
180281_a	7	160	0.0015	0.13	65-85
19028_1a	19	260	0.0229	2.05	65-85
25028_1a	19	265	0.0537	4.67	65-85
cooldown from 1600 °C					
16028_1a	5	380	0.0341	3.02	96-115
27028_1a	3	163	0.0002	0.02	65-85
02038_1a	7	296	0.0057	0.51	65-85

Table 2.2: Results of the analysis of the hydrogen absorbed in the specimens from the small-scale experiments.

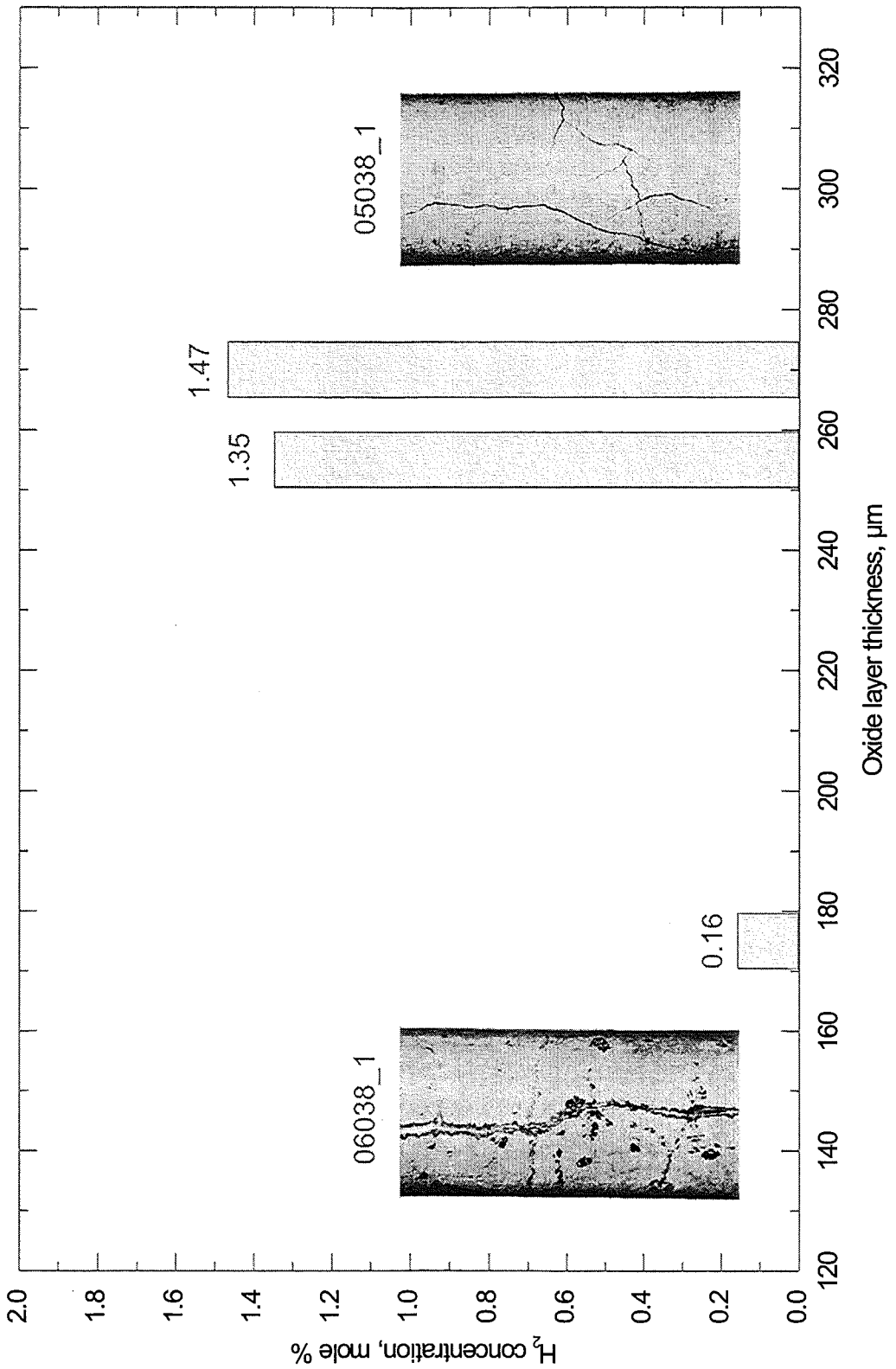

Figure 2.68: Dependence of the hydrogen concentration in the specimens cooled from 1100 °C from the oxide layer thickness.

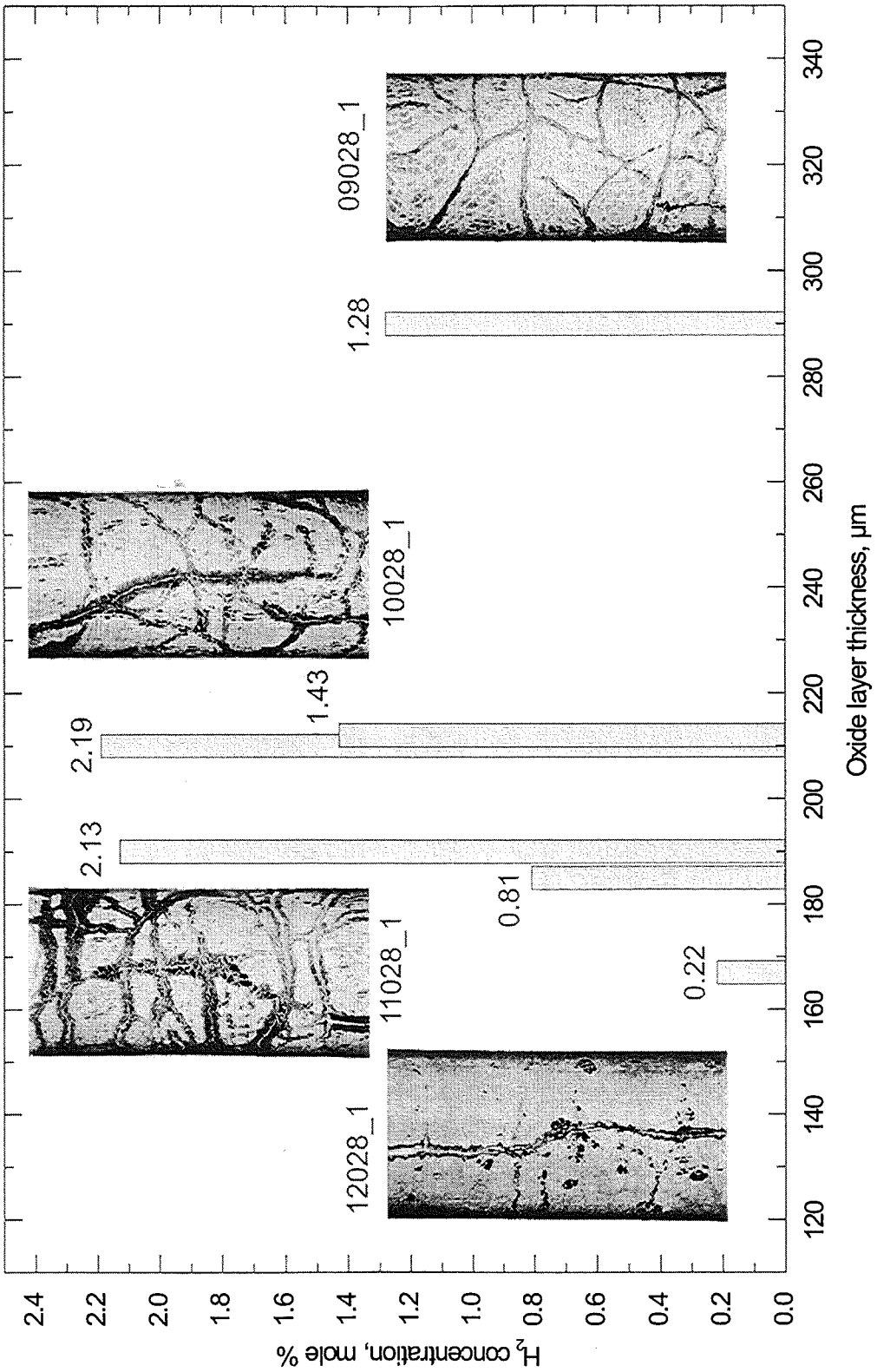

Figure 2.69: Dependence of the hydrogen concentration in the specimens cooled from 1200 °C from the oxide layer thickness.

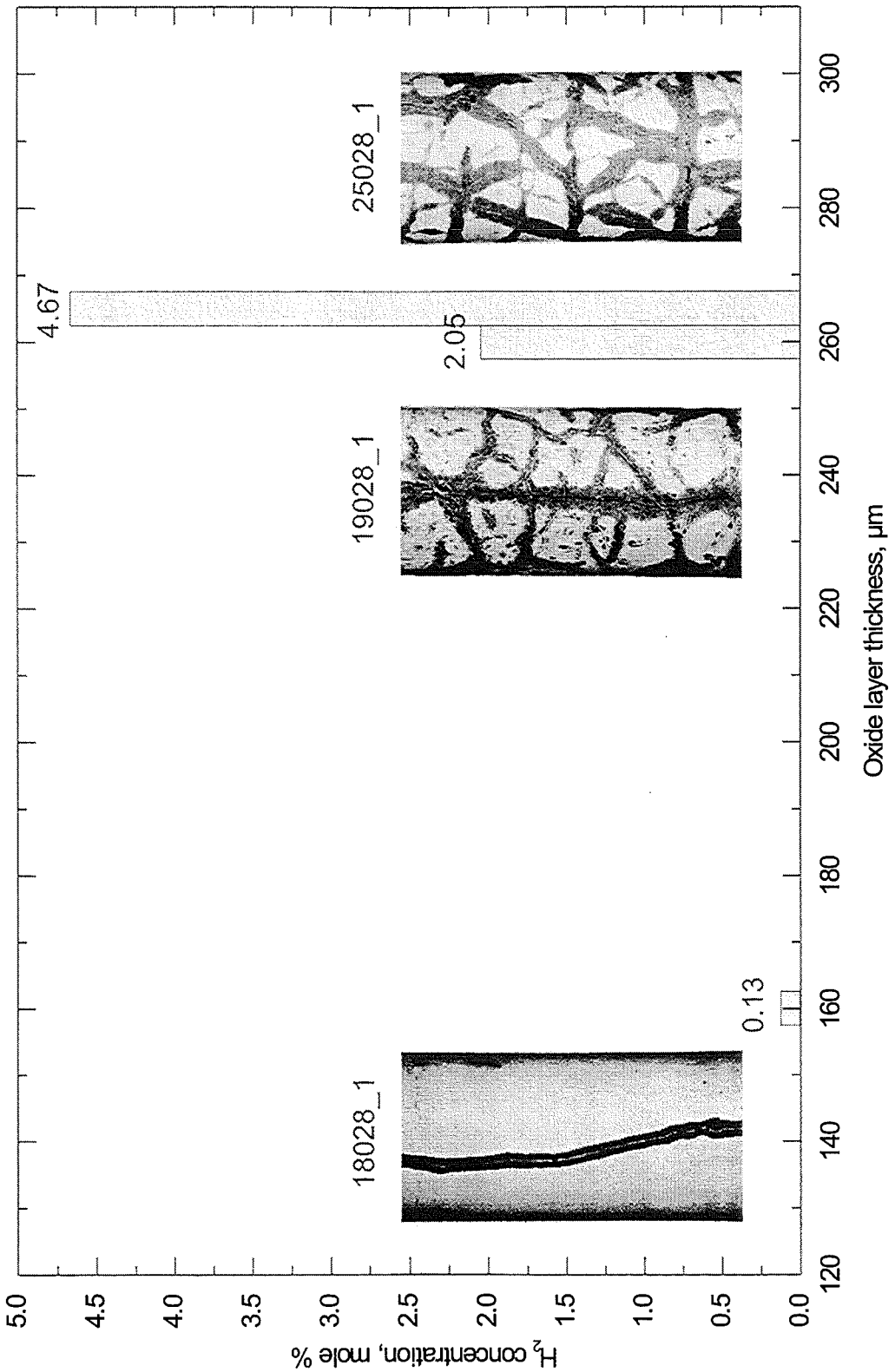

Figure 2.70: Dependence of the hydrogen concentration in the specimens cooled from 1400 °C from the oxide layer thickness.

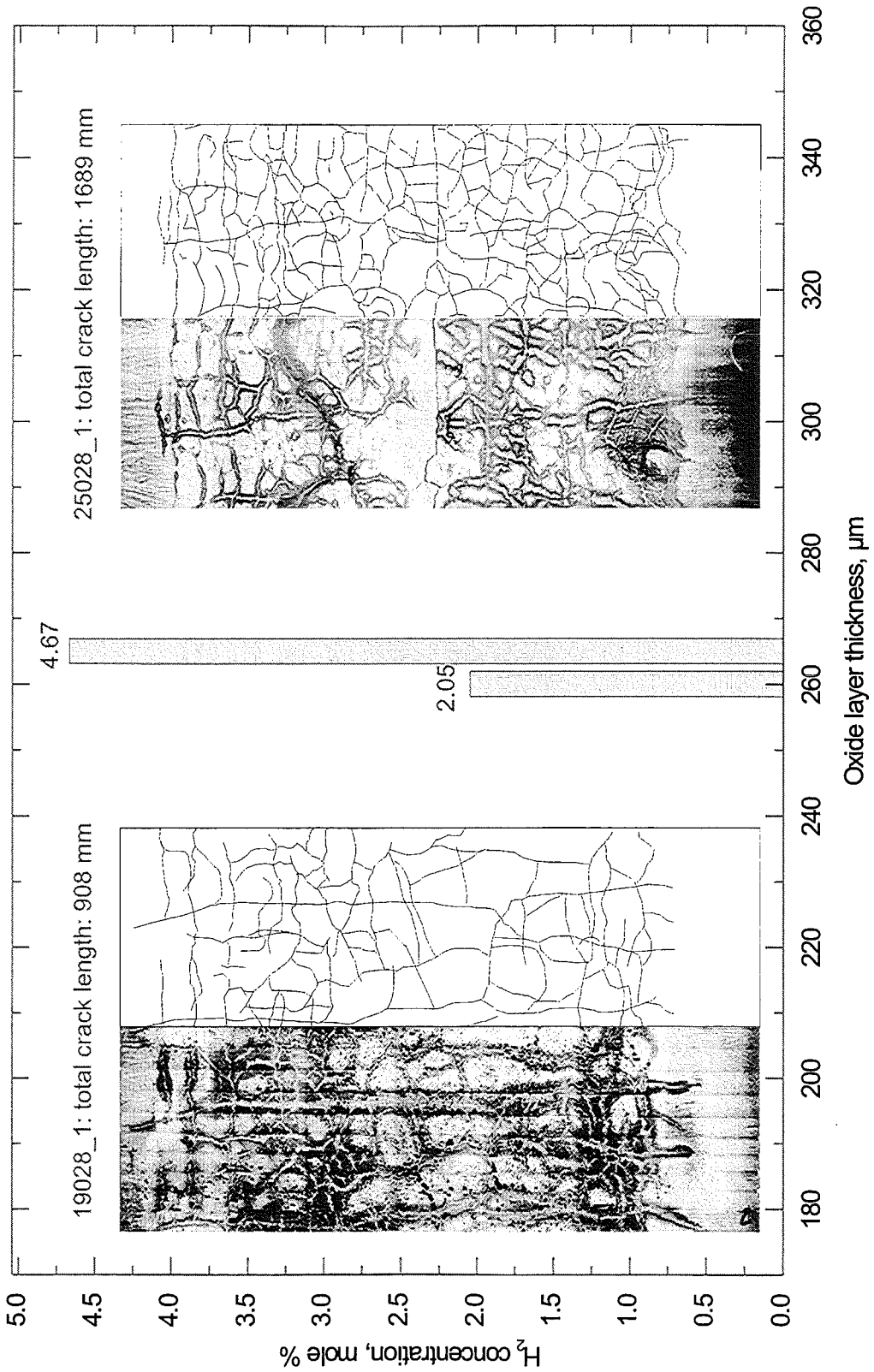

Figure 2.71: Hydrogen concentration in the specimens 19028_1 and 25028_1 cooled from 1400 °C.

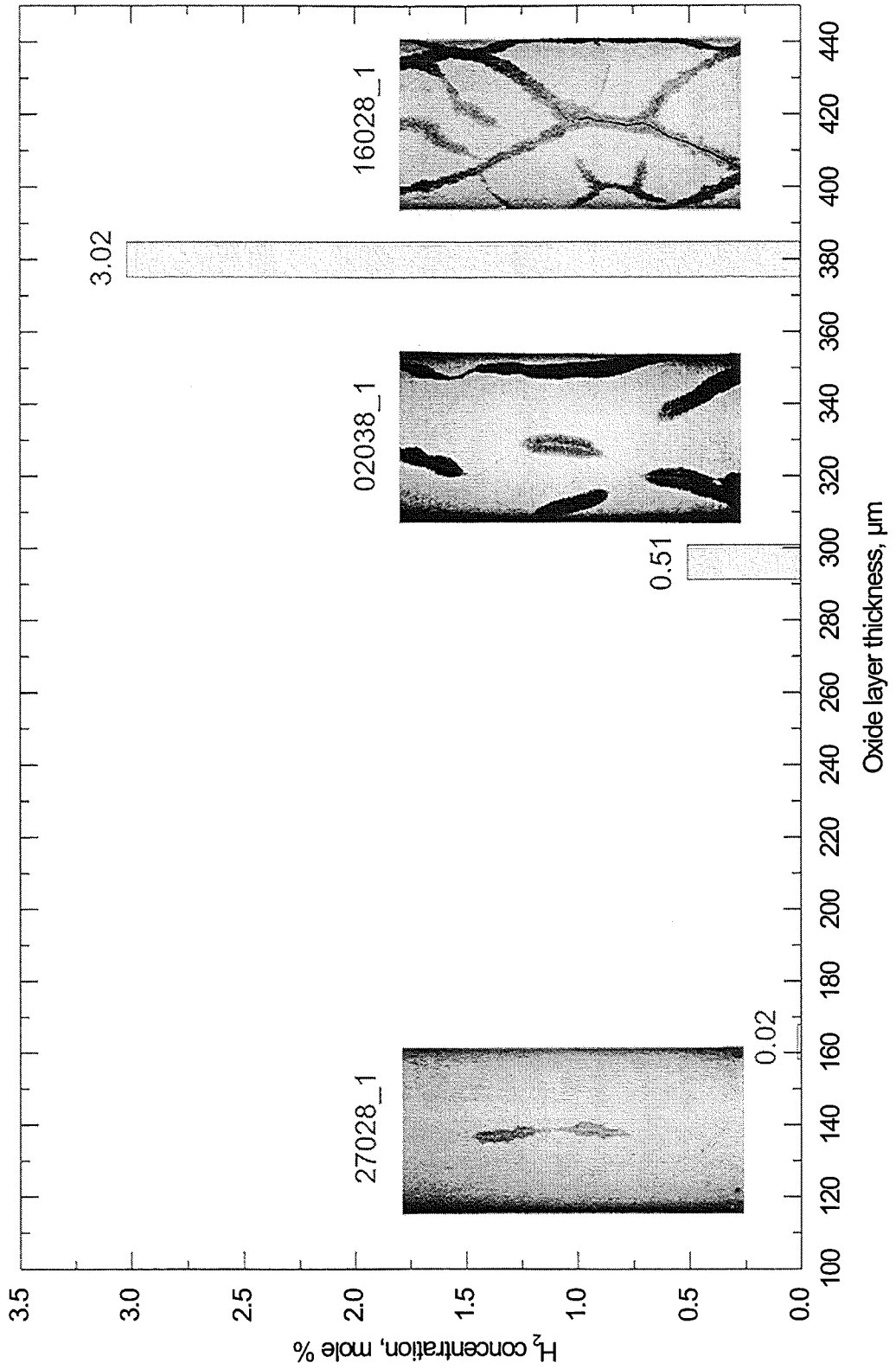

Figure 2.72: Dependence of the hydrogen concentration in the specimens cooled from 1600 °C from the oxide layer thickness.

3. Modeling of the quench phenomena

A.V. Berdyshev, A.V. Boldyrev, A.V. Palagin, V.E. Shestak, M.S. Veshchunov
Nuclear Safety Institute (IBRAE), Russian Academy of Sciences, Moscow

3.1 Verification of SVECHA/QUENCH code against the extended set of FZK quench experimental data

SVECHA/QUENCH (SQ) was developed for the detailed description of fuel rod quenching. The SQ code considers the following reflooding phenomena: heat exchange, oxidation of Zry, mechanical behavior of the cladding, hydrogen absorption and desorption in the Zry/ZrO_2 cladding.

Before applying the SQ code for the analysis of the FZK bundle reflooding experiments the set of verification calculations against the single rod quenching experimental data had to be performed. The main aim of such verification was to make sure that the code gives the adequate description of the heat exchange phenomena. The latter means *the stable reproduction of the experimentally observed temperature evolution curves in the full range of the single rod experiment conditions (different pre-oxidation and initial temperatures) without tuning and adjusting of the code parameters.* The code that fits this requirement is believed to be applicable for the description of the FZK bundle experiments with the main parameters (rod length, coolant channel cross-section, radiative heat exchange conditions) different from the verification set ones.

The present report describes the results of the first stage of the verification calculations performed with the new version of SQ code. The new version of the code includes the thermal-hydraulic module QBOIL, heat conduction module QTEM, oxidation module QOXI (based on the partial derivatives solution) with a steam starvation model implemented, and improved mechanical deformation module QDEF. The description of the main models was given in the previous work [14].

The experimental verification set includes 22 water-quenched and 6 steam-cooled experiments performed in 1995–1996. The obtained results are in satisfactory agreement with the full range of the experimental data.

3.1.1 Steam cooling experiments

3.1.1.1 Steam cooling experiments initial conditions

The experiments with the steam cooling used for the verification of the SQ code have been performed with the following initial conditions:

Test	Initial temperature	Pre-oxidation	Type
t16046_2	1400 °C	0 μm	40s
t16046_3	1200 °C	0 μm	20s
t16046_4	1550 °C	0 μm	60s
t26036_1	1600 °C	100 μm	61s
t26036_2	1600 °C	300 μm	63s
t27036_1	1200 °C	300 μm	23s

The last column in the above table represents the type of the experiment: the first figure corresponds to the initial temperature of the rod (hundreds of degrees), the second figure corresponds to the initial pre-oxidation (hundreds of microns), and the letter denotes the type of the cooling (steam or water).

3.1.1.2 Steam cooling verification calculations results

All the steam cooling verification calculations have been performed with the identical set of SQ code FORTRAN modules without any tuning and adjusting of the parameters.

Since the different thermocouples in the steam cooling experiments show very similar behavior, the calculations were performed with one vertical mesh of 15 cm height (50 nodes in radial direction and 70 nodes in axial direction).

The results of the 60s test type calculation are presented in Figures 3.1 – 3.2: the temperature evolution of the central TC for the time interval 1–15 s and 1–3 s.

The results of the 40s test type calculation are presented in Figures 3.3 – 3.4: the temperature evolution of the central TC for the time interval 1–15 s and 1–3 s.

The results of the 20s test type calculation (temperature evolution of the central TC for the

time interval 1–15 s) are presented in Figure 3.5.

The results of the 23s test type calculation (temperature evolution of the central TC for the time interval 1–14 s) are presented in Figure 3.6.

The results of the 61s test type calculation (temperature evolution of the central TC for the time interval 1–30 s) are presented in Figure 3.7.

The results of the 63s test type calculation (temperature evolution of the central TC for the time interval 1–30 s) are presented in Figure 3.8.

3.1.1.3 Analysis of the obtained results

At the very beginning of the steam cooling process, a small temperature escalation takes place in the case of zero pre- oxidation and high initial temperature (60s and 40s tests). This temperature escalation is satisfactory repeated by the calculation curve in the case of 60s test (Figure 3.2), but is not reproduced for the lower initial temperature (Figure 3.4). That may be due to some difficulties in the description of the very beginning of the oxidation process in the present oxidation module QOXI. To avoid these difficulties, an additional investigation and sensitivity study of the mutual influence of the heat exchange and oxidation modules with respect to time step and meshing should be performed.

The subsequent sharp temperature drop down to 1100 °C taking place in the time interval 0–4 s is mainly determined by the radiative heat flow

$$W_r = \epsilon\sigma(T_r^4 - T_s^4). \tag{3.1}$$

The heat flow to steam is given by

$$W_s = 0.023 Pr^{0.4} Re^{0.8} \frac{k}{R_2 - R_1}(T_r - T_s). \tag{3.2}$$

With the experimental steam mass flow rate 1.7 g/s the steam velocity in the rod channel is 4.84 m/s. Using Eq. 3.2 it can be shown that the steam contribution to the heat exchange in the temperature interval 1600–1100 °C comes to only several percent of the radiative heat flow contribution, Eq. 3.1.

As an illustration, the values of W_s and W_r are gathered in the following table:

T_r,°C	$W_s \cdot 10^4$, W/m^2	$W_r \cdot 10^4$, W/m^2	W_s/W_r
1650	4.45	68.25	0.0652
1600	4.31	61.43	0.0701
1550	4.16	55.13	0.0755
1500	4.02	49.32	0.0815
1450	3.88	43.99	0.0881
1400	3.73	39.10	0.0955
1350	3.59	34.63	0.1036
1300	3.44	30.56	0.1127
1250	3.30	26.85	0.1230
1200	3.16	23.50	0.1344
1150	3.01	20.47	0.1473
1100	2.87	17.74	0.1619
1050	2.72	15.29	0.1784

The results of the calculations presented in the Figures 3.1 – 3.8 show rather good agreement with the experimental data in the time interval discussed above, 0–4 s. Therefore, that the radiative heat exchange is adequately described by the SQ code.

The agreement of the calculation results with the experimental data after 10 s where the heat flow to the steam is more important is also rather satisfactory.

The remaining discrepancies of the calculated temperature evolution curves from the experimental data may be due to the uncertainty in the thermodynamic properties of the rod materials used in the SQ code.

3.1.2 Water quench experiments

3.1.2.1 Water quench experiments initial conditions

The experiments with the water quenching used for the verification of the SQ code have been performed with the initial conditions presented below.

Test	Initial temperature	Pre-oxidation	Water temperature	Type
t24066_1	1600 °C	0 μm	90 °C	60w
t31085_1	1600 °C	0 μm	90 °C	60w
t1056_1	1600 °C	100 μm	90 °C	61w
t1007_1	1600 °C	100 μm	90 °C	61w
t19066_1	1600 °C	300 μm	90 °C	63w
t1107_1	1600 °C	300 μm	90 °C	63w
t27095_1	1600 °C	300 μm	90 °C	63w
t21066_1	1400 °C	0 μm	90 °C	40w
t28085_1	1400 °C	0 μm	90 °C	40w
t29056_1	1400 °C	100 μm	90 °C	41w
t0507_1	1400 °C	100 μm	90 °C	41w
t05066_1	1400 °C	300 μm	90 °C	43w
t1207_1	1400 °C	300 μm	90 °C	43w
t10096_1	1400 °C	300 μm	90 °C	43w(2tc)
t2408_1	1200 °C	0 μm	90 °C	20w
t28095_1	1200 °C	0 μm	90 °C	20w
t04066_1	1200 °C	100 μm	90 °C	21w
t0607_1	1200 °C	100 μm	90 °C	21w
t29085_1	1200 °C	300 μm	90 °C	23w
t25095_1	1200 °C	300 μm	90 °C	23w
t30056_1	1200 °C	300 μm	90 °C	23w
t11096_1	1200 °C	300 μm	90 °C	23(2tc)w

As in the case of the steam, the last column in the above table represents the type of the experiment. The first figure corresponds to the initial temperature (hundreds of degrees), the second figure corresponds to the initial pre-oxidation (hundreds of microns), and the letter denotes the type of the cooling (water).

3.1.2.2 Water quenching verification calculations results

All the water quenching verification calculations have been performed with the identical set of SQ code FORTRAN modules without any tuning and adjusting of the parameters.

The calculations have been performed with 10 vertical meshes, each mesh 1,5 cm long. The total number of nodes: 50 in radial direction and 70 in axial direction.

The results of the 60w test type calculation are presented in Figures 3.9 – 3.14. Figures 3.9 and 3.10 present the temperature evolution of the lower TC for the time intervals 0–22 s and 0–4 s. Figures 3.11 and 3.12 present the temperature evolution of the central TC for the time intervals 0–22 s and 0–6 s. Figures 3.13 and 3.14 present the temperature evolution of the upper TC for the time intervals 0–22 s and 0–10 s.

The results of the 61w test type calculation are presented in Figures 3.15 – 3.20. Figures 3.15 and 3.16 present the temperature evolution of the lower TC for the time intervals 0–22 s and 0–6 s. Figures 3.17 and 3.18 present the temperature evolution of the central TC for the time intervals 0–22 s and 0–8 s. Figures 3.19 and 3.20 present the temperature evolution of the upper TC for the time intervals 0–22 s and 0–10 s.

The results of the 63w test type calculation are presented in Figures 3.21 – 3.26. Figures 3.21 and 3.22 present the temperature evolution of the lower TC for the time intervals 0–22 s and 0–8 s. Figures 3.23 and 3.24 present the temperature evolution of the central TC for the time intervals 0–22 s and 0–8 s. Figures 3.25 and 3.26 present the temperature evolution of the upper TC for the time intervals 0–22 s and 0–10 s.

The results of the 40w test type calculation are presented in Figures 3.27 – 3.32. Figures 3.27 and 3.28 present the temperature evolution of the lower TC for the time intervals 0–22 s and 0–6 s. Figures 3.29 and 3.30 present the temperature evolution of the central TC for the time intervals 0–22 s and 0–8 s. Figures 3.31 and 3.32 present the temperature evolution of the upper TC for the time intervals 0–22 s and 0–10 s.

The results of the 41w test type calculation are presented in Figures 3.33 – 3.38. Figures 3.33 and 3.34 present the temperature evolution of the lower TC for the time intervals 0–22 s and 0–6 s. Figures 3.35 and 3.36 present the temperature evolution of the central TC for the time intervals 0–22 s and 0–8 s. Figures 3.37 and 3.38 present the temperature evolution of the upper TC for the time intervals 0–22 s and 0–10 s.

The results of the 43w test type calculation are presented in Figures 3.39 – 3.44. Figures 3.39 and 3.40 present the temperature evolution of the lower TC for the time intervals 0–20 s and 0–6 s. Figures 3.41 and 3.42 present the temperature evolution of the central TC for the time intervals 0–20 s and 0–10 s. Figures 3.43 and 3.44 present the temperature evolution of the

upper TC for the time intervals 0–20 s and 0–13 s.

The results of the 20w test type calculation are presented in Figures 3.45 – 3.50. Figures 3.45 and 3.46 present the temperature evolution of the lower TC for the time intervals 0–22 s and 0–10 s. Figures 3.47 and 3.48 present the temperature evolution of the central TC for the time intervals 0–22 s and 0–8 s. Figures 3.49 and 3.50 present the temperature evolution of the upper TC for the time intervals 0–22 s and 0–10 s.

The results of the 21w test type calculation are presented in Figures 3.51 – 3.56. Figures 3.51 and 3.52 present the temperature evolution of the lower TC for the time intervals 0–20 s and 0–6 s. Figures 3.53 and 3.54 present the temperature evolution of the central TC for the time intervals 0–20 s and 0–8 s. Figures 3.55 and 3.56 present the temperature evolution of the upper TC for the time intervals 0–20 s and 0–10 s.

The results of the 23w test type calculation are presented in Figures 3.57 – 3.62. Figures 3.57 and 3.58 present the temperature evolution of the lower TC for the time intervals 0–17 s and 0–6 s. Figures 3.59 and 3.60 present the temperature evolution of the central TC for the time intervals 0–17 s and 0–9 s. Figures 3.61 and 3.62 present the temperature evolution of the upper TC for the time intervals 0–17 s and 0–9 s.

3.1.2.3 Analysis of the results obtained

As a whole, the calculation results are in satisfactory agreement with the experimental data. The self-consistent calculation of the different water-steam regions motion, heat release due to oxidation and steam starvation (see below, Sec.3) makes it possible to describe the variations of the heat transfer coefficients at the upper and central TCs elevations and to predict the temperature evolutions. However, there are some discrepancies of the calculation curves from the experimental ones. In the experiments with the initial pre-oxidation, the calculated temperature curves for the central and upper TCs in the time interval 0–4 s are located below the experimental ones (Fig. 17-20, 23-26, 37-38). In this time interval the central and upper TCs are in the steam environment (Pure Steam region), i.e. in the conditions quite similar to that in the experiments with the steam cooling. The only difference between these two cases is the velocity of the steam. In the steam cooling experiments the steam velocity is constant and equal to 4.8-4.9 m/s. In the water quench experiments the steam velocity in the PS region is time dependent and in the time interval 0–4 s may be less than the above value. However, the heat flow to steam is much less here than the radiative heat flow (see

Sec.2). So, the heat exchange in both cases is determined mainly by the radiation and should result in a similar temperature evolution. The steam cooling experimental results are quite well reproduced by the calculations in contrast to the water quench ones. The difference in the temperature behavior between these two cases is not clear yet.

Another discrepancy for the experiments with pre-oxidation is connected with a large deviation of the calculation results from the experimental data below 800 °C. This discrepancy is explained by the fact that the thermocouples used in this experiments (fixed by Zr ring) failed in this temperature region. The TCs failure has been discussed in the previous report [14] and was confirmed by the additionally performed experiments. Thus, only experimental data corresponding to the high temperature region (above $\approx$ 800 °C) may be considered as reliable ones and should be used for the verification of the S/Q code against the experiments with pre-oxidation.

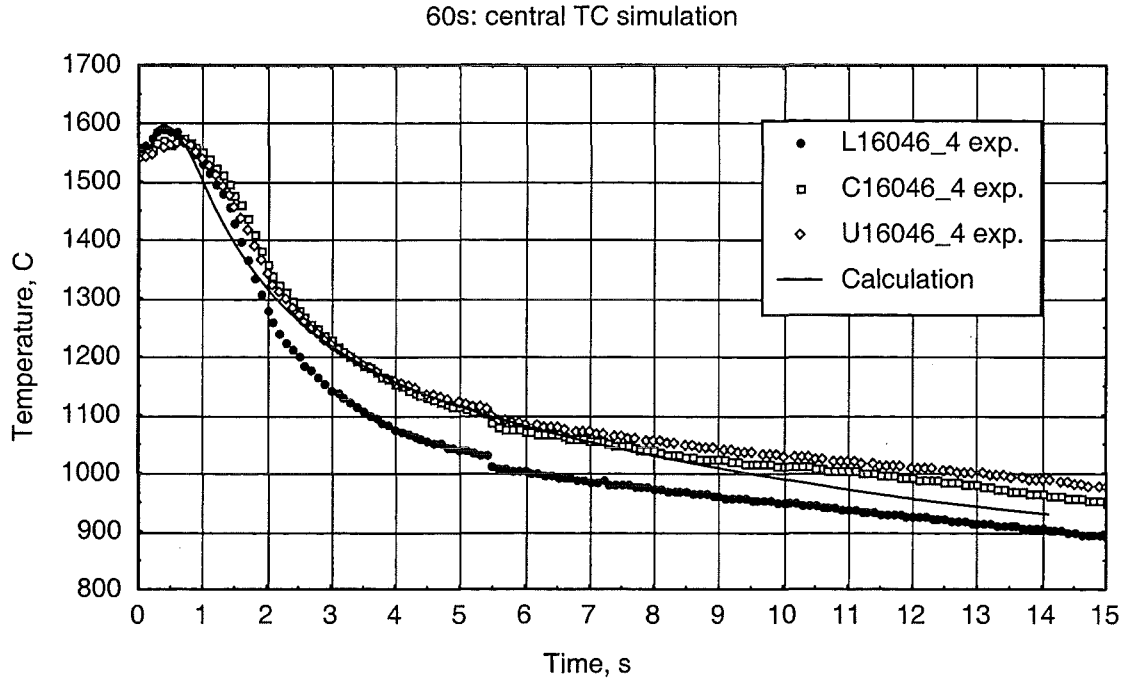

Figure 3.1: Temperature evolution of the central TC in the 60s type experiment (1600 °C, 0 µm pre-oxidation, steam cooling) in the time interval 0–15 s.

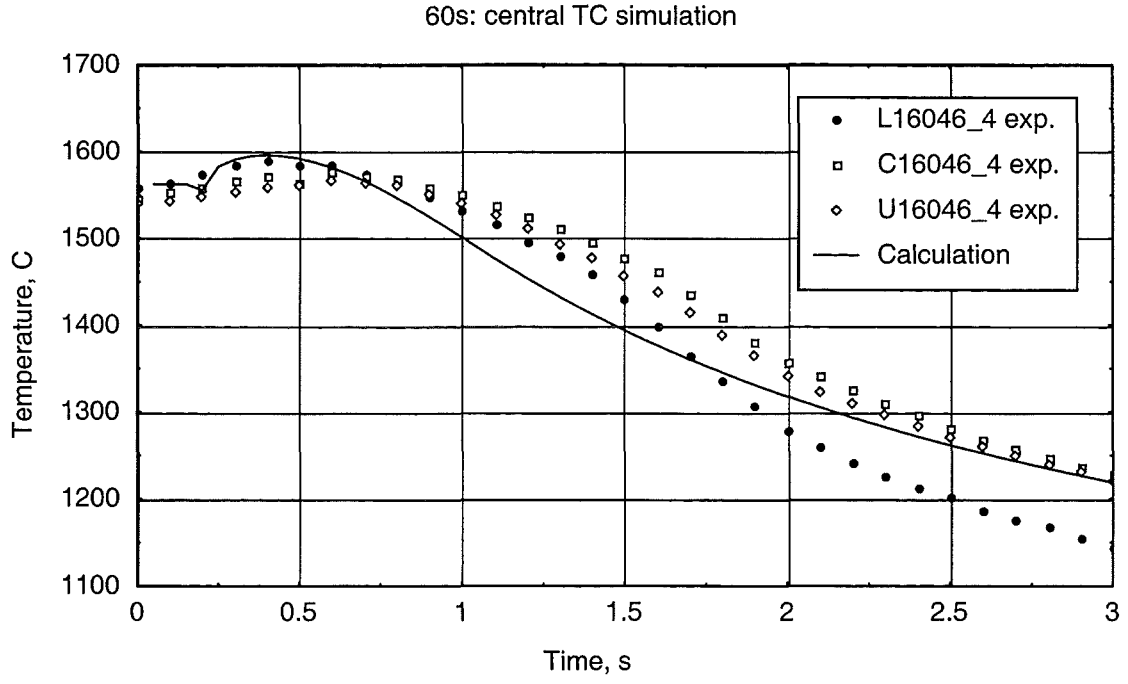

Figure 3.2: Temperature evolution of the central TC in the 60s type experiment (1600 °C, 0 µm pre-oxidation, steam cooling) in the time interval 0–3 s.

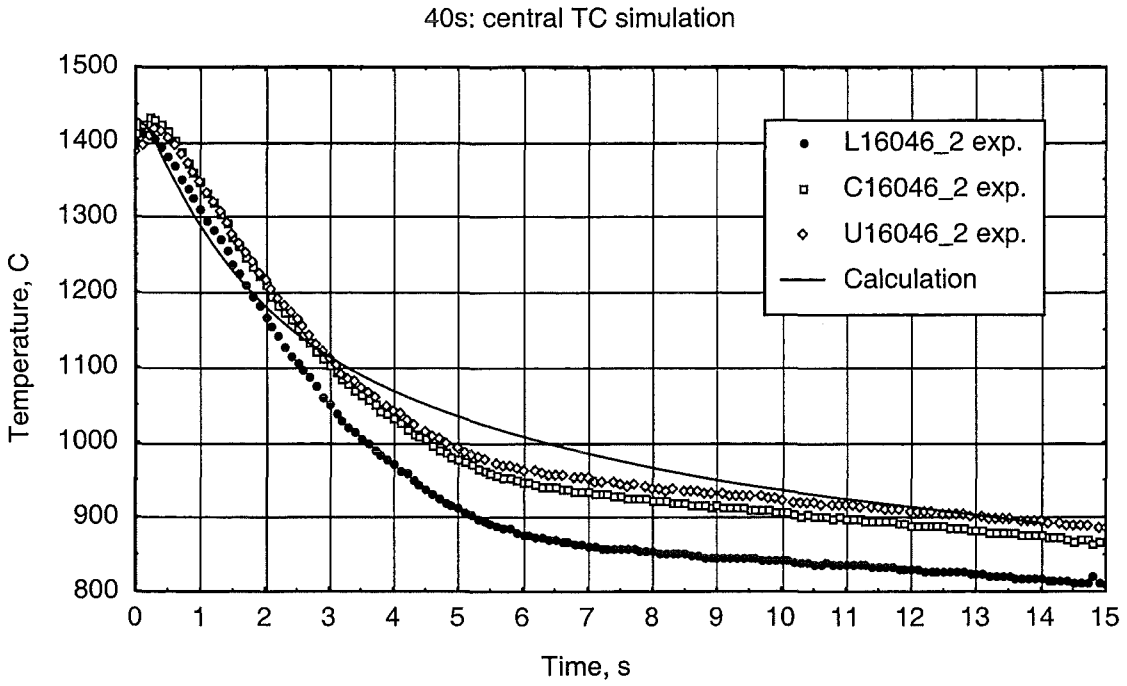

Figure 3.3: Temperature evolution of the central TC in the 40s type experiment (1400 °C, 0 µm pre-oxidation, steam cooling) in the time interval 0–15 s.

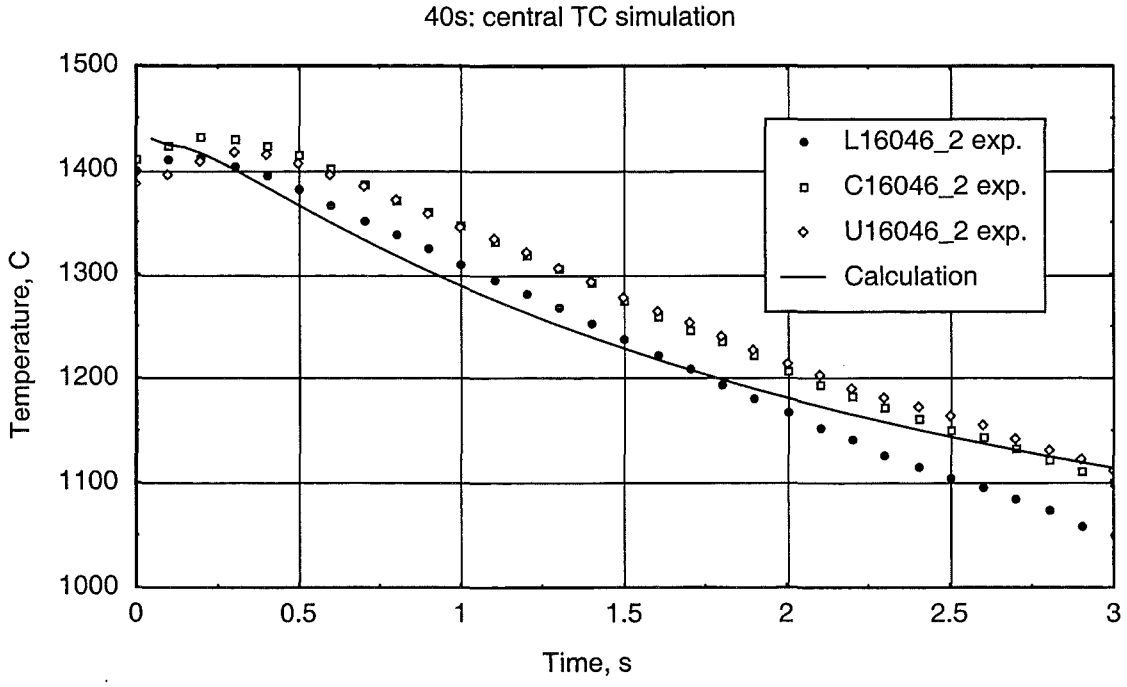

Figure 3.4: Temperature evolution of the central TC in the 40s type experiment (1400 °C, 0 µm pre-oxidation, steam cooling) in the time interval 0–3 s.

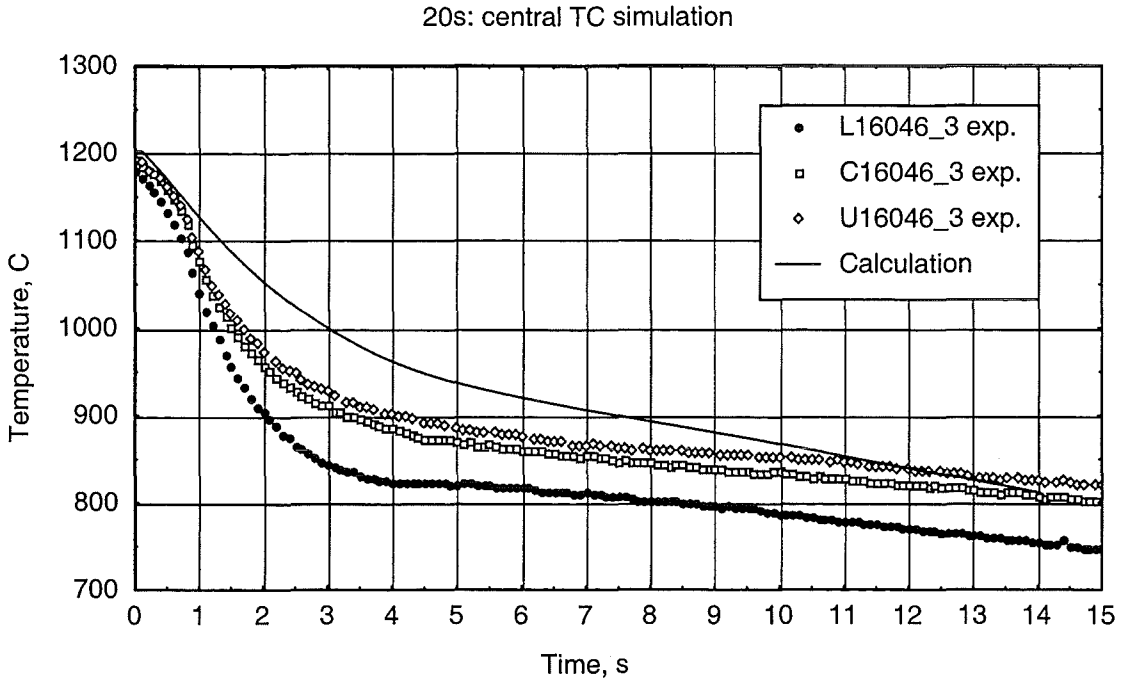

Figure 3.5: Temperature evolution of the central TC in the 20s type experiment (1200 °C, 0 µm pre-oxidation, steam cooling) in the time interval 0–15 s.

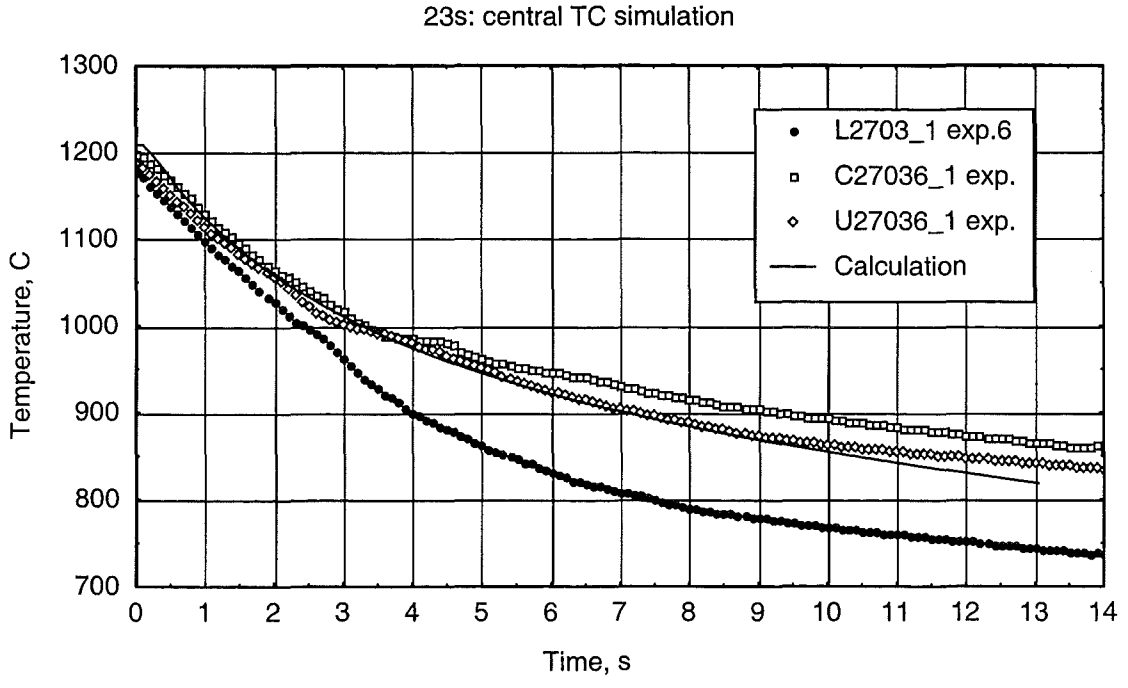

Figure 3.6: Temperature evolution of the central TC in the 23s type experiment (1200 °C, 300 µm pre-oxidation, steam cooling) in the time interval 0–14 s.

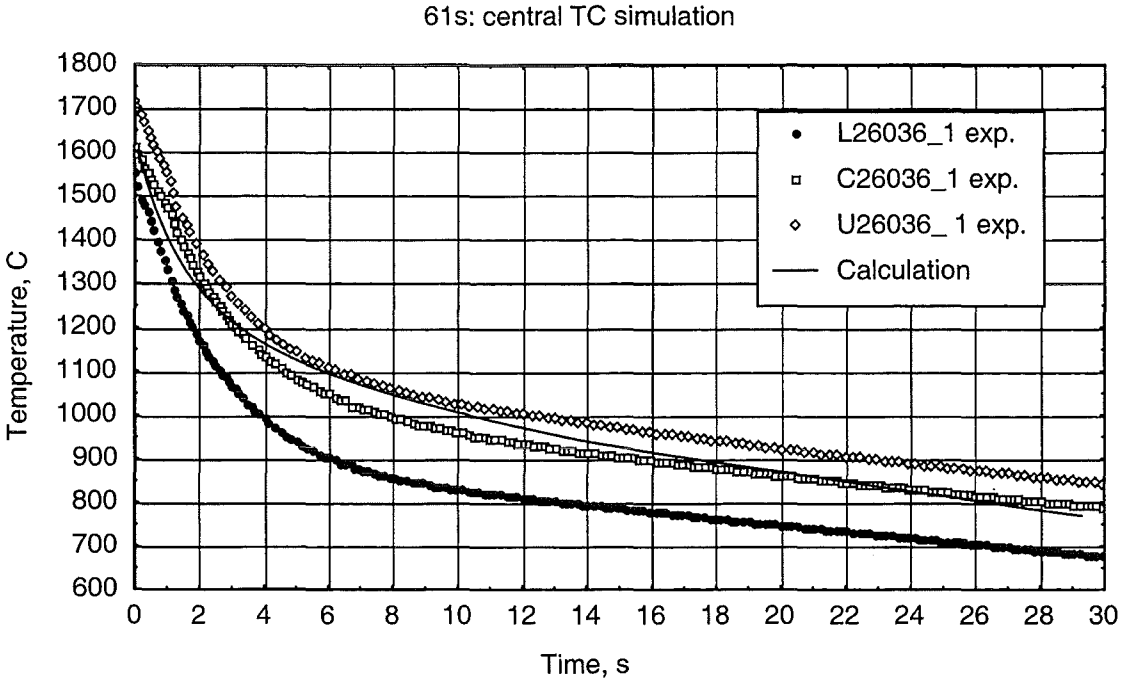

Figure 3.7: Temperature evolution of the central TC in the 61s type experiment (1600 °C, 100 µm pre-oxidation, steam cooling in the time interval 0–30 s.

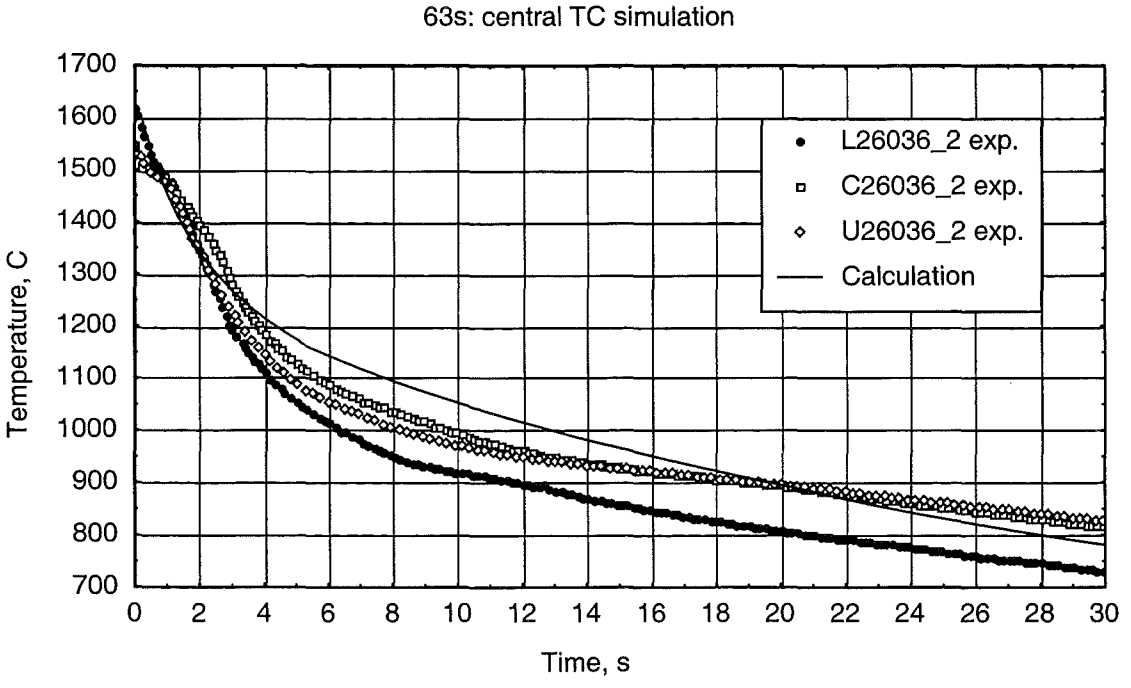

Figure 3.8: Temperature evolution of the central TC in the 63s type experiment (1600 °C, 300 µm pre-oxidation, steam cooling) in the time interval 0–30 s.

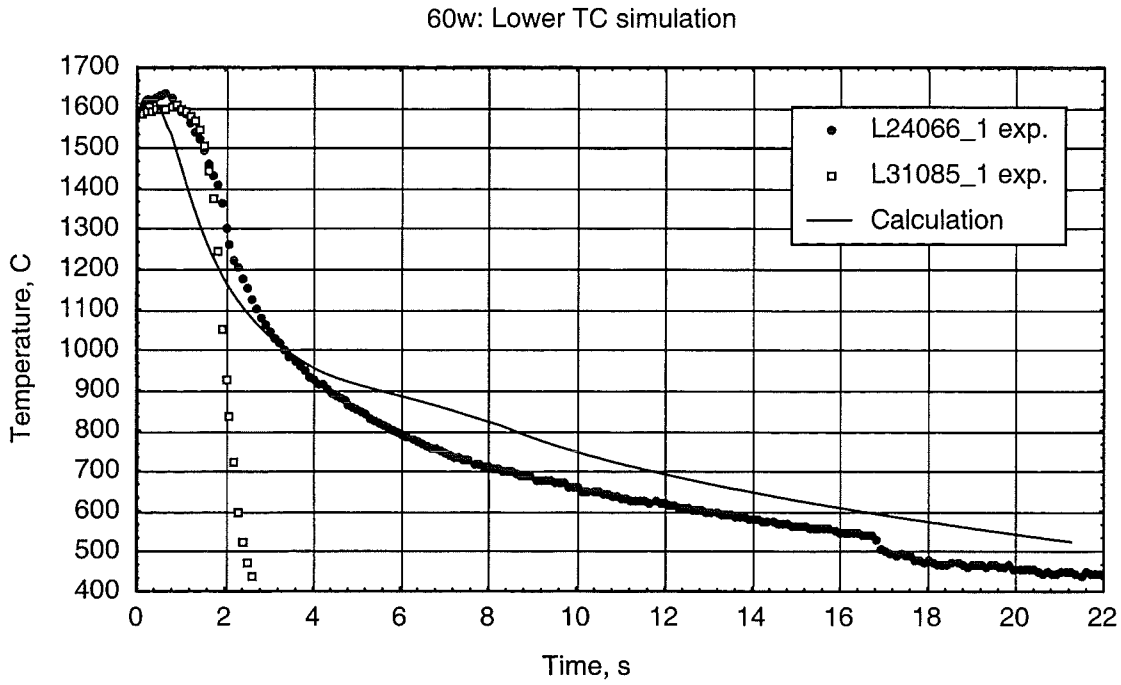

Figure 3.9: Temperature evolution of the lower TC in the 60w type experiment (1600 °C, 0 µm pre-oxidation, water quenching) in the time interval 0–22 s.

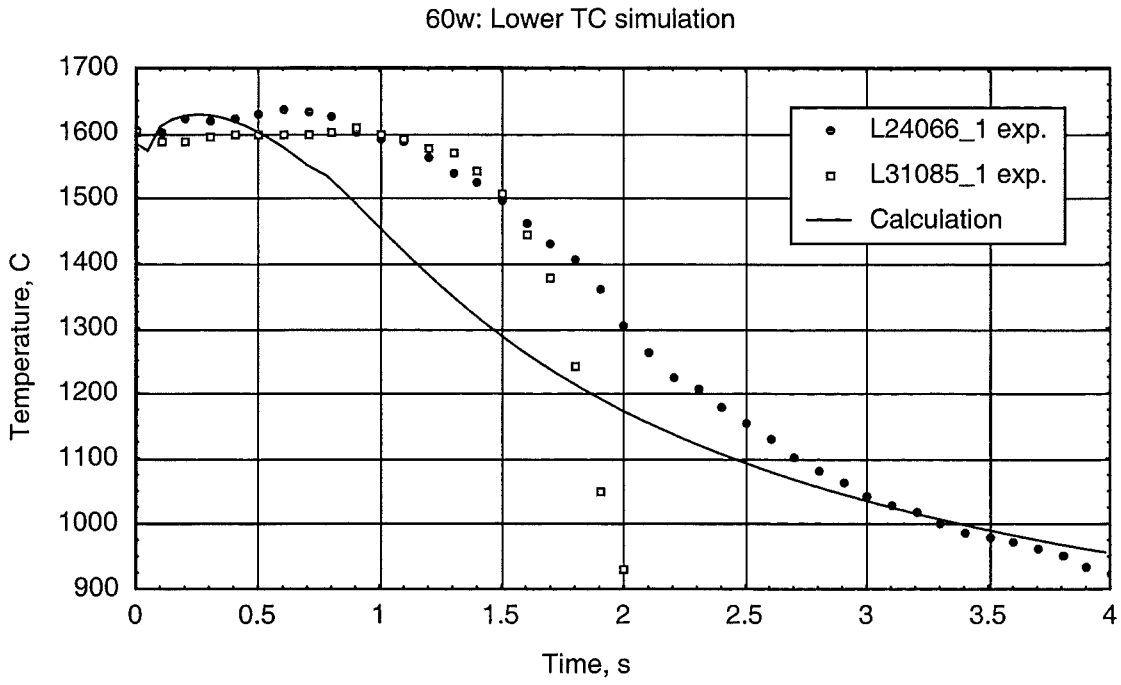

Figure 3.10: Temperature evolution of the lower TC in the 60w type experiment (1600 °C, 0 µm pre-oxidation, water quenching) in the time interval 0–4 s.

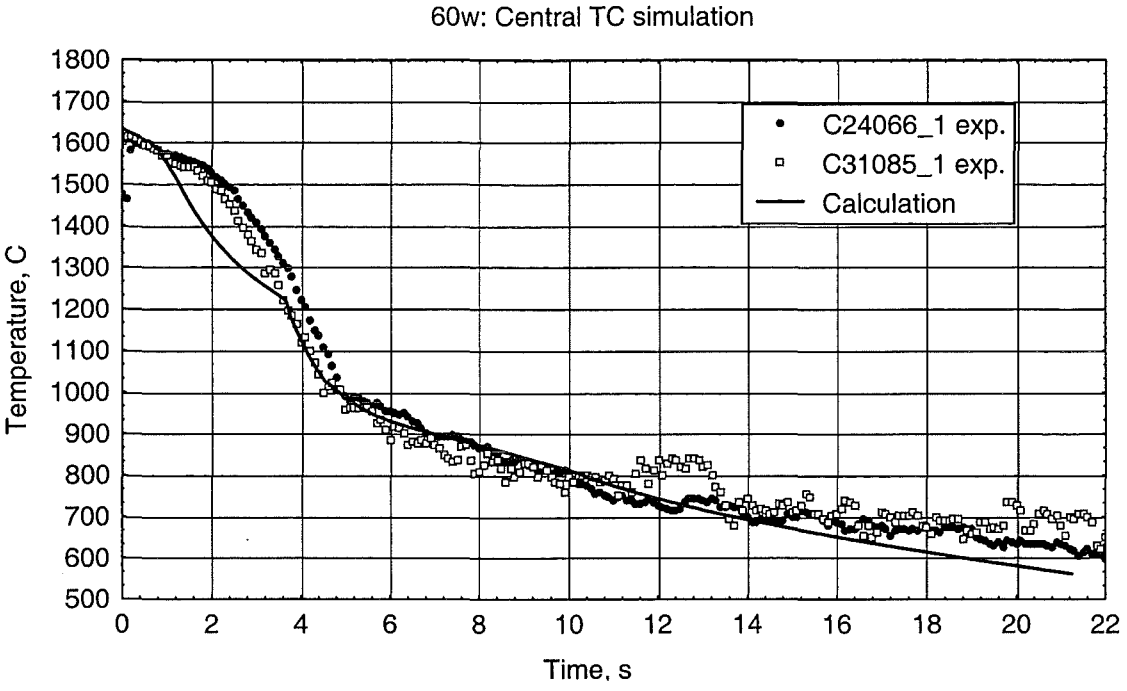

Figure 3.11: Temperature evolution of the central TC in the 60w type experiment (1600 °C, 0 µm pre-oxidation, water quenching) in the time interval 0–22 s.

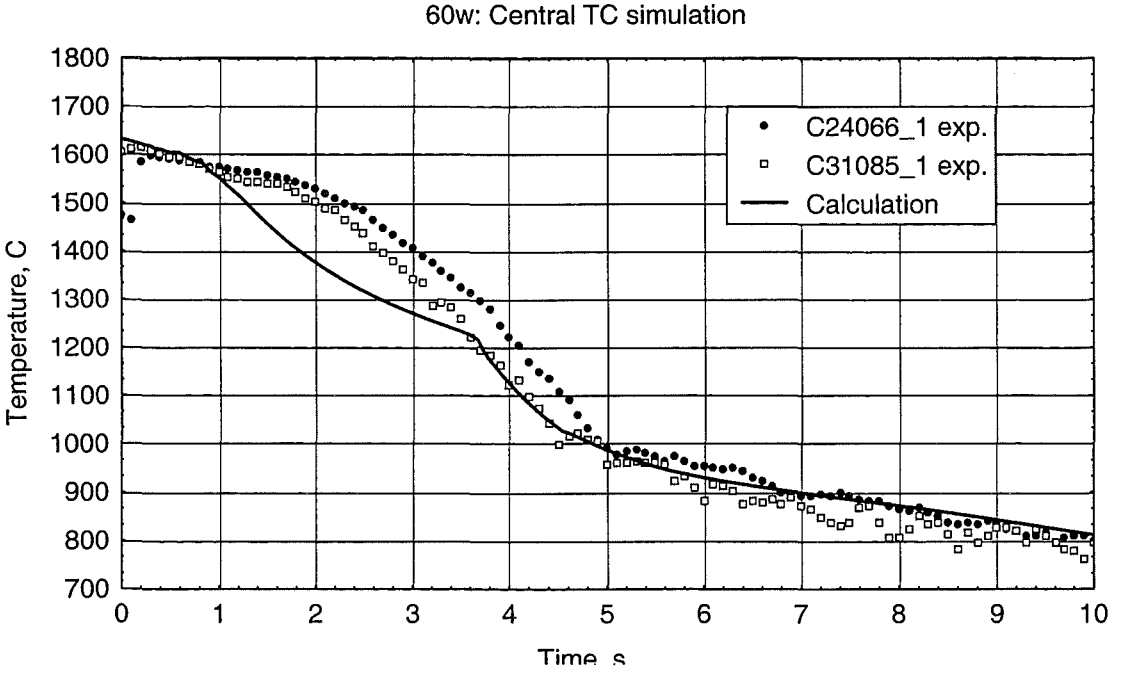

Figure 3.12: Temperature evolution of the central TC in the 60w type experiment (1600 °C, 0 µm pre-oxidation, water quenching) in the time interval 0–6 s.

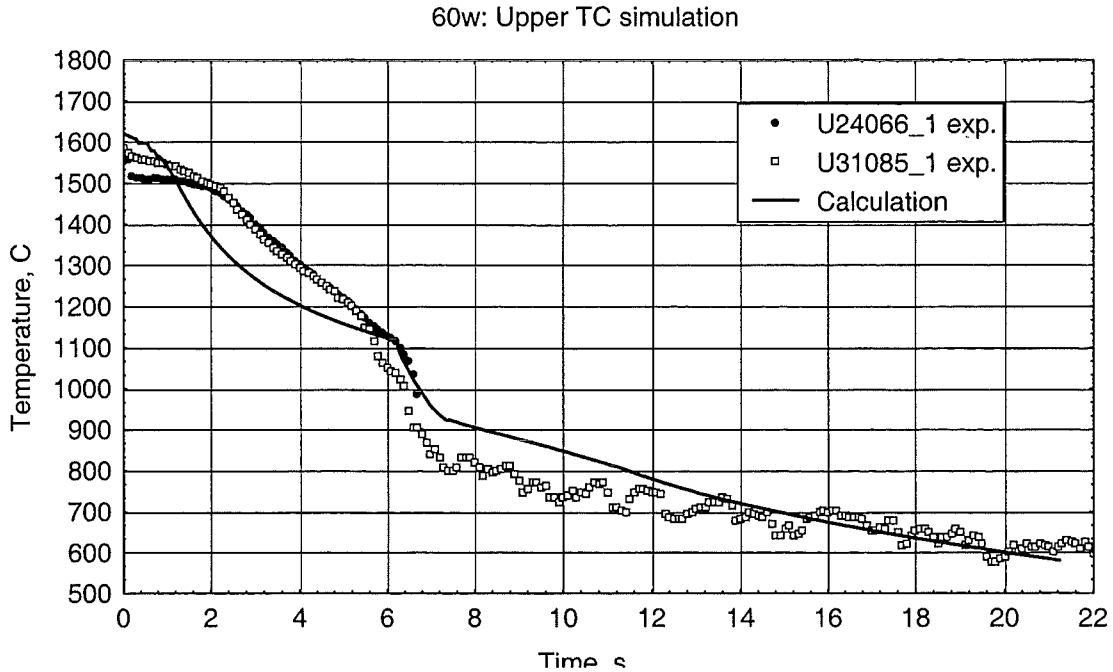

Figure 3.13: Temperature evolution of the upper TC in the 60w type experiment (1600 °C, 0 µm pre-oxidation, water quenching) in the time interval 0–22 s.

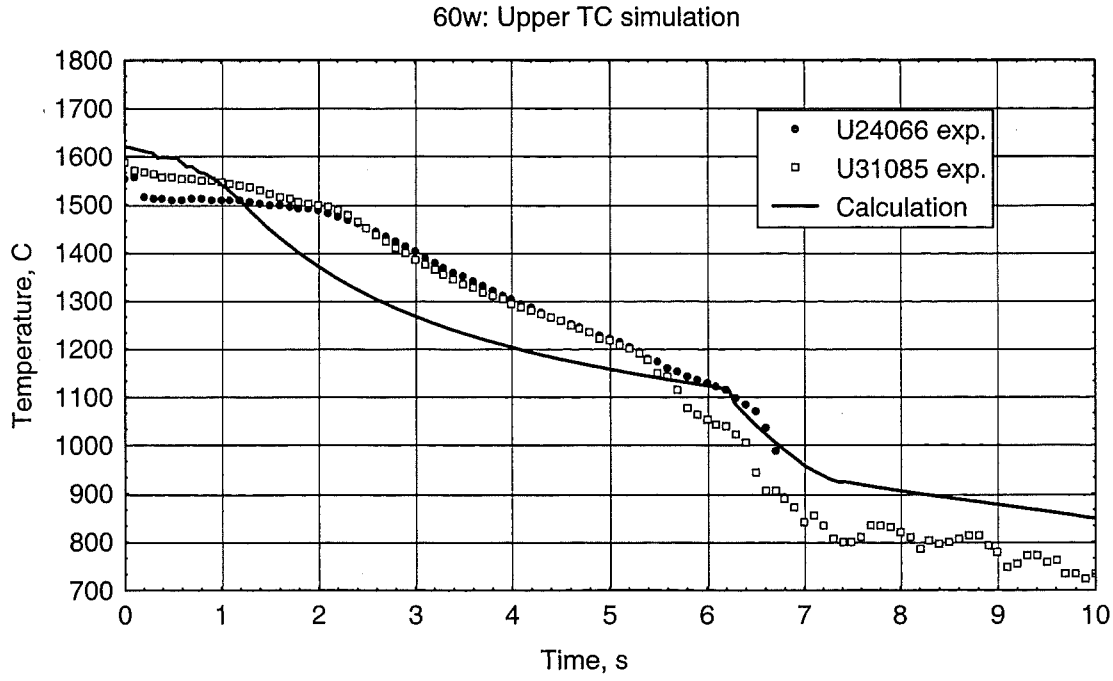

Figure 3.14: Temperature evolution of the upper TC in the 60w type experiment (1600 °C, 0 µm pre-oxidation, water quenching) in the time interval 0–10 s.

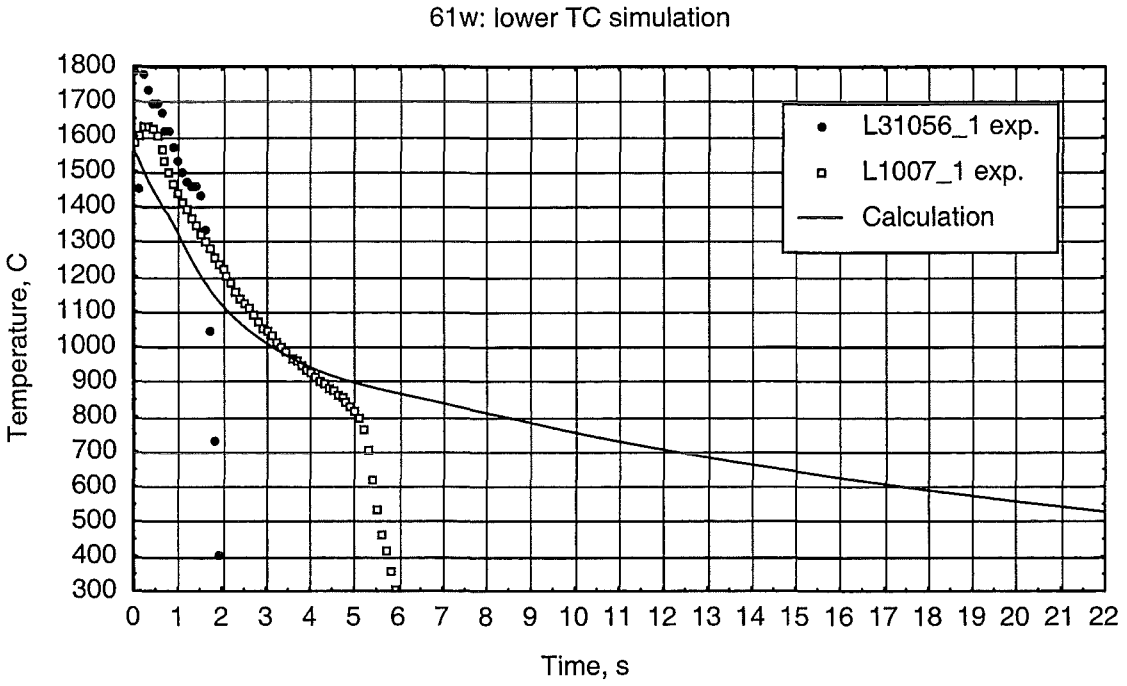

Figure 3.15: Temperature evolution of the lower TC in the 61w type experiment (1600 °C, 100 µm pre-oxidation, water quenching) in the time interval 0–22 s.

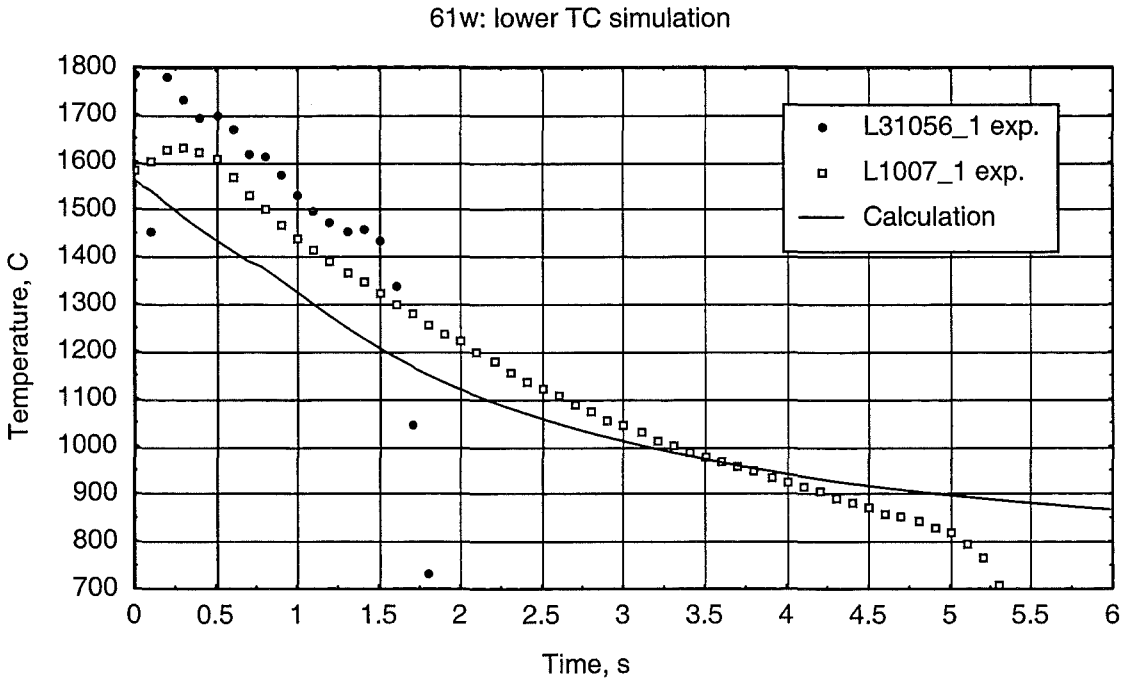

Figure 3.16: Temperature evolution of the lower TC in the 61w type experiment (1600 °C, 100 µm pre-oxidation, water quenching) in the time interval 0–6 s.

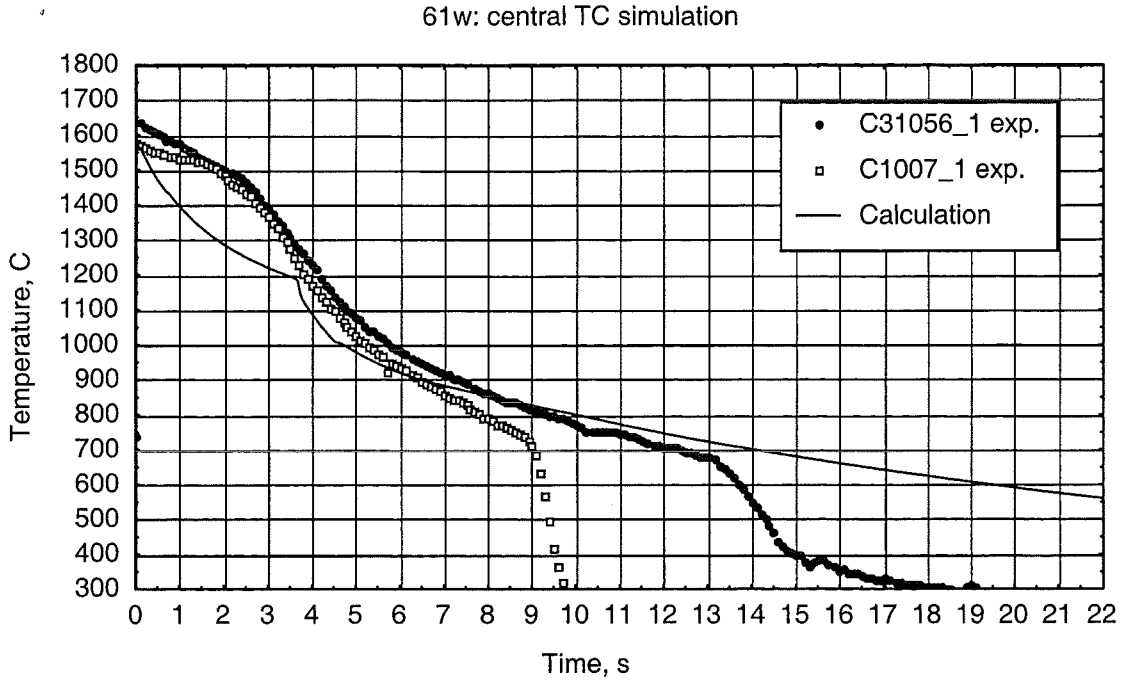

Figure 3.17: Temperature evolution of the central TC in the 61w type experiment (1600 °C, 100 µm pre-oxidation, water quenching) in the time interval 0–22 s.

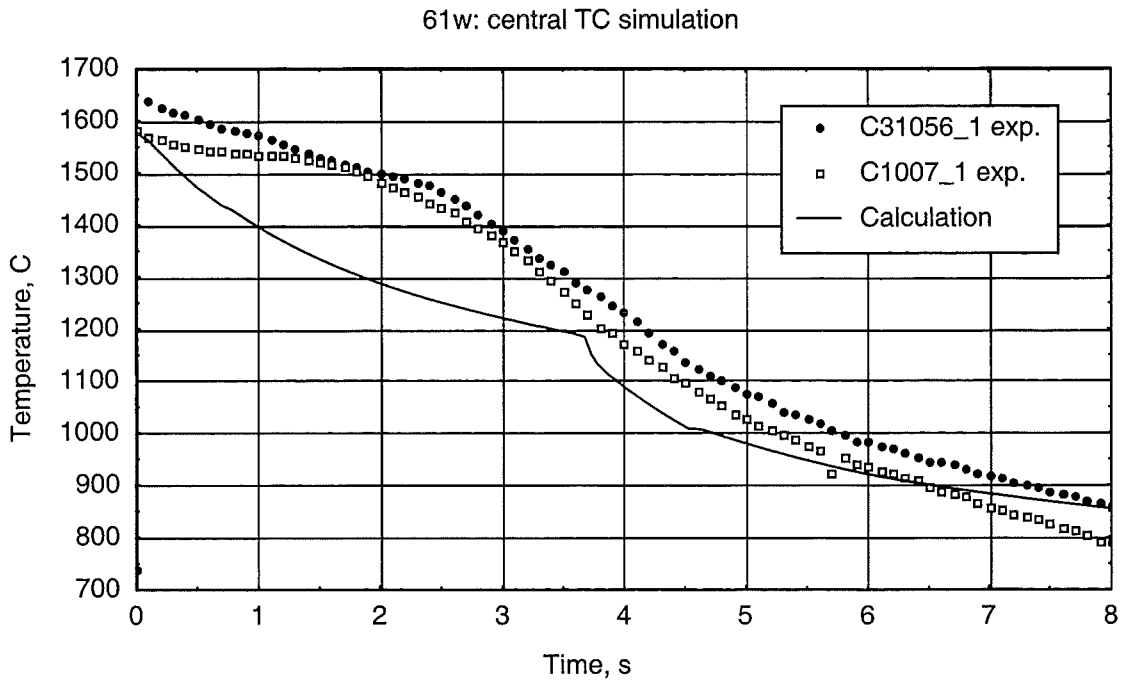

Figure 3.18: Temperature evolution of the central TC in the 61w type experiment (1600 °C, 100 µm pre-oxidation, water quenching) in the time interval 0–8 s.

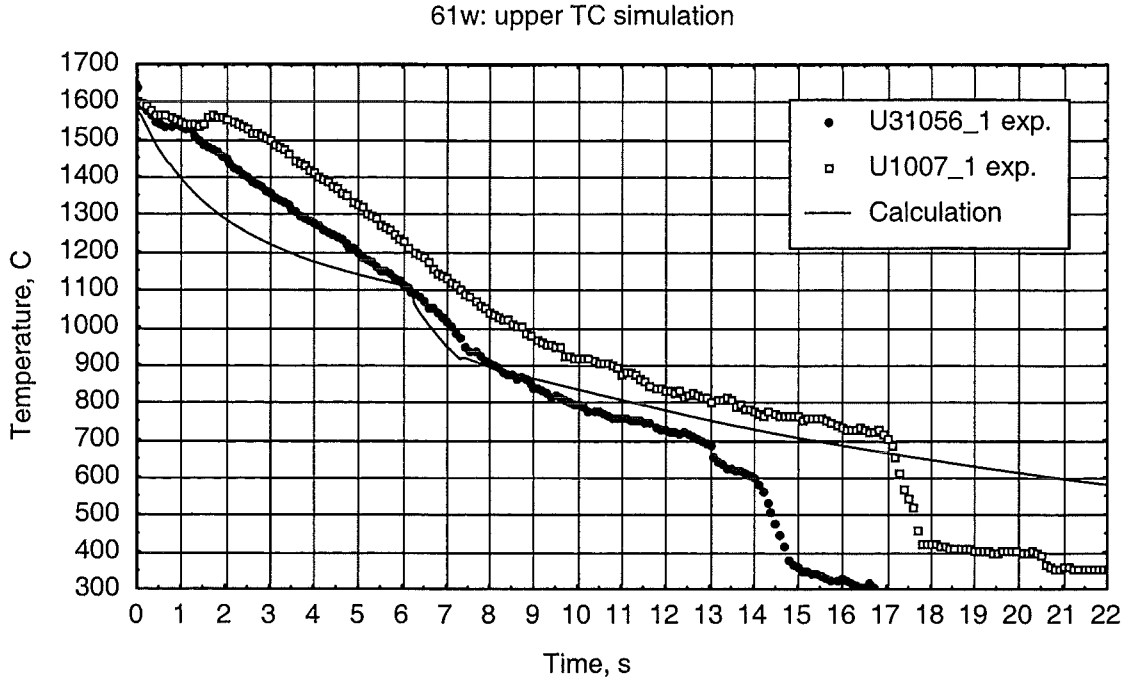

Figure 3.19: Temperature evolution of the upper TC in the 61w type experiment (1600 °C, 100 µm pre-oxidation, water quenching) in the time interval 0–22 s.

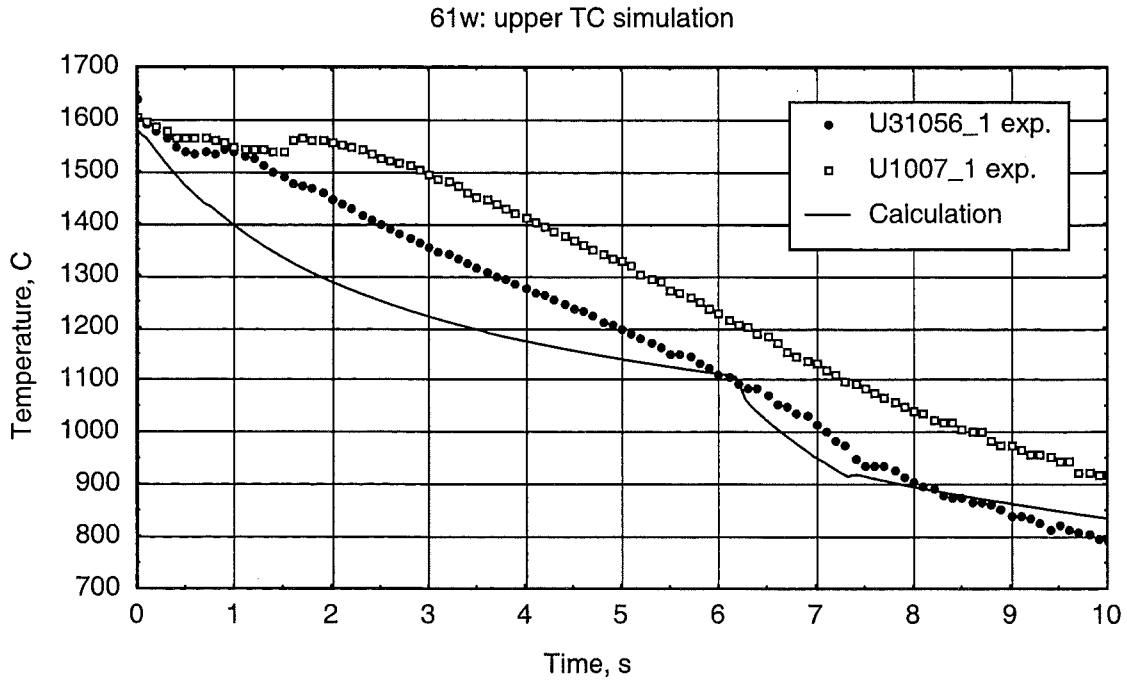

Figure 3.20: Temperature evolution of the upper TC in the 61w type experiment (1600 °C, 100 µm pre-oxidation, water quenching) in the time interval 0–10 s.

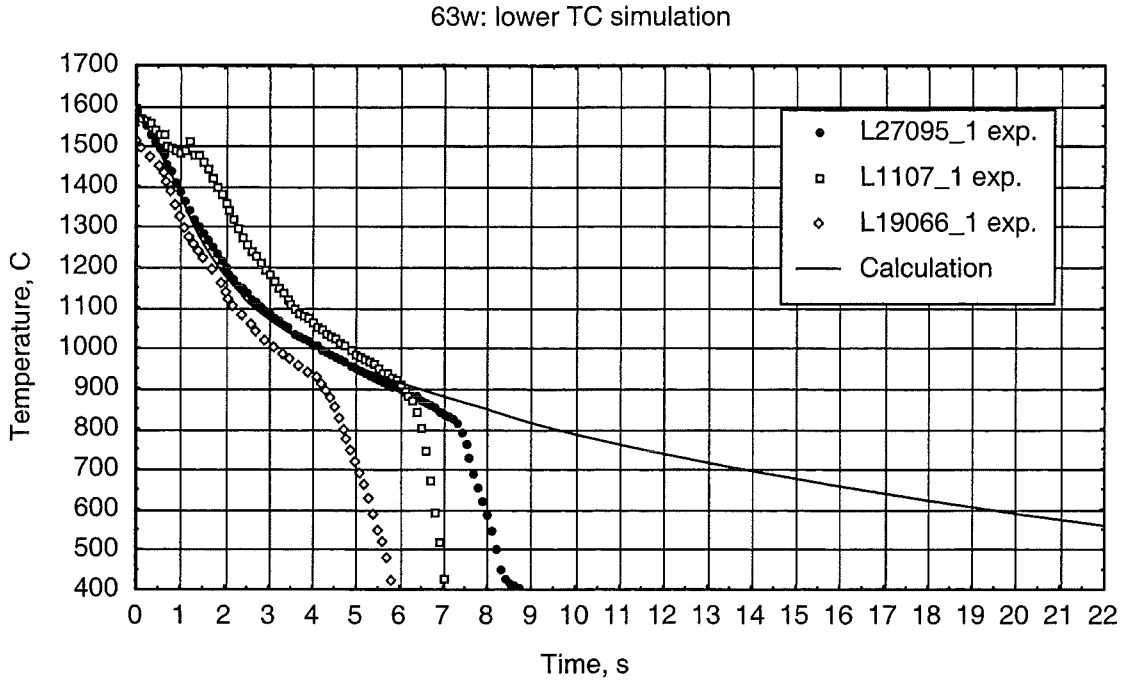

Figure 3.21: Temperature evolution of the lower TC in the 63w type experiment (1600 °C, 300 µm pre-oxidation, water quenching) in the time interval 0–22 s.

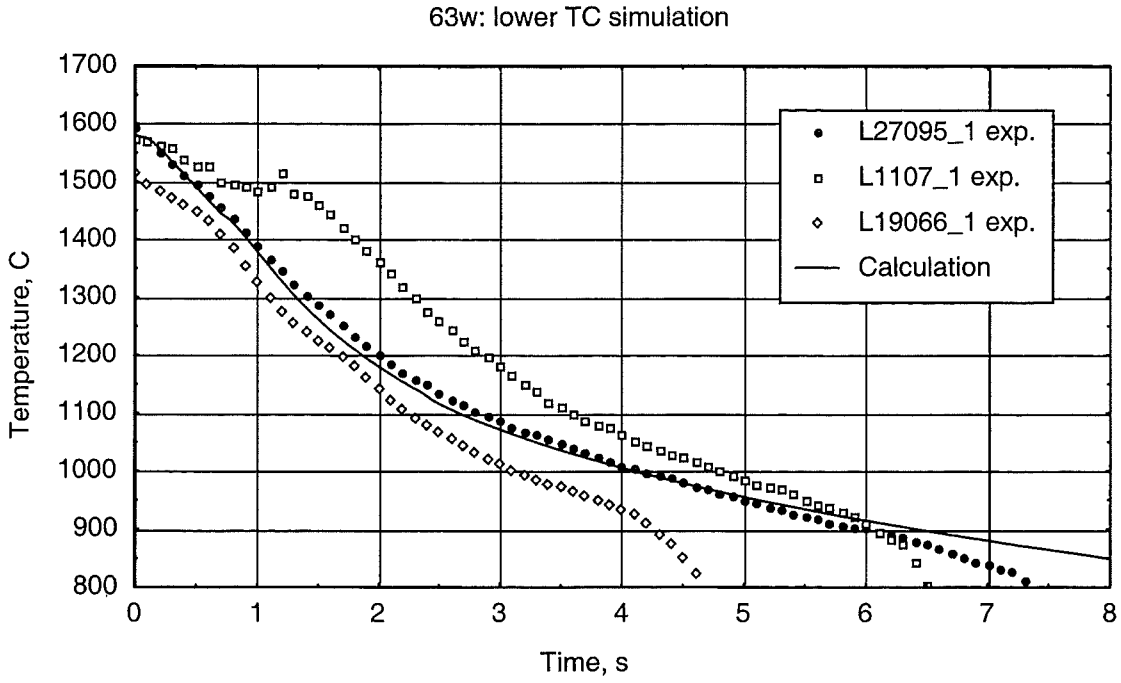

Figure 3.22: Temperature evolution of the lower TC in the 63w type experiment (1600 °C, 300 µm pre-oxidation, water quenching) in the time interval 0–8 s.

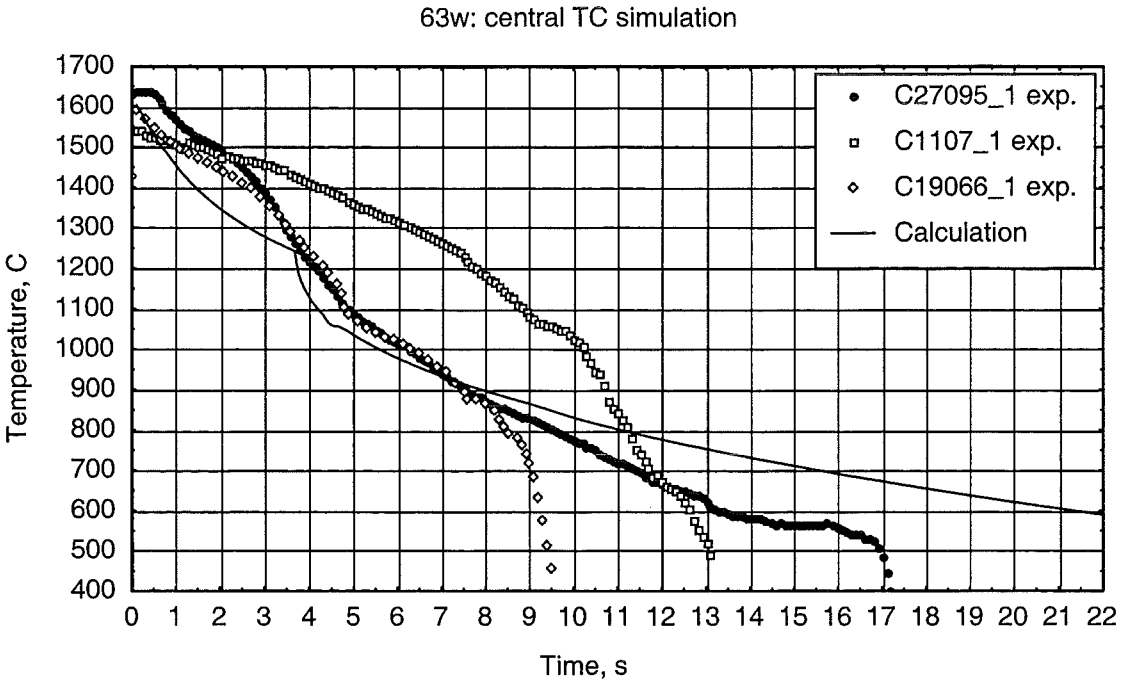

Figure 3.23: Temperature evolution of the central TC in the 63w type experiment (1600 °C, 300 μm pre-oxidation, water quenching) in the time interval 0–22 s.

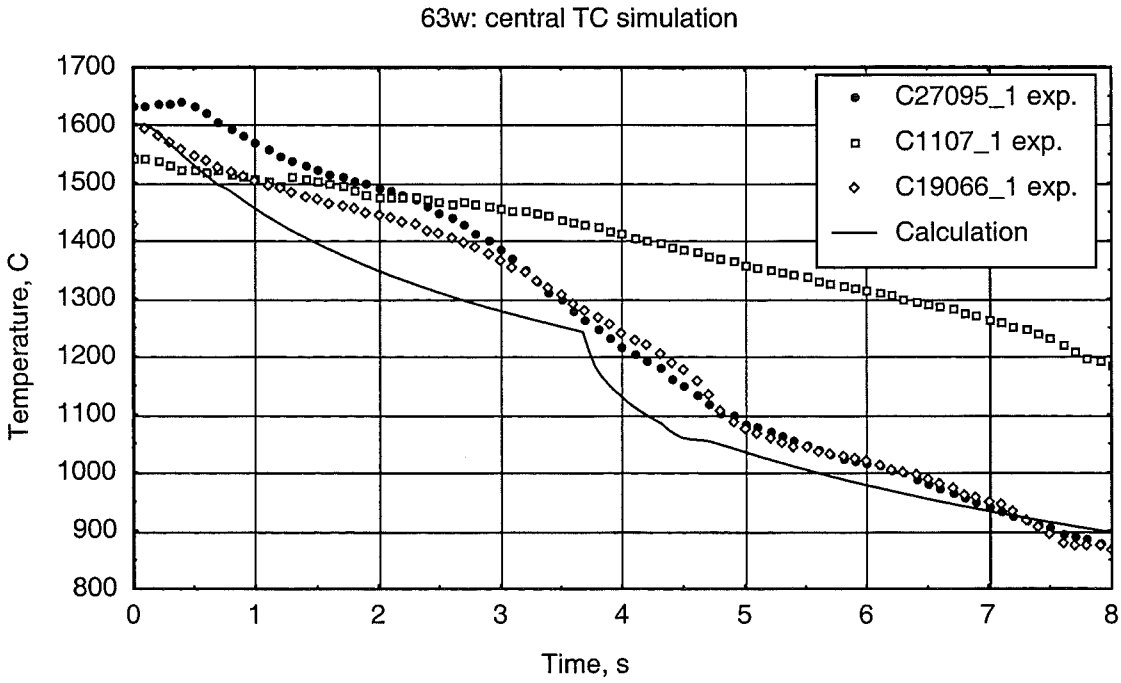

Figure 3.24: Temperature evolution of the central TC in the 63w type experiment (1600 °C, 300 μm pre-oxidation, water quenching) in the time interval 0–8 s.

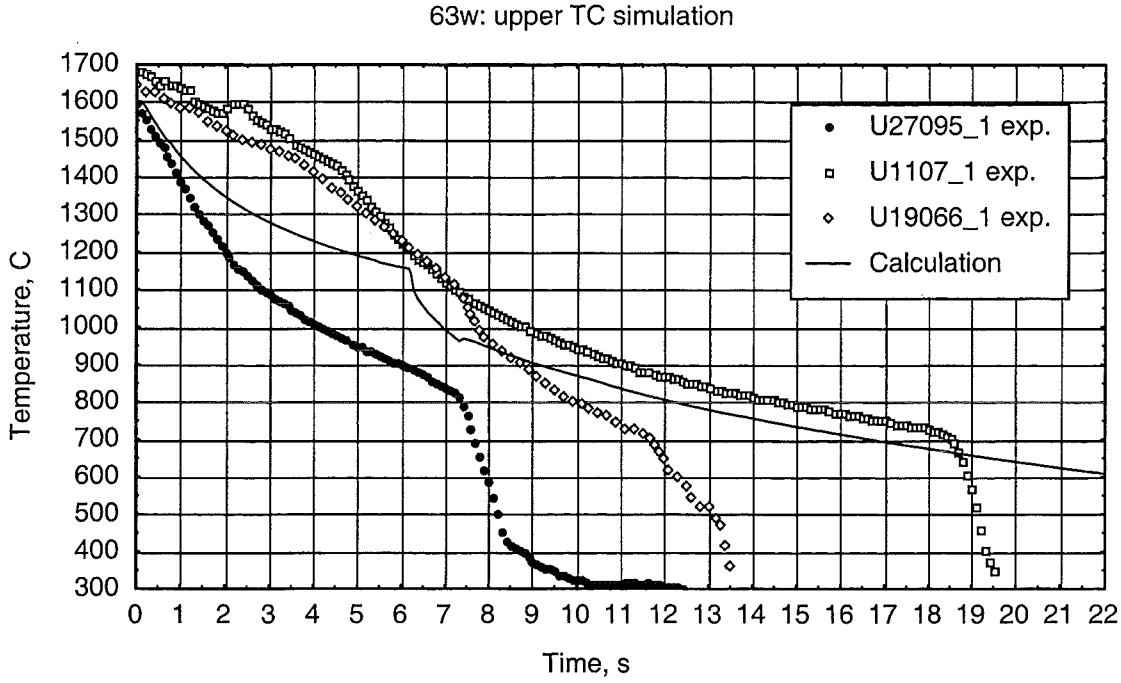

Figure 3.25: Temperature evolution of the upper TC in the 63w type experiment (1600 °C, 300 μm pre-oxidation, water quenching) in the time interval 0–22 s.

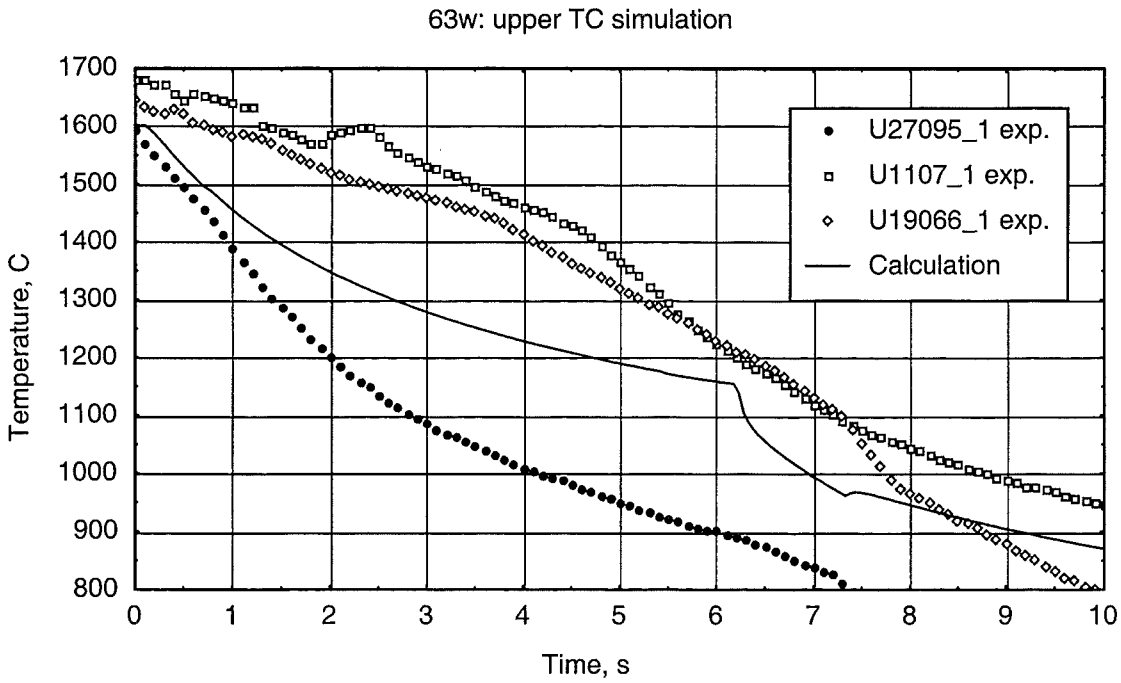

Figure 3.26: Temperature evolution of the upper TC in the 63w type experiment (1600 °C, 300 μm pre-oxidation, water quenching) in the time interval 0–10 s.

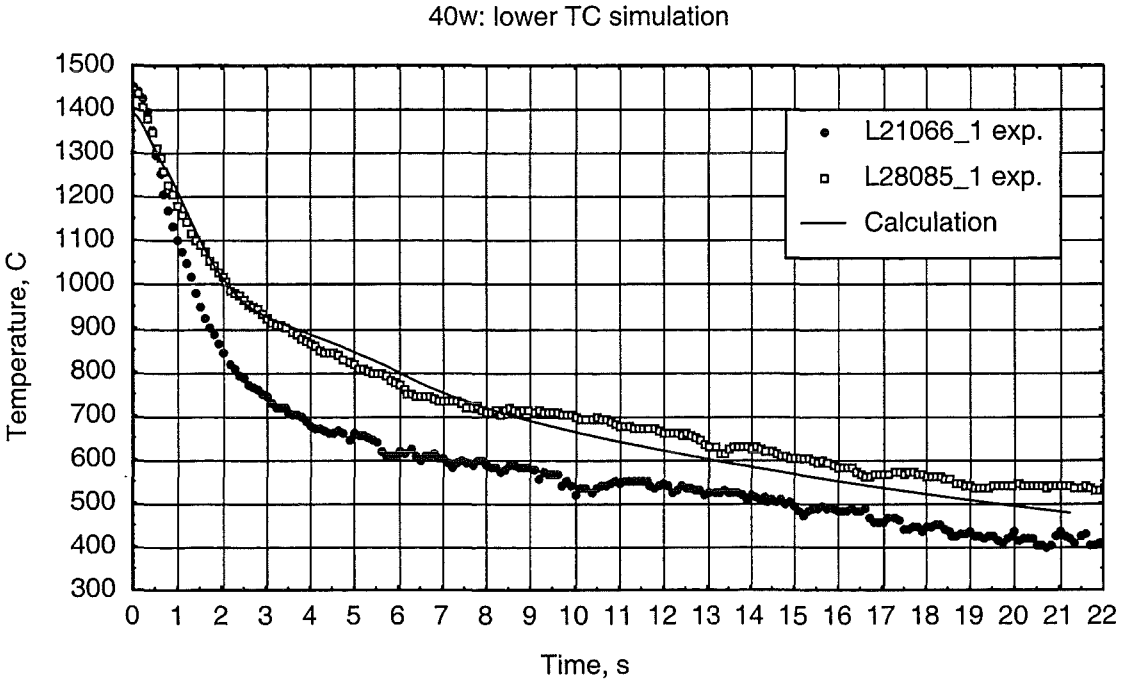

Figure 3.27: Temperature evolution of the lower TC in the 40w type experiment (1400 °C, 0 µm pre-oxidation, water quenching) in the time interval 0–22 s.

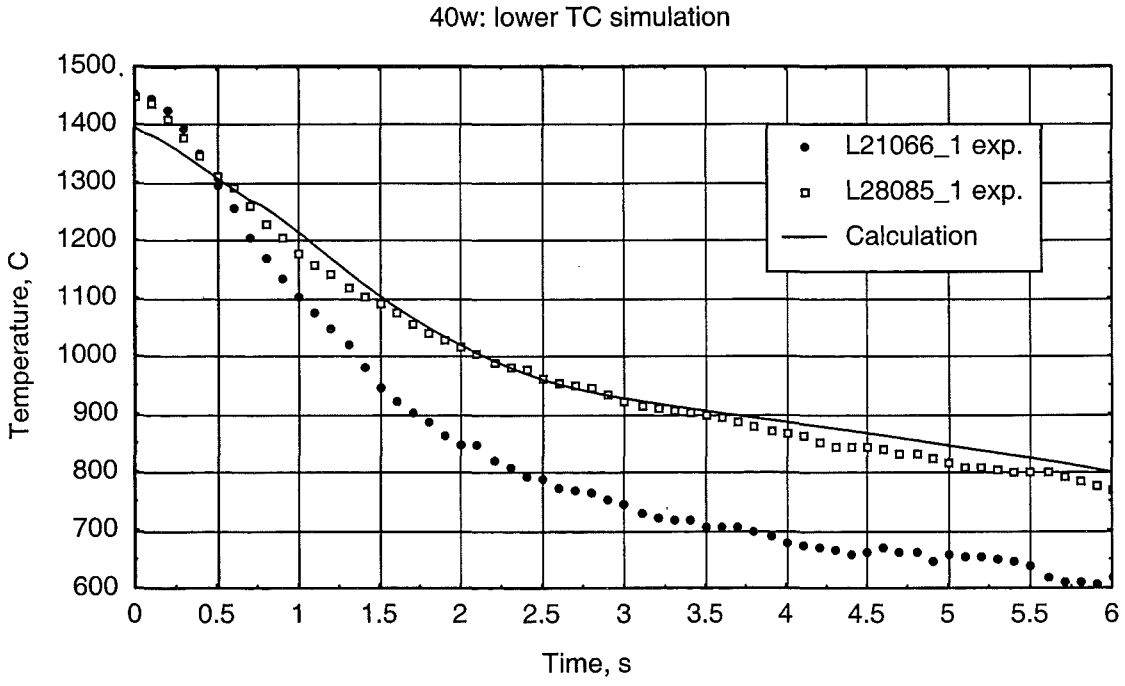

Figure 3.28: Temperature evolution of the lower TC in the 40w type experiment (1400 °C, 0 µm pre-oxidation, water quenching) in the time interval 0–6 s.

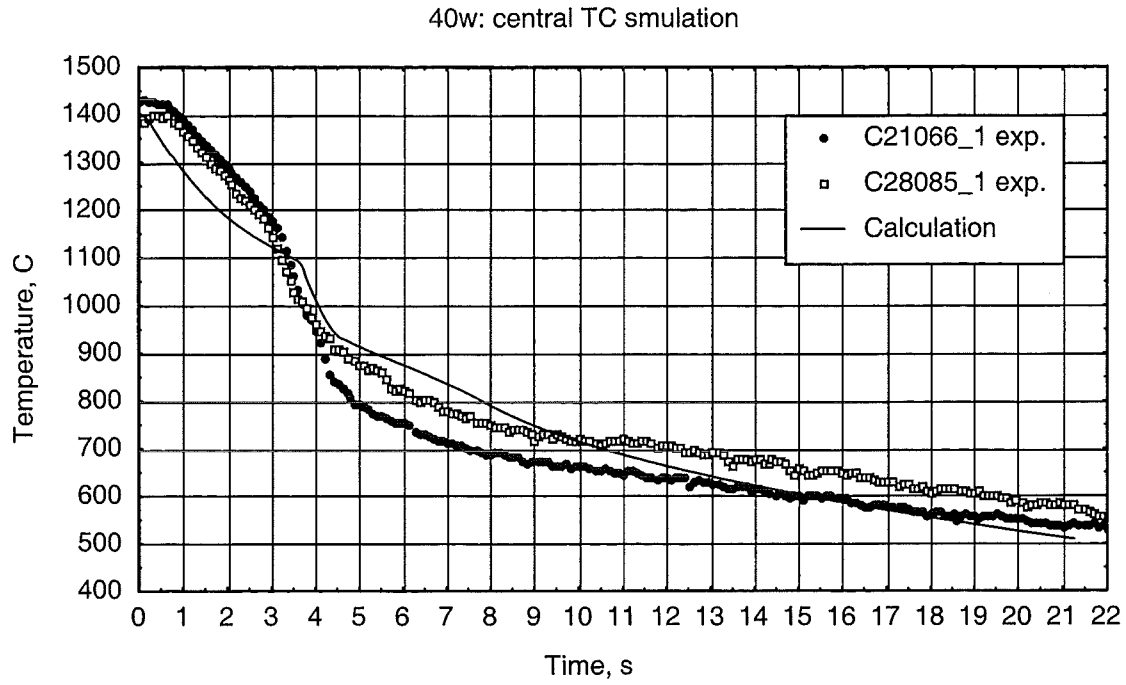

Figure 3.29: Temperature evolution of the central TC in the 40w type experiment (1400 °C, 0 µm pre-oxidation, water quenching in the time interval 0–22 s.

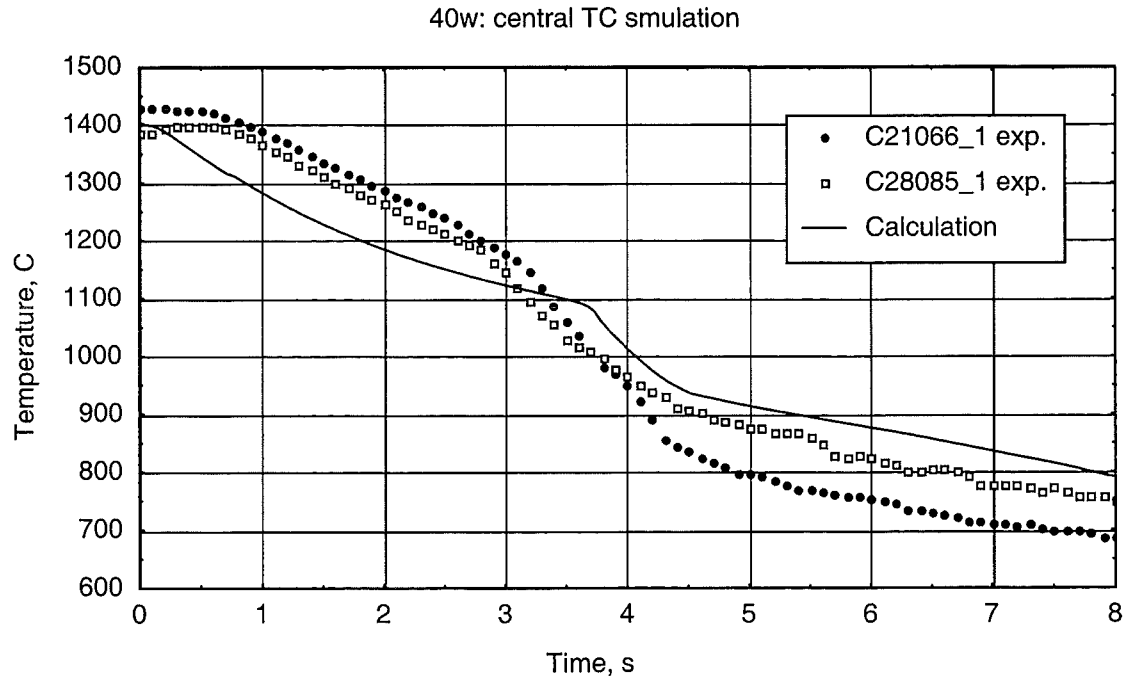

Figure 3.30: Temperature evolution of the central TC in the 40w type experiment (1400 °C, 0 µm pre-oxidation, water quenching in the time interval 0–8 s.

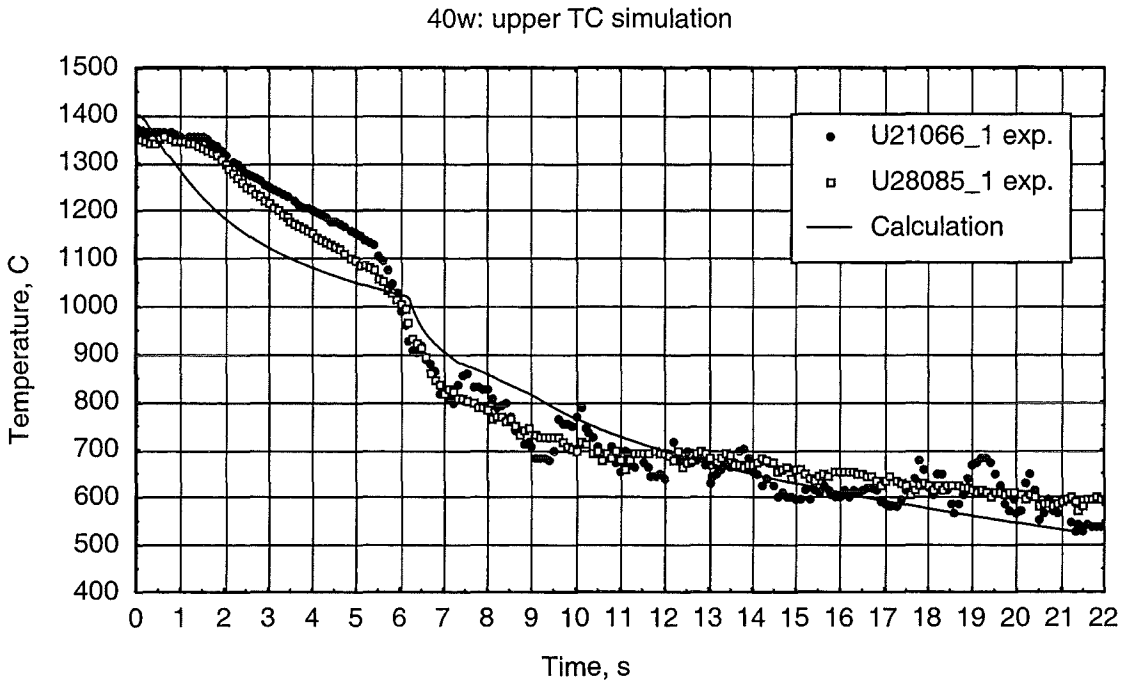

Figure 3.31: Temperature evolution of the upper TC in the 40w type experiment (1400 °C, 0 µm pre-oxidation, water quenching) in the time interval 0–22 s.

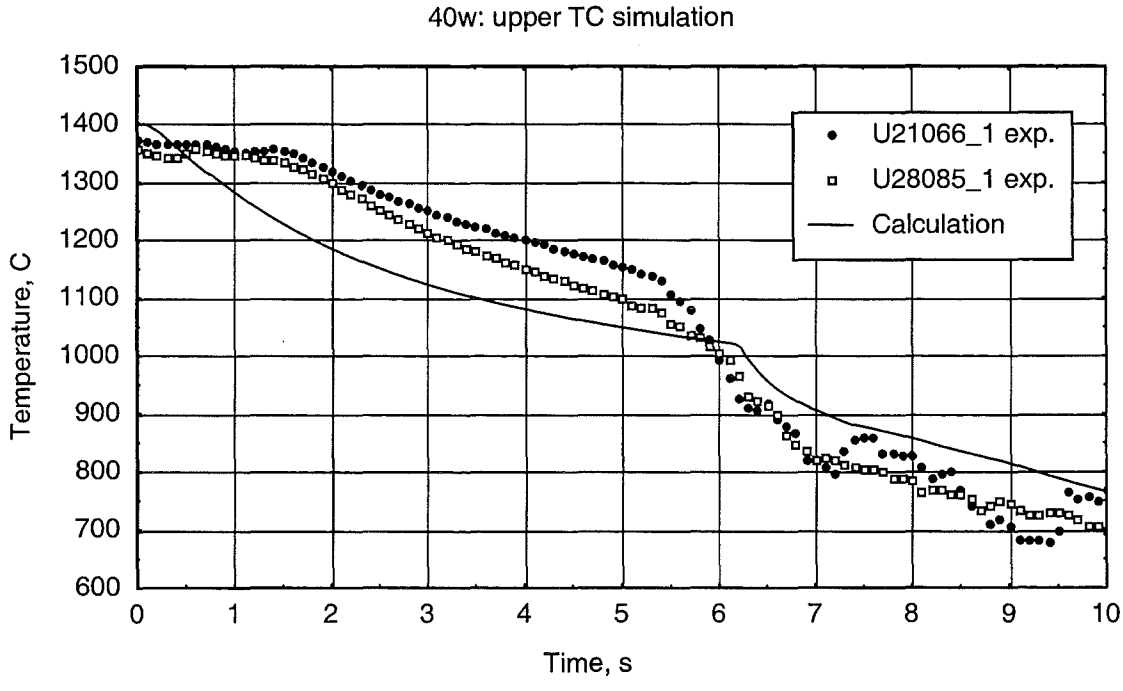

Figure 3.32: Temperature evolution of the upper TC in the 40w type experiment (1400 °C, 0 µm pre-oxidation, water quenching) in the time interval 0–10 s.

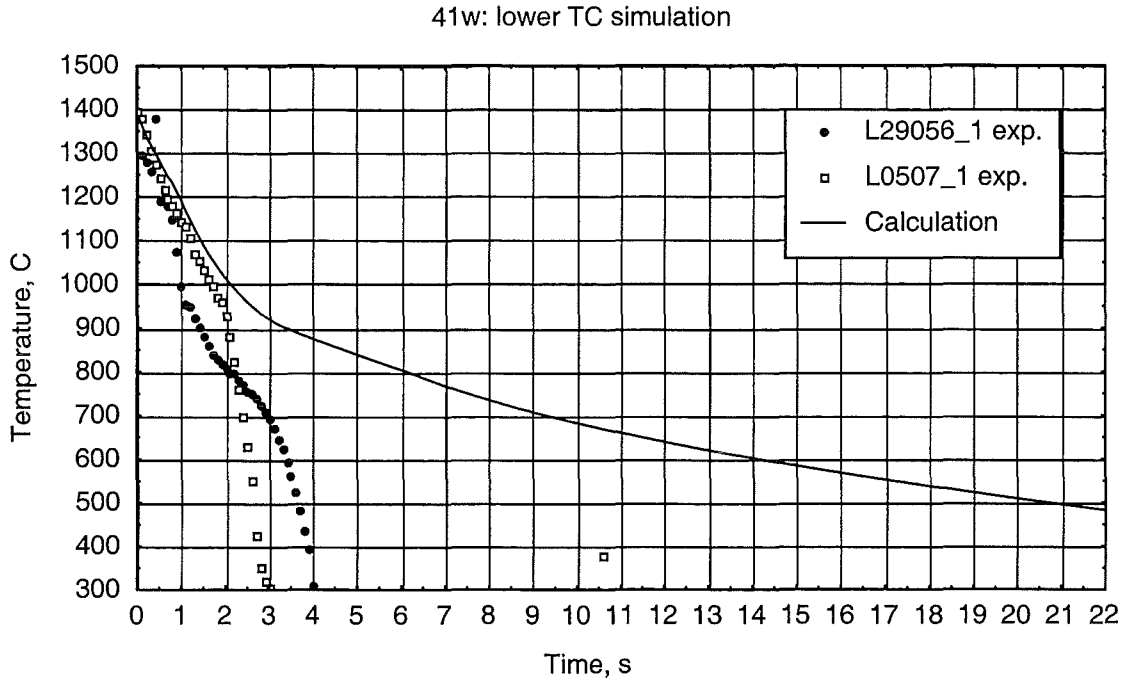

Figure 3.33: Temperature evolution of the lower TC in the 41w type experiment (1400 °C, 100 µm pre-oxidation, water quenching) in the time interval 0–22 s.

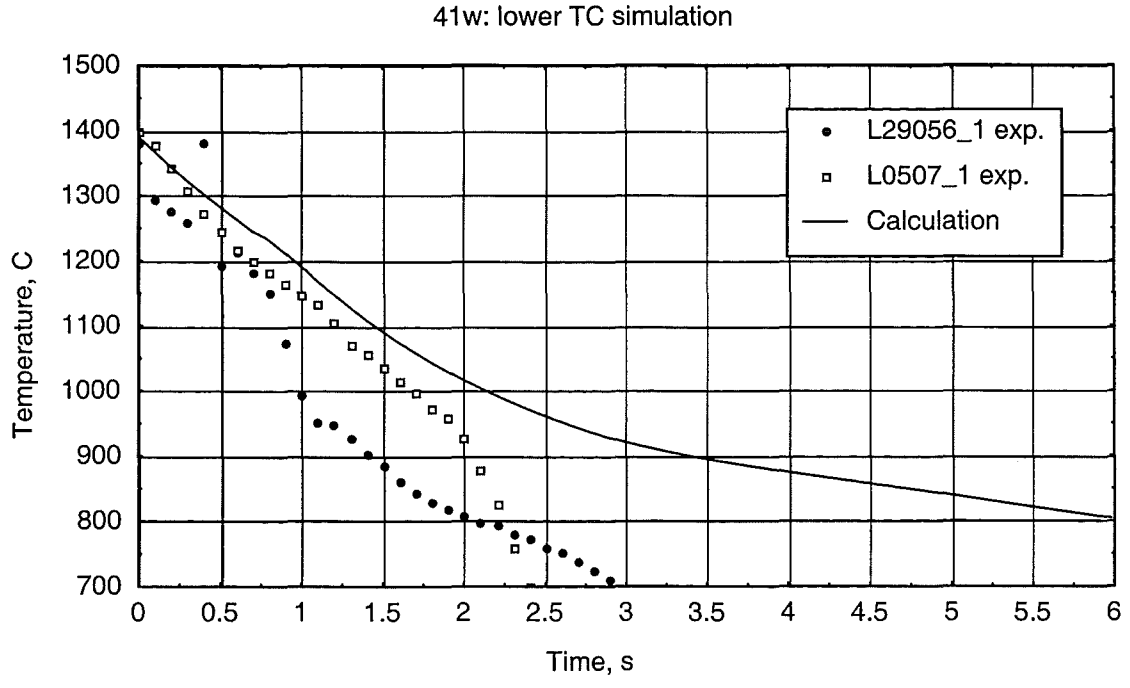

Figure 3.34: Temperature evolution of the lower TC in the 41w type experiment (1400 °C, 100 µm pre-oxidation, water quenching) in the time interval 0–6 s.

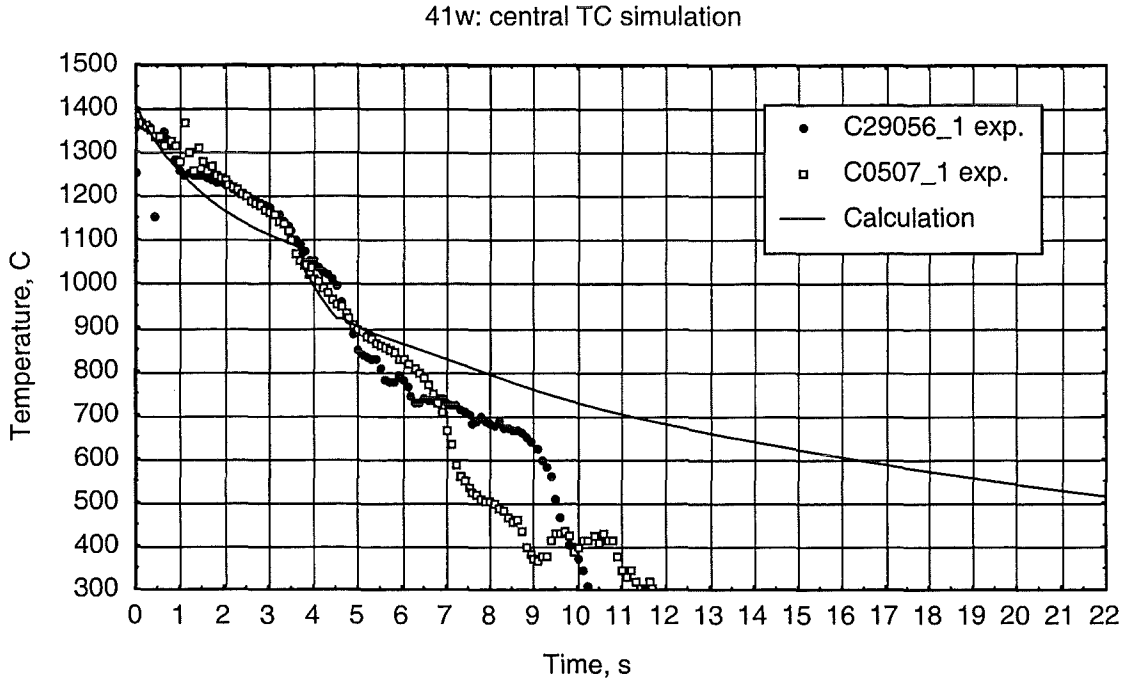

Figure 3.35: Temperature evolution of the central TC in the 41w type experiment (1400 °C, 100 µm pre-oxidation, water quenching) in the time interval 0–22 s.

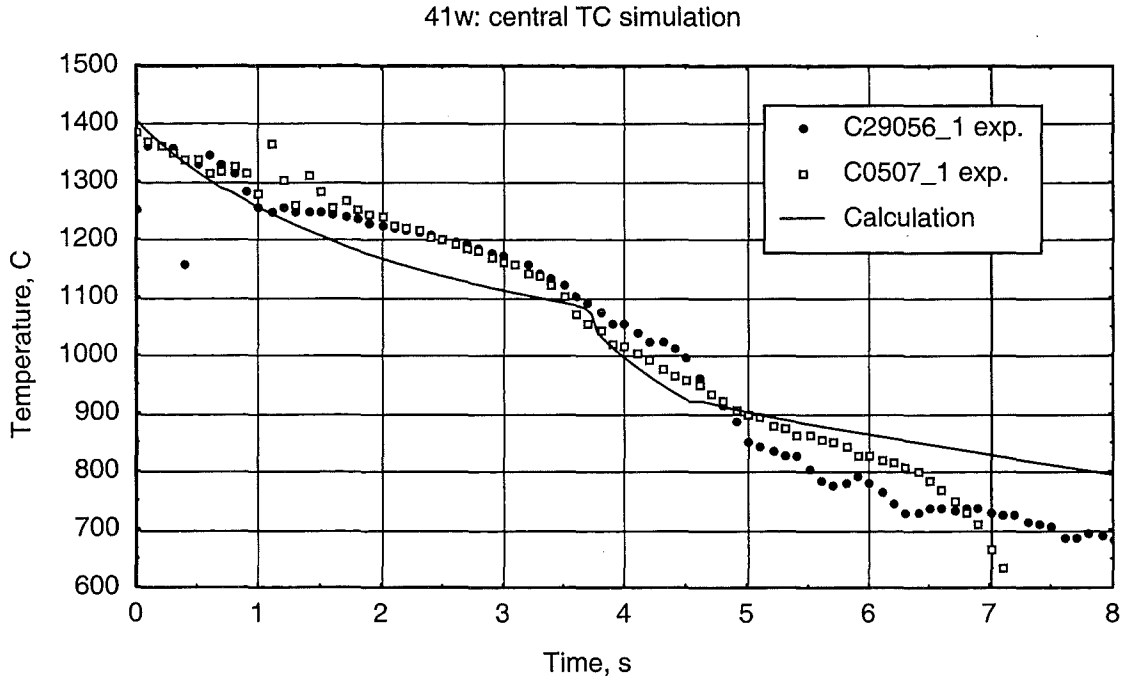

Figure 3.36: Temperature evolution of the central TC in the 41w type experiment (1400 °C, 100 µm pre-oxidation, water quenching) in the time interval 0–8 s.

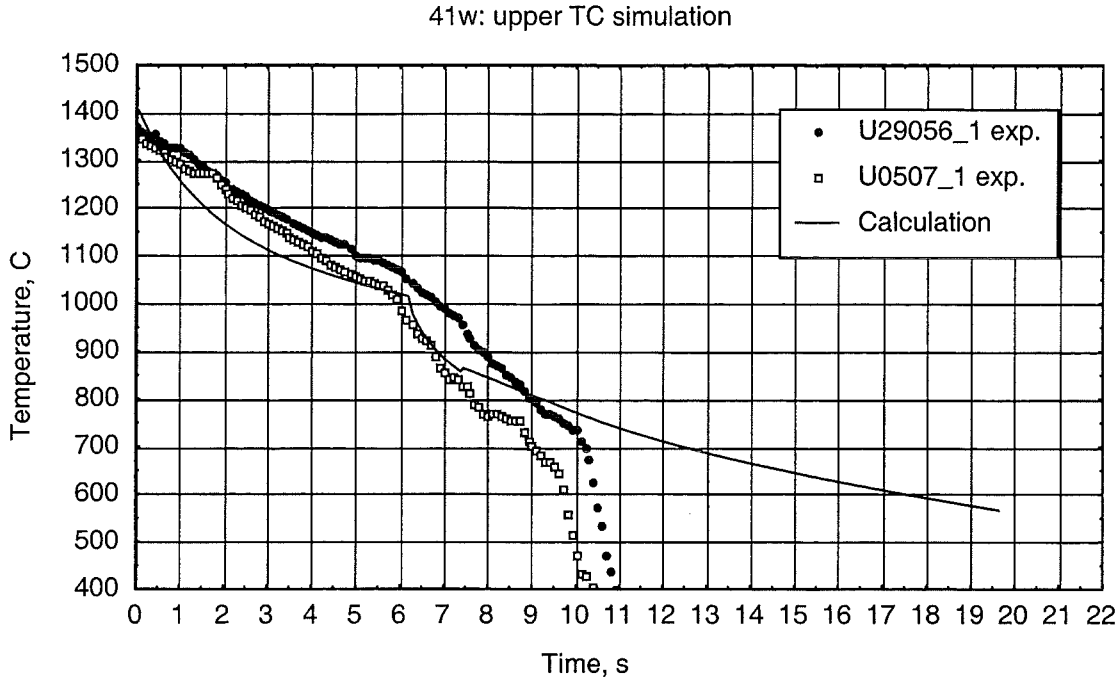

Figure 3.37: Temperature evolution of the upper TC in the 41w type experiment (1400 °C, 100 μm pre-oxidation, water quenching) in the time interval 0–22 s.

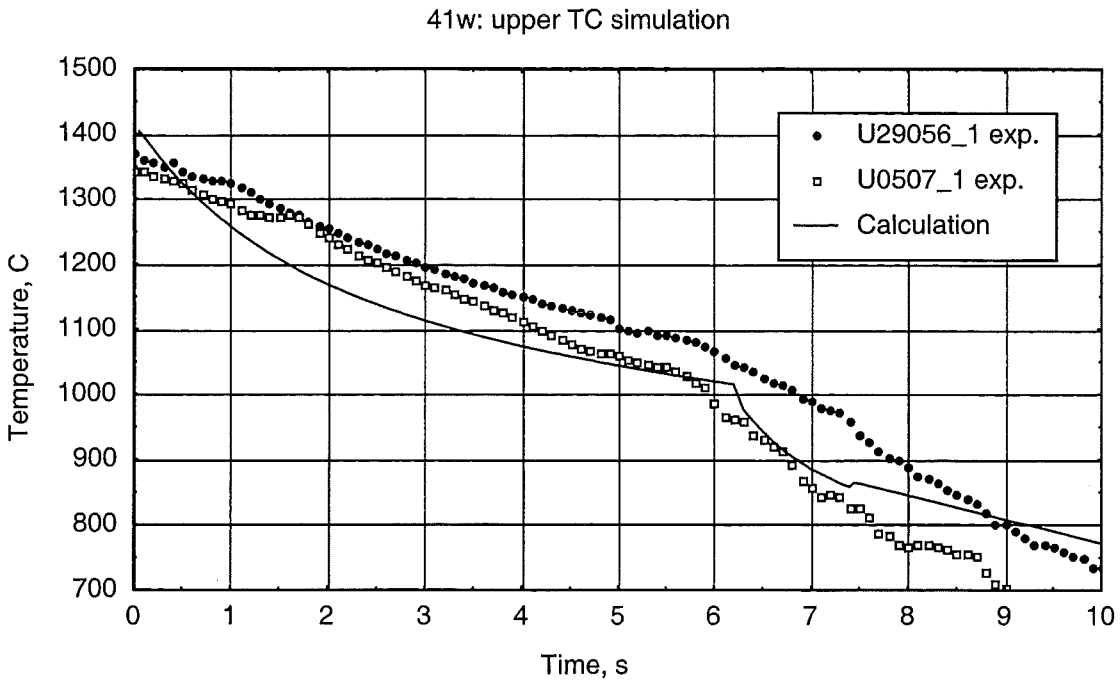

Figure 3.38: Temperature evolution of the upper TC in the 41w type experiment (1400 °C, 100 μm pre-oxidation, water quenching) in the time interval 0–10 s.

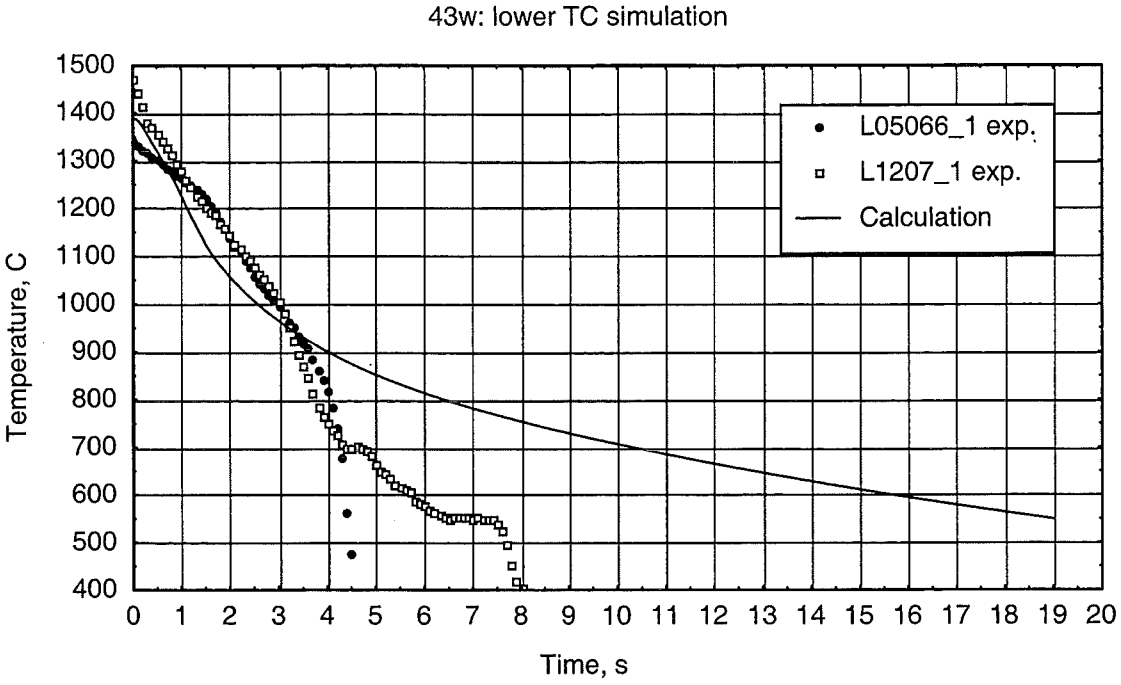

Figure 3.39: Temperature evolution of the lower TC in the 43w type experiment (1400 °C, 300 µm pre-oxidation, water quenching) in the time interval 0–20 s.

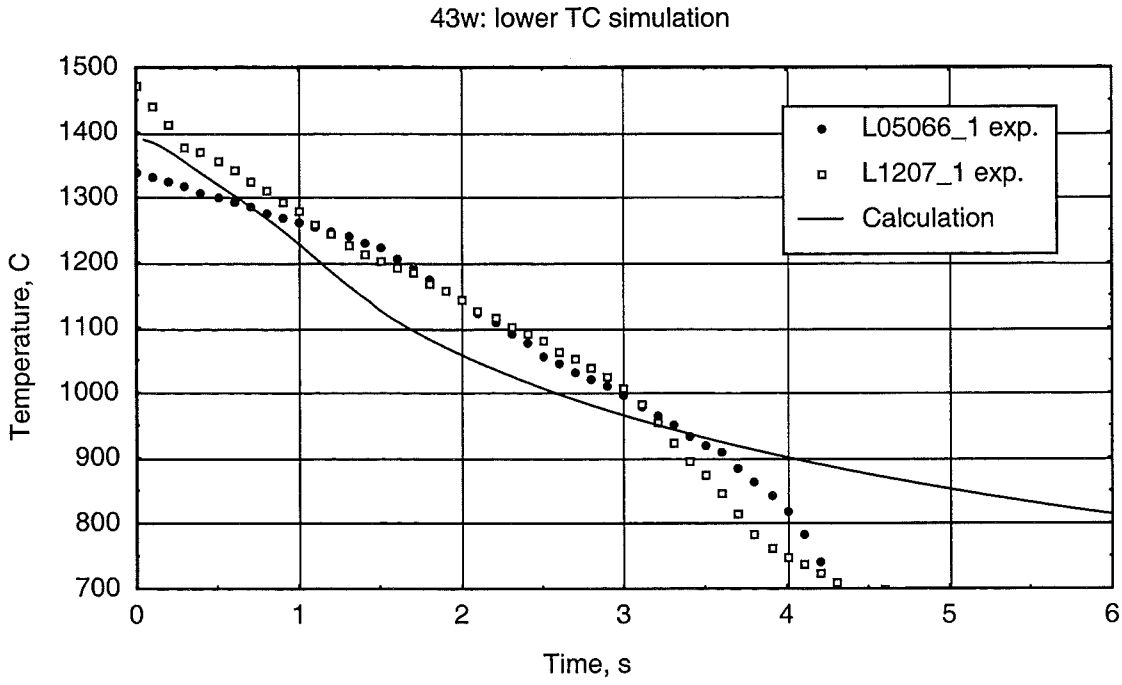

Figure 3.40: Temperature evolution of the lower TC in the 43w type experiment (1400 °C, 300 µm pre-oxidation, water quenching) in the time interval 0–6 s.

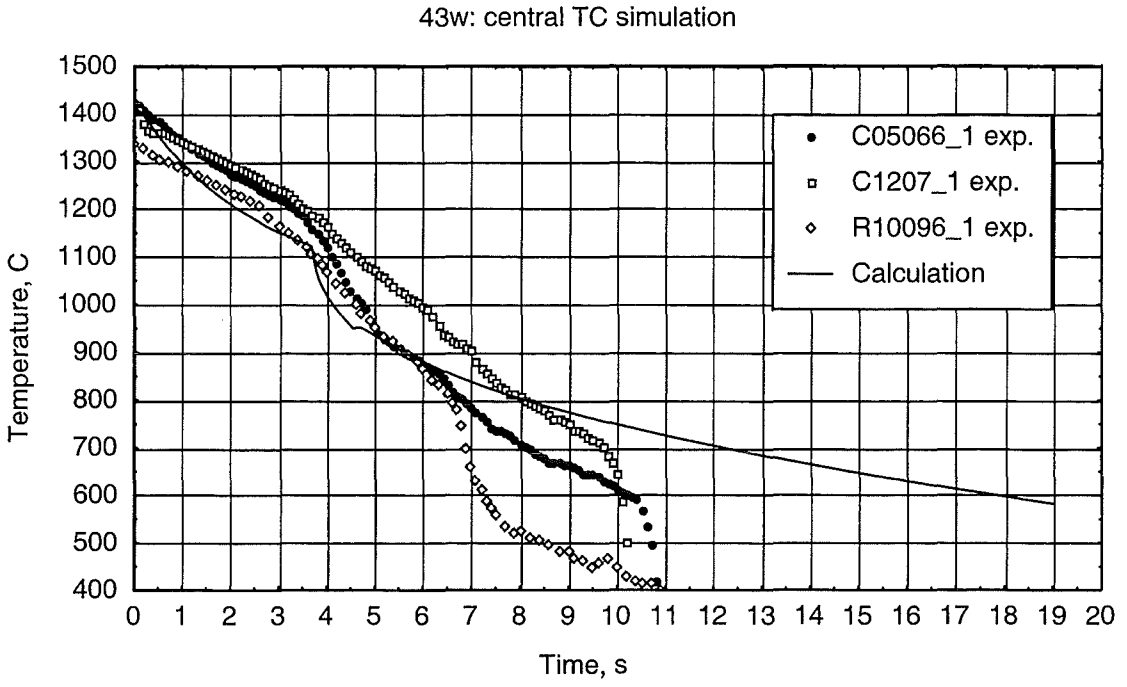

Figure 3.41: Temperature evolution of the central TC in the 43w type experiment (1400 °C, 300 µm pre-oxidation, water quenching) in the time interval 0–20 s.

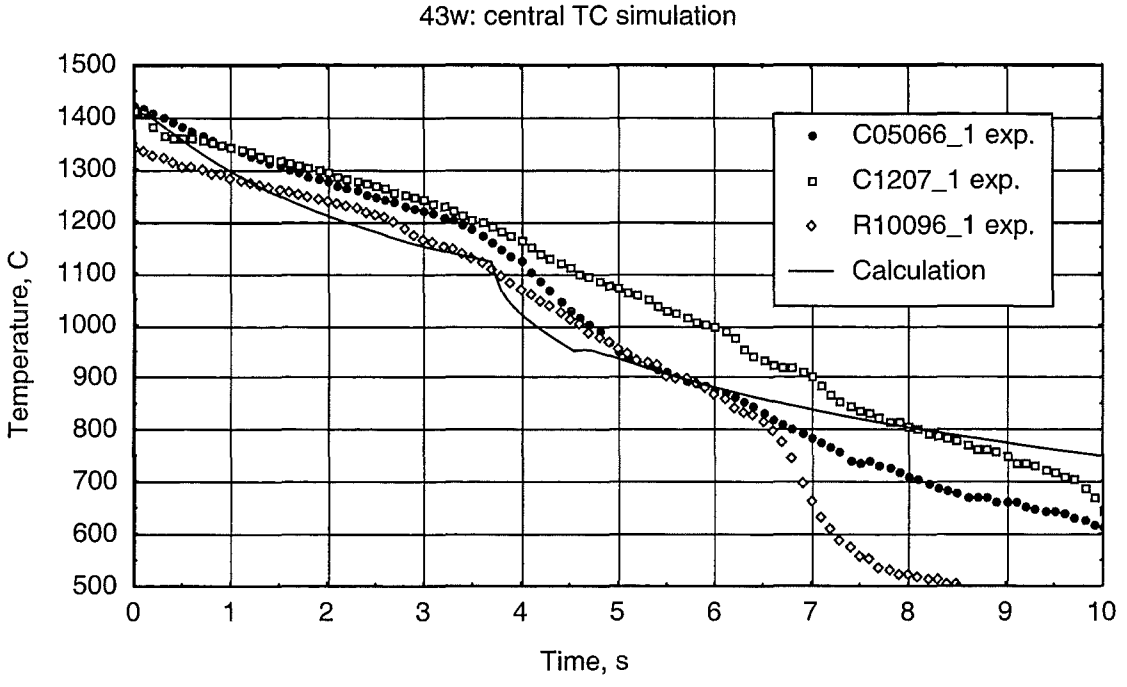

Figure 3.42: Temperature evolution of the central TC in the 43w type experiment (1400 °C, 300 µm pre-oxidation, water quenching) in the time interval 0–10 s.

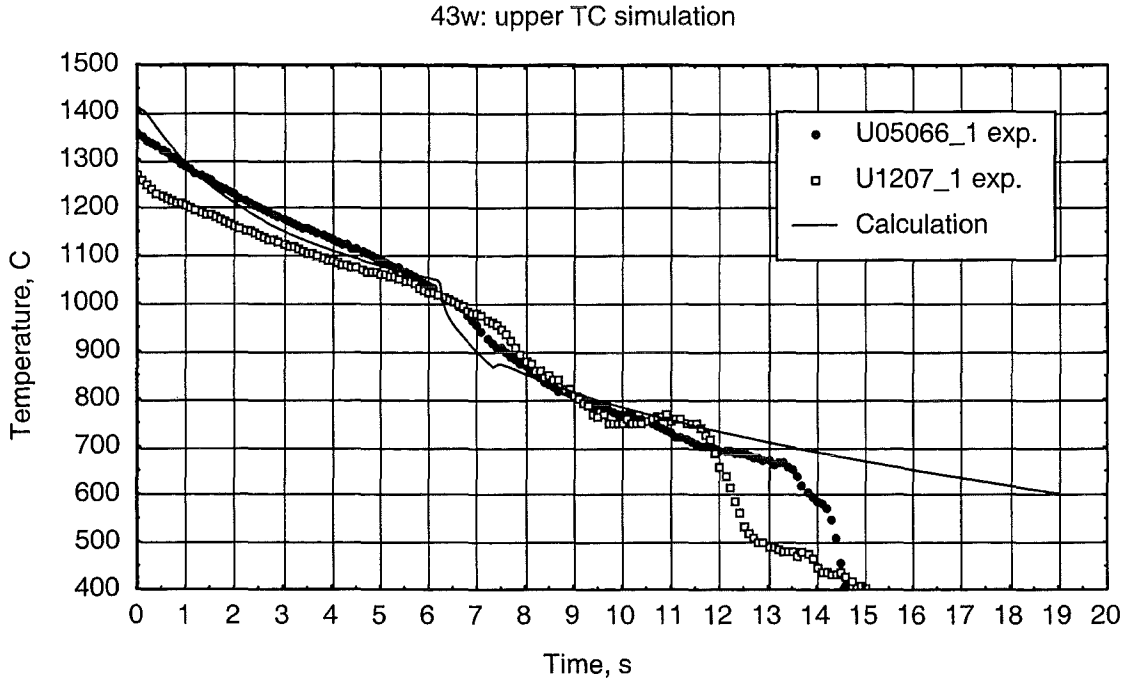

Figure 3.43: Temperature evolution of the upper TC in the 43w type experiment (1400 °C, 300 µm pre-oxidation, water quenching) in the time interval 0–20 s.

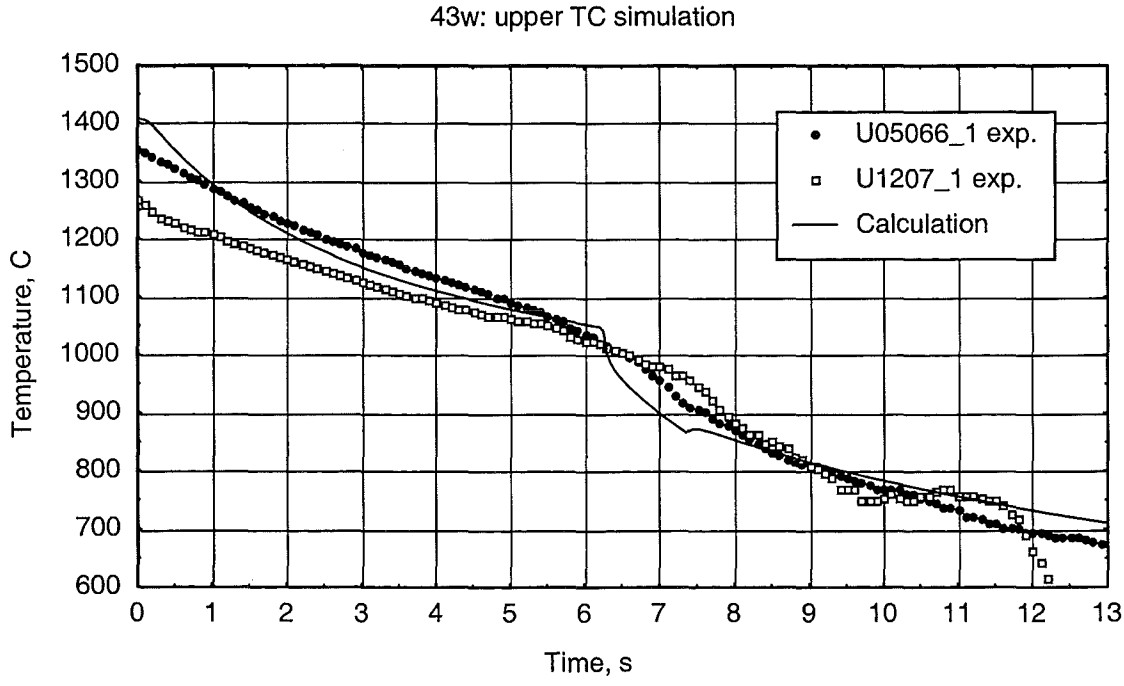

Figure 3.44: Temperature evolution of the upper TC in the 43w type experiment (1400 °C, 300 µm pre-oxidation, water quenching) in the time interval 0–13 s.

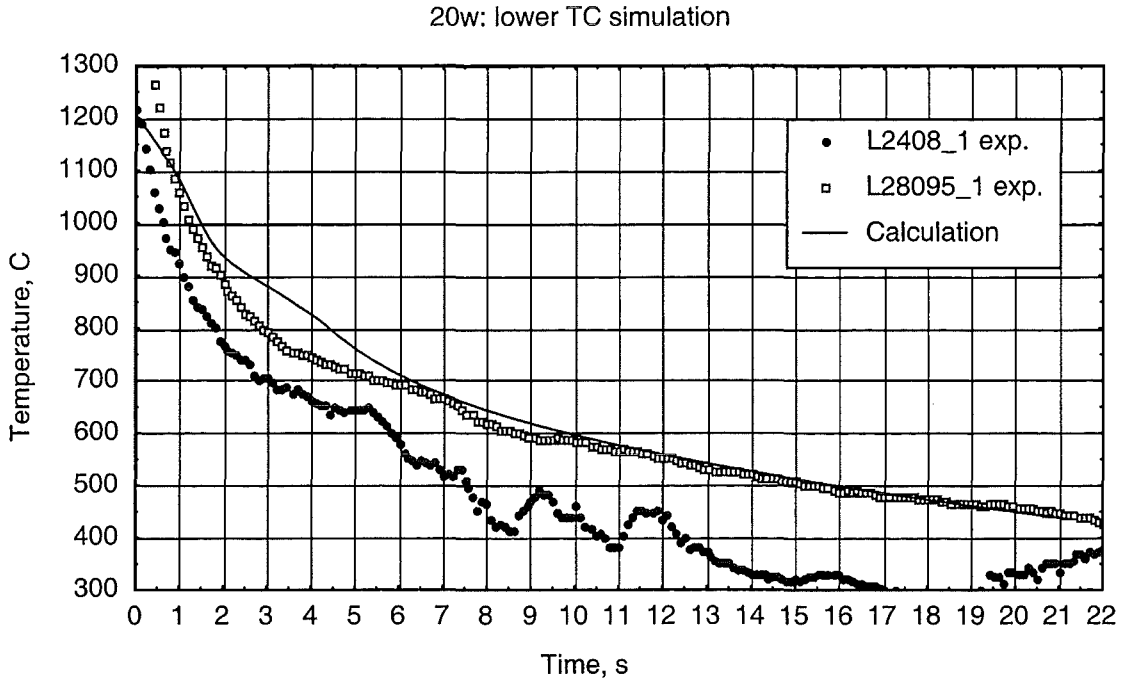

Figure 3.45: Temperature evolution of the lower TC in the 20w type experiment (1200 °C, 0 µm pre-oxidation, water quenching) in the time interval 0–22 s.

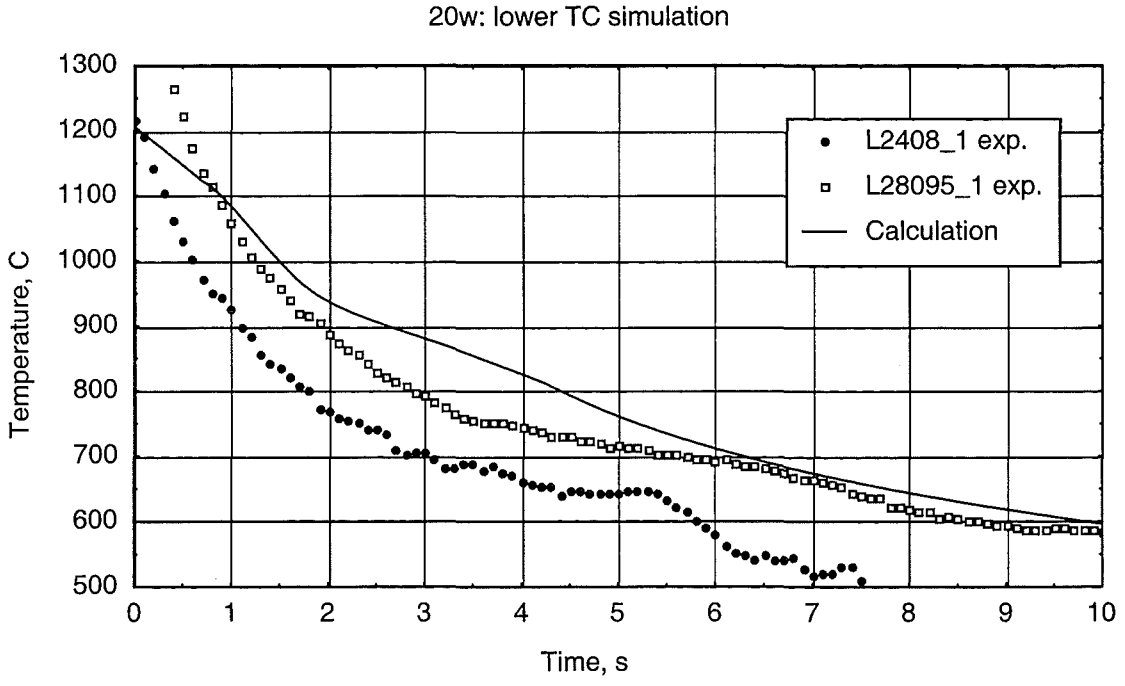

Figure 3.46: Temperature evolution of the lower TC in the 20w type experiment (1200 °C, 0 µm pre-oxidation, water quenching) in the time interval 0–10 s.

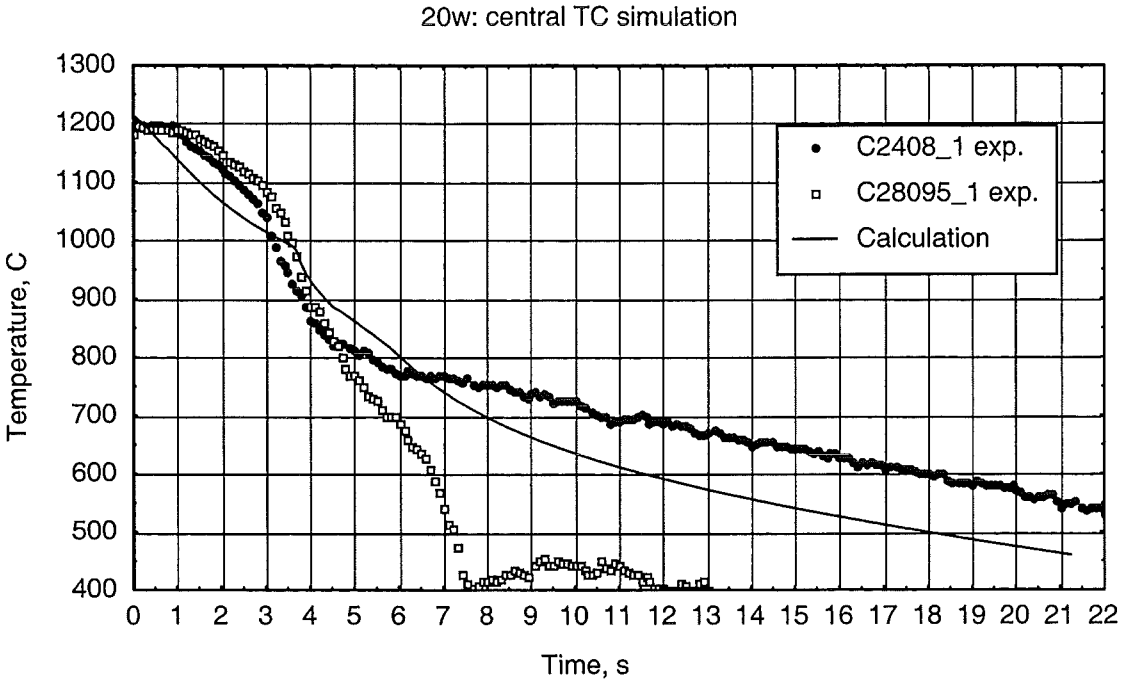

Figure 3.47: Temperature evolution of the central TC in the 20w type experiment (1200 °C, 0 µm pre-oxidation, water quenching) in the time interval 0–22 s.

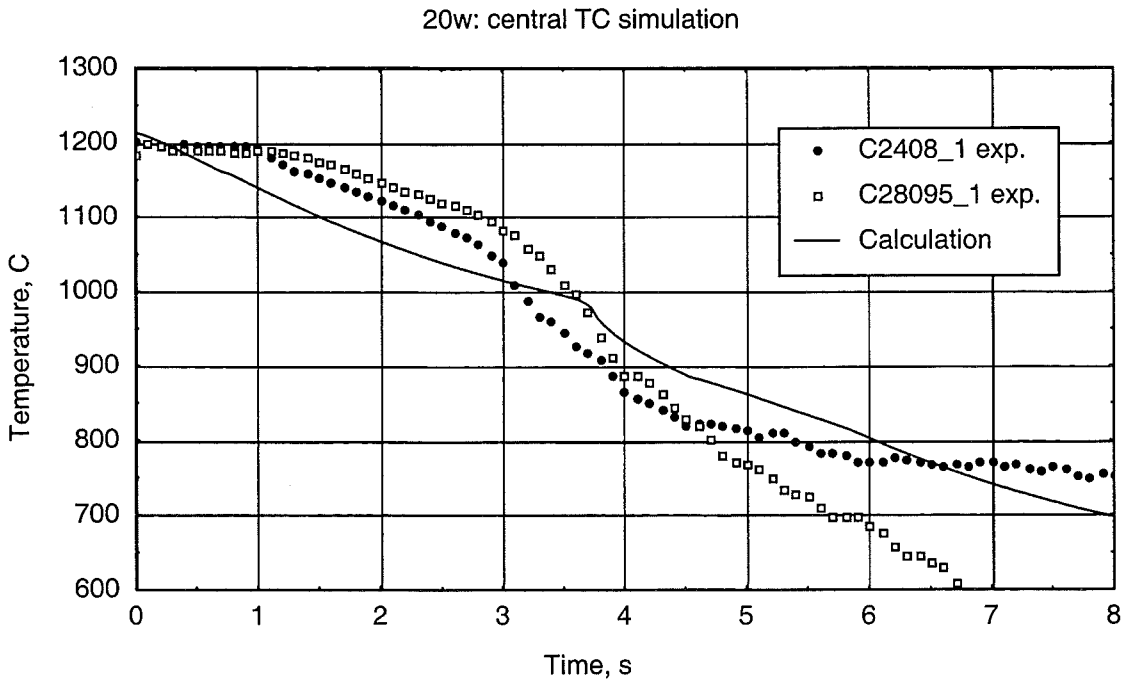

Figure 3.48: Temperature evolution of the central TC in the 20w type experiment (1200 °C, 0 µm pre-oxidation, water quenching) in the time interval 0–8 s.

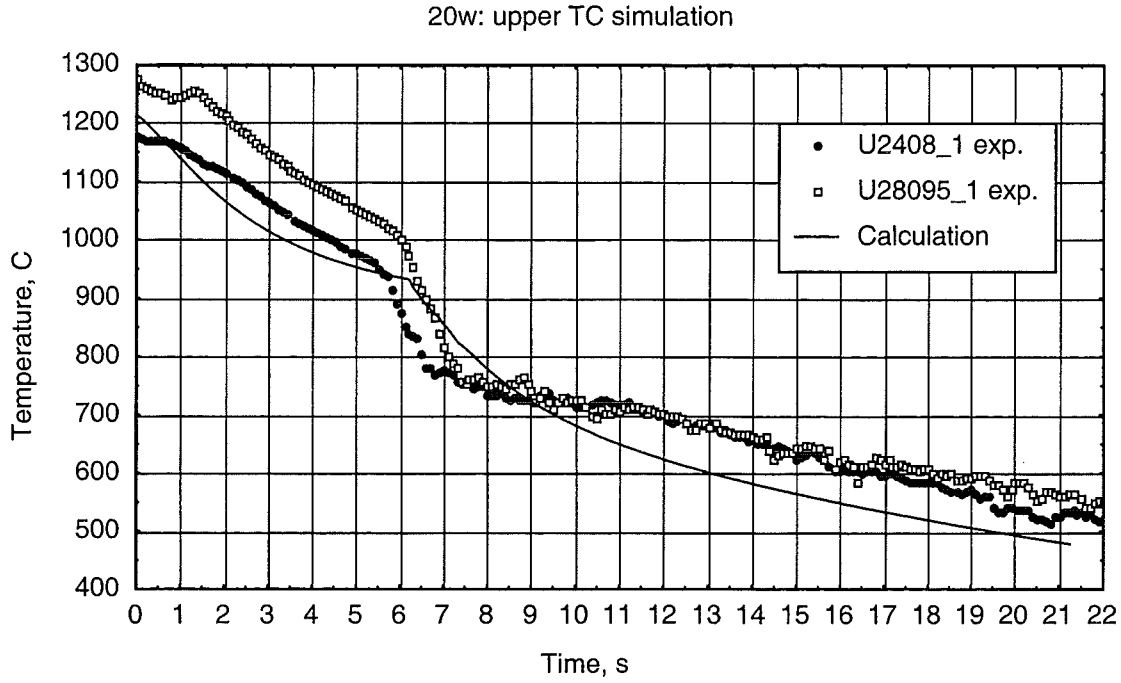

Figure 3.49: Temperature evolution of the upper TC in the 20w type experiment (1200 °C, 0 µm pre-oxidation, water quenching) in the time interval 0–22 s.

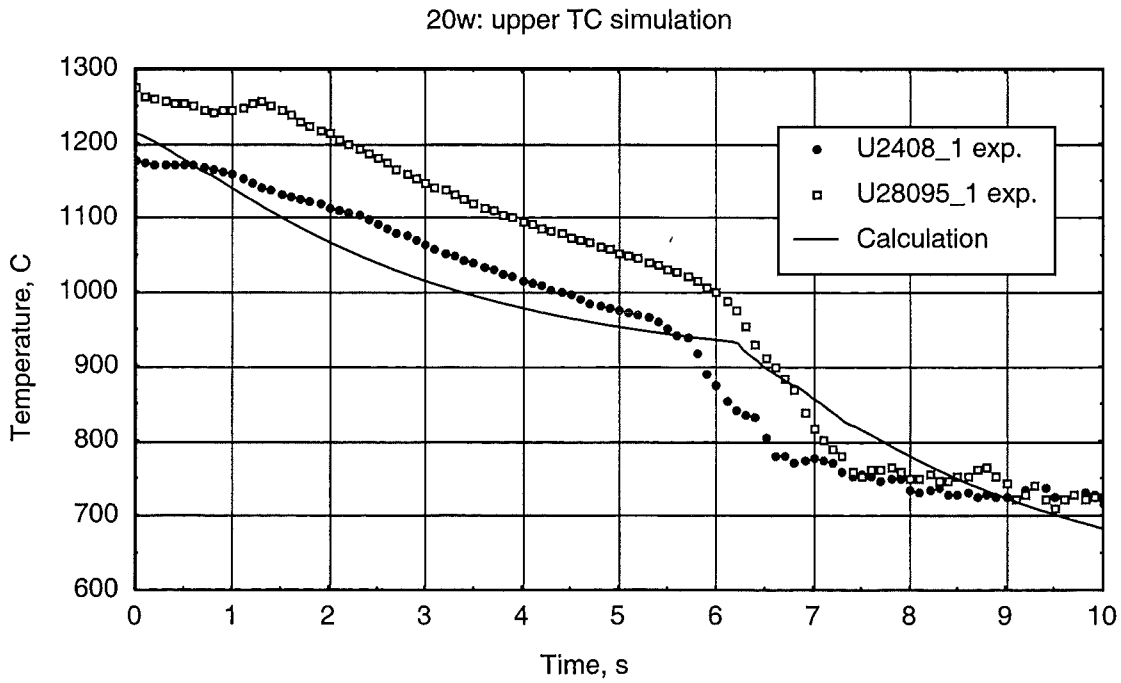

Figure 3.50: Temperature evolution of the upper TC in the 20w type experiment (1200 °C, 0 µm pre-oxidation, water quenching) in the time interval 0–10 s.

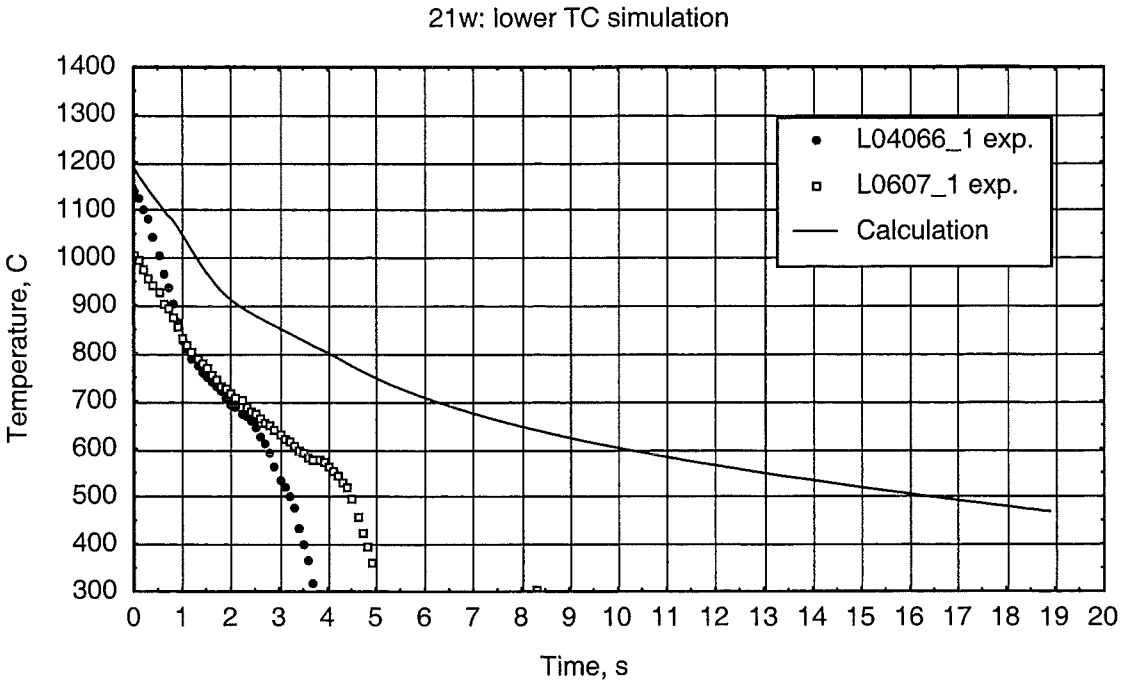

Figure 3.51: Temperature evolution of the lower TC in the 21w type experiment (1200 °C, 100 µm pre-oxidation, water quenching) in the time interval 0–20 s.

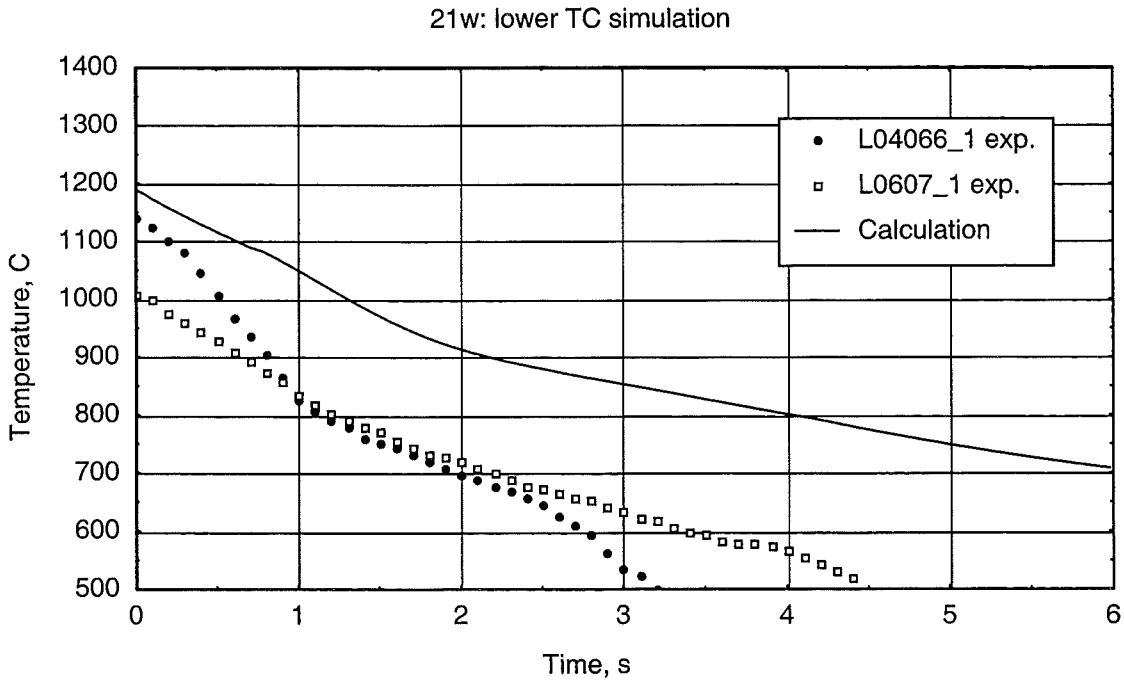

Figure 3.52: Temperature evolution of the lower TC in the 21w type experiment (1200 °C, 100 µm pre-oxidation, water quenching) in the time interval 0–6 s.

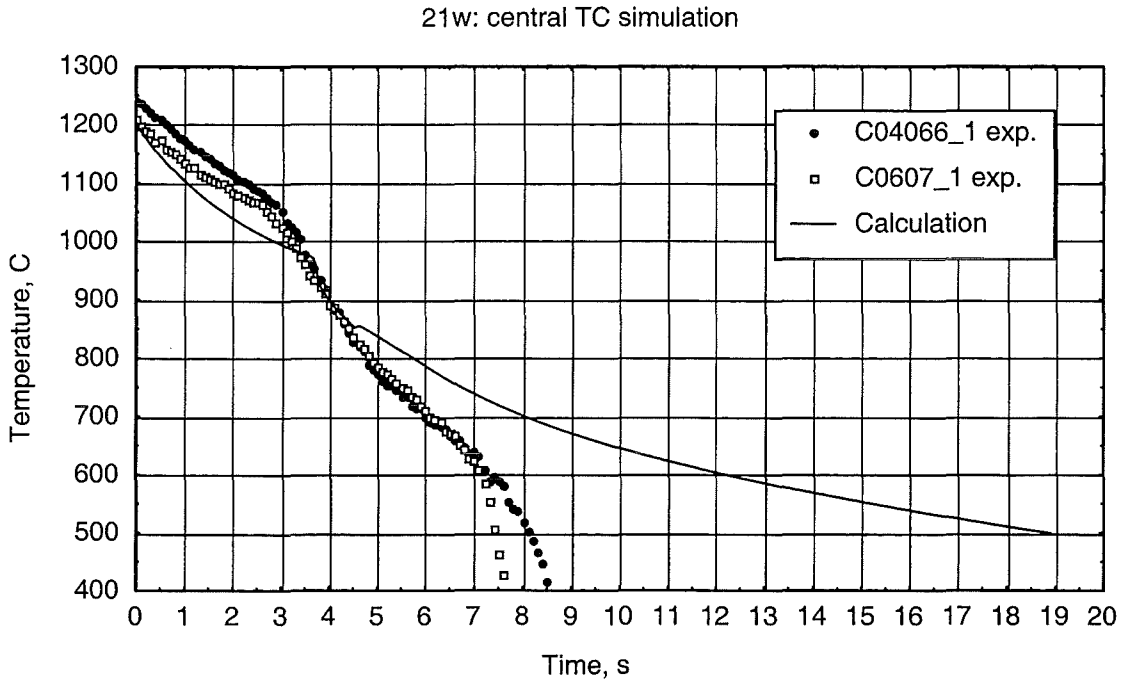

Figure 3.53: Temperature evolution of the central TC in the 21w type experiment (1200 °C, 100 µm pre-oxidation, water quenching) in the time interval 0–20 s.

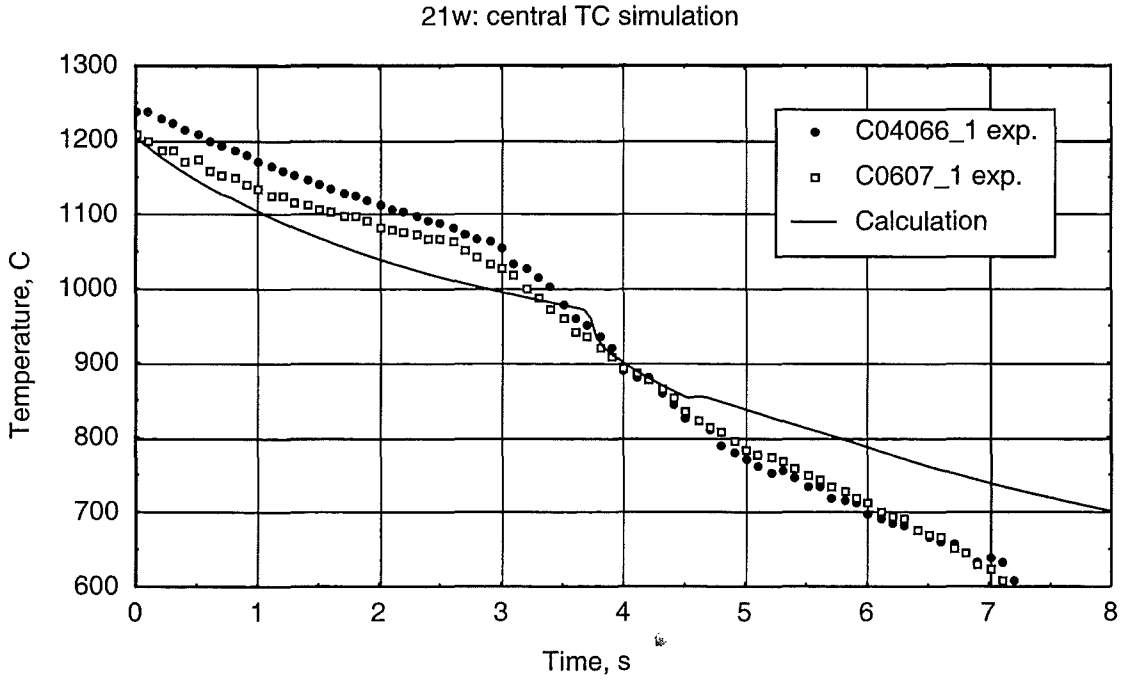

Figure 3.54: Temperature evolution of the central TC in the 21w type experiment (1200 °C, 100 µm pre-oxidation, water quenching) in the time interval 0–8 s.

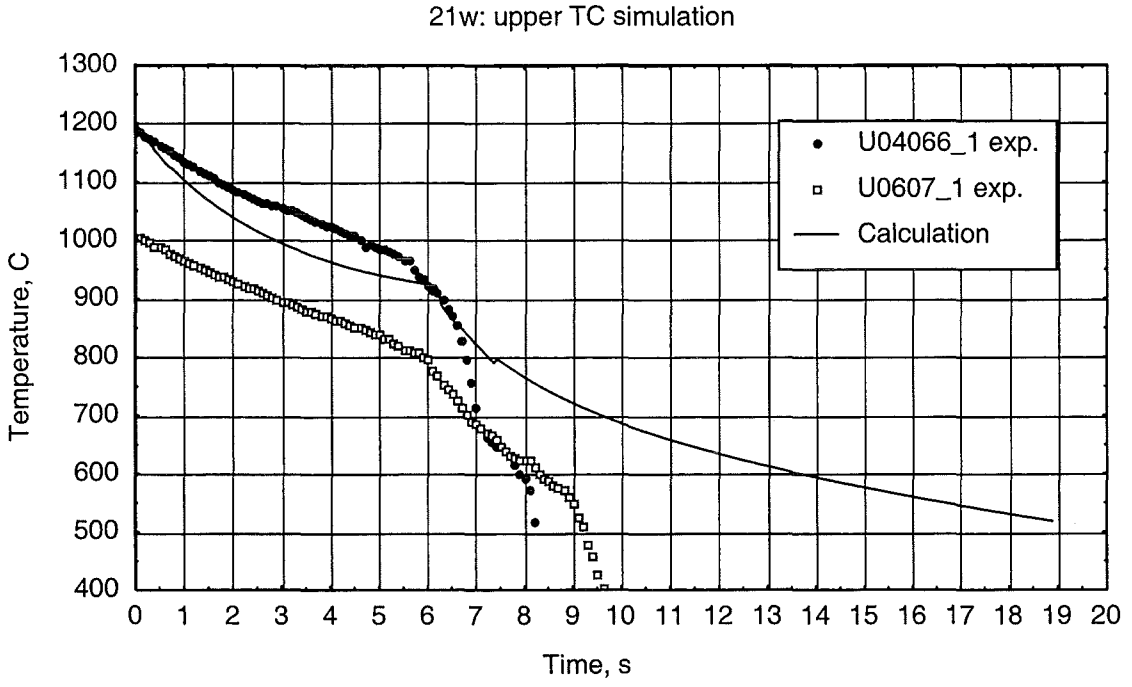

Figure 3.55: Temperature evolution of the upper TC in the 21w type experiment (1200 °C, 100 µm pre-oxidation, water quenching) in the time interval 0–20 s.

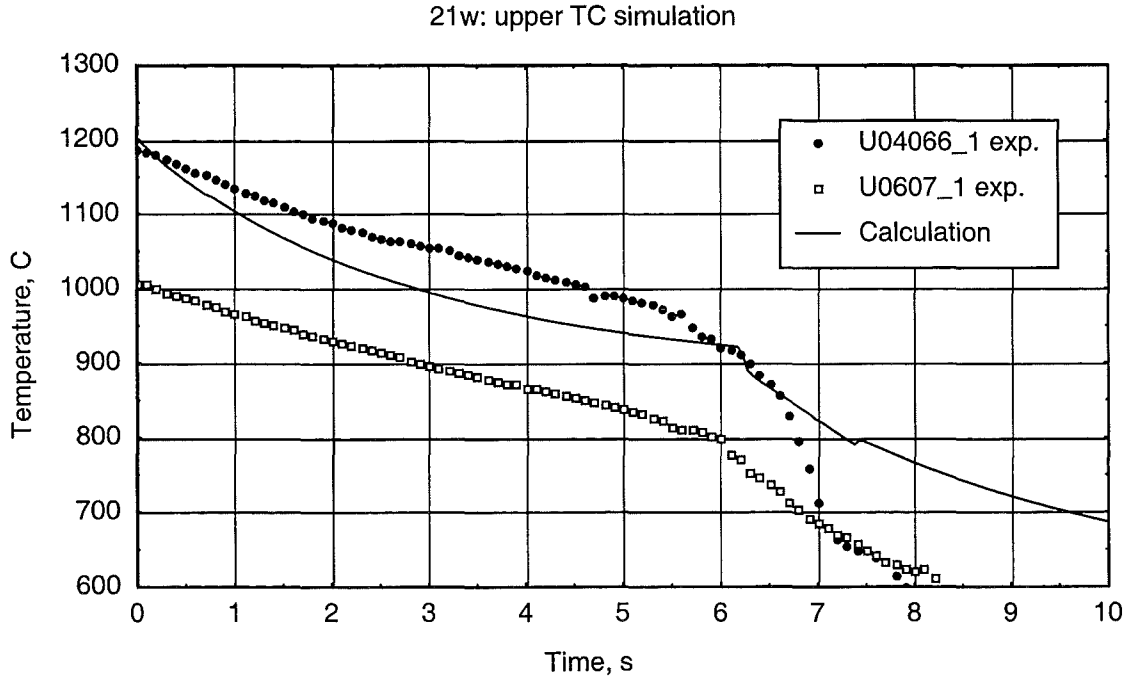

Figure 3.56: Temperature evolution of the upper TC in the 21w type experiment (1200 °C, 100 µm pre-oxidation, water quenching) in the time interval 0–10 s.

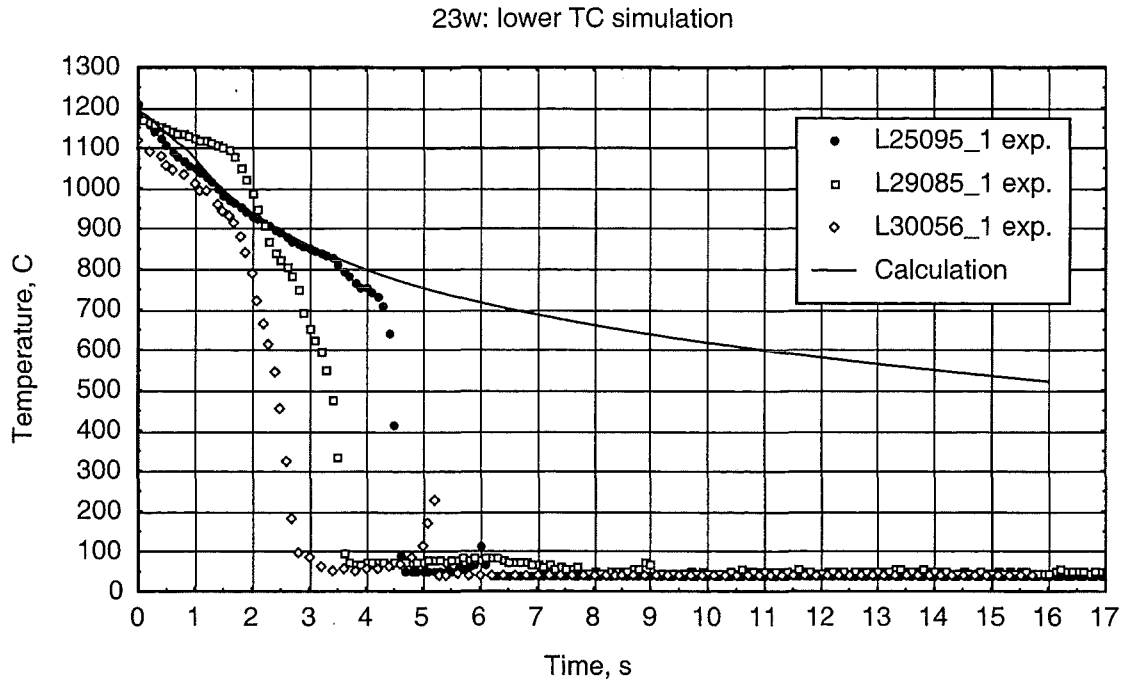

Figure 3.57: Temperature evolution of the lower TC in the 23w type experiment (1200 °C, 300 μm pre-oxidation, water quenching) in the time interval 0–17 s.

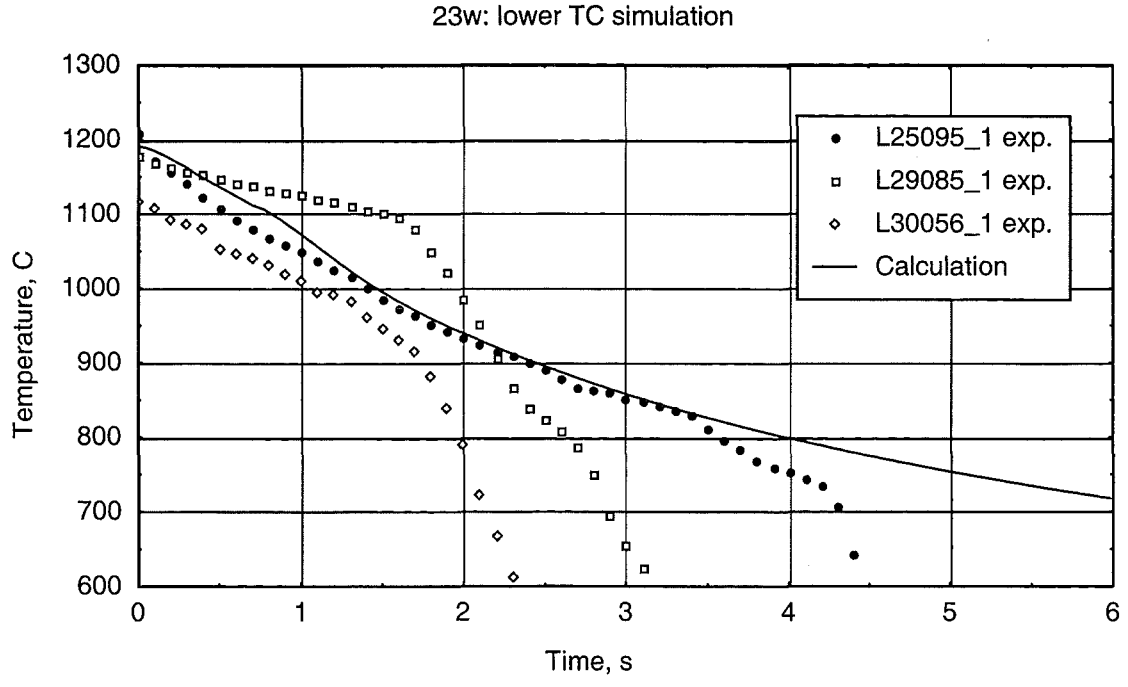

Figure 3.58: Temperature evolution of the lower TC in the 23w type experiment (1200 °C, 300 μm pre-oxidation, water quenching) in the time interval 0–6 s.

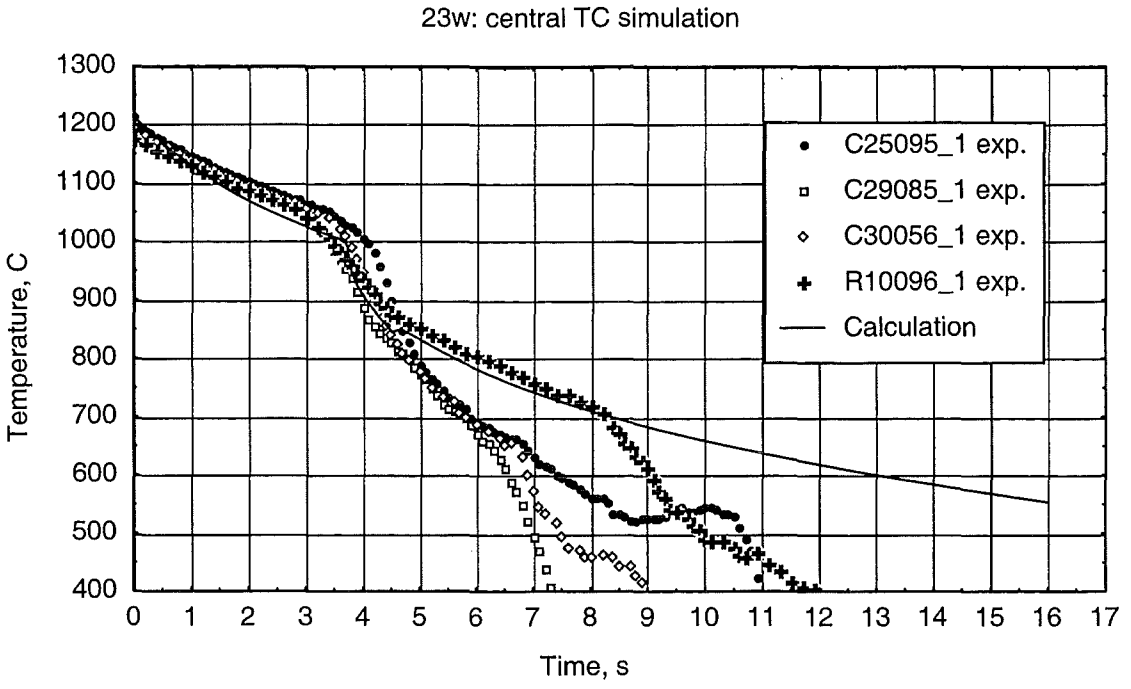

Figure 3.59: Temperature evolution of the central TC in the 23w type experiment (1200 °C, 300 µm pre-oxidation, water quenching) in the time interval 0–17 s.

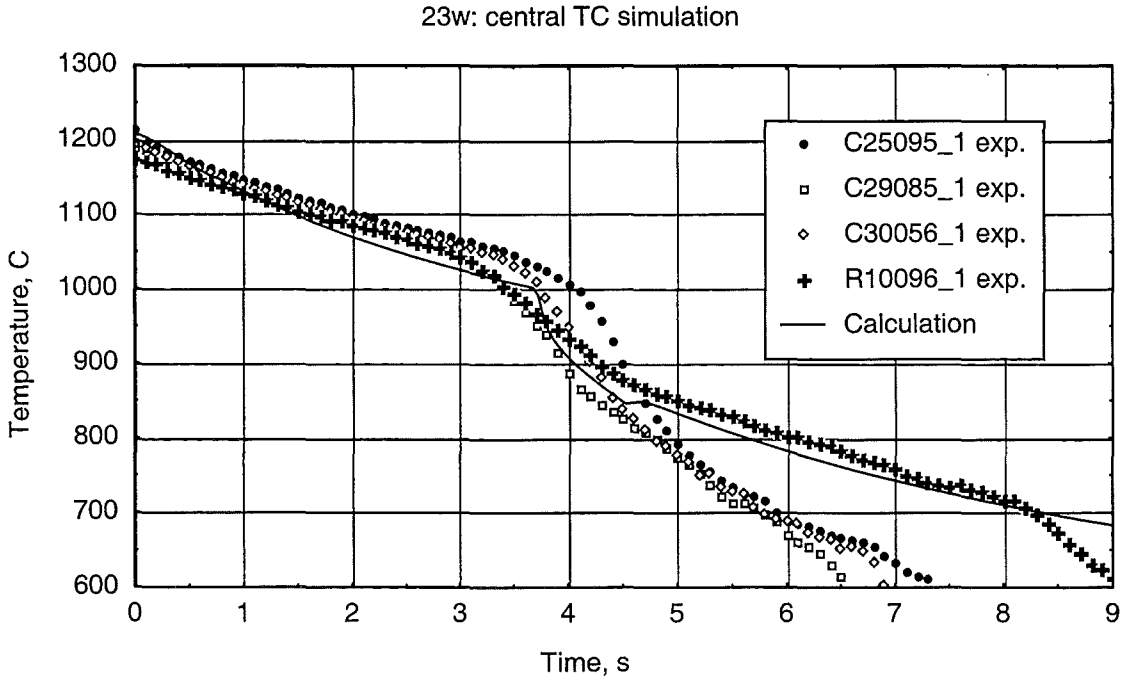

Figure 3.60: Temperature evolution of the central TC in the 23w type experiment (1200 °C, 300 µm pre-oxidation, water quenching) in the time interval 0–9 s.

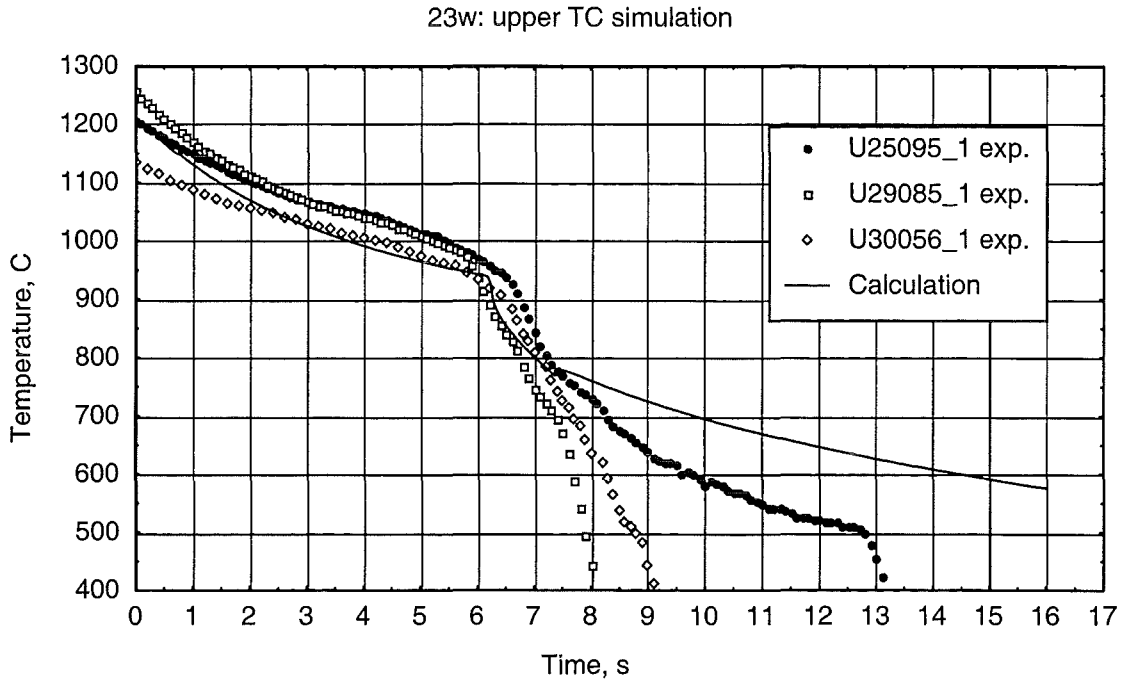

Figure 3.61: Temperature evolution of the upper TC in the 23w type experiment (1200 °C, 300 µm pre-oxidation, water quenching) in the time interval 0–17 s.

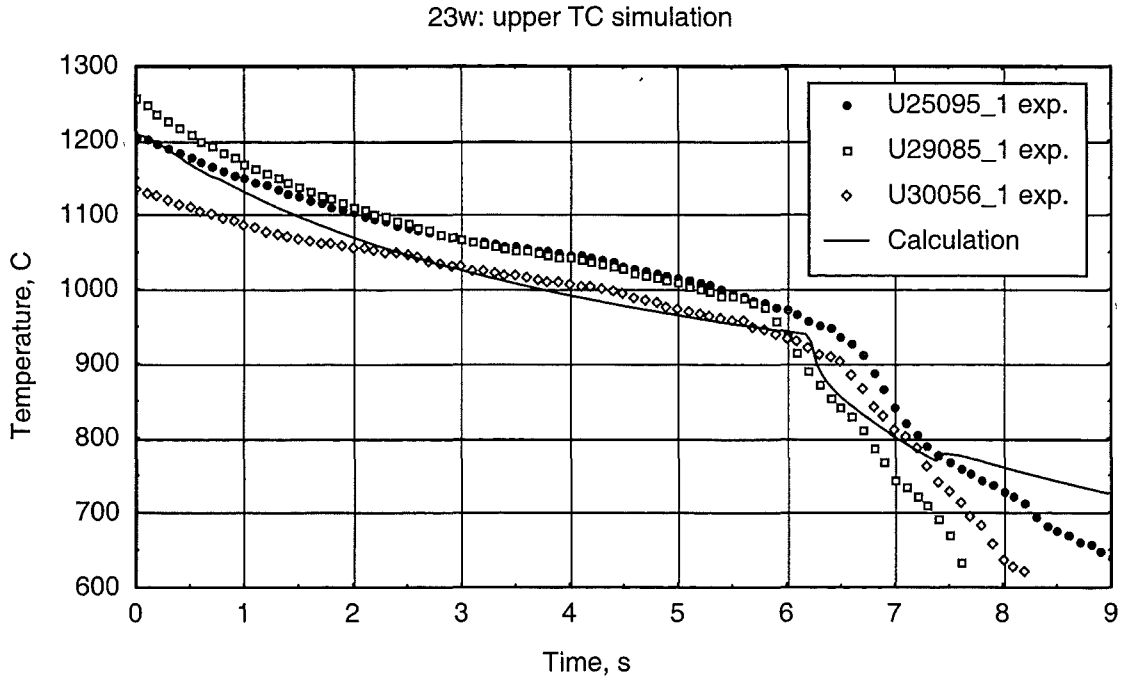

Figure 3.62: Temperature evolution of the upper TC in the 23w type experiment (1200 °C, 300 µm pre-oxidation, water quenching) in the time interval 0–9 s.

3.1.3 Steam mass transfer modeling

3.1.3.1 Steam starvation in the 60w type tests

Correct determination of steam supply boundary conditions is very important for the adequate description of the Zircaloy cladding oxidation kinetics and as consequence for the modeling of the temperature escalation. Steam depletion in the gas may result in incomplete oxidation of the cladding in the upper part of the fuel rod. Steam starvation occurs readily when the steam supply rate is low and the temperature of the cladding is high. Such situation takes place in the FZK water quench experiments with no pre-oxidation and initial temperature of 1600 °C.

Just like the analogous steam cooling tests (60s), at the very beginning of the water quench process, a small temperature escalation takes place in the 60w tests (lower TC). It should be noted, that the experimentally observed temperature evolution of the lower TC in both 60w type tests (t24066_1 and t31085_1) is very similar to the evolution of the TCs in the steam experiment 60s (see Figures 3.1, 3.2) in the time interval 0–2 sec. This fact means that in both cases the rods at lower TC elevation were in similar thermal conditions (boundary heat flows and oxidation heat release). The temperature escalation at the lower TC elevation in the 60w type tests may be quite well reproduced without accounting for the steam starvation effects.

However, the calculation results for the central and upper TCs in the above approximation (no steam starvation) are quite different from the experimental data (Figures 3.64, 3.65 solid curve). Such calculations give rather fast escalation and subsequent drop of the temperature, instead of the flat evolution observed in the experiments.

This slow temperature evolution at the rod higher elevations is explained by the fact that a partial steam starvation takes place at these elevations preventing fast escalation and oxide layer growth. The partial steam starvation results from the low evaporation rate at the beginning of the reflooding. The calculation by the SQ code gives for the average steam production rate $J_{pr} \approx 0.1$ g/s in the time interval of interest. This value should be compared with the steam flow involved in the oxidation reaction over the total surface of the rod J_{ox} calculated on the assumption that the starvation is absent. The SQ code calculation gives for the value of $J_{ox} \approx 0.2$ g/s in the first second of the process. Thus, the steam production is deficient in this time period to oxidize the whole surface of the rod. Since the evaporation takes place at the lower part of the rod, the main part of the evaporated steam is taken up by this lower

part, causing partial starvation of the upper parts. This consideration also explains the fact that the resulting oxide layer thickness at the upper elevations is less than at the lower one.

In order to account for this effect the steam starvation model was implemented in the SQ code. This makes it possible to describe correctly the oxidation kinetics in wide range of steam concentration values and reproduce the experimentally observed temperature evolution of the rod surface at the upper elevations in the 60w type tests (Figures 3.63, 3.64, dashed curve, Figures 3.11 – 3.14 of the verification set).

In the next subsection the description of this model is presented.

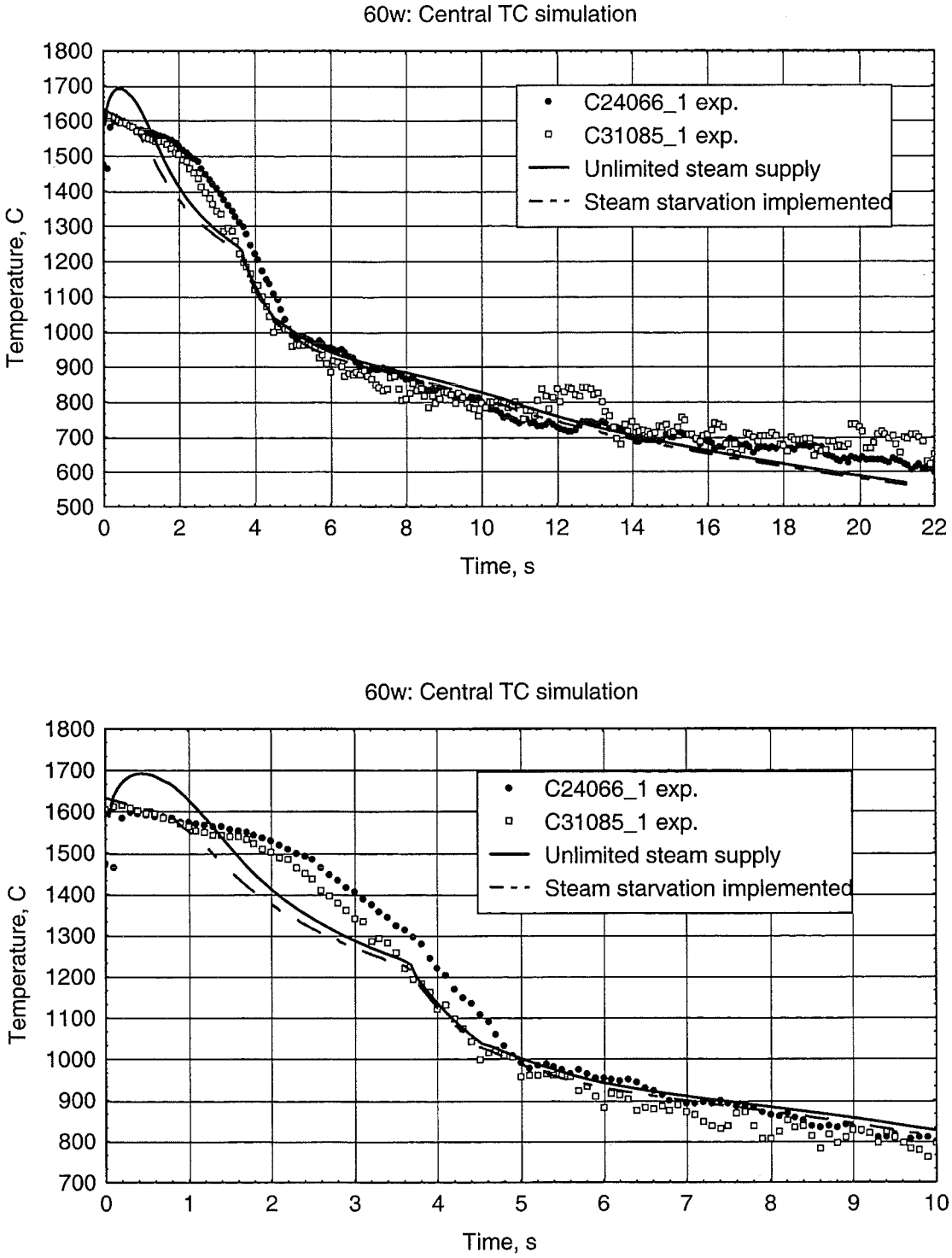

Figure 3.63: Effect of the steam starvation on the temperature evolution of the rod surface in the 60w type experiments (1600 °C initial temperature, 0 μm pre-oxidation, water quenching). Central TC. Solid line – steam starvation is not accounted for (unlimited steam supply), dashed line – steam starvation is accounted for.

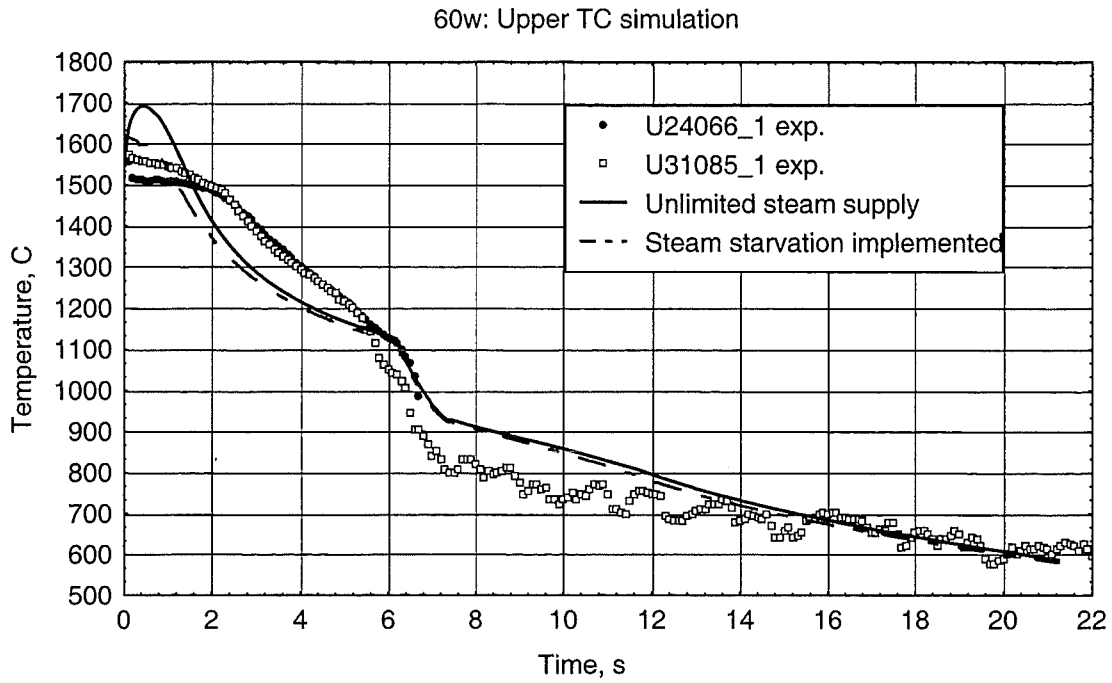

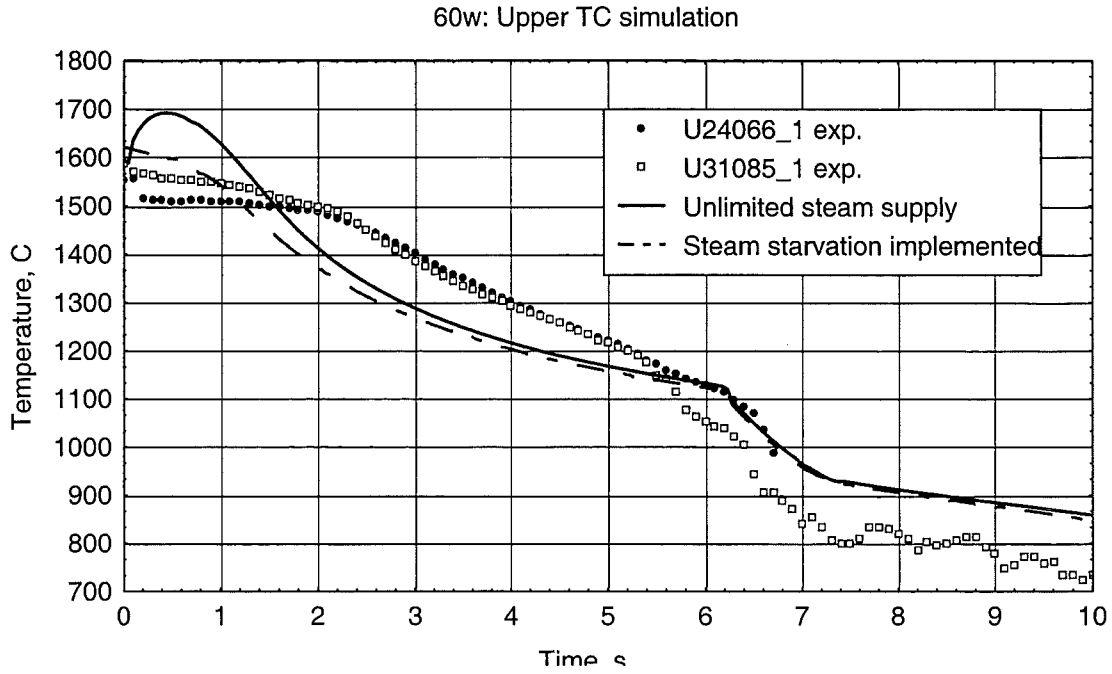

Figure 3.64: Effect of the steam starvation on the temperature evolution of the rod surface in the 60w type experiments (1600 °C initial temperature, 0 μm pre-oxidation, water quenching). Upper TC. Solid line – steam starvation is not accounted for (unlimited steam supply), dashed line – steam starvation is accounted for.

3.1.3.2 Steam starvation model

Steam mass transport in the bulk gas flow

The described model was proposed by D.R.Olander [19]. Because of the oxygen absorption by the cladding, the steam mole fraction in the gas at the surface of the cladding is smaller than that in the bulk gas. The oxygen uptake rate by the solid depends on the steam flow through the external gas phase boundary layer on the cladding surface.

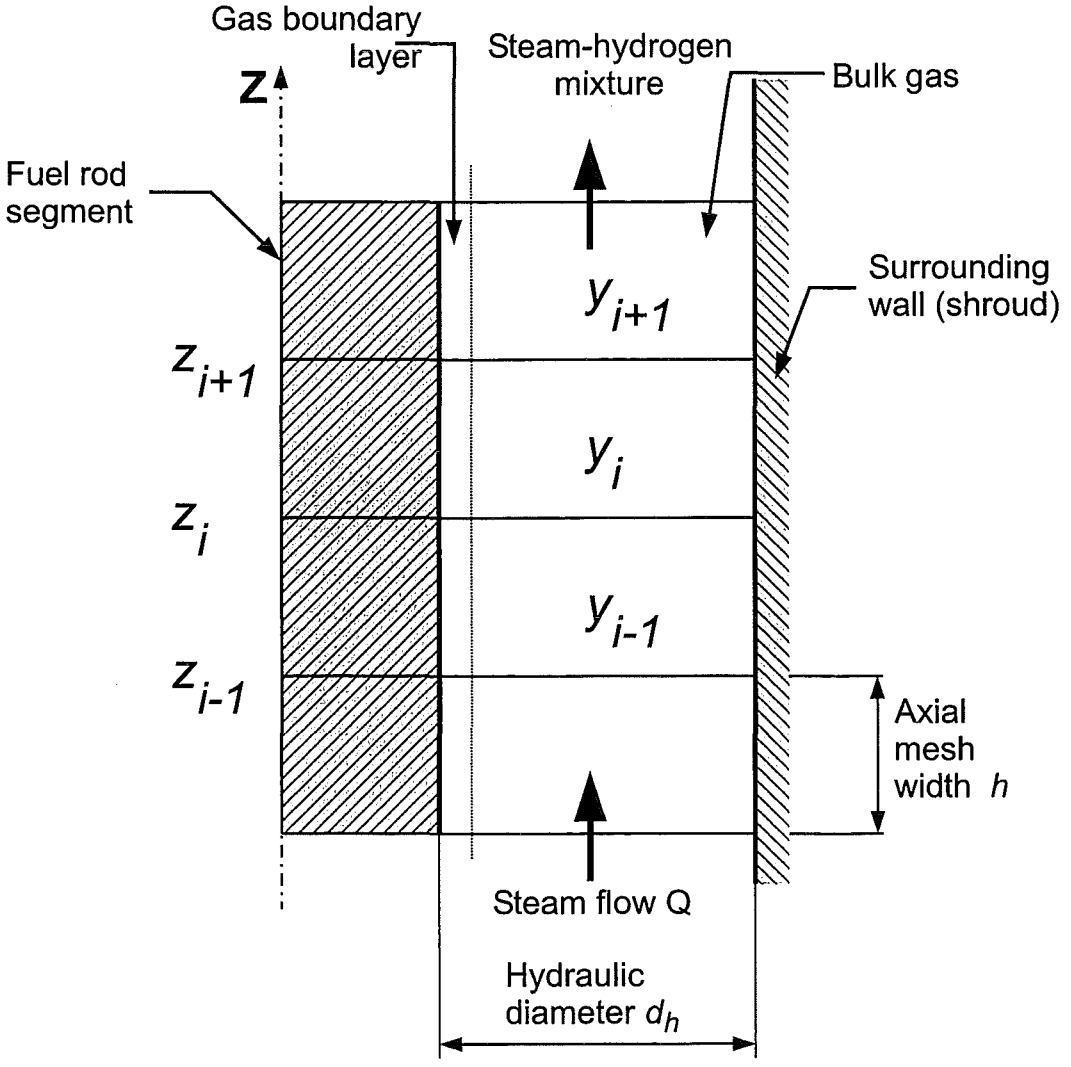

Figure 3.65: Nodalization of the fuel rod and its associated gas phase.

The oxygen-zirconium ratio in the solid at the surface is related to the steam-hydrogen ratio in the adjacent gas by the thermochemistry of the oxygen-zirconium system.

Figure 3.65 shows the segments into which a fuel rod of some length and its associated gas

phase are axially divided. Pure steam enters the first node at a specified constant molar flow rate and proceeds upwards, becoming converted to hydrogen as it rises. Because of the feed of nearly pure steam to the bottom of the fuel rod, the lowest segments may be much more oxidized in comparison with the upper of the fuel rod, where the gas may be sufficiently starved of steam.

The molar steam balance in the gas flow is given by equation

$$\frac{\partial \rho_s}{\partial t} + v\frac{\partial \rho_s}{\partial z} = -f_s, \tag{3.3}$$

where $\rho(z,t)$ is the molar density of the steam, the steam velocity is denoted by v, $f_s(z,t)$ is the molar steam discharge power due to oxygen absorption by the solid. The molar density of the gas depends on the total pressure and gas temperature T_g:

$$\rho_g = \frac{p_{tot}}{RT_g} = Const, \rho_g = \rho_s + \rho_h, \tag{3.4}$$

ρ_h – molar density of hydrogen. The initial steam velocity can be determined from the total gas molar flow rate:

$$v = \frac{Q}{S_g \rho_g}, \tag{3.5}$$

where Q is the initial molar steam flow rate, and S_g is the flow cross-section area. Using the value of steam mole fraction in the bulk gas

$$y(z,t) = \frac{\rho_s(z,t)}{\rho_g}, \tag{3.6}$$

the equation for steam molar density (3.3) may by converted into the equation

$$\frac{\partial y}{\partial t} + v\frac{\partial y}{\partial z} = -\frac{f_s}{\rho_g}. \tag{3.7}$$

For the axial spatial mesh shown on the figure z_i, $(i = 1, N)$, a finite difference approximation for equation (3.7) may be written in the form

$$\frac{1}{\Delta t}\left(y_i^{(n+1)} - y_i^{(n)}\right) = -\frac{v}{h}\left(y_i^{(n+1)} - y_{i-1}^{(n+1)}\right) - f_i^{(n)}, \tag{3.8}$$

where Δt is the time step and h – spatial mesh width. Boundary and initial conditions for the mole fraction of steam in the mesh nodes are:

$$y_1^{(n+1)} = 1, (n = 0, 1, \ldots); \; y_i^{(0)} = 1, (i = 1, N). \tag{3.9}$$

Gas phase boundary layer mass transfer

The molar water flux density through the gas boundary layer is given by

$$q_s = k_g \rho_g (y - y_b), \tag{3.10}$$

where k_g is the mass transfer coefficient, y – the steam mole fraction in the bulk gas and y_b is the steam mole fraction in the gas at the cladding surface. This gas phase transport equation describes equimolar counterdiffusion, since one mole of water decomposed at the surface produces one mole of hydrogen that returns to the bulk gas. Hydrogen absorption by the solid has been neglected.

The temperature and gas composition at the surface determines the oxygen-zirconium ratio at the solid/gas boundary. This function shows that the deviation from the exact stoichiometry takes place only after a many orders of magnitude decrease in the water mole fraction. This behavior permits the replacement of the continuous thermodynamic boundary conditions by simpler, discontinuous conditions. As long as there is even a small concentration of water vapor in the gas at the cladding surface, the oxide is very close to exact stoichiometry. And if oxide is not stoichiometric, the concentration of steam in the gas at the surface is supposed to be equal to zero. In accordance with this assumption the maximum value of the boundary molar oxygen flux density depends on the steam mole fraction in the bulk gas:

$$q_s^{(max)} = k_g \rho_g y. \tag{3.11}$$

The value $q_s^{(max)}$ is the upper limit of molar oxygen supply into the solid. It is used as boundary oxygen flow density for the oxidation kinetics calculation in the conditions of steam starvation.

The gas phase mass transfer at the outer cladding surface is estimated using the analogy between heat and mass transfer. The mass transfer coefficient in the steam-hydrogen mixture is

$$k_g = 3.7\frac{D_g}{d_h}, \text{ if } Re \leq 2000, \tag{3.12}$$

$$k_g = 0.023 Pr^{0.4} Re^{0.8}\frac{D_g}{d_h}, \text{ if } Re > 2000, \tag{3.13}$$

where d_h is the hydraulic diameter of the flow channel associated with the single fuel rod, D_g is the binary diffusion coefficient in steam-hydrogen mixtures, Pr – gas Prandtl number, Re – gas Reynolds number. The diffusion coefficient is given by

$$D_g = 10.3\left(\frac{T_g}{273}\right)^{1.68}\frac{1}{p_{tot}}. \tag{3.14}$$

3.2 Analysis of failure modes and mechanisms of the quenched specimens

The results of the integral CORA-13 experiments with water injection (quenching) show that the highest temperatures in the bundle were reached during reflooding. In the reflooding

stage of experiments up to 80 % of the generated hydrogen was produced. Temperature and hydrogen release escalation are the results of intensive oxidation in a steam atmosphere of the new Zircaloy metallic surfaces induced by the fuel cladding cracking and fragmentation. This specific deformation behavior of the fuel cladding is the result of stresses generated by a thermal shock in the oxygen-embrittled material.

The objectives of the present study are to clarify the possible reasons and criteria of the rod specimens failure under quenching conditions on the experimental data of the FZK separate-effects quench tests and to evaluate the influence of deformation behavior on oxidation kinetics and hydrogen release.

3.2.1 Qualitative consideration of experimental data

The available FZK quench experimental data were analyzed to obtain information concerning crack morphology, the extent of inner surface and crack oxidation, etc. In these tests the specimens were pre-oxidized in an oxygen-argon mixture and then quenched by water or steam. The results of this treatment are presented in [20]. The experimental results of these tests and their analysis are also presented in [14].

The results concerning hydrogen generation and storage were corrected in [14] and the new results of total hydrogen generation are presented in Tables 3.1 and 3.2. Hydrogen generation is believed to be a result of Zircaloy oxidation and characterizes the total amount of the oxidized material. The total hydrogen generation is a sum of the amount of hydrogen released in gaseous form and the amount of hydrogen dissolved in a specimen. Hydrogen in gaseous form was determined by two methods. A Caldos device determined the hydrogen concentration of the outlet gas by measurement of the electrical conductivity of the argon-hydrogen mixture. The outlet gas was also sampled at a predetermined rate for mass spectrometer measurements. The hydrogen concentration of one sample of each specimen was determined by the extraction method in the post-test examinations and it was assumed that the measured hydrogen concentration is the average hydrogen concentration of the specimen. Owing to unknown uncertainties of this procedure, the final results should be considered as semi-quantitative information [14]. Nevertheless, the analysis of these data is thought to be very useful to evaluate an influence of deformation behavior on the oxidation kinetics under quench conditions.

Consideration of the experimental data results in the following conclusions concerning the deformation behavior and oxidation during quenching:

- In the case of highly pre-oxidized specimens (300 μm) and initial quench temperatures ≤ 1400°C, with through-wall cracks generated in the initial stage of quenching provide the steam access to the inner cladding surface and surfaces of the cracks in metallic layers. The total hydrogen generation is comparable with values measured in the corresponding experiments with non-preoxidized specimens. The main reason of through-wall crack generation at these temperatures is the oxide phase transition from the tetragonal to the monoclinic phase.

- In the cases of intermediate pre-oxidation (100 μm) and initial temperatures ≤ 1400°C, the ductile β phase (thickness of β layer with ≤ 0.9 wt% oxygen is greater than 0.1 mm) prevents the penetration of the cracks generated in the brittle α phase during oxide phase transition, through the whole wall thickness (in accordance with criterion proposed in [21], [22]). Hence, the inner surface is not oxidized and the hydrogen generation is much smaller.

Initial oxide thickness, μm	Initial temperature, °C		
	1200	1400	1600
0	9.70	16.08	50.95
100	1.90	4.15	24.10
300	7.60	9.90	14.3

Table 3.1: Total hydrogen generation during quenching by water (mg).

Initial oxide thickness, μm	Initial temperature, °C		
	1200	1400	1600
0	12.51	19.00	44.48
100	0.88	5.54	17.87
300	15.56	19.77	7.42

Table 3.2: Total hydrogen generation during cooldown by steam (mg).

- For the case of steam-quenched specimens additional crack-induced oxidation is observed only on the crack metal surfaces, while for the case of quenching by water, crack surface oxidation is accompanied by oxidation of the inner cladding surface. This can be explained by small opening of the cracks under steam cooling conditions with negligible axial temperature gradient when the oxide phase transition accompanied by compressive

stress generation occurs at the same moment for the whole rod. For the case of water quenching a crack occurring in the lower cold part of the rod propagates to the hot upper part where, with the lack of strong compressive stresses, the width of the crack becomes large enough for steam supply through the open crack to the inner cladding surface.

- In the case of 100 μm pre-oxidation and 1600 °C initial temperature, the exposure of the specimen at high temperature in the argon atmosphere during 2 min after pre-oxidation stage leads to significant oxygen redistribution in the cladding and influences the mechanical properties of the generated layers. This can be explained by a partial dissolution of the oxide layer by the neighboring alpha layer which causes the extension of the alpha layer and the reduction of the beta layer thickness. This process is accompanied by increase of the beta layer oxygen content, since all the oxygen transferred from the oxide layer cannot be dissolved in the extended alpha layer. A more brittle structure of the oxygenated metal can be ruptured by the stresses generated either due to the phase transition in the oxide, or to the axial temperature gradient near the quench front at a late phase of the cooldown.

- In the case of 300 μm pre-oxidation and 1600 °C initial temperature the reasons of through-wall crack initiation can be the same as for the case of 100 μm pre-oxidation, i.e. oxide phase transition or axial temperature gradient. The difference is in the absence of the ductile beta layer that can arrest the crack propagation.

- The presence of through-wall unoxidized cracks for pre-oxidation 300 μm and initial temperature 1600 °C in the tests with cooldown by steam leads to a conclusion about a possible influence of azimuthal temperature difference on crack generation in the late stage. At low temperature when the oxygen-stabilized α phase becomes more brittle, small cracks in the layer acting as a stress concentrators can be the reason of the rupture and formation of unoxidized cracks.

- The relatively high hydrogen generation and absence of the inner cladding and crack surface oxidation for the initial temperature 1600 °C and pre-oxidation 100 and 300 μm can be explained by rapid oxidation of substoichiometric oxide (formed under starvation conditions in the pure argon atmosphere during heating from pre-oxidation to initial temperature) and the appearance of the oxide cubic phase near the temperature 1500 °C, with higher oxygen diffusion coefficient.

Another set of tests were carried out for the case of pre-oxidation and cooling of the specimens

by steam with post-test examinations of the geometry and density of the through-wall cracks by stereomicroscope and the liquid penetrants for crack visualization along with standard metallography method [18]. It was found that:

- Crack density is a step function of the oxide thickness with a critical thickness near 200 μm in the case of initial temperature 1200 and 1400 °C and does not depend on steam velocity.
- For the case of oxide thickness greater than 200 μm, axial and circumferential cracks are observed.
- In the interval between 100 and 200 μm of oxide thickness, a few axial cracks are formed.
- There are no cracks if the oxide thickness is less than 100 μm.
- No inner surface oxidation, only crack surface oxidation is observed.
- Variation of the through-wall crack density along the specimen axis is considerable. It can be explained by variation of oxide thickness from the cold lower part of the rod to the hot upper part, since the crack formation is more pronounced for thicker oxide scales. Difference in oxide layer thickness along axial circumferential directions may attain a magnitude of 50–100 μm.

These observations confirm previous qualitative conclusions:

- Rupture is absent in the case of the thick ductile beta layer;
- Crack density depends on the oxide layer thickness,

and provide new features:

- Axial cracks dominate in the interval of oxide thickness between 100 and 200 μm,
- For thicker oxide scales, crack density follows a step-wise distribution function.

In the framework of the above-presented consideration these observations can be interpreted in the following way. The criterion proposed in [21], [22] predicts that a cladding which has

a part of the beta layer with $\leq 0.9\,wt\%$ oxygen content thicker than $100\,\mu m$, withstands any thermal shock including that due to quenching. This criterion is only a conservative one, hence, it does not exclude that in some cases a metal layer with a smaller width and higher oxygen content can prevent the crack propagation. However, even in the cases when cracks are formed (e.g. due to the oxide phase transition), it can be generally concluded that an existing beta layer prevents any breach opening, while in the opposite case the formation of wide breaches is quite probable.

From the data [18] the newly generated metallic surface for the case of pre-oxidation $300\,\mu m$ can be evaluated. It is easy to calculate that if the crack density is equal to $1\,mm/mm^2$, then the new metal surface open for oxidation by penetrating steam becomes approximately equal the outer cladding surface.

For the case of cooldown by steam one can find that the total amounts of hydrogen generated in the two cases of zero and $300\,\mu m$ pre-oxidation are very similar to each other at 1200 and $1400\,°C$, respectively (see Table 3.2), and oxidation of crack surfaces is observed in the pre-oxidized rods. From [18] one can find that cracks density is 0.55 and $0.35\,mm/mm^2$ for initial temperature 1200 and $1400\,°C$, respectively (tests 210271 and 040771). Hence, the maximum surface increase is close to a half of the outer surface. This result is apparently not consistent with the total hydrogen amount measurements, since from that data one expects to obtain comparable areas of the outer and newly generated surfaces.

From this consideration one can conclude that even in the case of very brittle cladding not all cracks can be distinguished by the applied visualization method [18]. Hence, the determined function of the cracks density can be of another type.

3.2.2 Modeling of Zircaloy cladding deformation behavior under quench conditions

From the above consideration the following main factors of the oxide scale cracking or the rupture (i.e. through-wall crack formation) of the oxidized Zircaloy fuel cladding under quenching conditions can be recovered:

- Phase transitions in the cladding materials ($\beta \rightarrow \alpha$ in the metal phase and tetragonal to monoclinic in the oxide) which are accompanied by sharp changes in thermal strains.

- Radial, azimuthal and axial temperature gradients which are thought to reach their maximum values near the quench front when the film boiling changes to nucleate boiling.

In order to describe numerically these and other observed features of the rod behavior under quench conditions, the mechanical deformation module QDEF of the SVECHA/QUENCH code (SQ) was applied.

3.2.2.1 The residual deformation strength of the oxide layer after cracking

In the previous version of the mechanical deformation module [14] the following assumption was made: if the tensile stresses in the oxide scale exceed the strength limit, then the oxide cracks, i.e. microcracks which do not penetrate into the metal sublayer, emerge and lead to the loss of the oxide deformation strength. If oxidation continues, then a new uncracked oxide layer appears and influences the stress state of the cladding. This simplified assumption on the loss of the deformation strength of the cracked oxide works well for the case of the cladding heatup when internal pressure plays a dominant role in the cladding deformation behavior and leads to rapid cladding rupture due to ballooning. In the case of quenching the influence of a thick oxide layer on a stress state of the cladding is more important and, hence, the residual deformation strength of the oxide after cracking should be taken into consideration. Since analytical calculation of the residual deformation strength of the cracked oxide is overcomplicated, the following approach was used: after cracking only a part of the oxide thickness is assumed to have no deformation strength:

$$t^{ox}_{def} = t^{ox}(1 - \lambda), \tag{3.15}$$

where t^{ox}_{def} is the residual thickness of the oxide with deformation strength after cracking; t^{ox} – the oxide thickness before cracking; λ – parameter, $0 \leq \lambda \leq 1$, which denotes the part of the oxide thickness without deformation strength. It is considered as a tuning parameter and its real value can be adjusted by the comparison of simulation and experimental results. It is assumed that after oxide scale cracking the stresses in the oxide relax to zero level.

Evolution of the layer thickness and stresses at elevation 75 mm of the FZK quench rig specimen with pre-oxidation 100 µm during quenching by water and from the initial temperature 1400 °C are presented in Fig. 3.66 and Fig. 3.67 (indices r, t and z denote the radial, circumferential and axial directions of the cylindrical coordinate system and indices ox, alp and bet denote the oxide, alpha and beta layers of the oxidized cladding). Initial values of the

layer thickness and the level of the stresses are the result of the pre-oxidation stage. One can see that at the moment ≈2 second the circumferential and axial stresses in oxide reach the strength limit, oxide cracks and stresses relax to zero. This occurs due to the difference in the thermal expansion coefficients of the oxide and metallic phases. After cracking of the oxide, the oxide thickness with residual deformation strength $Th_{ox,res.def}$ decreases ($\lambda = 0.1$ was used in the simulations), the uncracked thickness $Th_{ox,uncr}$ becomes equal to zero. Since at these temperatures and total oxide thickness $Th_{ox,tot}$ oxidation rate is negligible, a new uncracked oxide layer practically does not appear during subsequent time interval. The next sharp decrease of the oxide thickness with residual deformation strength appeared at ≈3 second is the result of the oxide phase transformation which leads to intensive oxide cracking due to the strong increase of the temperature deformation of the oxide [23], Fig. 3.68. After the phase transformation the oxide layer with deformation strength becomes very thin. Temperature evolution of the cladding layers in these simulations was predicted by the SQ code.

The oxide as well as other brittle materials, has different strength limits under tensile and compressive loads, hence, for the equivalent stress calculation the following expression was used:

$$\sigma_{eqv} = \sigma_1 - \Psi\sigma_3, \tag{3.16}$$

where σ_{eqv} – the equivalent stress; Ψ – the ratio of the tensile and the compressive strength limit; σ_1 and σ_3 – the first and the third principal stresses ($\sigma_1 \geq \sigma_2 \geq \sigma_3$). The oxide has to crack if the equivalent stress attains the tensile strength limit. The tensile strength limit data of the oxide are taken from [23], however, the data of the compressive strength limit are not available. It is assumed in the calculations that the absolute value of the compressive strength limit is 3 times as large as that of the tensile one.

3.2.2.2 Phase transition in the metal phase

With the lack of data on the oxygen-stabilized alpha phase density as a function of temperature, the unknown values are generated from the oxygen-free Zircaloy data under the (generally accepted) assumption that the dissolved oxygen does not change a specific volume of the material and its mass contributes to the density of the oxygen-free Zircaloy [24]. In its turn, the specific volume of the oxygen-free material is temperature dependent and determined by the thermal strains in accordance with the linear relationship (from [23]). On this basis the density of the oxygen-stabilized α phase at temperatures above the phase transition point ≈1100 K can be calculated. In order to make such a calculation, it is assumed that the thermal

strain of the stabilized α phase can be obtained by interpolation of the α phase "branch" of the thermal strain curve for oxygen-free Zircaloy (Fig. 3.68) to high temperatures. Then, calculating the specific volume of the Zr matrix and adding the mass of dissolved oxygen to the mass of this matrix, one can obtain the density of the oxygen-stabilized α phase.

To verify this assumption the following calculations were performed: the thermal strains of the α and β phases of the oxygen-free Zircaloy were taken from [23] and the α phase fraction as a function of temperature in the temperature interval of the two phase $(\alpha+\beta)$ coexistence of the oxygen-free Zircaloy were taken from [24] (see Fig. 3.69). T hen the density of $\alpha+\beta$ region was calculated using the mixture rule:

$$\rho^{\alpha+\beta}(T) = \Omega^{\alpha}\rho^{\alpha}(T) + \Omega^{\beta}\rho^{\beta}(T), \tag{3.17}$$

where $\rho^{\alpha+\beta}(T)$ – density in the $\alpha+\beta$ region; $\rho^{\alpha}(T), \rho^{\beta}(T)$ – densities of the α and β phases, correspondingly, interpolated to the $(\alpha+\beta)$ temperature region; $\Omega^{\alpha}, \Omega^{\beta}$ – weight fraction of the α and β phases, correspondingly. Comparison of the calculated and experimental data is presented in Fig. 3.70, which demonstrates a satisfactory agreement between these data. Thus, it indirectly confirms the above-accepted assumption.

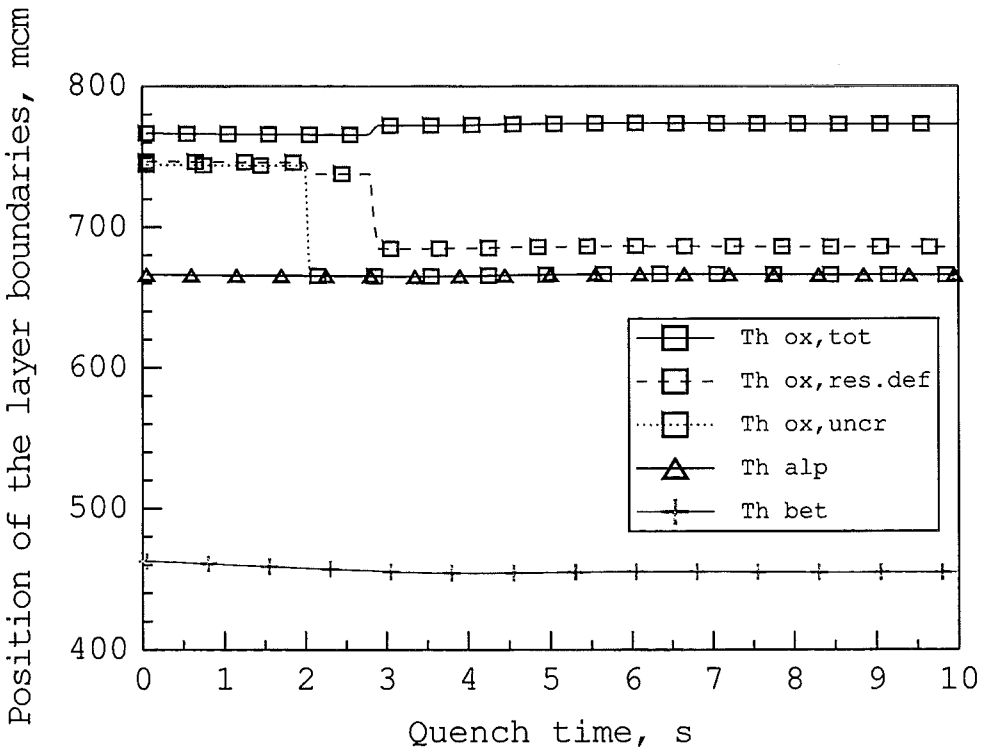

Figure 3.66: Simulation of the layer thickness evolution during water quenching. $T_0 = 1400\,°C$. 100 μm pre-oxidation. Location 75 mm.

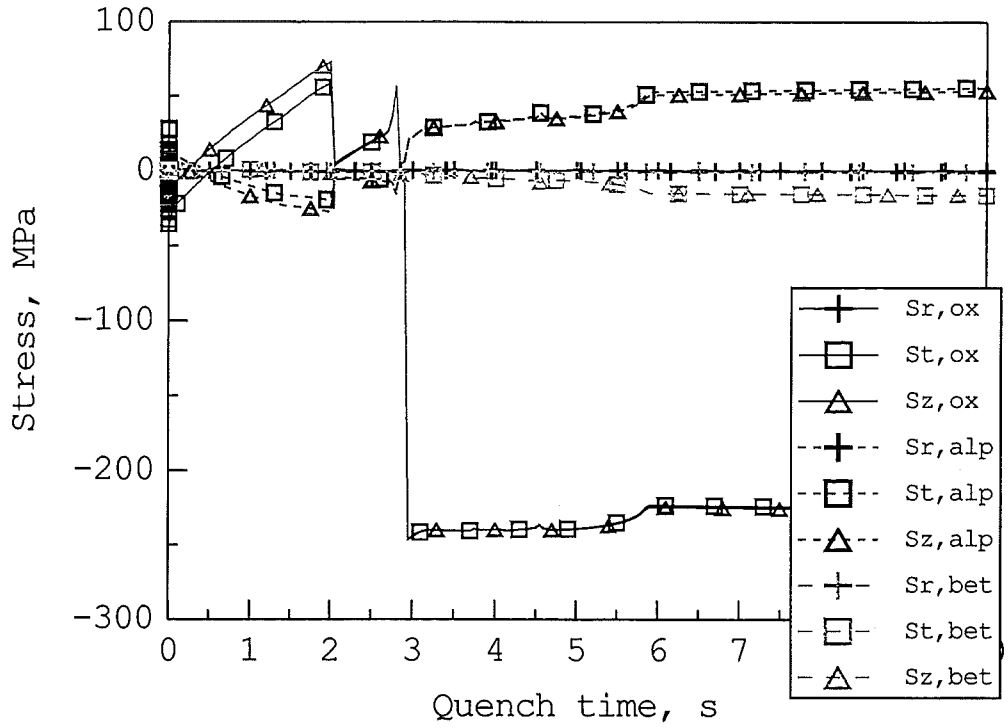

Figure 3.67: Simulation of the stress evolution during water quenching. $T_0 = 1400\,°C$. 100 µm pre-oxidation. Location 75 mm.

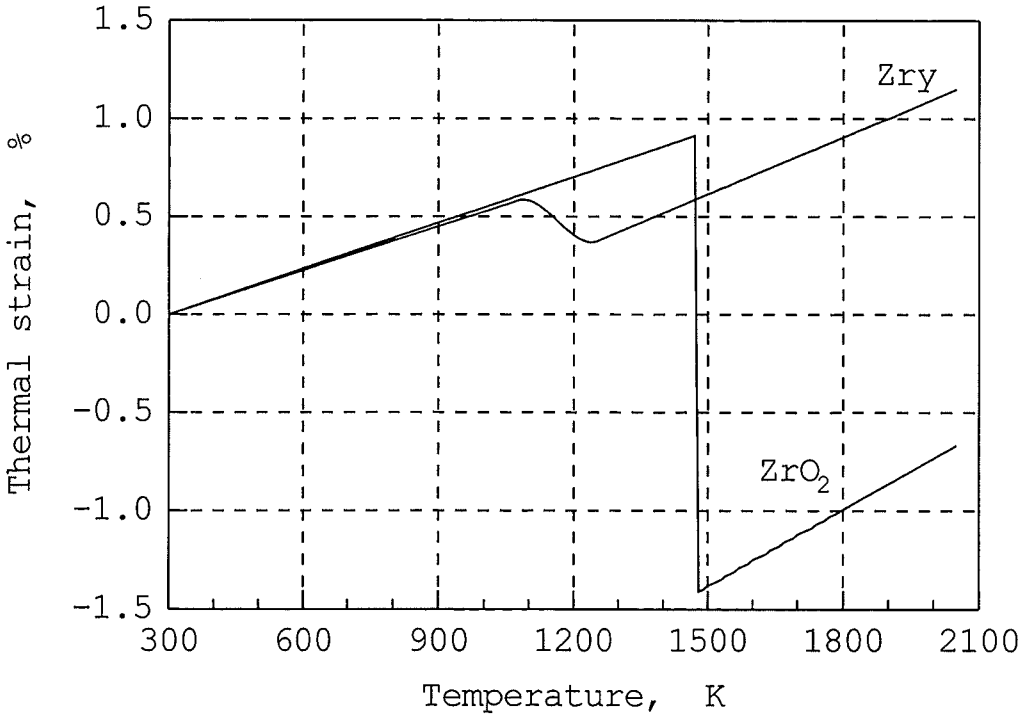

Figure 3.68: Thermal strains of oxygen-free Zircaloy and oxide as a function of temperature.

Analogously, the same approach can be applied to obtain the thermal strain of the β phase with dissolved oxygen (using the β phase "branch" of the thermal strain curve of oxygen-free Zircaloy) as well as for the mixture of the two phases. As one can see from the Zry-O equilibrium phase diagram in Fig. 3.71, the α/β phase transformation starts at different temperatures depending on oxygen content. After calculation of the phase weight fractions in the $\alpha + \beta$ region, performed by the so-called "lever rule" on the base of the phase diagram, the mixture thermal strain may be found. Thermal strain as a function of temperature is presented in Fig. 3.72 for the various oxygen contents.

The difference in the thermal strains of β and α phases can explain the presence of the cracks in the alpha layer in the case of quenching of the non-pre-oxidized specimens. In this case the oxide layer is too thin to generate high level stresses in the thick metal sublayer. Difference in the thermal strains of the metal layers leads to a high tensile stress in the alpha layer. In Figs. 3.73 and 3.74 the simulation results of quenching by water from the initial temperature 1400 °C of the non-oxidized specimens (in the FZK quench rig) are presented. One can see the influence of the beta layer thermal strain on the stress state of the alpha and oxide layers, and the high tensile circumferential and axial stresses generated in the alpha layer.

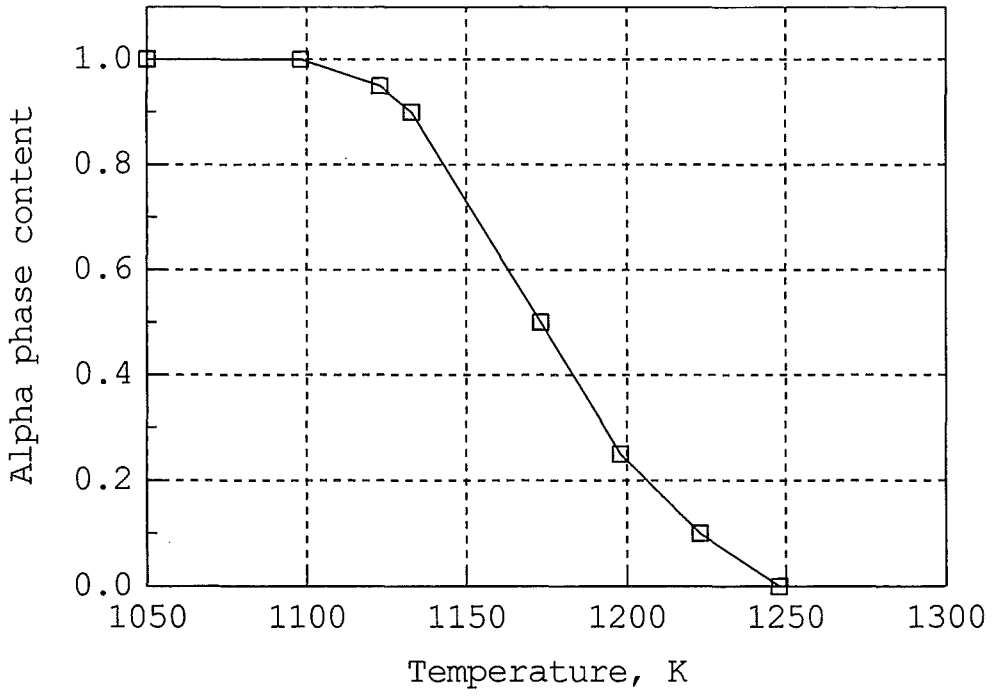

Figure 3.69: Alpha phase fraction in the oxygen-free Zircaloy as a function of temperature.

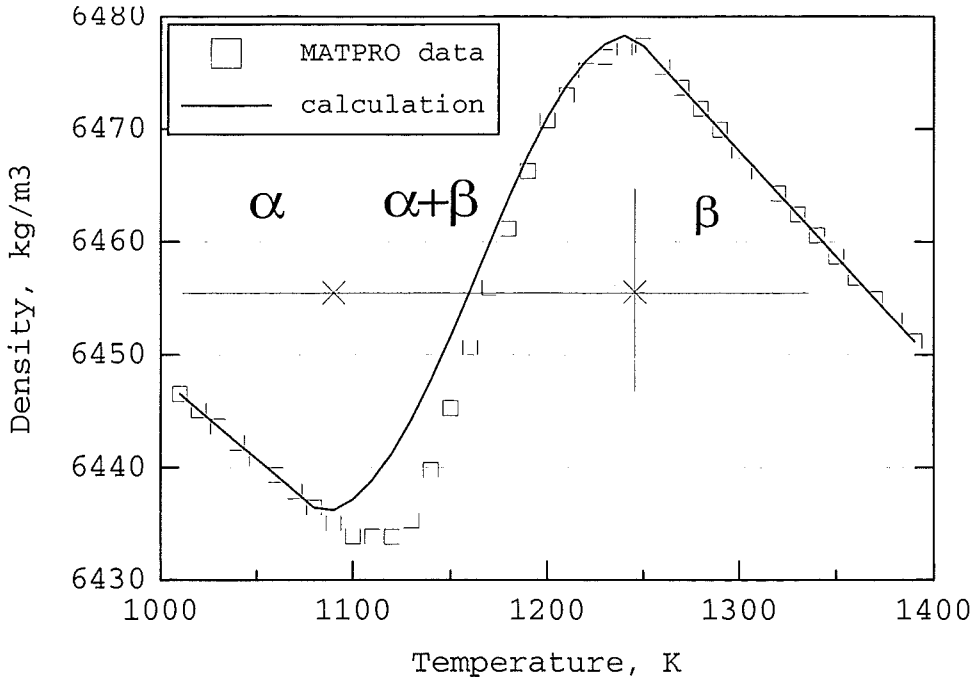

Figure 3.70: Comparison of the experimental data of oxygen-free Zircaloy density with calculation results.

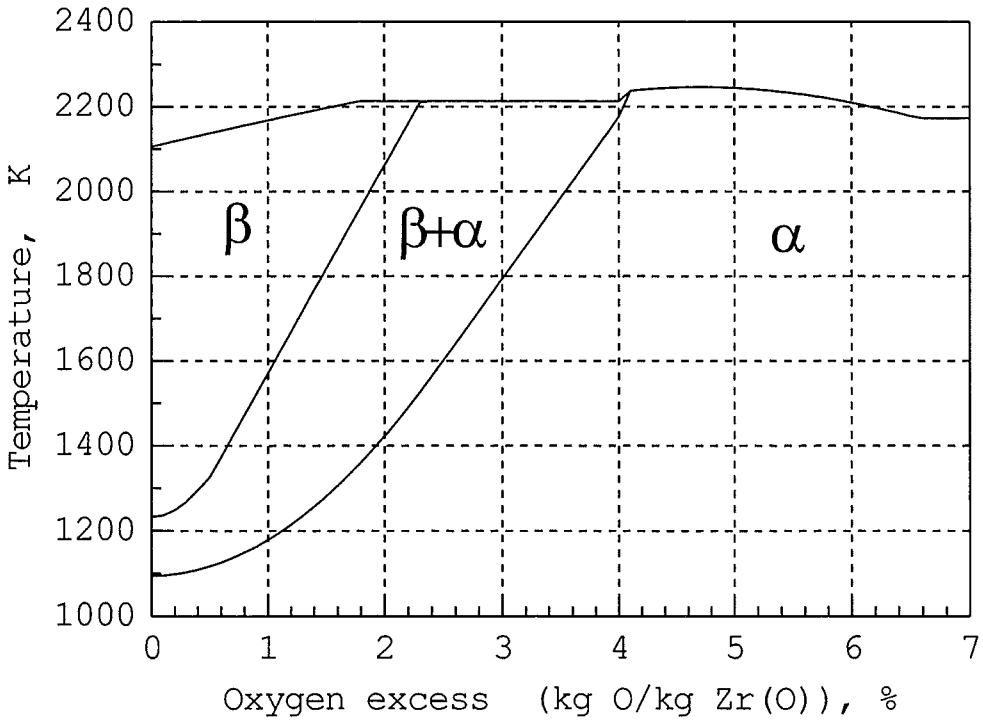

Figure 3.71: Part of the simplified equilibrium pseudo-binary Zry-O phase diagram.

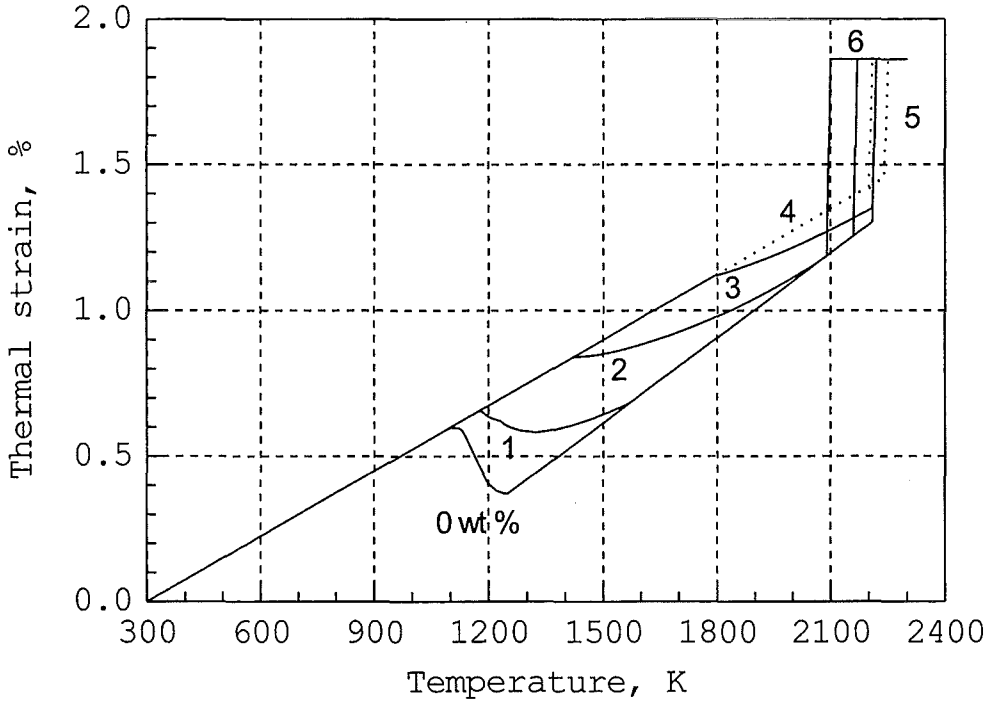

Figure 3.72: The thermal strain of the Zircaloy metal phases as a function of temperature and oxygen content.

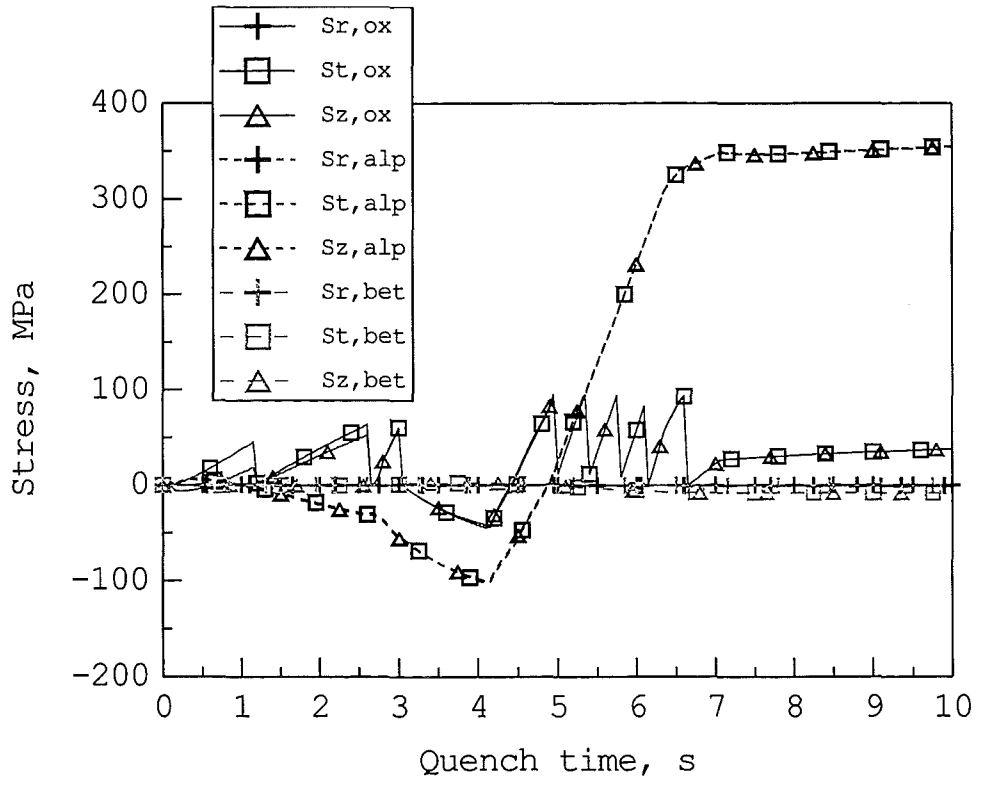

Figure 3.73: Simulation of the stress evolution during water quenching. $T_0 = 1400\,°C$. No pre-oxidation. Location 75 mm.

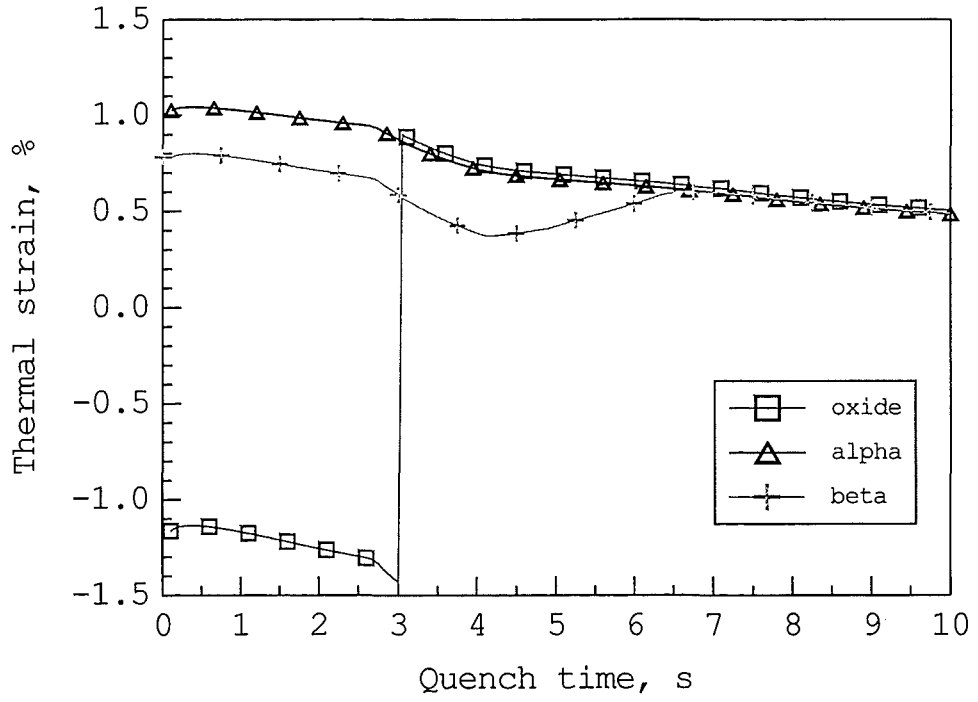

Figure 3.74: Simulation of thermal strain evolution during water quenching. T_0 = 1400 °C. No pre-oxidation. Location 75 mm.

3.2.2.3 Phase transition in the oxide

The real oxide scale is nonstoichiometric and the average oxygen content can vary with the pre-oxidation history, influencing the deformation behavior under quench conditions. From the consideration of the FZK quench data one can see that in the tests performed at the initial temperature 1000 °C, the surfaces of the specimens were free from the visually observed macrocracks.

It is known [23] that the tetragonal to monoclinic phase transformation in the stoichiometric oxide occurs at the temperature ≈1200 °C. One can see from Fig. 3.75 that the lower oxide oxygen content the lower is the temperature of the phase transition. Phase transition of the nonstoichiometric oxide is smoother and, hence, the stresses induced in the metal layers by the phase transformation have enough time to relax by plastic deformation in the metal layers and/or by the oxide cracking. Significant decrease of the average oxygen concentration may be connected with the test procedure, since the cooling (or heating) of the pre-oxidized specimen from the oxidation temperature 1400 °C to the quench starting temperature occurred in the argon atmosphere, i. e. under oxygen-starved conditions, that leads to the average oxygen

concentration decrease.

To calculate the thermal strain of the nonstoichiometric oxide, an approach similar to the one for the metal phase transformation description, was used, i.e. the thermal strain of the stoichiometric oxide was found from [23], then on the basis of the simplified Zry-O phase diagram (Fig. 3.75) the weight fractions of the tetragonal and monoclinic phases were calculated at the given oxygen content and finally the mixture rule was applied to obtain the thermal strain as a function of temperature. It was assumed that the oxide specific volume does not strongly depend on oxygen content. Calculated by the present approach thermal strain as a function of temperature is presented in Fig. 3.76 for the various oxygen contents.

The results of simulation of the oxidized cladding thermal strains for the case of 100 μm preoxidation and quenching from initial temperature of 1400 °C are shown in Fig. 3.77. From this figure it is seen that the stresses (see Fig. 3.78) are generated in the cladding layers due to the oxide phase transformation from the tetragonal to monoclinic phase. When stresses in the oxide scale attain the limit value, cracking occurs and stresses drop to zero level. In general, the high level stresses relax by plastic deformations of the alpha layer, or by the oxide layer cracking, or by the oxide exfoliation from the alpha sublayer. To evaluate stress level during this process, a special procedure is used. Let us assume that the oxide cannot crack under any stresses after the beginning of the transformation (≈3 s, see Fig. 3.77). From Fig. 3.78 one can see that under such assumption stresses reach very high level. The trend of the stress increase in the alpha and oxide layers determines where the strength limit will be attained initially. If the stresses reach the strength limit in the oxide, then the oxide microcracking is thought to occur. In the opposite case the alpha layer cracks and, if beta layer can not arrest the cracking propagation then cracks penetrate through the metal and the bending moments induced in the remaining oxide scale lead to through-wall crack formation. In the considered example (1400 °C, 100 μm) the thickness of oxygen-depleted beta layer is quite enough to prevent formation of the through-wall cracks.

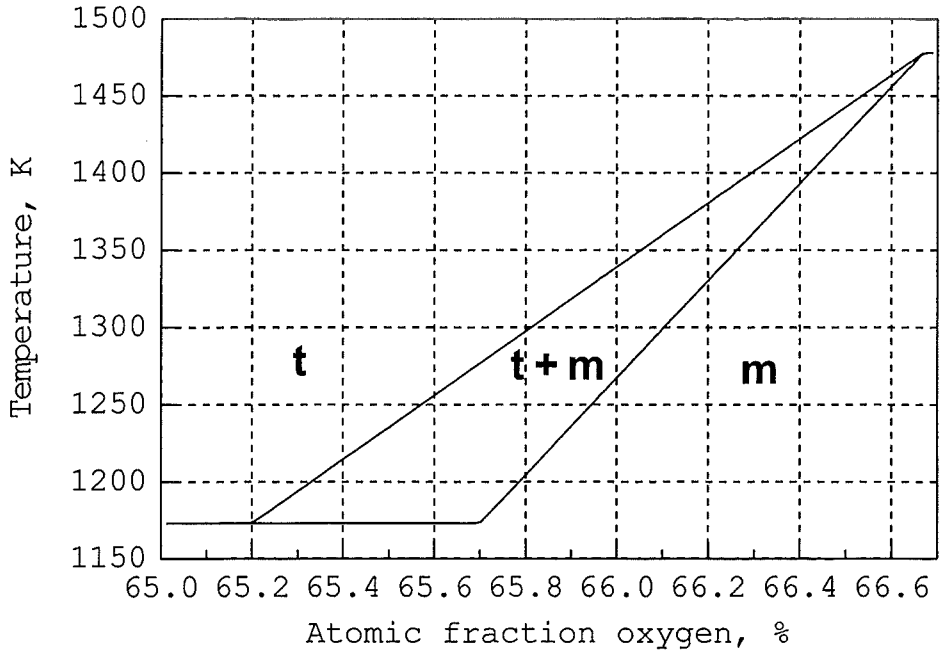

Figure 3.75: Part of simplified pseudobinary Zry-O phase diagram.

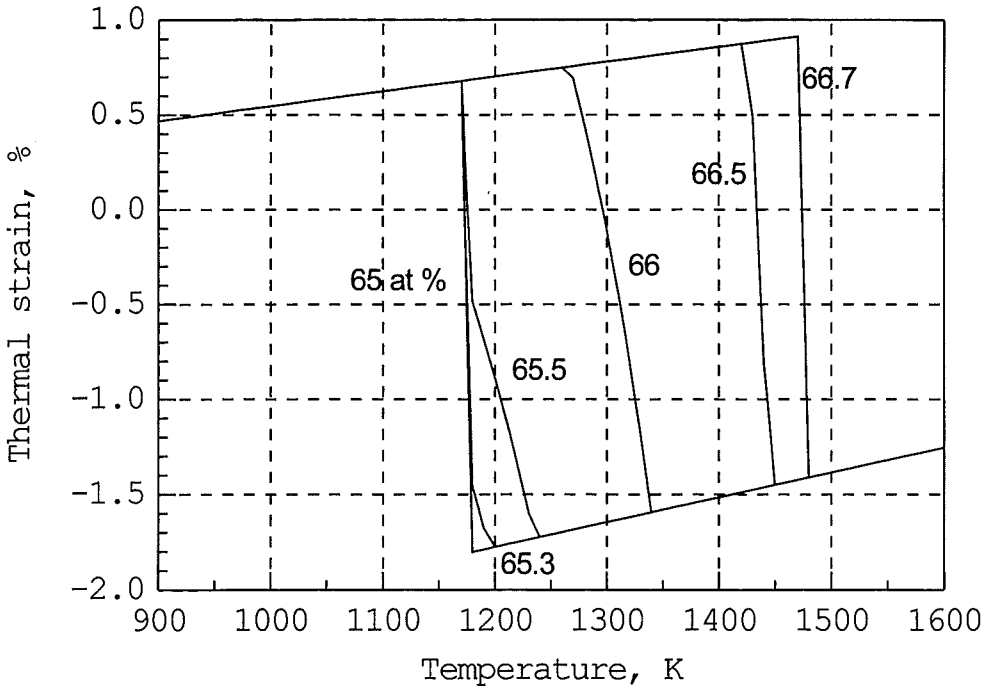

Figure 3.76: The oxide thermal strain as a function of temperature and oxygen content.

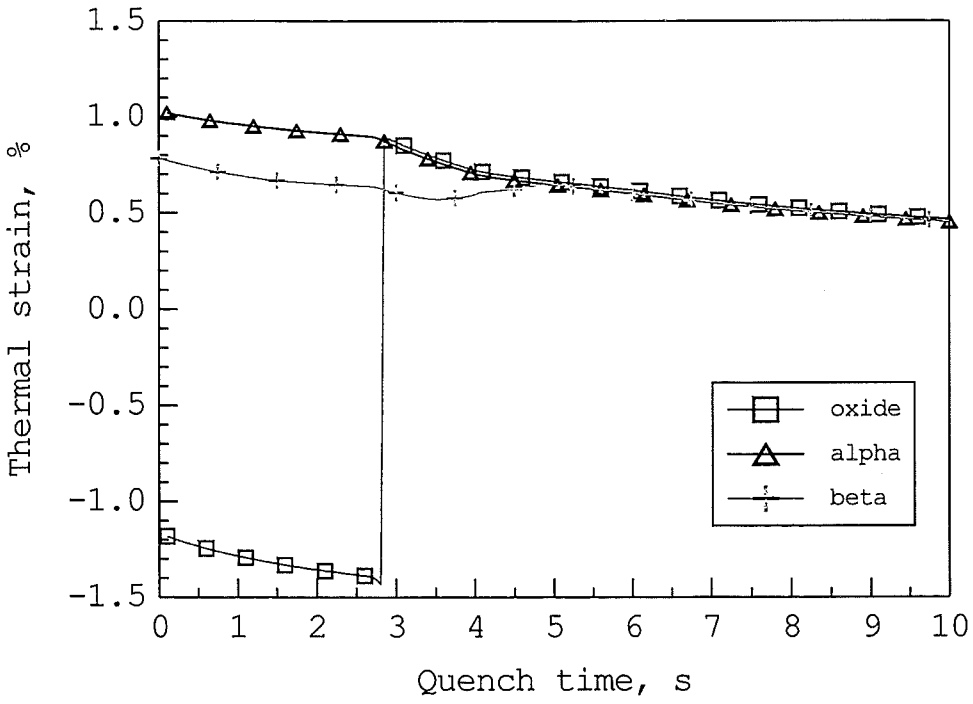

Figure 3.77: Simulation of the thermal strain evolution during water quenching. $T_0 = 1400\,°C$. 100 µm pre-oxidation. Location 75 mm.

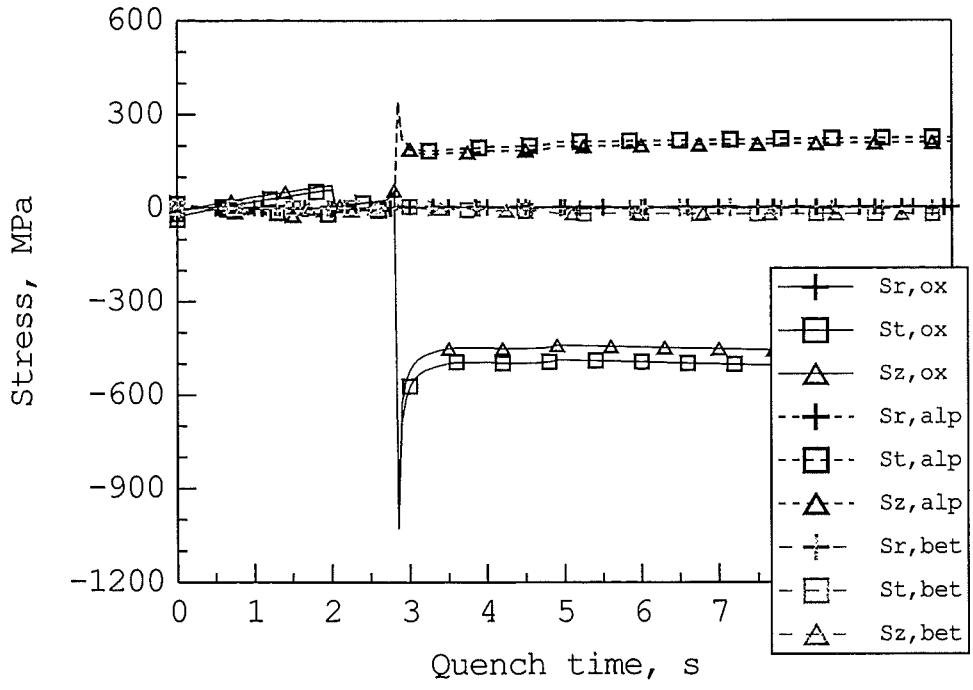

Figure 3.78: Simulation of the stress evolution during water quenching. Oxide cannot crack after beginning of the oxide phase transformation. $T_0 = 1400\,°C$. 100 µm pre-oxidation. Location 75 mm.

3.2.2.4 Radial temperature gradient

From the calculations of the radial temperature distribution by the SQ code it was found that radial temperature gradients in the metal layers are negligible and the radial temperature distribution in the external oxide layer may be approximated by a linear function. Due to the small ratio of oxide thickness to the average oxide radius, the influence of the cylindrical geometry becomes negligible and the average oxide temperature T^{ox} can be determined as the average of the external T^{ox}_{ext} and internal T^{ox}_{int} surface temperatures:

$$T^{ox} = \frac{T^{ox}_{ext} + T^{ox}_{int}}{2}. \tag{3.18}$$

The temperature of the internal oxide surface is assumed to be equal to the average temperature of the alpha layer, due to the small radial gradients in the metal layers. Hence, the temperature drop in the oxide scale can be calculated as:

$$\Delta T^{ox} = T^{ox}_{int} - T^{ox}_{ext} = 2(T^{\alpha} - T^{ox}). \tag{3.19}$$

Thus, the radial oxide temperature drop can be determined with the help of the input values of the average temperatures of the oxide and alpha layers. Under the assumption of a thin oxide layer the following expression of linear elasticity theory for the surface circumferential and axial stresses caused by the radial temperature drop can be applied [25]:

$$\begin{aligned} \sigma^{ox}_{\theta}(r^{ox}_e) = \sigma^{ox}_z(r^{ox}_e) &= \frac{E^{ox}\alpha^{ox}\Delta T^{ox}}{2(1-\nu^{ox})}, \\ \sigma^{ox}_{\theta}(r^{ox}_i) = \sigma^{ox}_z(r^{ox}_i) &= \frac{E^{ox}\alpha^{ox}\Delta T^{ox}}{2(1-\nu^{ox})}, \\ \sigma^{ox}_r(r^{ox}_i) = \sigma^{ox}_r(r^{ox}_e) &= 0, \end{aligned} \tag{3.20}$$

where σ^{ox}_r, σ^{ox}_{θ}, σ^{ox}_z – the radial, circumferential and axial stresses in the cylindrical coordinate system; r^{ox}_i, r^{ox}_e – the internal and external oxide scale radii; E^{ox}, ν^{ox} – Young's modulus and Poisson's ratio of the oxide at the average temperature T^{ox}.

To provide the given temperature drop ΔT^{ox}, Eq. 3.19, for the oxide scale with uniform temperature distribution T^{ox}, the external surface should be cooled and the internal surface should be heated. The temperature increment is $\Delta T^{ox}/2$. If the initial state is free from stress then the linear stress distribution with the boundary stresses Eq. 3.20 will be induced due to the temperature drop. The oxide strain at the internal oxide boundary will be the following:

$$\epsilon^{ox}_{\theta} = \frac{1}{E^{ox}}(\sigma^{ox}_{\theta} - \nu(\sigma^{ox}_r + \sigma^{ox}_z)) + \frac{\alpha^{ox}\Delta T^{ox}}{2}, \tag{3.21}$$

where ϵ_θ^{ox} – the circumferential oxide strain in the cylindrical coordinate system. Substitution of Eq. 3.20 into Eq. 3.21 gives:

$$\epsilon_\theta^{ox} = \frac{1}{E^{ox}}\left(-\frac{E^{ox}\alpha^{ox}\Delta T^{ox}}{2(1-\nu^{ox})} + \nu^{ox}\frac{E^{ox}\alpha^{ox}\Delta T^{ox}}{2(1-\nu^{ox})}\right) + \frac{\alpha^{ox}\Delta T^{ox}}{2} = 0. \qquad (3.22)$$

The same calculation gives zero axial strain. Thus, the linear temperature distribution in the oxide layer does not generate the stresses in the metal sublayers and the stresses in the oxide layer can be calculated as superposition of the oxide stresses due to average temperatures of all the cladding layers (this situation is treated by the previously developed deformation module QDEF [14]) and the stresses due to linear temperature distribution, Eq. 3.20 in the stand-alone oxide shell.

If the tensile stress on the external surface exceeds the oxide strength limit, then microcracks are thought to be formed. If the tensile stress acts in the whole oxide layer, then the microcracks penetrate through the oxide scale up to the alpha layer and then stopped by compressive stress in the alpha layer. If the compressive stresses are induced in the part of oxide layer, then the microcracks penetrate up to the radial location of this compressive stress. The calculation results of the oxide stresses (average and surface stresses) due to radial temperature gradient during quenching (1400 °C, 100 μm) are presented in Figs. 3.79 and 3.80. Temperature evolution is the result of simulation by the SQ code. Oxide cracks when circumferential stress on the external surface exceeds the strength limit. The decrease of the surface stress amplitude is induced by intensive oxide cracking due to oxide phase transition.

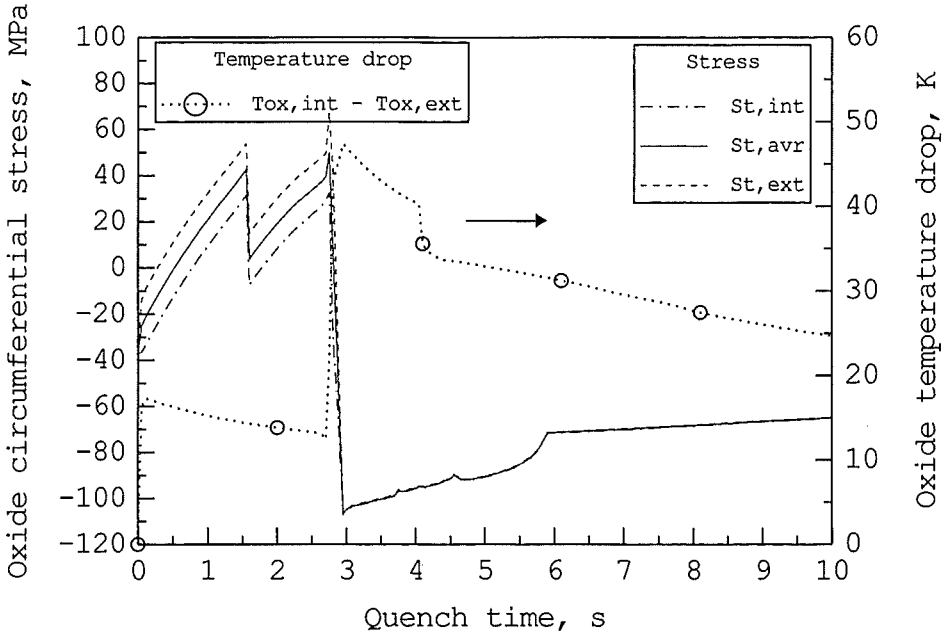

Figure 3.79: Simulation of the average, external and internal surface circumferential stresses in the oxide layer, and the oxide temperature drop (difference between temperature on the internal and external surfaces) evolution during water quenching. T_0 = 1400 °C. 100 µm pre-oxidation. Location 75 mm.

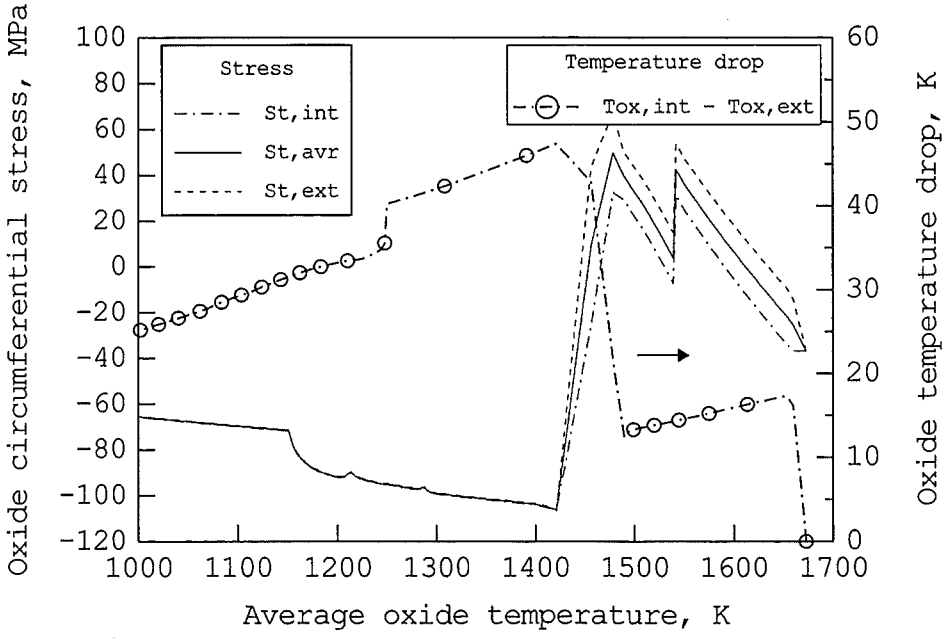

Figure 3.80: Simulation of the average, external and internal surface circumferential stresses in the oxide layer, and the oxide temperature drop (difference between temperature on the internal and external surfaces) evolution during water quenching. T_0 = 1400 °C. 100 µm pre-oxidation. Location 75 mm.

3.2.2.5 Azimuthal temperature gradient

The observation of unoxidized through-wall cracks in the set of the FZK quench tests leads to the conclusion that formation of these cracks occurs at low temperature when oxidation is not intensive, i.e. at temperatures ≤ 1100 K. Since the radial temperature gradient cannot lead to crack initiation, the possible reason of crack formation are azimuthal or axial temperature gradients. Let us consider the azimuthal temperature gradient influence on the stress state of the oxidized cladding.

Let us assume that the deformation strength of the alpha layer has a dominant influence on the deformation behavior of the highly oxidized cladding (i.e. in the case of pre-oxidation greater than 100 μm, since lower pre-oxidation does not lead to formation of through-wall cracks due to thick layer of a metal phase with low oxygen content). This assumption is confirmed by preliminary simulations of deformation under quench conditions. The simulation results (see, for example, Figs. 3.66 and 3.67) show that the deformation strength of the oxide layer decreases due to cracking in the preceding high temperature stage of the quenching, when the phase transition in the oxide takes place. For the case of the beta layer (if it exists) the deformation strength decreases, due to high plastic strains, however, in the alpha layer the plastic strains is highly decreased by the dissolved oxygen [26]. Hence, the brittle alpha layer at low temperatures can be treated as a separate cylinder from the elastic material. In this case the solution for the stress determination under "flowering" conditions can be applied [27]. The main term in the expression for the maximum tensile stress in the layer due to azimuthal temperature difference is given by:

$$\sigma_\theta^\alpha = \alpha^a \Delta T_\theta^\alpha E^\alpha \frac{t^\alpha}{4R^\alpha}, \tag{3.23}$$

where ΔT_θ^α – the azimuthal temperature difference; t^α, R^α, – the thickness and the middle radius of the alpha layer. The results of maximum tensile stress calculation with the help of this dependence for the case of the alpha layer thickness 200 μm (corresponding to 100 μm pre-oxidation) for various azimuthal temperature differences are presented in Fig. 3.81. One can conclude from the presented results that the azimuthal temperature difference cannot lead to cracking of the alpha phase and, hence, the observed through-wall cracks were formed in the low temperature stage of the quenching.

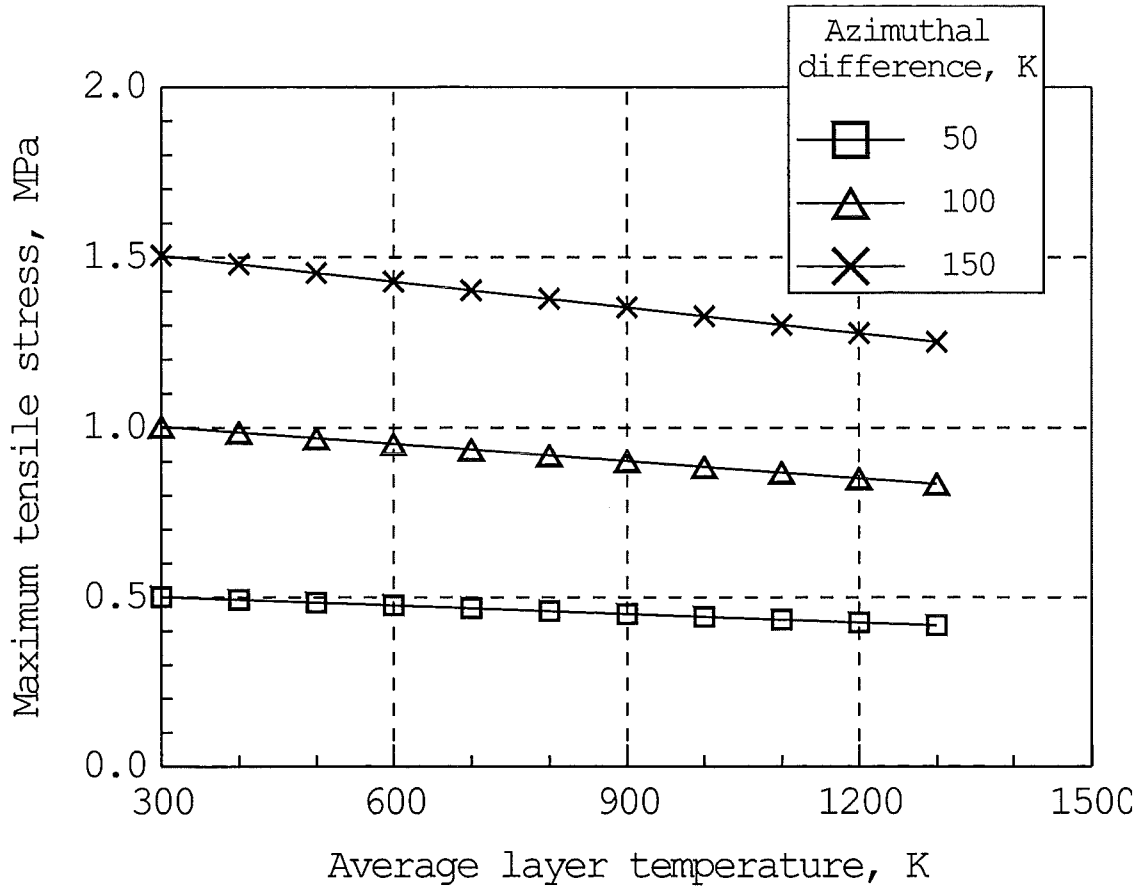

Figure 3.81: Maximum tensile stress in the alpha layer as a result of azimuthal temperature difference.

3.2.2.6 Axial temperature gradient

From the above consideration of the influence of the radial and azimuthal temperature gradients on the stress state of the highly oxidized Zircaloy cladding one can deduce that the axial temperature gradient is the main reason for through-wall crack formation in the late stage of quenching by water.

As for the case of azimuthal temperature distribution, a separate cylinder of the α phase will be treated. Axially symmetrical temperature distribution is assumed, this leads to the following characteristics of the stress-strain state:

$$\begin{aligned} v &= 0, \\ \tau_{r\theta} &= 0, \\ \tau_{z\theta} &= 0, \end{aligned} \tag{3.24}$$

where v is the displacement in the circumferential direction of the cylindrical coordinate system; $\tau_{r\theta}, \tau_{z\theta}$ are components the of shearing stress; all parameters hereafter are presented for the case of the alpha layer, and the index "α" is dropped. It is assumed in accordance with [25] that the influence of the radial and shearing stress on the deformation is negligible and that layer thickness change is negligible comparing with radial displacement u. The radial coordinate r of any point before deformation is given by:

$$r = R + \xi, \tag{3.25}$$

where R is the radial coordinate of the layer middle surface in the cylindrical coordinate system; ξ is the distance from the middle surface along radial direction. With the assumptions above, the displacements at any location are given by [25]:

$$\begin{aligned} u &\approx u_0, \\ w &= w_0 - \xi \frac{\partial u_0}{\partial z}, \end{aligned} \tag{3.26}$$

where u, u_0 are the radial displacement and middle plane displacements, correspondingly; w, w_0 are the axial displacement and middle plane displacement in the cylindrical coordinate system, correspondingly (positive direction of the z-axis is from the top to the bottom of the vertically-oriented sample). Due to $v = 0$, the strains are:

$$\begin{aligned} \epsilon_\theta &= \frac{u}{r} \approx \frac{u}{R}, \\ \epsilon_z &= \frac{\partial w}{\partial z} = \frac{dw_0}{dz} - \xi \frac{d^2u}{dz^2}. \end{aligned} \tag{3.27}$$

The average temperature variation with respect to the reference temperature is a function of the axial coordinate:

$$T = F(z). \tag{3.28}$$

The strains are:

$$\begin{aligned} \epsilon_\theta &= \frac{1}{E}(\sigma_\theta - \nu(\sigma_z + \sigma_r)) + \alpha F, \\ \epsilon_z &= \frac{1}{E}(\sigma_z - \nu(\sigma_r + \sigma_\theta)) + \alpha F. \end{aligned} \tag{3.29}$$

Since the radial stress is neglible, one obtains:

$$\begin{aligned} \sigma_\theta &= \frac{E}{1-\nu^2}\left(\frac{u}{R} + \nu\frac{dw_0}{dz} - \nu\xi\frac{d^2u}{dz^2}\right) - \frac{E\alpha}{1-\nu}F, \\ \sigma_z &= \frac{E}{1-\nu^2}\left(\frac{dw_0}{dz} - \xi\frac{d^2u}{dz^2} + \nu\frac{u}{R}\right) - \frac{E\alpha}{1-\nu}F. \end{aligned} \tag{3.30}$$

The integral axial force is equal to zero, hence:

$$\int_{-t/2}^{t/2} \sigma_z 2\pi R d\xi = 0. \tag{3.31}$$

After substitution of Eq. 3.30 into Eq. 3.31 and integration of the relationship obtained, the derivative dw_o/dz can be determined:

$$\frac{Et}{1-\nu^2}\left(\frac{dw_o}{dz} + \nu\frac{u}{R} - \nu F\right) = 0. \tag{3.32}$$

Using Eq. 3.32 the variable w_0 can be eliminated from Eq. 3.30:

$$\sigma_\theta = \frac{Eu}{R} - \frac{E\nu}{1-\nu^2}\xi\frac{d^2u}{dz^2} - E\alpha F,$$
$$\sigma_z = \frac{E}{1-\nu^2}\xi\frac{d^2u}{dz^2}. \tag{3.33}$$

Let us introduce the bending moments and circumferential force:

$$M_\theta = \int_{-t/2}^{t/2} \sigma_\theta \xi d\xi = -\nu D\frac{d^2u}{dz^2},$$
$$M_z = \int_{-t/2}^{t/2} \sigma_z \xi d\xi = -D\frac{d^2u}{dz^2}, \tag{3.34}$$
$$N = \int_{-t/2}^{t/2} \sigma_\theta d\xi = ET\left(\frac{u}{R} - \alpha F\right),$$

where M_θ, M_z, N are the circumferential and axial bending moments and circumferential normal force, respectively; all the values are determined per unit length; D is the cylindrical stiffness:

$$D = \frac{Et^3}{12(1-\nu^2)}. \tag{3.35}$$

For each cylinder element the following balance equations can be deduced:

$$\frac{dM_z}{dz} - Q = 0,$$
$$\frac{dQ}{dz} - \frac{N}{R} = 0, \tag{3.36}$$

where Q is the shearing stress per unit length. After substitution of Eq. 3.34 into Eq. 3.36 for the case of the cylindrical shell with constant thickness one can obtain:

$$\frac{d^4u}{dz^4} + \frac{12(1-\nu^2)}{t^2R^2}u = E\alpha\frac{t}{R}F. \tag{3.37}$$

This equation may be solved numerically using the axial grid of the heat-exchange module for the function:

$$F(z) = \frac{1}{t} \int_{R-t/2}^{R+t/2} T(r,z)dr. \tag{3.38}$$

If the stresses exceed the alpha layer material strength limit and the beta layer cannot prevent the crack propagation, then the through-wall cracks are thought to form.

Implementation of this approach to the mechanical deformation module QDEF may be especially important for long rods, when crack formation or cladding fragmentation at the lower cold end of the rod lead to steam supply to the inner surface of the upper hot end of the rod.

3.2.3 Quantitative consideration of experimental data

The deformation behavior module presented above (see subsection 3.2.2) is used to explain the specific features observed in the quench tests (see subsection 3.2.1). The results presented below are obtained by application of the SVECHA/QUENCH code. Temperature evolution is predicted by the heat-exchange module QTEM, and oxidation kinetics are simulated by the oxidation module QOXI.

3.2.3.1 Quenching of 100 μm pre-oxidized rods

Quenching by water of 100 μm pre-oxidized rods from the initial temperature $\leq$1400 °C leads to spalling of the oxide layer without oxidation of newly-formed metallic surfaces and without formation of through-wall cracks. The possibility of these rods to withstand thermal shock during quenching can be explained by the experimentally found criterion [21], [22]. This criterion can be formulated as following [22]:

"The calculated thickness of cladding with $\leq$0.9 wt% oxygen, based on the average wall thickness at any axial location, should be greater than 0.1 mm."

In Fig. 3.82 the oxygen distributions along radial direction in the beta layer for the different extents of pre-oxidation are presented. Pre-oxidation was performed at 1400 °C. One can see that the rupture criterion is valid up to pre-oxidation of $\approx$130 μm. Hence, if pre-oxidation at any location does not exceed 130 μm then the through-wall cracks are absent. This conclusion

is confirmed by experimental observations. In Table 3.3 quench tests without formation of through-wall cracks are presented.

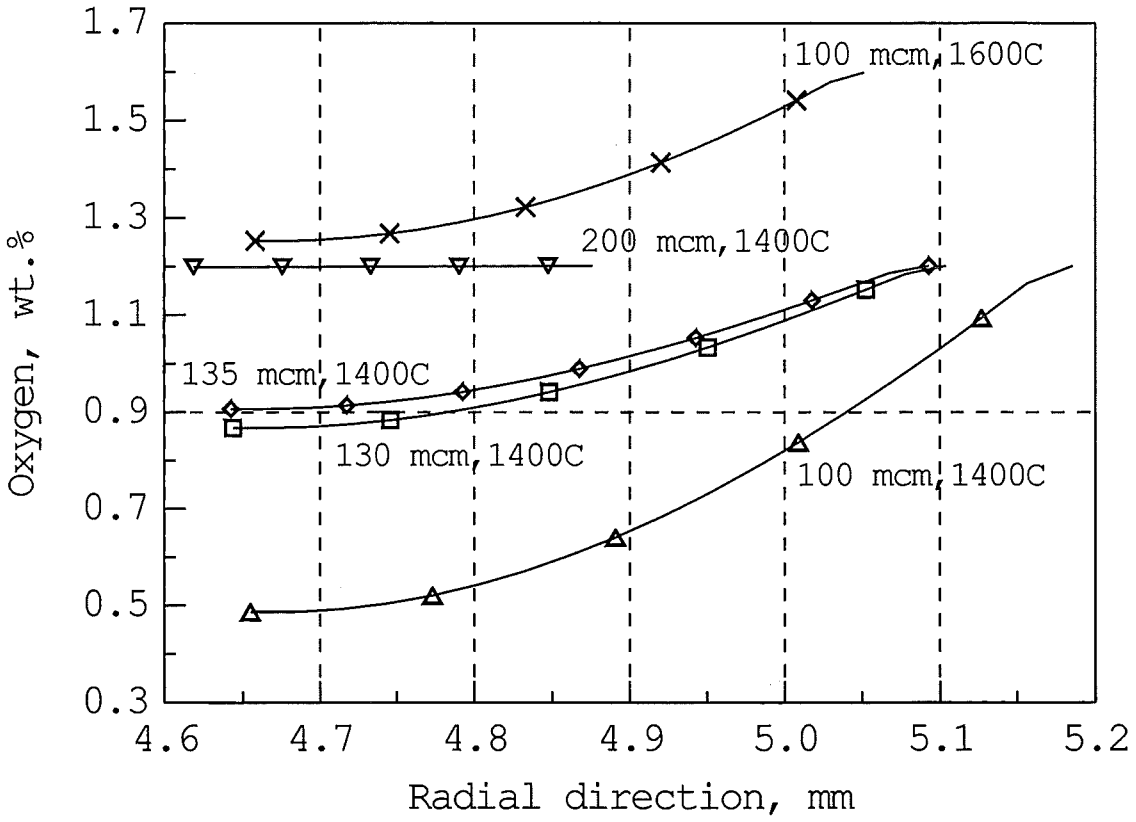

Figure 3.82: Oxygen distribution along the radial direction in the beta layer for the different extents of pre-oxidation.

As mentioned above this criterion provides only a conservative estimation and does not exclude that in some cases a metal layer with a smaller width and higher oxygen content can prevent the crack propagation. An example of such a behavior is the test 110471 (cooldown by steam from 1200 °C with steam pre- oxidation 123–189 μm). However, currently this is the only one example, since all other specimens with pre-oxidation 130–200 μm and initial temperature $\leq$1400 °C have a few axial cracks. Hence, high level tensile stresses generated in the alpha layer during the oxide phase transition lead to the alpha layer cracking, and the remaining beta layer cannot prevent through-wall propagation of cracks.

In Fig. 3.83 stresses generated in the layers of the oxidized cladding during cooldown by steam are presented. Cladding pre-oxidation is 100 μm, initial temperature 1200 °C. In this case through-wall cracks do not appear, since the beta layer is thick (see Fig. 3.82). One can see that the oxide phase transition leads to generation of tensile stresses in the alpha layer,

while in the oxide layer the level of compressive stresses is rather high despite partial stress relaxation due to cracking. This explains why microcracks in the alpha layer are observed very clearly under the metallographic analysis and oxide scale seems to be free of the microcracks.

In Fig. 3.84 the evolution of stresses during the phase transition is presented; only circumferential and axial stresses in the alpha and oxide layers are shown, the other stresses are negligible.

Test	Initial temperature, °C	Oxide thickness, μm	Quenching	Pre-oxidation
18105_1	1000	115 (upper) 115 (central) 115 (lower)	water	oxygen-argon
04066_1	1200	100*	water	oxygen-argon
06075_1	1200	120 120 120	water	oxygen-argon
05075_1	1400	120 120 120	water	oxygen-argon
29056_1	1400	100*	water	oxygen-argon
16046_1	1200	100 105 100	steam	oxygen-argon
25036_1	1400	85 90 90	steam	oxygen-argon
25027_2	1200	100 90 100	steam	steam
24027_1	1400	100 100 115	steam	steam

Table 3.3: Quench tests for 100 μm pre-oxidized rods without through-wall crack formation. *Oxide scale thickness was estimated from the pre-oxidation duration.

Since many microcracks in the alpha layer are observed after quenching, the alpha layer is thought to crack before the oxide compressive stresses reach the limit value. From the analysis of Fig. 3.84, this leads to the assumption that the tensile strength limit of the alpha layer is close to the same value in the oxide.

As mentioned above the oxide can exfoliate from the metal sublayer during phase transition to relax the stresses. If the stresses after exfoliation drop to zero, then the stress state of this part of exfoliated oxide is given by Eq. 3.20 and depends on the radial temperature drop across the oxide. The radial temperature drop necessary for generation of the stresses on the external surface exceeding the tensile limit strength is presented in Fig. 3.85. It is assumed that the external stresses attaining the limit value lead to oxide cracking and spalling from the metal sublayer. One can see from the figure that the critical temperature drop has a relatively high value that decreases at lower temperatures. This explains that spalling is observed only in the water-quenched specimens, since the temperature drop in the steam-quenched rods is much smaller.

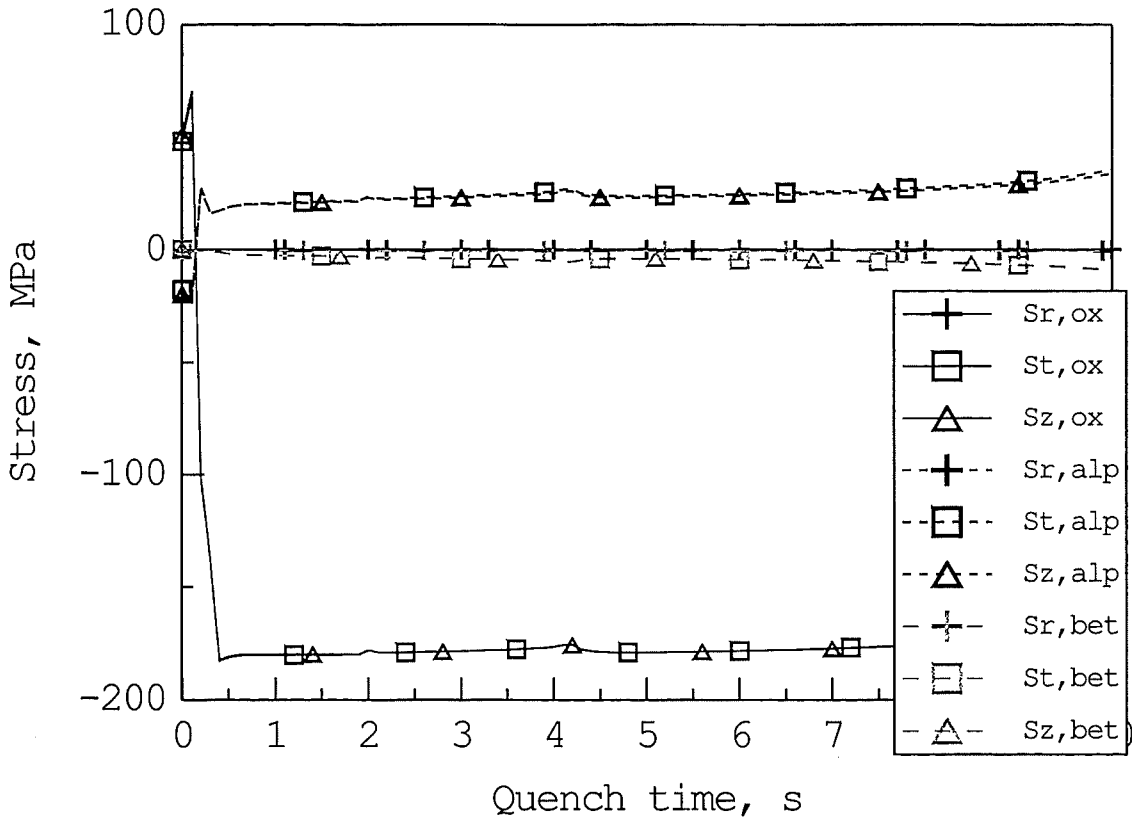

Figure 3.83: Simulation of the stress evolution during cooldown by steam. T_0 = 1200 °C. 100 µm pre-oxidation. Location 75 mm.

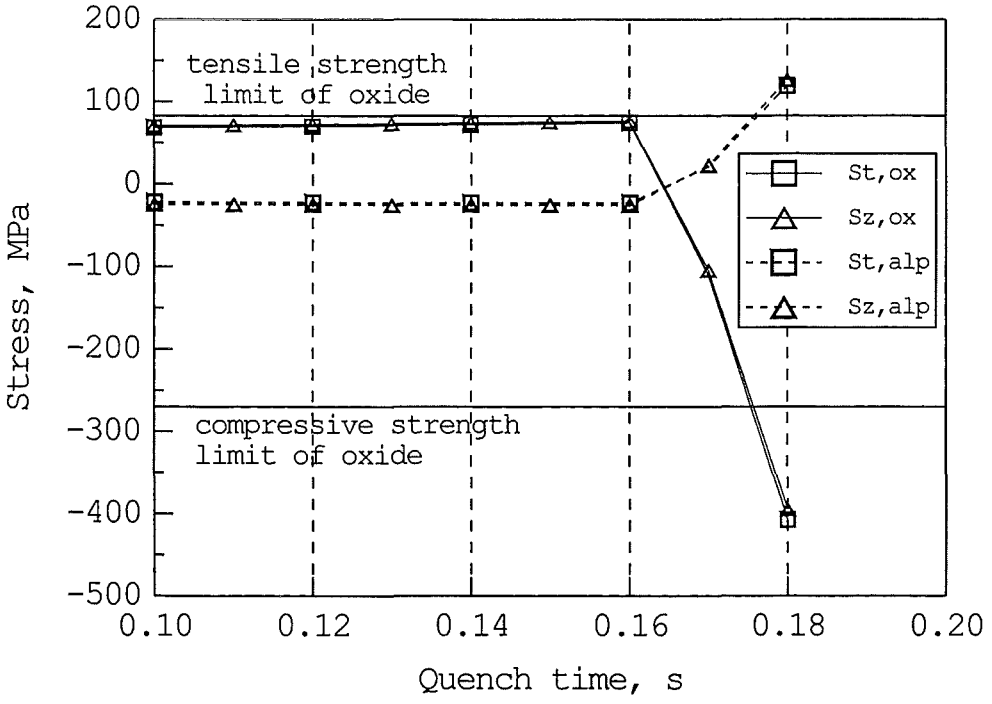

Figure 3.84: Simulation of the stress evolution during the oxide phase transition under steam cooling conditions. $T_0 = 1200\,°C$. 100 µm pre-oxidation. Location 75 mm.

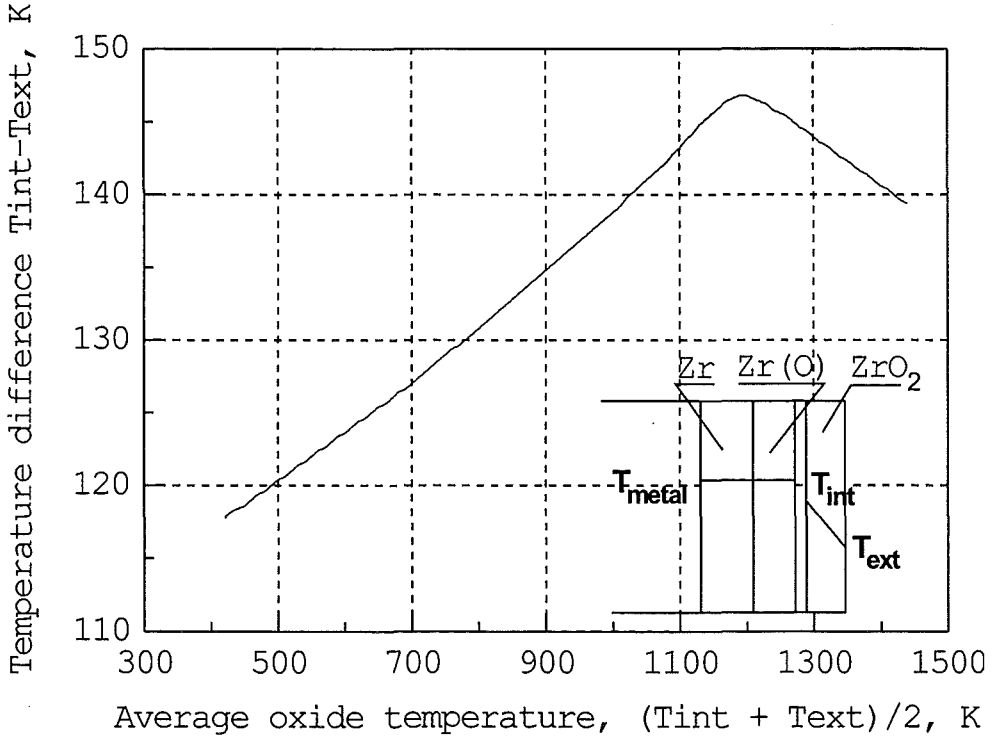

Figure 3.85: Radial temperature drop across the oxide layer leading to the oxide scale spalling as a function of average oxide temperature.

There are two maximum temperature drops in the case of the water-quenched rods, one occurs at temperature of the oxide phase transition and another – at the quench front temperature (when transformation from the nucleate boiling to the film boiling takes place). At the quench front temperature the cladding oxidation is negligible and newly-formed metal surfaces do not contribute to the hydrogen generation.

For the case of the initial quench temperature 1600 °C the oxygen content of the beta layer is higher than 0.9 wt.% for all radial locations due to oxygen homogenization during 2 min heating in argon atmosphere from the pre-oxidation temperature (1400 °C) to the initial quench temperature. For this reason, the cladding is rather brittle. Other specific features of the high initial temperature are a sharp decrease of the oxide strength limit at high temperatures and intensive oxide cracking due to different rates of the thermal strain variation of the oxidized cladding layers at the first stage of quenching (before the temperature of oxide phase transition will be reached), see Fig. 3.86 (only circumferential and axial stresses in the alpha layer and the oxide are shown, the others stresses are negligible).

In Fig. 3.87 the evolution of stresses during the phase transition is presented, only circumferential and axial stresses in the alpha layer and the oxide are shown, other stresses are negligible. One can see that firstly the stresses in the oxide layer reach their critical value and this leads to microcrack formation in the oxide layer. So far as the tensile stresses act in the alpha layer, these microcracks can propagate through this layer, however, low level of accumulated elastic energy prevents further microcrack penetration through the more ductile beta layer (in which the tensile stresses relax due to plastic strains). In the case of initial temperature $\leq$1400 °C the residual compressive stresses in oxide and tensile stresses in the alpha layer are retained.

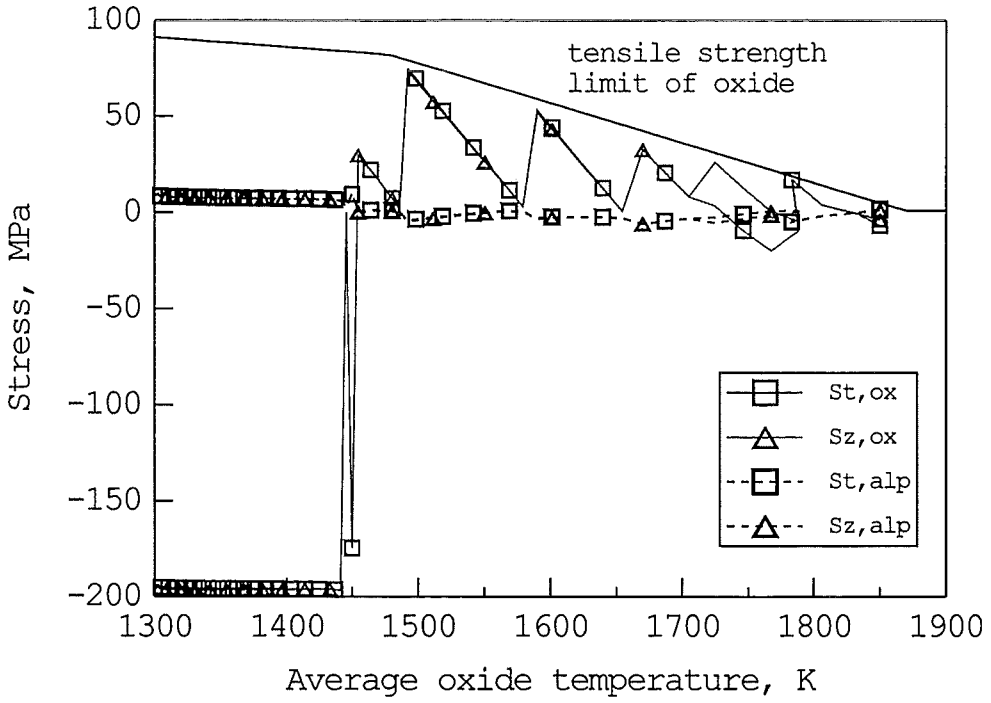

Figure 3.86: Simulation of the stress evolution during cooldown by steam. T_0 = 1600 °C. 100 µm pre-oxidation. Location 75 mm.

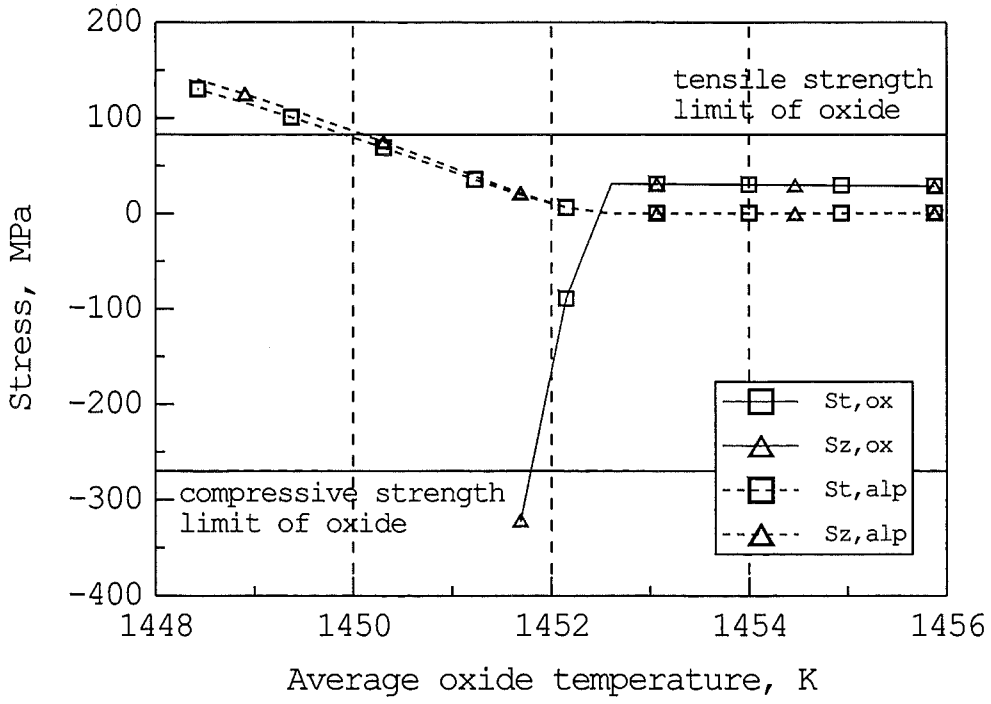

Figure 3.87: Simulation of the stress evolution during the oxide phase transition under steam cooling conditions. T_0 = 1600 °C. 100 µm pre-oxidation. Location 75 mm.

3.2.3.2 Quenching of 300 μm pre-oxidized rods

The analysis presented above is also valid for the case of 300 μm pre-oxidation. The main difference is the absence of ductile beta layer that can prevent formation of through-wall cracks. In Fig. 3.88 the stress evolution in the alpha and oxide layers is shown (pre-oxidation 300 μm, initial temperature 1200 °C). Under these conditions firstly the circumferential and axial tensile stresses in the alpha phase reach their critical values. This leads to axial and circumferential through-wall crack formation under quenching from the initial temperature $\leq$1400 °C.

With the lack of the ductile beta layer, opening of the cracks wide enough to supply the steam for oxidation of newly-formed metal surfaces occurs. In the case of water quenching more intensive oxidation of the hotter upper part takes place. Crack opening in this case is larger owing to the higher thermal strain of the upper part and can provide the steam supply either to the crack surface or to the cladding inner surface.

In Fig. 3.89 the stresses generated during oxide phase transition under steam cooling from 1600 °C are shown. One can see that firstly the oxide cracks. In the absence of the ductile beta layer some cracks can penetrate through the alpha layer owing to the tensile stress in this layer, hence, few through-wall cracks can form. However, due to the low level of the alpha layer stresses the number of these cracks should be much smaller in comparison with the case of initial temperature $\leq$1400 °C. The crack opening is also smaller, since the oxide scale with residual deformation strength is thinner. The smaller crack density and crack opening cannot explain the observed hydrogen release. As proposed above the possible reason of hydrogen generation in this case is rapid oxidation of substoichiometric oxide. This assumption is confirmed by the numerical simulations. Calculated results are presented in Figs. 3.90 – 3.92. In Fig. 3.90 the total hydrogen generation for the rod are shown; one can see that calculated amount of hydrogen is close to the measured values (see Table 3.2). Fig. 3.91 shows that the intensive hydrogen release occurs when oxide is strongly substoichiometric. Intensive oxygen consumption should lead to temperature increase; comparison of the calculated and experimental temperature variations is shown in Fig. 3.92. Temperature peaks corresponding to this increased oxygen consumption can be observed in both curves. Hence, the oxidation of substoichiometric oxide may be an important source of the hydrogen release at high initial temperatures.

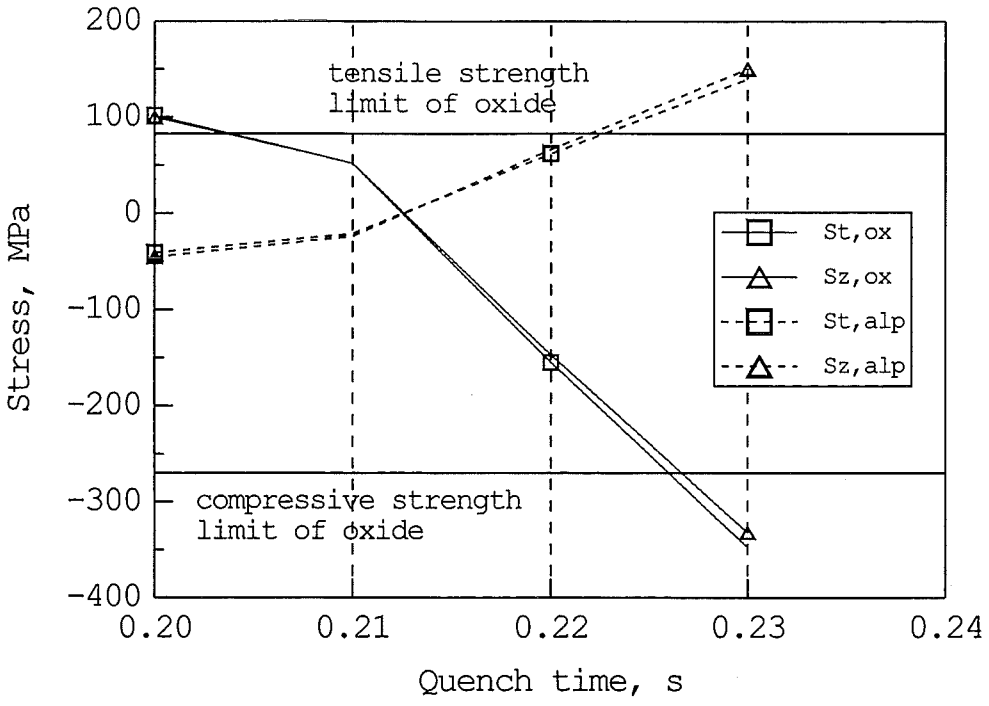

Figure 3.88: Simulation of the stress evolution during oxide phase transition under steam cooling conditions. $T_0 = 1200\,°C$. 300 µm pre-oxidation. Location 75 mm.

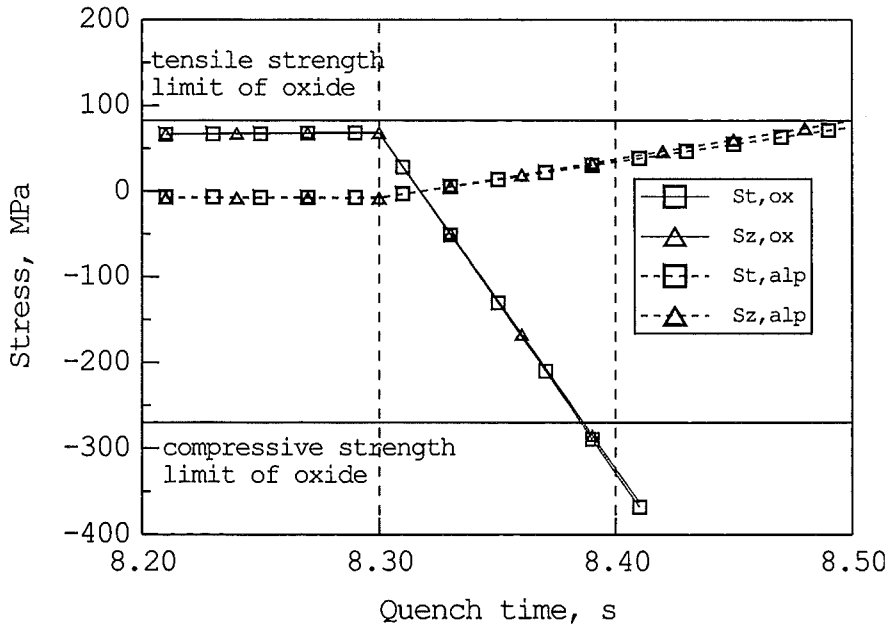

Figure 3.89: Simulation of the stress evolution during oxide phase transition under steam cooling. $T_0 = 1600\,°C$. 300 µm pre-oxidation. Location 75 mm.

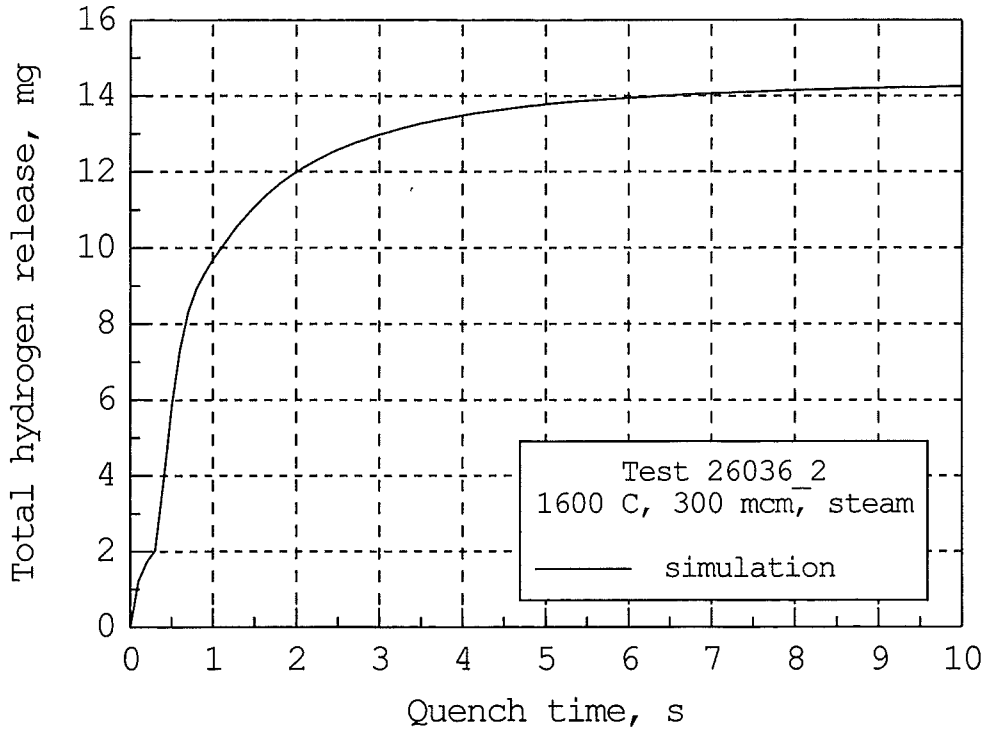

Figure 3.90: Simulation of the total hydrogen generation during steam cooling. $T_0 = 1600\,°C$. 300 µm pre-oxidation.

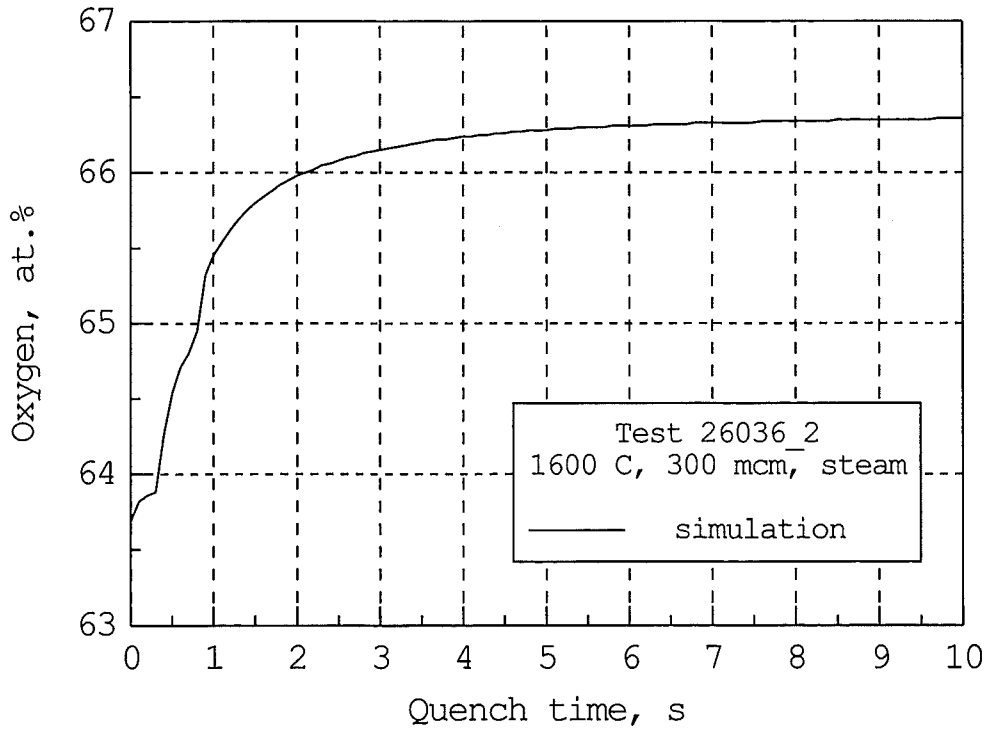

Figure 3.91: Simulation of the average oxygen content evolution in the oxide during steam cooling. $T_0 = 1600\,°C$. 300 µm pre-oxidation. Location 75 mm.

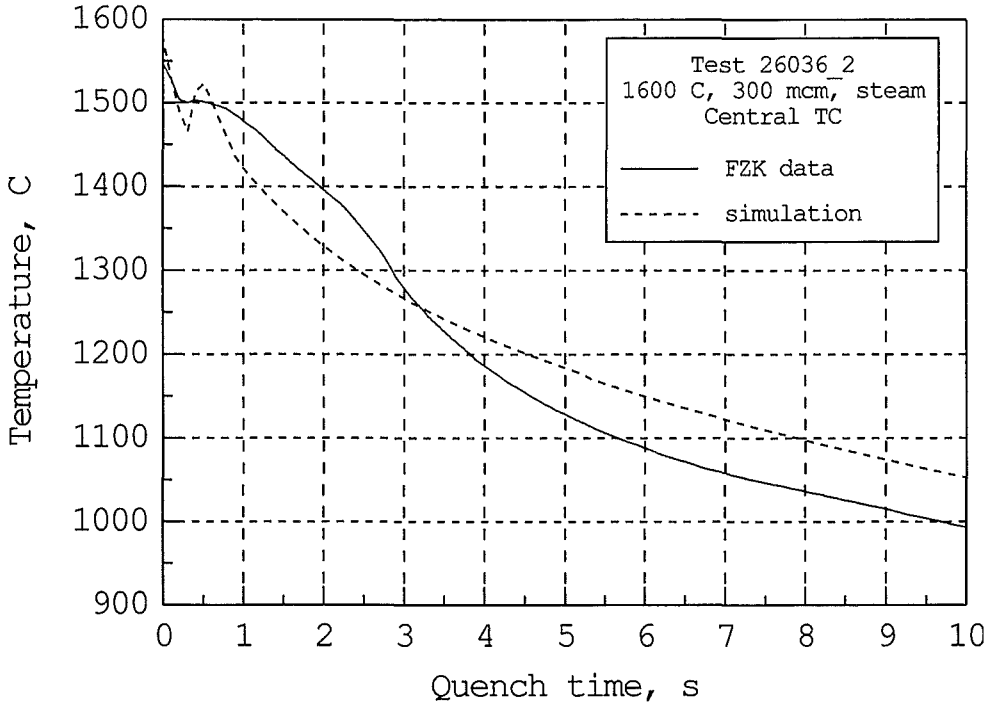

Figure 3.92: Simulation of the temperature evolution during steam cooling. T_0 = 1600 °C. 300 µm pre-oxidation. Location 75 mm.

3.3 Kinetic model of hydrogen uptake and release by Zircaloy at high temperatures

Up-to-date there are many published experimental works dealing with hydrogen absorption by metal Zr alloys under various conditions [28, 29, 30, 31, 32], nevertheless, they are mainly concentrated on thermodynamic aspects of the phenomenon (i.e. measurements of hydrogen solubility in the metal as a function of temperature and hydrogen partial pressure). Kinetics of the hydrogen uptake and release by Zry-4 (along with its solubility limits) at high temperatures have been recently specially studied in the FZK in separate-effects tests supporting the single-rod quench program [33].

Specimens investigated in the tests [33] are Zircaloy-4 cladding tube segments. The tests are performed in a small STA (Simultaneous Thermal Analysis) facility coupled with a mass spectrometer. The furnace of the STA facility is designed for temperatures up to 1600 °C. A sophisticated gas supply system provides various argon/hydrogen mixtures with hydrogen content between 0 and 100 %. The dependence of the hydrogen solubility of Zircaloy-4 on temperature (950–1450 °C) and hydrogen partial pressure (0–1 bar) was investigated along with

the kinetics of the uptake and release processes. It was found in the tests with hydrogen partial pressure increase from 0 bar to 0.5 bar and subsequent decrease from 0.5 bar to 0 bar, that the uptake and release of hydrogen by Zircaloy was a reversible process but non-symmetrical in time. The hydrogen uptake was a rather rapid process, thus, measured mass increase of a sample due to hydrogen uptake occurs practically simultaneously with growth of the hydrogen partial pressure in the gas mixture. The hydrogen release in these tests, however, was characterized by a comparatively large time delay after the hydrogen partial pressure drop.

A kinetic model describing experimental observations of hydrogen interactions with metal Zry in the FZK tests is presented below.

3.3.1 Model description

Gas flow under experimental conditions is described by the model with the approximation of a constant and homogeneous pressure in the gas phase. This approximation is well grounded, since the process of the pressure homogenization is the fastest transfer process in the system and has the characteristic time $\tau_p \sim d/C_s \sim 10^{-4}$ ($d \sim 1$ cm is a characteristic hydraulic diameter and $C_s \sim 10^{-4}$ cm/s is the sound velocity in the gas mixture). In the experiments [33], considerable hydrogen absorption or release take place, hence, in order to afford constant total pressure in the gas, an additional convective flow across the gas hydraulic channel (Stefans flow) occurs. Therefore, mass fluxes of hydrogen and argon in the diffusion boundary layer of the gas phase near the metal surface take the form:

$$J^{H_2} = J_D^{H_2} + J_{St}^{H_2} = k_{H_2}(C_{H_2,g}(s) - C_{H_2,g}(b)) - v_{St}C_{H_2,g}(s), \tag{3.39}$$

$$J^{Ar} = J_D^{Ar} + J_{St}^{Ar} = k_{Ar}(C_{Ar,g}(s) - C_{Ar,g}(b)) - v_{St}C_{Ar,g}(s), \tag{3.40}$$

where $c_{i,g} = P_{i,g}/RT$ is the molar density of the i-th component in the gas mixture with corresponding partial pressure $P_{i,g}$, R is the gas constant and T is the gas temperature; indices s and b designate values near the oxide surface and in the bulk of the gas phase (outside the diffusion boundary layer), respectively, v_{St} is the velocity of the Stefans convection flow which affords constant total pressure in the gas, $P_{tot,g} = P_{H_2,g} + P_{Ar,g} = 1$ bar; k_{H_2} is the mass transfer coefficient of hydrogen in the gas phase. In Eqs. 3.39 and 3.40 the gas phase mass transfer is estimated using a well-known analogy between heat and mass transfer.

Since the diffusion of Ar and H_2 takes place under conditions of the constant total pressure, the corresponding diffusion fluxes must locally compensate each other:

$$J_D^{H_2} = -J_D^{Ar}. \tag{3.41}$$

Flux matches for the two gas components at the metal surface take the form:

$$J_D^{H_2} + J_{St}^{H_2} = 0.5 J_{sol}^{H}, \tag{3.42}$$

$$J_D^{Ar} + J_{St}^{Ar} = 0, \tag{3.43}$$

where $J_{sol}^{H} = -D_H \left.\frac{\partial C_H}{\partial x}\right|_S$ is the hydrogen boundary diffusion flux in the solid phase, D_H is the diffusion coefficient of hydrogen atoms in the metal. From equations 3.42 and 3.43 it follows:

$$2k_{H_2}(C_{H_2,g}(b) - C_{H_2,g}(s)) = D_H \left.\frac{\partial C_H}{\partial x}\right|_S \frac{(C_{tot,g} - C_{H_2,g}(s))}{C_{tot,g}}, \tag{3.44}$$

where $C_{tot,g} = C_{Ar,g} + C_{H_2,g} = P_{tot,g}/RT$ is a constant value. Near the gas/solid interface, hydrogen concentration in the solid state and hydrogen partial pressure in the gas phase are related by Sievert's law:

$$P_{H_2,g}^2(s) = k_s C_H(s), \tag{3.45}$$

where K_s is the Sievert's constant.

Substitution of Eq. 3.45 into Eq. 3.44 finally leads to:

$$D_H \left.\frac{\partial C_H}{\partial x}\right|_S = \frac{2k_{H_2}}{RT} \frac{P_{tot,g}}{(P_{tot,g} - P_{H_2,g}(s))} \left(P_{H_2,g}(b) - \frac{C_H^2(s)}{k_s^2}\right). \tag{3.46}$$

Hydrogen concentration distribution in the solid phase is found from the diffusion equation:

$$\frac{\partial C_H}{\partial t} = D_H \frac{\partial^2 C_H}{\partial x^2}, \tag{3.47}$$

with the boundary condition Eq. 3.46 at the outer and at the inner surfaces of the tube.

Under the real experimental conditions of the FZK tests, gas flows inside and outside of the Zircaloy tube might be significantly different and their accurate description becomes a rather complicated problem. In the present work a simplified approach to this problem is used, in which an effective mass transfer coefficient of hydrogen in the gas phase is considered as an unknown fitting parameter.

3.3.2 Qualitative analysis of the model

For the qualitative analysis of the kinetics of hydrogen absorption/desorption by the metal zirconium, which can be performed on the basis of analytical consideration, a further simplification of Eqs. 3.46 and 3.47 can be attained using the following additional assumptions:

1. The zirconium layer is rather thin, so that the characteristic hydrogen diffusion time in the solid phase $\tau_D \sim L^2/D_H$ (L is the thickness of the solid phase) is much smaller than the characteristic time of the mass transfer in the gas phase $\tau_g \sim (L/4K_{H_2})(C_{Zr}/C_{H_2,g}(b))$ (C_{Zr} is the zirconium molar density);

2. $P_{tot,g}/(P_{tot,g} - P_{H_2,g}(s)) \sim 1$, since this assumption did not strongly influence the final results of calculations by the complete numerical model (as will be seen further).

The first assumption allows consideration of hydrogen spatial distribution in the metal as a constant value dependent only on time. In such a case, integration of Eq. 3.47 on the spatial coordinate across the metal phase and substitution of the boundary condition, Eq. 3.46, lead to the ordinary differential equation:

$$\frac{L}{2}\frac{dC_H(s)}{RT} = \frac{2k_{H_2}}{RT}\left[P_{H_2,g}(b) - \frac{C_H^2(s)}{k_s^2}\right]. \tag{3.48}$$

For the case of hydrogen absorption, when hydrogen partial pressure in the gas phase changes stepwise from zero to $P_{H_2,g}(b)$ and the metallic zirconium is initially free of hydrogen, $C_H(s, t = 0) = 0$, solution of Eq. 3.48 has form:

$$C_H(s) = k_s^2 P_{H_2,g}(b)\frac{1 - \exp(-2t\gamma)}{1 + \exp(-2t\gamma)}, \tag{3.49}$$

where $\gamma = 4(k_{H_2}/L)(1/RTk_s^2)$.

The kinetics of hydrogen release are considered for a zirconium sample which is initially in equilibrium with the gas mixture with a finite hydrogen partial pressure and, hence, contains some hydrogen, $C_H(t = 0) = C_{H,0}$, in accordance with Sievert's law. Then, in accordance with experimental procedure the hydrogen partial pressure in the gas drops to zero and the system starts to relax to a new equilibrium state. This process is described by Eq. 3.48 with $P_{H_2,g}(b) = 0$:

$$\frac{dC_H(s)}{dt} = \frac{4k_{H_2}}{LRT}\frac{C_H^2(s)}{k_s^2}, \tag{3.50}$$

which has the following solution:

$$C_H(s) = \frac{C_{H,0}}{1 + \gamma t}. \tag{3.51}$$

As one can see from the comparison of the solutions Eqs. 3.49 and 3.51, the hydrogen uptake and release occur in different ways. The hydrogen release is described by a slow hyperbolic function of time, whereas the hydrogen uptake obeys a rapid exponential time law.

It should be emphasized, that the hyperbolic time law, Eq. 3.51, of the hydrogen release from zirconium sample is valid only in one particular case, namely, when the hydrogen partial

pressure $P_{H_2,g}(b)$ in the gas flow drops exactly to zero; otherwise, the system during hydrogen desorption is described by Eq. 3.48 with non-zero value of $P_{H_2,g}(b)$ and relaxes to the new equilibrium state exponentially. Hence, the model predicts that in possible tests with the gas hydrogen partial pressure drop to non-zero value, the kinetics of hydrogen absorption and release will be more similar and obey the same exponential time law.

3.3.3 Numerical illustrations

The diffusion equation Eq. 3.47 with the boundary conditions Eq. 3.46 is numerically solved by the method of finite-differences with the following set of the parameters:

$D_H = 6.3 \cdot 10^{-3} \exp(-4250/T[K])$ cm^2/s, [34],

$k_s = 1.4 \cdot 10^{-3}$ exp(8102.7/T[K]) atom ratio/atm$^{1/2}$, [33],

$K_{H_2} = 4$ cm/s, (fitting to the experimental data [33]).

The calculated kinetics of hydrogen absorption and desorption by the Zircaloy tube segment are presented in Fig. 3.93. In these calculations the temperature decreased from 1150 °C to 1050 °C and the hydrogen partial pressure varied in the interval 0–0.5 bar, in accordance with the experimental conditions [33]. The calculated behavior of the system is fairly close to that observed in the experiments and corresponds to the qualitative consideration.

As was explained in the previous section, a more symmetrical behavior of the system during absorption and release stages can be attained if the hydrogen partial pressure drops to non-zero value during the release stage. This assertion is illustrated in Fig. 3.94, where calculation results are presented for the case (not examined experimentally) when the hydrogen partial pressure is varied in the interval 0.2–0.5 bar.

In the presented calculations the hydrogen mass transfer coefficient in the gas phase was used as a fitting parameter, because gas flows along the Zircaloy tube placed on the solid disc (closing the tube hole from one side) are quite complicated. This deficiency of the model can be easily avoided in tests with a Zircaloy cylinder (instead of a tube with a hole closed from one side). For such an experimental geometry the hydrogen mass transfer coefficient can be estimated more unambiguously. Preliminary calculations are presented in Fig. 3.95 for a cylindrical Zircaloy sample with the same diameter as the outer diameter of the tube.

In this case the system behavior is qualitatively similar to the previous case, however, the characteristic times of hydrogen uptake and release processes become greater, because of the increase of the metal slab thickness.

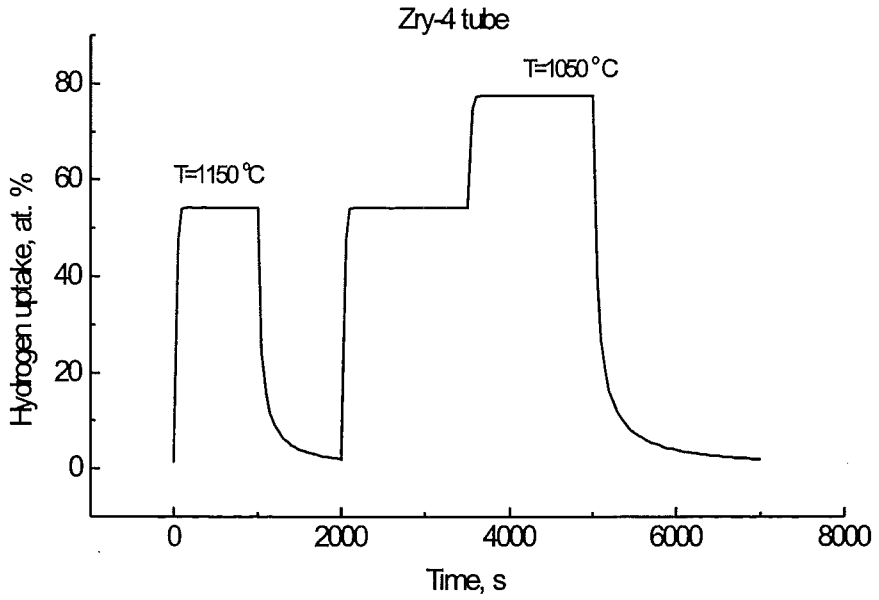

Figure 3.93: Hydrogen uptake and release of Zircaloy-4 tube segment: P_{H_2} = 0/0.5 atm, T=1050–1150 °C.

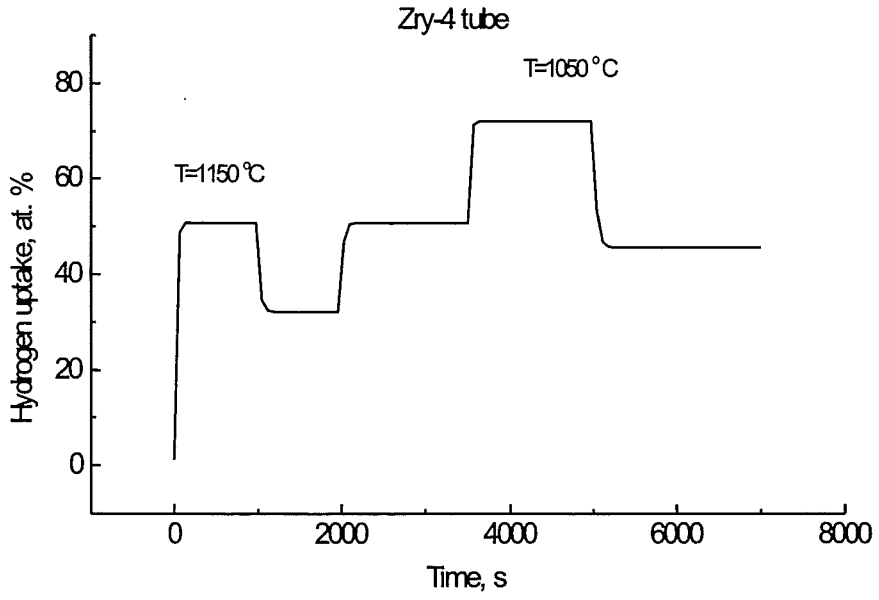

Figure 3.94: Hydrogen uptake and release of Zircaloy-4 tube segment: P_{H_2} = 0.2/0.5 atm, T=1050–1150 °C.

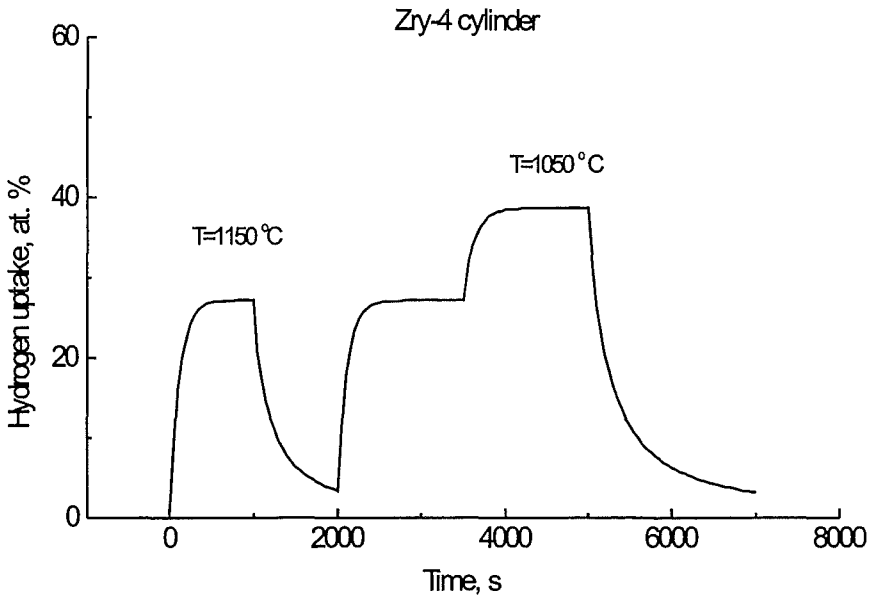

Figure 3.95: Hydrogen uptake and release of Zircaloy-4 cylinder: $P_{H_2} = 0/0.5$ atm, T=1050–1150 °C.

3.4 Modeling of hydrogen absorption by zirconium alloys during high temperature oxidation in steam

Hydrogen absorption by zirconium alloys during their oxidation in water and steam has been studied in the last three decades since the primary concern of this process is the embrittlement which it might cause during pressurized water reactor normal operation (see, for example review [35]). It was shown that, in parallel with the oxide film formation process in water or steam, a fraction of the hydrogen generated by decomposition of the water entered the metal. The relationship between the amount of oxidation occurring and the amount of hydrogen absorbed is not a simple function, although it follows a characteristic pattern which seems to be general for all zirconium alloys, provided the analytical technique is sensitive enough to distinguish changes in the "uptake fraction" (that fraction of the hydrogen liberated by the corrosion process during any time period and which is absorbed by the metal).

Far fewer experimental data are available for high temperature hydriding. In the literature one can frequently find only observations or trends instead of quantitative relations. Recently new tests [36, 37, 38, 39, 40] were performed in which the absorption phenomena were studied at high temperatures corresponding to the conditions of a severe accident at nuclear power plants. In [36] data on hydrogen uptake by Zr1%Nb during oxidation were given in the temperature range 900–1100 °C. The concentration of absorbed hydrogen was in the range 100–1000 ppm after steam exposure 10–30 min. It corresponds to a relative hydrogen uptake of 10–70%. Under the same experimental conditions far lower hydrogen concentration in Zircaloy-4 was found (4–100 ppm, corresponding to a relative hydrogen uptake 1-10%).

In the latest tests [40] hydrogen uptake was also studied simultaneously with measurements of Zr1%Nb alloy oxidation kinetics in steam under the pressure 1atm in the temperature interval 900–1200 °C. Clear qualitative tendencies and quantitative correlations between oxidation kinetic rates and hydrogen uptake have been revealed in these experiments. Below 1050 °C the hydrogen content of oxidized samples increased constantly with time up to the longest exposure (10^4 s) being proportional to the oxidation mass gain. At higher temperatures (1100–1200 °C) a maximum was reached after a relatively short time (500–1000 s), this content being definitely less at the same mass gains compared with the lower temperature ones. On the basis of the detailed experimental studies [40], development of a theoretical model of the hydrogen absorption phenomena is attempted in the present paper.

3.4.1 Hydrogen penetration mechanism through the oxide layer

In order to develop a model for hydrogen absorption by Zr cladding in the course of its oxidation in steam, firstly it is necessary to identify a physical mechanism of hydrogen migration through the oxide ZrO_2 scale. In surveying the results on hydrogen absorption one should distinguish between two possible routes; first, direct reaction with molecular hydrogen (gaseous hydriding), and second, absorption of hydrogen liberated by the decomposition of water or steam during the oxidation process and absorbed as part of the oxidation mechanism [35].

As it became clear from studies of gaseous hydriding of ZrO_2 slabs, both the solubility and the diffusivity of the solute in the solid are extremely small. For example, in the tests [41] the solubility and release kinetics of hydrogen in single-crystal zirconia were investigated by the infusion-extraction method. Equilibration in hydrogen at pressures between 1.4 and 11 atm and at temperatures from 1300 to 1600 °C produced H/Zr ratios varying from $4 \cdot 10^{-5}$ to $1.3 \cdot 10^{-4}$. The solubility behavior and the kinetics of release indicated that hydrogen atoms are strongly trapped by distinct binding sites in the solid with detrapping activation energies from 67 to 80 kJ/mole.

Such small values of the solubility and mobility apparently cannot provide rather large quantities of hydrogen transported through the oxide and dissolved in the metal phase as observed in the above-mentioned tests [36, 37, 38, 39, 40] on absorption of hydrogen during the oxidation process. Indeed, in these tests the fraction of hydrogen generated by decomposition of the steam entering the metal in the course of high-temperature zirconium alloy (Zry-4 or Zr1%Nb) oxidation reached several tens of percent. Analogous behavior has been also observed at lower temperatures (characteristic of reactor normal operation conditions) [35]. In particular, in a recent paper [42] oxidation and hydrogen uptake of Zr-based Nb alloys were studied as functions of Nb content and heat treatment at 400 °C under 10 MPa steam atmosphere. The percentage of hydrogen uptake in these tests after 58 days oxidation varied from 10 to 40% depending on the Nb content.

An important conclusion drawn by Park and Olander in [41] was that in the result of H_2 gas interactions with zirconia (gaseous hydriding) hydrogen apparently penetrates into the solid phase in the form of neutral atoms. Assignment of dissolved hydrogen as a neutral atom rather than as a proton was necessary to produce the dependence of solubility on the square root of the pressure observed in [41] (i.e. Sievert's law).

On the other hand, Wagner [43] measured the solubility of water vapor in yttria-stabilized

zirconia. The dissolution process was interpreted in terms of the reaction:

$$H_2O(g) + V_O^{2+} = 2H_i^+ + O_O(ox), \tag{3.52}$$

where $O_O(ox)$ is an oxygen ion on a regular lattice site, V_O^{2+} is a doubly charged anion vacancy, H_i^+ is an interstitial proton. This reaction predicts the dependence of solubility S with the square root of the water vapor pressure, $S \propto P_{H_2O}^{1/2}$, which was observed in the experiment.

The dissolution process observed in [43] differs in the charge state of the hydrogen in the gas from that in [41]; with H_2, the hydrogen is neutral, whereas, with H_2O, the hydrogen has a single positive charge. It appears that hydrogen in the solid oxide retains the charge state that it had in the gas, so that the two dissolution processes are fundamentally different ([41]).

It is important also to notice that amounts of dissolved hydrogen in the two tests [41] and [43] were quite comparable (H/Zr ~ 10^{-5}) despite ~8 orders of magnitude difference of the partial H_2 pressures in the gas phases. In the test [41] $P_{H_2} \approx 1 - 10$ atm at T=1300–1600 °C, whereas in [43] (performed in the steam atmosphere under the pressure $P_{H_2O} \approx 10^{-2}$ atm at temperatures 900–1000 °C) the partial pressure of H_2 can be evaluated as $P_{H_2} \sim 10^{-7}$ atm. Such a significant difference of the hydrogen solubility in the two tests apparently confirms the conclusion about the fundamentally different dissolution mechanisms occurring under conditions of these tests.

In addition to measurement of solubility, Wagner also measured the kinetics of water uptake by yttria-stabilized zirconia [43]. The data were interpreted in terms of diffusion of interstitial hydrogen in the solid. The measured diffusivities were rather high ~ $8 \cdot 10^{-7}$ cm^2/s at 890 °C and ~ $1.3 \cdot 10^{-6}$ cm^2/s at 990 °C. This discrepancy with the results of the tests [41] (in which extremely low mobility of hydrogen owing to strong trapping was detected) was also attributed in [41] to the nature of the diffusing species in Wagner's experiments (protons rather than neutral hydrogen atoms). A possible explanation of the very high mobility of protons in comparison with neutral hydrogen atoms is that both protons and oxygen ions must penetrate the solid at the same rate to preserve local electrical neutrality in the crystal. Since diffusivity of negatively charged oxygen ions in zirconia is rather high, they carry along positively charged protons in the same direction.

As mentioned above, it is easy to estimate that the extremely small solubilities and diffusivities of the neutral hydrogen atoms in the zirconia measured in [41] cannot provide significant hydrogen transport through the oxide layer into the metal observed in the tests [36, 37, 38, 39, 40] on the zirconium alloys oxidation in steam. Therefore, these observations can be

naturally explained only by the suggestion that the hydrogen dissolution in the oxide during Zr oxidation in steam takes place by the alternative mechanism, i.e. in the form of positively charged protons rather than neutral atoms.

In accordance with this conclusion, a standard consideration of the Zr oxidation mechanism in steam should be modified and completed. It is usually proposed that hydrogen absorption proceeds in three steps (see, for example, [35]). First, reaction of an adsorbed water molecule H_2O with an anion vacancy V_O^{2+} to leave two protons $2H_{ad}^{+}$ on the surface and an oxygen anion $O_O(ox)$:

$$H_2O(g) + V_O^{2+} = 2H_{ad}^{+}(ox) + O_O(ox). \tag{3.53}$$

Second, discharge of the protons on the surface by electrons migrating from the oxide/metal interface, i.e. cathodic reaction at the oxide/gas interface:

$$H_{ad}^{+}(ox) + e_\beta(ox/g) = H_{ad}(ox), \tag{3.54}$$

and anodic reaction at the metal/oxide interface:

$$ZrO_2(ox) + 2V_O^{2+} + 4e_\alpha(m/ox) = Zr(m) + 2O_O(ox). \tag{3.55}$$

Hydrogen adsorbed on the oxide ZrO_2 surface may be either released as hydrogen gas molecules:

$$2H_{ad}(ox) = H_2(g), \tag{3.56}$$

or absorbed in the oxide phase:

$$H_{ad}(ox) = H_{ab}(ox). \tag{3.57}$$

Hydrogen absorbed $H_{ab}(ox)$ should then diffuse through the matrix oxide (see also [42]).

However, in accordance with the above presented consideration and estimations, the amount of hydrogen absorbed via Eq. 3.57 is extremely small and cannot provide the observed (under steam oxidation conditions) mass transfer to the metal phase. For this reason, it should be proposed that only a part of adsorbed protons $H_{ad}(ox)$ is discharged at the oxide/gas interface by electrons in accordance with Eq. 3.54. The remaining part penetrates into the oxide in the form of protons:

$$H_{ad}^{+}(ox) = H_{ab}^{+}(ox), \tag{3.58}$$

diffuses through the oxide and discharges by electrons only at the oxide/metal interface:

$$H_{ab}^{+}(ox) + e_\alpha(ox/m) = H_{ab}(m). \tag{3.59}$$

As a result, the behavior of the absorbed hydrogen at the gas/oxide interface is described by the same chemical equation 3.52 (obtained by superposition of the two Eqs. 3.53 and 3.58), as in the tests [43] on water vapor dissolution:

$$H_2O(g) + V_O^{2+} = 2H_{ab}^{+}(ox) + O_O(ox),$$

and, thus, obeys the same quantitative dependencies, i.e. high solubilities and diffusivities in the oxide. Finally, the system of equations describing chemical processes on the oxide surface should be completed by the equation specifying possible transition of the oxygen anions $O_O(ox)$ to the gas molecules $O_2(g)$:

$$2O_O(ox) = O_2(g) + 2V_O^{2+} + 4e_\beta(ox/g), \tag{3.60}$$

being there in equilibrium with dissociating water molecules:

$$2H_2O(g) = O_2(g) + 2H_2(g). \tag{3.61}$$

3.4.2 Modeling of hydrogen uptake

For quantitative description of hydrogen uptake by Zr during its oxidation in steam, mass transfer in the three layers: gas, oxide and metal, and at corresponding interfaces: gas/oxide and oxide/metal, should be considered.

3.4.2.1 Mass transfer in the gas phase

Gas phase mass transfer is estimated using the analogy between heat and mass transfer. Under conditions of the laboratory tests [40] ($P_{H_2O} \approx 1$ atm, $T = 900 - 1200\,^{\circ}C$, steam supply rate 7.5 mg/s, corresponding to steaming velocities ~10 cm/s and the Reynolds number $Re \sim 10$) laminar regime of the steam flow occurs. In this regime, the mass transfer Nusselt number ≈3.7, thus, mass transfer coefficient k_i of the i-th species in the gas phase is estimated as:

$$k_i \approx 3.7 D_i/d, \tag{3.62}$$

where D_i is the effective diffusivity of the gas species, d is the hydraulic diameter of the flow channel.

However, it should be taken into account that the above presented value of the Nusselt number is valid only for long enough cladding tubes, namely with lengths more than $h \sim$

$(0.1-1)Re(d/2)$ [44]. In the tests [40] $d \sim 10\,mm$ and thus the value of the transition region h is quite comparable with the whole length of short cladding segments, 40 mm. In this case the mass transfer coefficient becomes dependent on the axial position x of the tube slowly decreasing to the asymptotic value expressed by Eq. 3.62, obeying an axial dependence if $x^{1/2}$ [44]. For these reasons, the value of the effective mass transfer coefficient in Eq. 3.62 is underestimated and may be considered only as a qualitative one. For more definite results it is recommended to reproduce such tests with longer cladding tubes (>40 cm).

In the simplified consideration of the oxidation process it is usually proposed that the gas phase transport equation describes equimolar counterdiffusion, since one mole of water decomposed at the surface produces one mole of H_2 that returns to the bulk gas (compare, for example, with [45]). Thus, such an approach involuntarily provides conservation of a constant pressure in the bulk of the gas phase.

However, under real conditions of considerable hydrogen absorption additional convection (Stefan) flows in the gas should be taken into account. Therefore, mass fluxes of the three gas components (steam, hydrogen and oxygen) take the form:

$$J_i^{(g)} = k_i(c_i(s) - c_i(b)) - c_i(s)v, \tag{3.63}$$

where $i = 1, 2, 3$ denote H_2, O_2, H_2O, respectively, $c_i = P_i/RT$ is the molar density of the i-th component in the gas mixture with corresponding partial pressure P_i, indices s and b designate values near the oxide surface and in the bulk of the gas phase (outside the diffusion boundary layer), respectively (see Fig. 3.96), v is the velocity of the convection flows which afford constant total pressure in the gas, $P_{tot} = P_{H_2O} + P_{H_2} + P_{O_2} = 1\,atm$.

Conservation laws for the three components at the oxide surface take the form:

$$k_1(c_1(s) - c_1(b)) - c_1(s)v = J_{diss} - (1/2)J_H^{(ox)}, \tag{3.64}$$

$$k_2(c_2(s) - c_2(b)) - c_2(s)v = (1/2)J_{diss} - (1/2)J_O^{(ox)}, \tag{3.65}$$

$$k_3(c_3(s) - c_3(b)) - c_3(s)v = J_{diss}, \tag{3.66}$$

where J_{diss} specifies dissociation flux of the H_2O molecules at the oxide surface (see Fig. 3.96), $J_H^{(ox)}$, $J_O^{(ox)}$ are diffusion fluxes of the two components (protons and oxygen anions) in the oxide phase.

Since only two amongst the three variables c_i are independent ($c_1 + c_2 + c_3 = P_{tot}/RT$) the multi-component Stefan-Maxwell equations for their interdiffusion fluxes result in a simple

relationship:

$$k_3(c_3(s) - c_3(b)) = -[k_1(c_1(s) - c_1(b)) + k_2(c_2(s) - c_2(b))]. \qquad (3.67)$$

In the considered case of small concentrations of the two gas components O_2 and H_2 (which are the products of equilibrium dissociation of H_2O in the gas), the effective diffusivities (see Eq. 3.62) of these molecules are very close to the binary diffusivities in the H_2O/H_2 and H_2O/O_2 mixtures and thus the mass transfer coefficients k_1 and k_2 are well defined values.

It should be noted that the three Eqs. 3.64–3.66 are written in the form analogous to the case when dissociation of H_2O molecules in the bulk of the gas phase is not considered and the two components H_2 and O_2 are independent. In the real situation a consideration of mutual transformations of the components significantly modifies the interdiffusion fluxes in the bulk of the gas phase. The local gas composition is determined by the equilibrium reaction $2H_2O(g) = O_2(g) + 2H_2(g)$ and for this reason obeys the mass action law:

$$\ln P_{O_2} + 2\ln P_{H_2} = 2\ln P_{H_2O} + 2\Delta G/RT, \qquad (3.68)$$

where in accordance with [44]:

$$\Delta G/RT = 6.61 - 29600/T. \qquad (3.69)$$

This equation provide an additional restriction to the solution of the diffusion problem in the gas phase for the two components H_2 and O_2 which at present cannot be considered as independent.

Nevertheless, as demonstrated in the Appendix, despite this limitation the hydrogen flux at the gas/oxide interface completely retains its form, Eq. (A.13), whereas the oxygen flux – only partially, since a finite renormalization of the mass transfer coefficient $k_2 \to k_2'$ (in accordance with Eq. (A.14)) is necessary in Eq. 3.65.

Superposition of Eqs. 3.64–3.67 results in a simple relationship for the convection velocity in the gas:

$$(c_1 + c_2 + c_3)v = (1/2)[J_O^{(ox)} + J_H^{(ox)} - J_{diss}]. \qquad (3.70)$$

Simple estimations show that in the initial stage of the oxidation process surface hydrogen pressure $P_{H_2}(s)$ exceeds the corresponding bulk value $P_{H_2}(b)$ by several orders of magnitude, continuously reduces with time and finally reaches the bulk value in the end of the process. This means that during the most part of the oxidation time an inequality $P_{H_2}(s) \gg P_{H_2}(b)$ is valid. In accordance with Eq. 3.68, this leads to $P_{O_2}(s) \ll P_{O_2}(b)$ and, therefore, $\Delta P_{O_2} \ll \Delta P_{H_2}$

(since $P_{H_2}(b) \approx 2P_{O_2}(b)$ Owing to these inequalities, the convection term gives input only in the steam flux $J^{(g)}_{H_2O}$ in Eq. 3.66. For the same reason, the oxygen flux $J^{(g)}_{O_2}$ can be generally neglected in comparison with the hydrogen flux $J^{(g)}_{H_2}$. For these reasons, Eq. 3.65 can be simplified:

$$J^{(ox)}_O \approx J_{diss}, \tag{3.71}$$

as well as Eq. 3.66 after substitution of Eq. 3.67:

$$k_1 c_1(s) + (1/2)J^{(ox)}_O + (1/2)J^{(ox)}_H \approx (3/2)J_{diss}. \tag{3.72}$$

After substitution of Eq. 3.71 into Eq. 3.72 one finally obtains the relationship:

$$k_1 c_1(s) + (1/2)J^{(ox)}_H = J^{(ox)}_O, \tag{3.73}$$

which has a clear physical sense: neglecting the small flux $J^{(g)}_{O_2}$, the flux $J^{(ox)}_O$ is exactly equal to the steam flux $J^{(g)}_{H_2O}$ which delivers oxygen to the oxide surface through the gas; in its turn, the hydrogen solid phase flux $J^{(ox)}_H$ matches the resulting flux delivering hydrogen (via H_2 and H_2O molecules) to the surface through the gas $2(k_1 c_1(s) - J^{(g)}_{H_2O}) = 2(k_1 c_1(s) - J^{(ox)}_O)$.

3.4.2.2 Mass transfer through the oxide/gas interface

The derived Eq. 3.73 determines a relation between the fluxes of various components in the gas and solid phases. In order to calculate these fluxes, it is necessary to determine relations between concentrations of these components at the oxide/gas interface.

Results of numerous investigations of the high-temperature Zr cladding oxidation kinetics evidence that the rate-determining step of this process (under unlimited steam supply conditions) is the oxygen diffusion in the oxide phase. In particular, a parabolic time law of the oxidation kinetics observed in such tests (as well as in [40]) directly confirms this statement. This means that surface kinetic processes of oxygen transition from the gas to the oxide phase are so quick (in comparison with the bulk diffusion processes), that the condition of thermodynamic equilibrium for the oxygen component prevails at the gas/oxide interface.

For these reasons, it can be concluded that at least a part of the chemical reactions at the gas/oxide interface considered in section 1 should be regarded as equilibrium:

- dissolution of water molecules at the oxide surface, Eq. 3.52 (obtained by superposition of Eqs. 3.53 and 3.58):

$$H_2O(g) + V^{2+}_O = 2H^+_{ab} + O_O(ox);$$

- oxygen transition from the oxide to the gas phase, Eq. 3.60:

$$2O_O(ox) = O_2(g) + 2V_O^{2+} + 4e_\beta(ox/g);$$

- dissociation of water molecules in the gas phase, Eq. 3.61:

$$2H_2O(g) = O_2(g) + 2H_2(g).$$

Correspondingly, for each of these equilibrium reactions the mass action law can be applied:

$$P_{H_2O}(s)C_v = \alpha C_{H+}^2, \tag{3.74}$$

$$P_{H_2O}(s)^2 = kP_{H_2}(s)^2P_{O_2}(s), \tag{3.75}$$

$$P_{O_2}(s)C_v^2C_e^4 = \beta, \tag{3.76}$$

where $P_i(s)$ is the i-th component partial gas pressure at the interface, α, β, k are the equilibrium constants of the corresponding chemical reactions (the constant k is determined in Eqs. 3.68 and (A.3)), C_v, C_e, C_{H+} are concentrations of anion vacancies V_O^{2+}, electrons and protons in the oxide near the interface, respectively.

An additional assumption about thermodynamic equilibrium at the interface for the hydrogen component, which obeys a superposition of the chemical Eqs. 3.54 and 3.56:

$$H_{ab}^+(ox) + e_\beta(ox/g) = (1/2)H_2(g),$$

leading to the corresponding mass action law:

$$C_{H+}^2 = \gamma P_{H_2}(s)/C_e^2, \tag{3.77}$$

is not really important for further calculations, since it results only in an additional relationship amongst the equilibrium constants of Eqs. 3.74–3.77:

$$\alpha\gamma/k\beta^{1/2} = 1.$$

Mass transfer of various components at the gas/oxide interface determined by the above described chemical processes can be schematically represented by a diagram in Fig. 3.97.

The charge neutrality condition at the interface completes the defect relations:

$$2C_v + C_{H+} = C_e. \tag{3.78}$$

Under conditions of the tests [40]:

$$P_{H_2O}(s) \approx P_{H_2O}(b) = 1 \text{ atm.} \tag{3.79}$$

Equations 3.74–3.79 can be solved and yield:

$$2\alpha C_{H+}^3 + C_{H+}^2 - (k\beta^{1/2}/\alpha)^{1/2} P_{H_2}(s)^{1/2} = 0. \tag{3.80}$$

In the tests [40] performed under conditions of unlimited steam supply, the surface ZrO_{2-x} composition is close to stoichiometric with substoichiometry deviation $x \leq 10^{-5}$ [45]. In this case Eq. 3.78 can be simplified, since C_v being determined by x becomes extremely small $C_v/C_{Zr} \sim x \leq 10^{-5}$ in comparison with concentration of protons $C_{H+}/C_{Zr} \sim 10^{-2} - 10^{-3}$ (see below Eq. 3.86):

$$C_{H+} \approx C_e. \tag{3.81}$$

Correspondingly, Eq. 3.80 can be also simplified:

$$C_{H+} = A(P_{H_2}(s)/RT)^{1/4} = A(c_1(s))^{1/4}, \tag{3.82}$$

where $A = [k\beta^{1/2}/\alpha RT)]^{1/4}$.

It should be noted that only in the case $C_{H+} \ll C_v$ (occurs, for example, under steam starvation conditions), the usually proposed in the literature neutrality condition $2C_v = C_e$ for the Zr oxidation in steam is valid. Therefore, the relation based on this last neutrality condition between oxygen partial gas pressure P_{O_2} and solid oxide substoichiometry x which is used as a boundary condition in the problem of Zr oxidation in steam [45], turns to be inaccurate under conditions of unlimited steam supply.

Under steam starvation conditions when $P_{H_2O}/P_{H_2} \rightarrow 0$ (instead of Eq. 3.79) and $2C_v = C_e$ (instead of Eq. 3.81), for the proton concentration in the oxide one gets:

$$C_{H+} \propto P_{H_2O}^{1/3} P_{H_2}^{1/6}. \tag{3.83}$$

Therefore, under conditions of the tests [41] on the H_2 gas interactions with zirconia (i.e. $P_{H_2O} \rightarrow 0$) the proton concentration should turn to zero, $C_{H+} \rightarrow 0$, this is in accordance with observations [41] (since hydrogen was dissolved in zirconia in the form of neutral atoms rather than protons, see section 1).

3.4.2.3 Mass transfer in the oxide phase

In the analysis of the tests [40] performed under conditions of unlimited steam supply it is natural to assume that a relatively small amount of hydrogen dissolved in the oxide practically

does not influence the stoichiometric composition of its surface. In the opposite case noticeable deviations of the oxidation kinetics from the parabolic time law should be expected. In reality such deviations were not observed in the tests [40] as well as in many other high temperature oxidation tests. Under such an assumption the oxygen flux in the oxide phase can be presented in the standard form:

$$J_O^{(ox)} = D_O^{(ox)} \Delta C_O / \delta(t), \tag{3.84}$$

where $D_O^{(ox)}$ is the oxygen diffusivity in the oxide, ΔC_O is the oxygen concentration fall across the oxide layer (invariant in time in accordance with the above mentioned assumption), $\delta(t) \propto t^{1/2}$ is the oxide layer thickness determined by the self-consistent solution of the oxygen diffusion problem in the multilayered system (gas/oxide/metal) and directly measured in the tests [40].

Analogously, the hydrogen flux in the oxide layer depends on the proton concentration fall $\Delta C_{H+} = C_{H+}(s) - C_{H+}(b)$ across this layer (see Fig. 3.97):

$$J_H^{(ox)} = D_H^{(ox)} \Delta C_{H+} / \delta(t), \tag{3.85}$$

where $D_H^{(ox)}$ is the hydrogen ions (protons) diffusivity in the oxide (estimated in [43] at 900 and 1000 °C as $\approx 8 \cdot 10^{-7}$ and $1.3 \cdot 10^{-6}$ cm^2/s, respectively); $C_{H+}(s)$ denotes hereafter the proton concentration at the gas/oxide interface (denoted above as C_{H+}). As noticed in [41] the value of $D_H^{(ox)}$ has the same order of magnitude as $D_O^{(ox)}$. Since the fluxes $J_O^{(ox)}$ and $J_H^{(ox)}$ have also comparable values within one order of magnitude (as follows from the measurements of absorbed to generated hydrogen ratio which varied in the tests [40] from 50 to 10%, see Fig. 3.98), the value ΔC_{H+} can be estimated as:

$$\Delta C_{H+} \approx (0.1 - 1) \Delta C_O.$$

In the initial stage of the oxidation tests when $C_{H+}(s) \gg C_{H+}(b)$, this allows an estimation:

$$C_{H+}(s) \approx 10^{-4} - 10^{-5} \text{ mol/cm}^3,$$

or

$$C_{H+}/C_{Zr} \sim 10^{-2} - 10^{-3}. \tag{3.86}$$

It should be noted that in Eqs. 3.84 and 3.85 the quasistationary approximation for the diffusion problem in the oxide (well checked for oxygen and consequently for hydrogen, since $D_H^{(ox)} \sim D_O^{(ox)}$) was applied and for this reason linear concentration profiles in the oxide were taken.

3.4.2.4 Qualitative analysis of the model

In the initial stage of the oxidation process (when $C_{H+}(s) \gg C_{H+}(b)$ and relative reduction of metal layer thickness is small) a self-consistent solution of the problem of hydrogen mass transfer in the gas and oxide phases and absorption in the metal phase can be derived from the system of equations 3.73, 3.82, 3.84 and 3.85. Time dependence of hydrogen uptake can be analyzed qualitatively from these equations.

Indeed, in this case $J_O^{(ox)} \sim J_H^{(ox)}$ as indicated in the previous section. Therefore, hydrogen concentration $c_1(s)$ in the gas near the interface can be estimated from Eq. 3.73:

$$c_1(s) = J_O^{(ox)}/k_2 \propto \delta(t)^{-1}.$$

In accordance with Eq. 3.80:

$$C_{H+}(s) \propto c_1(s)^{1/4} \propto \delta(t)^{-1/4}, \tag{3.87}$$

thus, substituting this last relationship into Eq. 3.85 one gets:

$$J_H^{(ox)} = D_H^{(ox)} \Delta C_{H+}/\delta(t) \propto \delta(t)^{-5/4} \propto t^{-5/8}.$$

Since this flux determines an amount of absorbed hydrogen in the metal phase $C_H(m)$:

$$\partial C_H^{(m)}/\partial t \propto J_H^{(ox)} \propto t^{-5/8},$$

finally one can obtain for the value measured in [40]:

$$C_H^{(m)} \propto t^{3/8}. \tag{3.88}$$

The accuracy of the hydrogen uptake measurements [40] is relatively low owing to small absolute values of the measured concentrations ($\sim 10^2 - 10^3$ p.p.m.). Within these accuracy limits the difference between the obtained time dependence $t^{3/8}$ and $t^{1/2}$ is insignificant, therefore, results of the measurements [40] at $t < 1000$ s (see Fig. 3.99) can be satisfactorily described by both the time laws. For this reason, a combination of the model constants determining coefficient B in the derived dependence $C_H^{(m)} = Bt^{3/8}$ can be obtained from the measured in [40] approximate linear dependence $C_H^{(m)}$ on $\Delta m \sim \delta(t) \sim t^{1/2}$ (in the initial stage of the process) presented in Fig. 3.100.

It is assumed that hydrogen transition from the oxide to the metal phase as a result of the anodic reaction, Eq. 3.59:

$$H_{ab}^{+}(ox) + e_{\alpha}(ox/m) = H_{ab}(m),$$

is a quick process (in comparison with the bulk diffusion processes), so that the condition of thermodynamic equilibrium at the interface is valid. In this case hydrogen concentration $C_{H+}(b)$ in the oxide near the oxide/metal interface increases along with $C_H^{(m)}$, these values being proportional to each other (see Eq. 3.89 below).

Simultaneously the hydrogen concentration $C_{H+}(s)$ in the oxide at the opposite interface decreases along with $c_1(s)$ in accordance with Eq. 3.87. Therefore, at some moment t^* the hydrogen concentration gradient across the oxide layer disappears (see Fig. 3.101) and the flux $J_H^{(ox)}$ turns to zero (in accordance with Eq. 3.85). Since $C_{H+}(s)$ continues to decrease, after this moment both ΔC_{H+} and $J_H^{(ox)}$ become negative and hydrogen desorption commences, leading to $C_H^{(m)}$ decreasing.

Such a behavior was observed in the tests [40] at 1100 and 1200 °C (see Fig. 3.100). At lower temperatures 900 and 1000 °C the tests were terminated before the moment of the absorption/desorption regime transformation. It is quite natural that at lower temperatures the period of absorption increases, since the hydrogen solubility in the metal phase also increases (in accordance with the equilibrium binary H/Zr phase diagram, Fig. 3.103).

At temperatures below ≈550 °C solubility of hydrogen atoms in the metal matrix drastically reduces (Fig. 3.103). For this reason the hydrogen concentration gradient in the oxide keeps a nonzero value for an extremely long period of time, and hydrogen diffusionally transported through the oxide along this gradient is continuously absorbed (after relatively quick saturation of the metal matrix) in the form of hydride precipitates.

After the above mentioned moment of absorption/desorption regime transformation, the hydrogen flux in the oxide phase changes its direction and slightly increases from zero value providing desorption of hydrogen from the metal phase. However, it remains rather small since lowering of the partial hydrogen pressure $P_{H_2}(s) \propto c_1(s)$ at the oxide surface is a very slow process (along with the oxide layer growth) in later stages of Zr oxidation. For this reason, the hydrogen concentration distribution in the oxide can be approximately considered as homogeneous: $C_{H+}(x) \approx C_{H+}(s)$ (see Fig. 3.102). Thus, neglecting the hydrogen flux $J_H^{(ox)}$ in comparison with the oxygen one $J_O^{(ox)}$, that results in $c_1(s) \approx J_O^{(ox)}/k_2$, one can get a relationship analogous to Eq. 3.87: $C_{H+} \propto c_1(s)^{1/4} \propto \delta(t)^{-1/4}$, but for the spatially homogeneous concentration profile $C_{H+}(x) \approx C_{H+}$. As mentioned above, the boundary condition at the oxide/metal interface imposes a linear relation between this value C_{H+} and hydrogen concentration in the metal phase $C_H^{(m)}$ (see Eq. 3.89 below), which finally results in a slow

reduction of the latter with time:

$$C_H^{(m)} \propto C_{H+} \propto \delta(t)^{-1/4} \propto t^{-1/8}.$$

This qualitative consideration of hydrogen behavior in the initial and late stages of the oxidation process is fairly well reproduced by more exact numerical calculations presented below in the subsection 3.4.3.

3.4.2.5 Mass transfer through the oxide/metal interface

For the quantitative description of the hydrogen uptake during all the oxidation period additional equations determining hydrogen behavior in the metal phase and at the oxide/metal interface should be derived. In accordance with the assumption about thermodynamic equilibrium at the oxide/metal interface (see section 3.4.2.4), both the anodic reactions described by Eqs. 3.55 and 3.59:

$$ZrO_2(ox) + 2V_O^{2+} + 4e_\alpha(m/ox) = Zr(m) + 2O_O(ox),$$

and

$$H_{ab}^+(ox) + e_\alpha(ox/m) = H_{ab}(m).$$

should be considered as equilibrium. Correspondingly, application of the mass action law for these reactions, taking into account that anion vacancy concentration is strictly determined by the limiting oxide nonstoichiometry in the equilibrium binary Zr/O phase diagram, results in a simple linear relations between interface hydrogen concentrations in the oxide $C_{H+}(b)$ and in the metal $C_H^{(m)}\big|_I$ (see Fig. 3.104):

$$C_{H+}(b) = \gamma\, C_H^{(m)}\big|_I. \tag{3.89}$$

Therefore, Eq. 3.89 determines a boundary condition for the hydrogen diffusion problem in the metal phase which may be considered as a quasi-one dimensional problem due to the small thickness of the cladding wall in comparison with its radius:

$$\partial C_H^{(m)}(x,t)/\partial t = D_H^{(m)} \partial^2 C_H^{(m)}(x,t)/\partial x^2,$$

where $D_H^{(m)}$ is the hydrogen diffusivity in the metal phase. Taking into account that $D_H^{(m)}$ is larger than the diffusivity in the oxide $D_H^{(ox)}$ by several orders of magnitude [46], with a sufficiently good accuracy one can consider hydrogen distribution in the metal as homogeneous:

$$C_H^{(m)}(x,t) \approx C_H^{(m)}(t)\big|_I. \tag{3.90}$$

In this case the solution of the diffusion problem in the metal phase is reduced to the hydrogen balance equation (under one-sided oxidation conditions):

$$d(L_m(t)C_H^{(m)})/dt = J_H^{(ox)} - d[\delta(t)(C_{H+}(s) + C_{H+}(b))/2]/dt, \quad (3.91)$$

where $L_m(t) = L_m(0) - \delta(t)/B$, is the metal layer thickness, $B \approx 1.5$ is the Pilling-Bedworth ratio, $J_H^{(ox)}$ is determined by Eq. 3.85. Substituting Eqs. 3.85, 3.89 and 3.90 into Eq. 3.91 and neglecting the slow time variation of C_{H+} in comparison with that of $\delta(t)$ (see Eq. 3.87) one can finally get:

$$D_H^{(ox)}[(C_{H+}(s) - C_{H+}(b))/\delta(t)] - 0.5(C_{H+}(s) + C_{H+}(b))d\delta(t)/dt = d(L_m(t)C_H^{(m)})/dt. \quad (3.92)$$

Self-consistent solution of Eq. 3.92 (appropriately modified for the case of double-sided oxidation) together with Eqs. 3.73, 3.82, 3.84 and 3.85 allows calculation of the complicated dependence $C_H^{(m)}(t)$ measured in the tests [40].

3.4.3 Numerical solution of the model

The complete system of the equations 3.73, 3.80, 3.84, 3.85, 3.89 and 3.92 describing hydriding of the Zr cladding in the course of its oxidation in the steam atmosphere (after modification to the case of double-side oxidation) can be easily reduced to the following two equations:

$$\frac{dC_H^{(m)}}{dt} = \frac{2D_H^{(ox)}}{L_m(t)}\frac{(C_{H+}(s) - \gamma C_H^{(m)})}{\delta t} - \frac{C_H^{(m)}}{L_m}\frac{dL_m}{dt} - \frac{1}{L_m}\frac{d\left[\delta(C_{H+}(s) + \gamma C_H^{(m)})\right]}{dt}, \quad (3.93)$$

$$k_2\left(\frac{(C_{H+}(s)}{A}\right)^4 + \frac{D_H^{(ox)}}{2}\frac{(C_{H+}(s) - \gamma C_H^{(m)})}{\delta t} = D_0^{(ox)}\frac{\Delta C_0}{\delta(t)}. \quad (3.94)$$

The parameters A and γ entering in the final Eqs. 3.93 and 3.94 are functions of the poorly known equilibrium constants of the interface chemical reactions, and currently lacking experimental data can not be calculated independently. However, these parameters may be explicitly derived within the framework of the present model by fitting of calculations to the experimental data [40]. Indeed, from Eqs. 3.93 and 3.94 it follows that the maximum value of the hydrogen concentration in the metal is roughly estimated as:

$$C_H^{(m)}(max) = \frac{A}{\gamma}\sqrt[4]{\frac{D_0^{(ox)}\Delta C_0}{\delta(t)k_2}}. \quad (3.95)$$

This maximum value is attained at time:

$$\tau_0 = \left(\frac{L_m\alpha}{D_H^{(ox)}\gamma}\right)^2, \quad (3.96)$$

where α is the rate constant of the oxide scale growth: $\delta(t) = \alpha\sqrt{t}$. Hence, knowledge of the maximum value of the hydrogen content in the metal and hydriding kinetics allows calculation of the two unknown thermodynamic parameters A and γ.

In the experiment [40] hydrogen uptake was studied along with measurements of the Zr1%Nb cladding oxidation kinetics in the temperature range from 900 to 1200 °C. By processing of the available data on mass gain and the ZrO_2 layer thickness growth kinetics (see, for example, [48]), the oxygen diffusion coefficient in the oxide scale can be determined at different temperatures and approximated by the formula:

$$D_O^{(ox)} = 3.33e^{-42418/RT}, \tag{3.97}$$

where T is in K, R = 1.987 cal/Kmol.

Wagner's data on the diffusivity of hydrogen ions H^+ in zirconia [43] refer to the yttria-stabilized samples. In the case of Zr1%Nb oxide these coefficients may be somewhat different. Lacking such data, however, the diffusion coefficients measured in [43] at 900 and 1000 °C and extrapolated to the high temperature region:

$$D_H^{(ox)} = 4 \cdot 10^{-4}e^{-14405/RT}, \tag{3.98}$$

are used in the present calculations.

The other model parameters specifying conditions of the tests [40] are:

$L_m(0) = 0.07$ cm, $\delta(t) = 0.46\exp(-19919/RT)\sqrt{t}$ cm, ([40]), $\Delta C_0 = 7 \cdot 10^{-4}$ mol/cm^3 (see, for example, [45]) and $k_2 = 75$ cm/s, in accordance with Eq. 3.62. As seen either from Eq. 3.95 or directly from Eq. 3.94, some underestimation of the value k_2 (discussed in section 3.4.2.1) does not strongly influence the calculated value of A owing to a rather weak dependence of A on k_2.

In Figs. 3.105 and 3.106 experimental data [40] are compared with calculation results by the present model. The parameters A and γ obtained by fitting of experimental and theoretical data are shown in Table 3.4:

Temperature, °C	A, $(mol/cm^3)^{3/4}$,	γ
900	0.032	0.005
1000	0.042	0.01
1100	0.11	0.18
1200	0.17	0.37

Table 3.4: Calculated values of the model parameters A and γ.

and can be approximated by the formulas:

$$A = 1.86 - 3.18(T/1000) + 1.38(T/1000)^2 \ , \ (mol/cm^3)^{3/4}, \tag{3.99}$$

$$\gamma = 6.56 - 10.97(T/1000) + 4.63(T/1000)^2. \tag{3.100}$$

The values of γ obtained for temperatures 1100 and 1200 °C seem to be too large, however, this can be attributed to an error of the hydrogen diffusion coefficient extrapolation by Eq. 3.98 to these temperatures (not measured directly). It can be shown that increase of the diffusion coefficient will result in proportional reduction of the calculated value of γ (see Eq. 3.96).

In general, the calculations show that hydrogen absorption by Zr1%Nb cladding during steam oxidation can be fairly well (practically within the accuracy of the experiment) represented by the model in the temperature range of the measurements [40] (from 900 to 1200 °C).

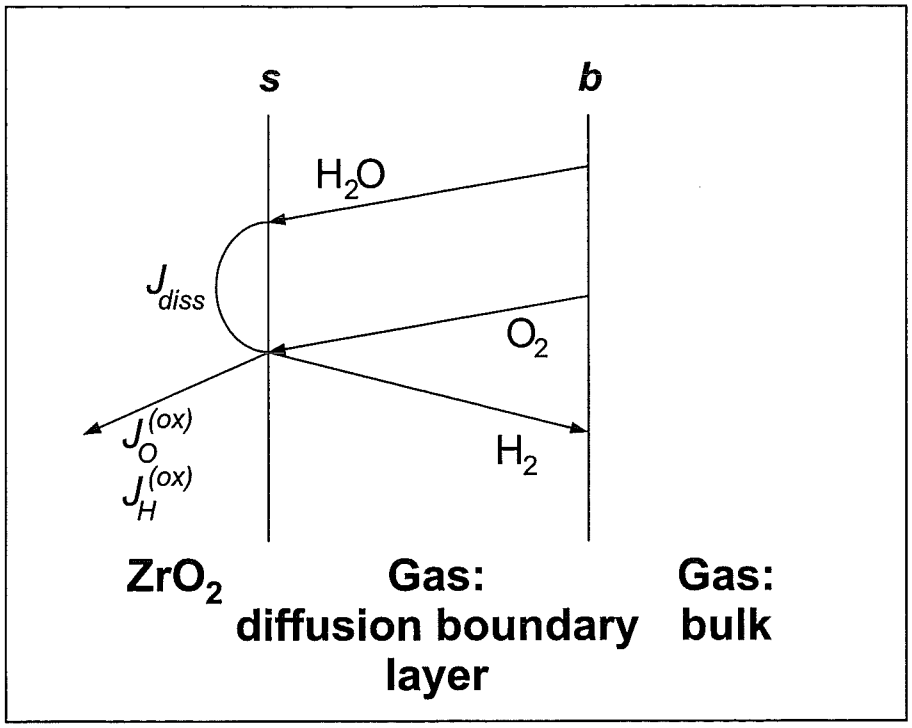

Figure 3.96: Schematic representation of the flux balances at the gas/oxide interface.

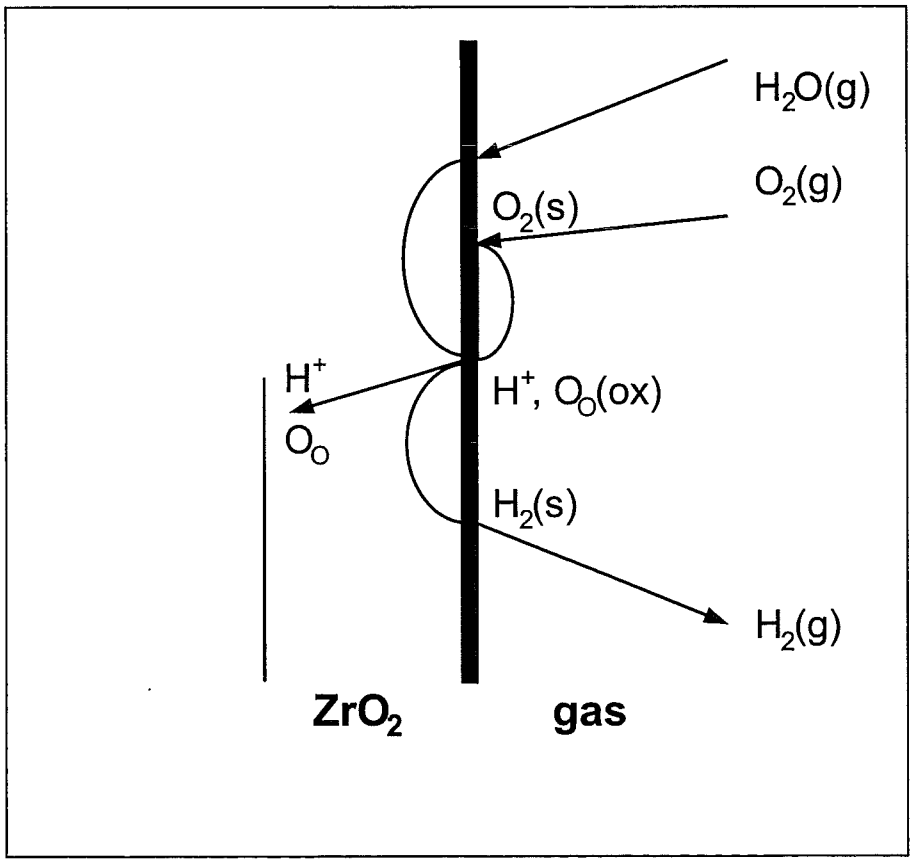

Figure 3.97: Schematic representation of chemical reactions at the gas/oxide interface.

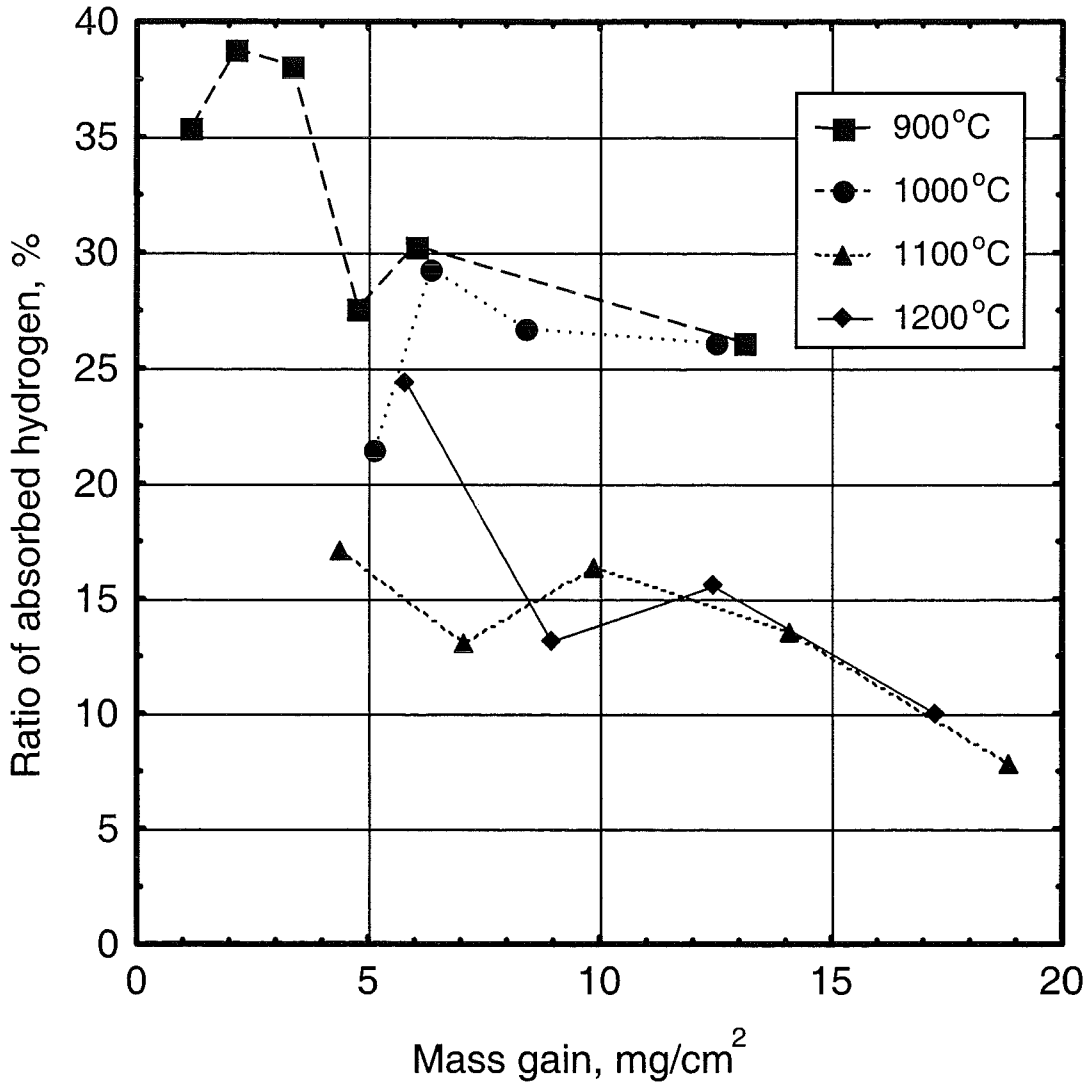

Figure 3.98: Ratio of absorbed hydrogen in Zr1%Nb vs. mass gain during steam oxidation (from [40]).

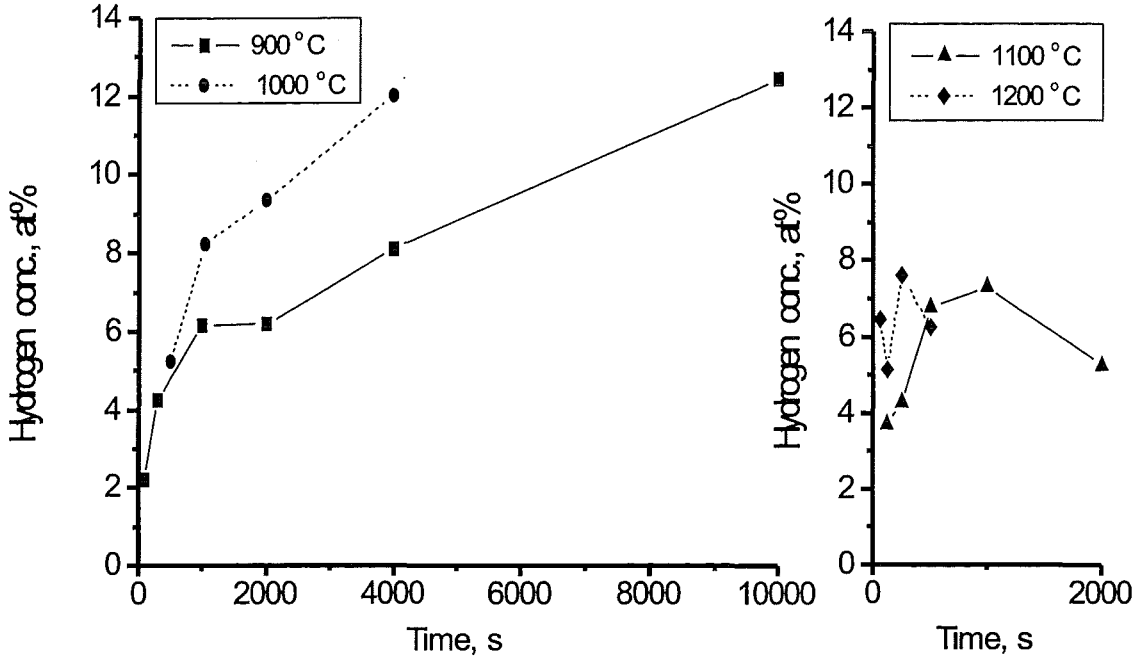

Figure 3.99: Hydrogen concentration of Zr1%Nb samples after isothermal steam exposure (from [40]).

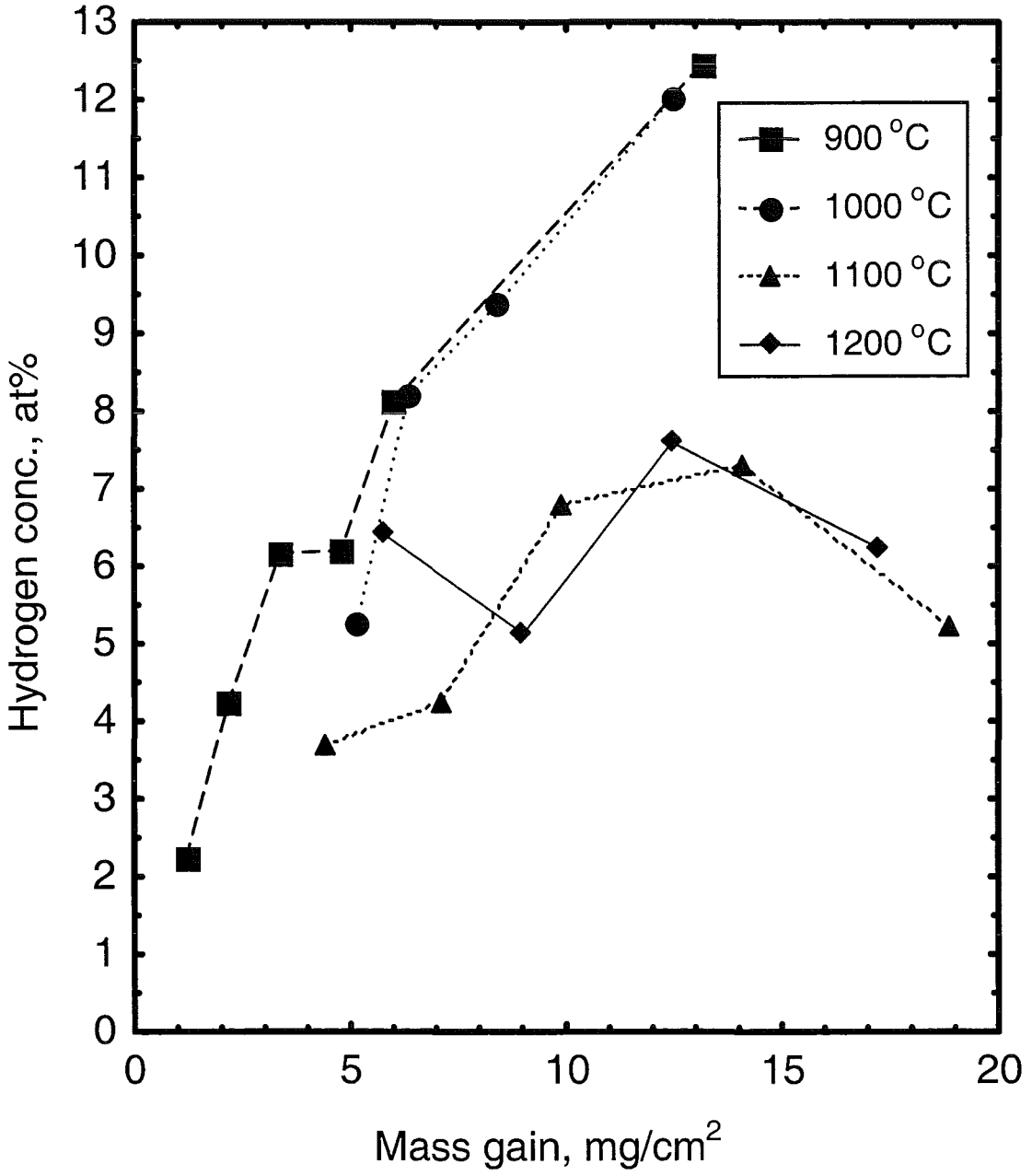

Figure 3.100: Zr1%Nb hydrogen uptake vs. mass gain during steam oxidation (from [40]).

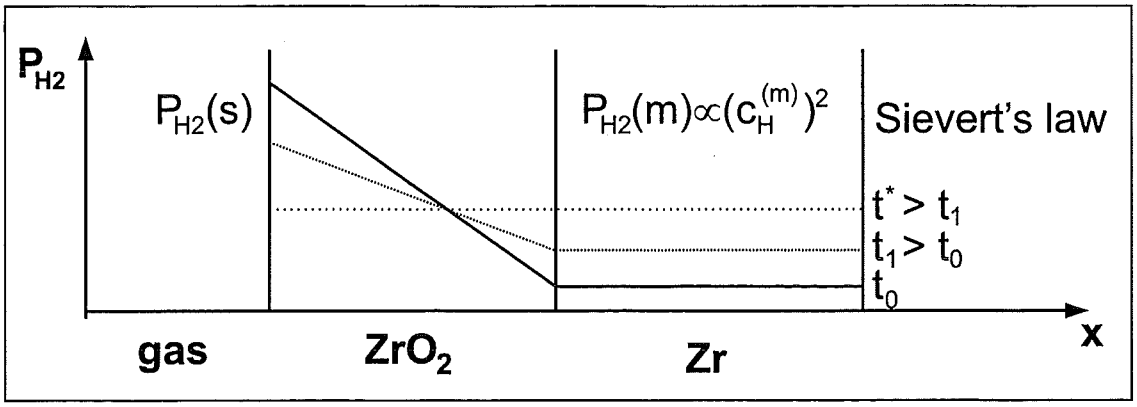

Figure 3.101: Schematic representation of hydrogen partial pressure (chemical potential) distribution in the cladding layers in the initial stage of oxidation process.

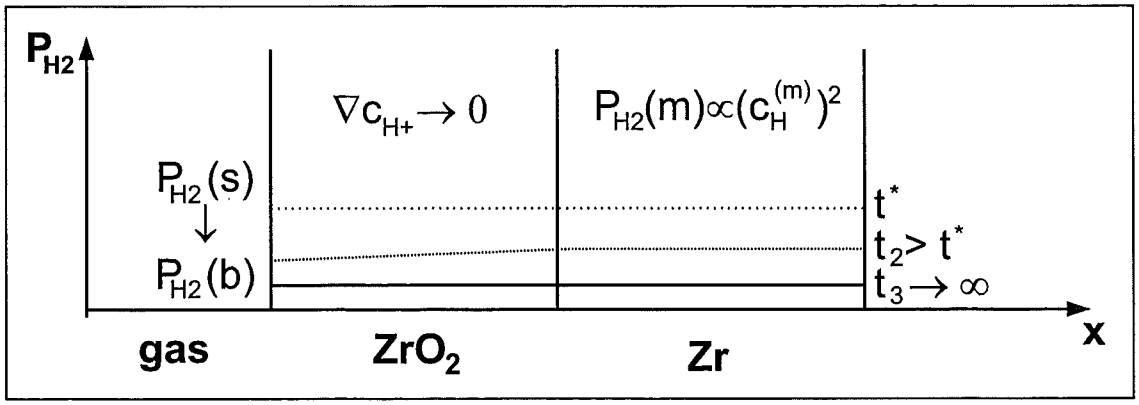

Figure 3.102: Schematic representation of hydrogen partial pressure (chemical potential) distribution in the cladding layers in the late stage of oxidation process.

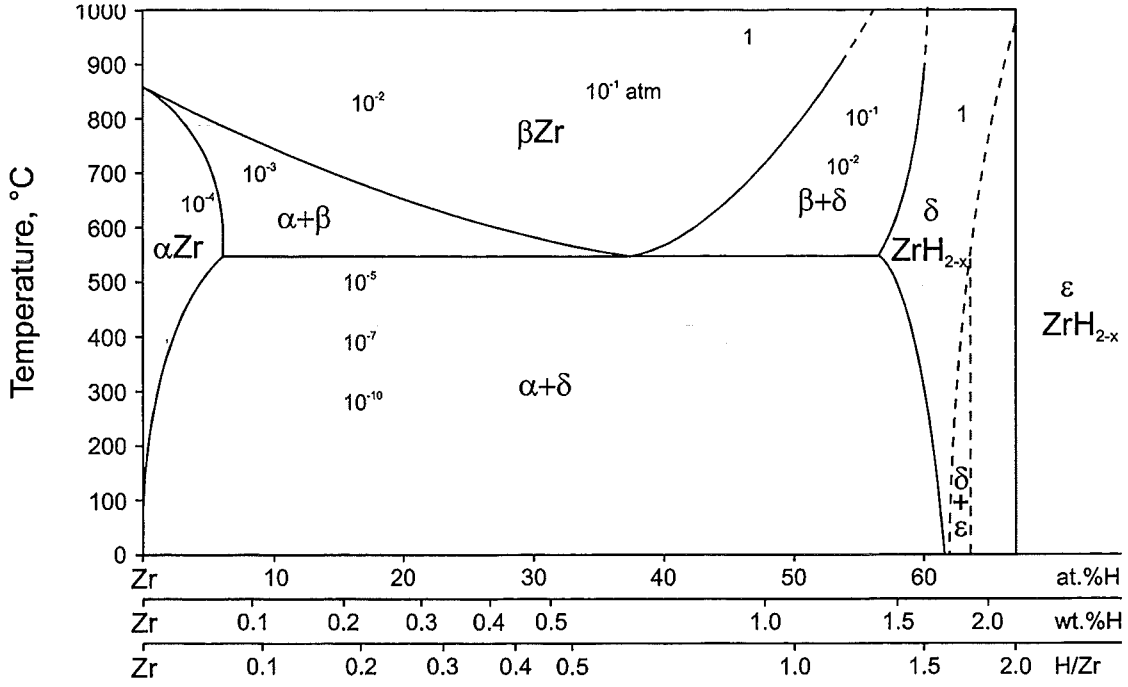

Figure 3.103: Binary zirconium-hydrogen phase diagram and equilibrium hydrogen pressures.

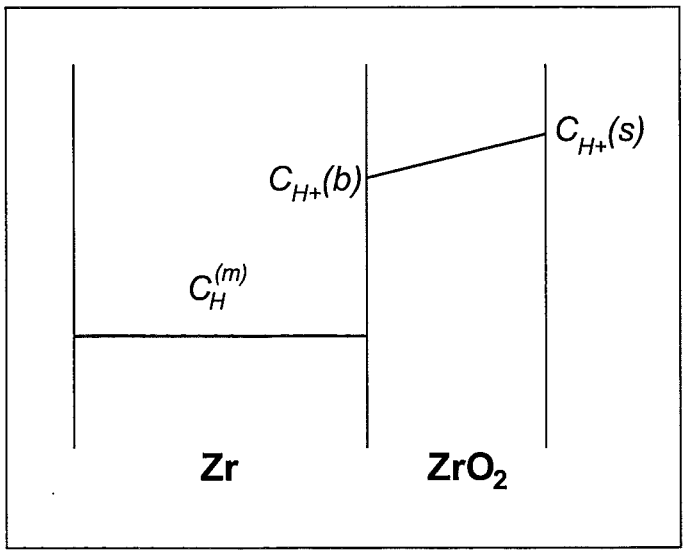

Figure 3.104: Schematic representation of hydrogen concentration profiles in the oxide and metal phases.

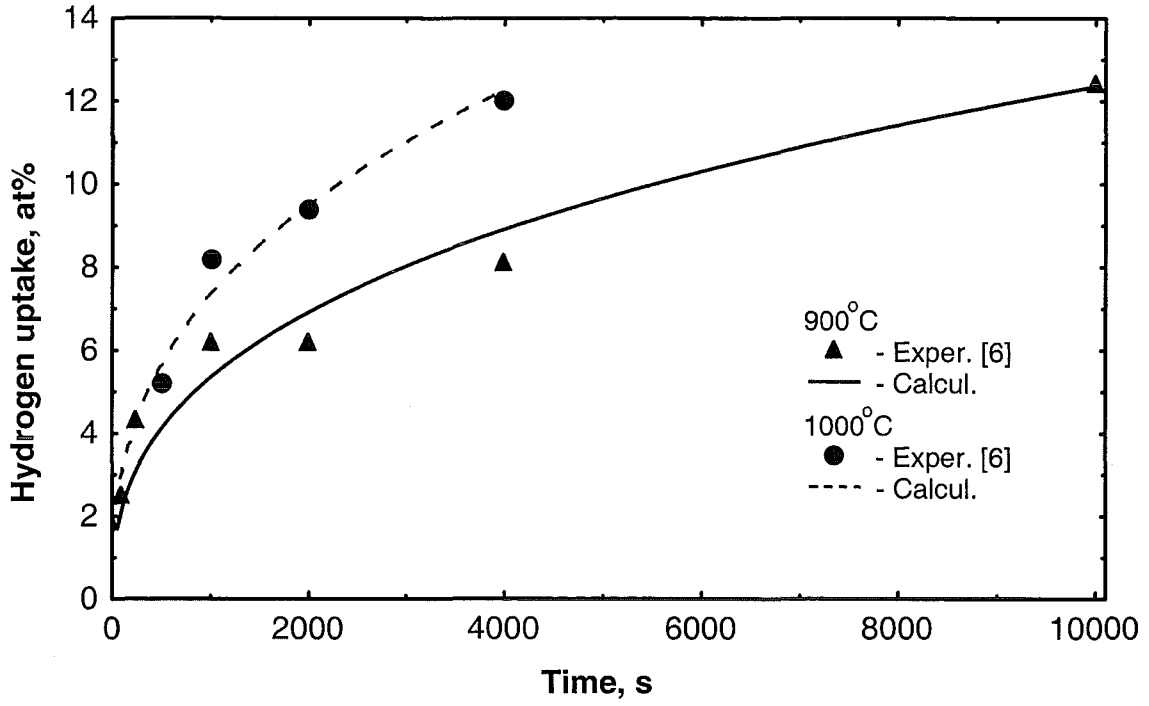

Figure 3.105: Comparison of the calculated and measured [40] hydrogen uptake by Zr1%Nb cladding during isothermal steam oxidation at T=900 and 1000 °C.

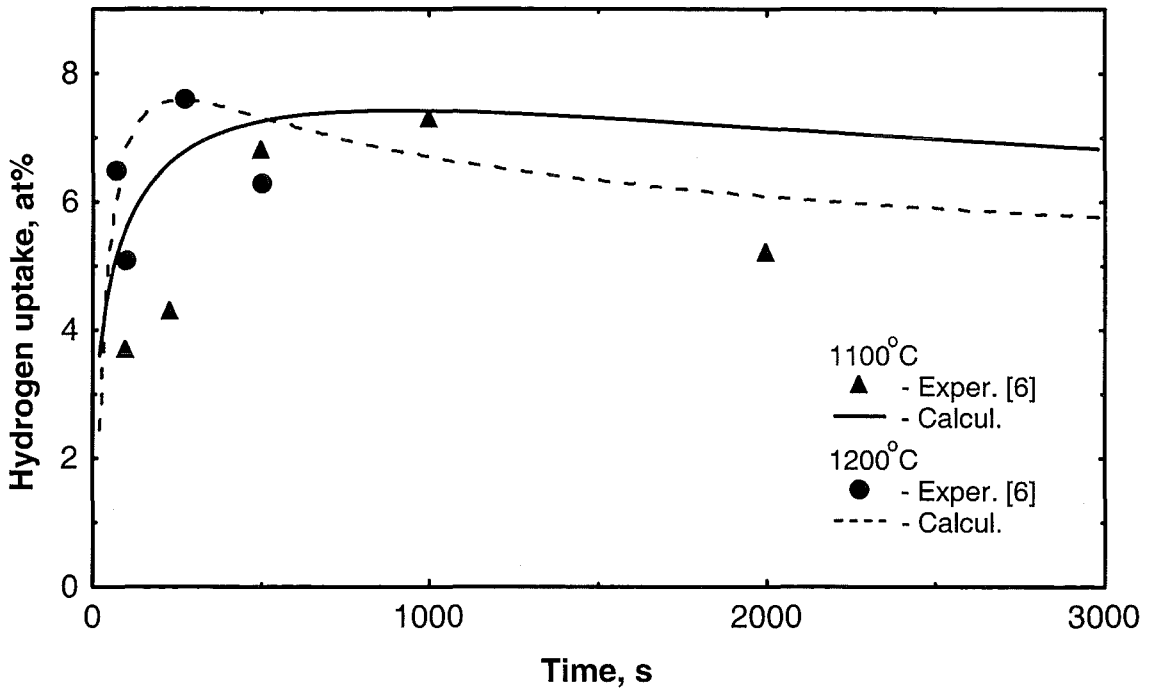

Figure 3.106: Comparison of the calculated and measured [40] hydrogen uptake by Zr1%Nb cladding during isothermal steam oxidation at T=1100 and 1200 °C.

4. Summary and conclusions

The separate-effects tests with short LWR fuel rod segments to determine the critical conditions (oxide layer thickness, temperature at onset of quenching) which result in crack formation and fragmentation of the oxygen-embrittled cladding in the pre-oxidized Zircaloy cladding tubes during fast cool-down in a steam flow have been continued. It is assumed that the newly formed metallic surfaces result in enhanced oxidation and hydrogen generation during quenching as observed in the TMI-2 accident and in several integral large-scale bundle tests.

The tube specimen of a length of 150 mm, filled with ZrO_2 pellets, is suspended inside a quartz tube which is surrounded by an induction heating coil. Pre-oxidation of the Zircaloy tube specimen ($0-300\,\mu m$ ZrO_2 layer thickness) is executed at 1400 °C by a steam/argon gas mixture in the QUENCH rig before quenching. The specimen is then heated or cooled to the desired quench temperature in the same atmospher. The specimen is then rapidly cooled down by injected steam of 1.0 g/s. During the quench test the temperature of the specimen at three elevations and the hydrogen generation are continuously recorded. The quench experiments comprised 4 groups with the same temperature at onset of quenching: 1100, 1200, 1400, 1600 °C. Formation of macroscopic through-wall cracks can be observed in steam-quenched experiments with ZrO_2 layer thicknesses larger than 200 µm. Crack formation is more pronounced at lower specimen temperatures at the onset of quenching. In most cases the crack patterns consist of two to four axial cracks extending over the "hot" length of the tube and smaller cracks going into the circumferential direction. The cracks which cause breaking up of the specimen are circumferential cracks in most cases. The group with 1600 °C initiating temperature has also two to four axial cracks but only a few oblique cracks connecting the axial cracks and no orthogonal cracks. The oxide layer thickness limit for break-up is higher than for the lower temperature experiments. The surfaces of the cracks in the remaining metallic part of the cladding tubes are oxidized. Oxidation of crack surfaces increases with decrease of the specimen temperature at the onset of quenching.

Due to the experimental conduct on the basis of measured hydrogen it is not possible to prove that the crack oxidation during quench contributes to the overall hydrogen generation, which was clearly demonstrated in the experiments performed before (pre-oxidized in an Ar/O_2 mixture) [14].

The amount of absorbed hydrogen in specimens of the test series discussed in this report was analyzed. In general, the results show that after reaching certain oxide layer thickness (about 200 μm) and crack density, the amount of hydrogen absorbed in the metallic part of the Zircaloy tube increases considerably. The amount of the absorbed hydrogen correlates not only with the extent of the pre-oxidation at the onset of cooldown, but also with the total crack length. The uptake of the hydrogen in Zircaloy and its additional release during oxidation of the metal and during the quench phase can influence the kinetics of hydrogen release and has therefore to be studied quantitatively in more detail.

The verification calculations against the experimental set including 22 water quenching and 6 steam cooling experiments were performed with the new version of SVECHA/QUENCH (SQ) code. The new version of the code includes thermal-hydraulic module QBOIL, the heat conduction module QTEM, the oxidation module QOXI (based on the partial derivatives equations) with steam starvation model implemented, and the improved mechanical deformation module QDEF. The new version of the SQ code provides a satisfactory reproduction of the experimentally observed temperature evolution curves in the full range of the single rod experiments conditions (different pre-oxidation and initial temperatures) without tuning and adjusting of the code parameters. The implementation of the steam starvation model makes it possible to describe the corresponding effect in the case of high temperature water quench tests.

The present analysis of the quench experimental data by the mechanical deformation module QDEF shows that deformation behavior of the oxidized Zircaloy fuel cladding under cold water injection into the reactor core (quenching) may have a great influence on further accident evolution and may lead to dramatic temperature and hydrogen release escalation caused by oxidation of newly formed metal surfaces and beginning of the inner cladding oxidation. These new metal surfaces appear due to cracking of the oxidized fuel cladding. The main reasons of the cladding rupture are either the oxide phase transformation from the tetragonal to the monoclinic phase, or a steep temperature gradient near the quench front.

The oxide transition from the tetragonal to monoclinic phase occurs at a temperature of ≈1200 °C. The oxide phase transition provokes through-wall cracks leading to the inner cladding tube and through-wall crack surface oxidation. Since the cladding temperature is rather high, this oxidation may lead to a new temperature escalation. The barrier that prevents the through-wall cladding rupture is a ductile beta layer with the dissolved oxygen content less than the critical value.

Radial temperature gradients and difference in the thermal expansion coefficients of the oxidized cladding phases lead to the formation of microcracks in the oxide layer without cladding rupture. These processes accelerate the oxidation by decreasing the protective thickness of the formed oxide scale. An axial temperature gradient has no great influence on the oxide scale and cladding rupture at high temperatures.

However, an axial temperature gradient is the main reason for the cladding rupture (through-wall crack formation or fragmentation) at low temperatures. The maximum axial gradient in the tube specimen exists near the quench front when the transition from film to nucleate boiling occurs, i.e. near the Leidenfrost temperature. At this temperature the oxidation is too slow, hence, the cladding rupture does not lead to a temperature escalation and increased hydrogen release.

Numerical simulations show that the formation of through-wall cracks and, hence, intensive hydrogen generation depends on stresses generated in the alpha and oxide phase. If the stresses in the alpha layer attain the strength limit firstly and the beta layer is absent, then through-wall cracks appear. If the stresses in the oxide layer firstly attain the limit value, then the failure behavior depends on the type of the stresses in the alpha layer. If these stresses are compressive then microcracks are generated in the oxide layer during cool down from the pre-oxidation temperature to temperatures above the oxide phase transition. If the stresses are tensile then several through-wall cracks form in the absence of a beta layer, or, in the case of a thick beta layer microcracks form in the alpha and oxide layers. However, in the oxide layer these microcracks can hardly be observed, due to the residual compressive stresses in this layer. Simulations show that the tensile strength limit of the alpha phase appears to be close to the strength limit of the oxide layer.

In order to simulate the hydrogen absorption by the Zr cladding observed in the separate-effects tests on the high temperature cladding interactions with pure hydrogen and pure steam atmospheres, respectively, two separate kinetic models were developed.

For quantitative description of the hydrogen uptake and release by Zircaloy, mass transfer in the gas and metal phases as well as at the oxide/metal interface, is considered. The hydrogen diffusion equation in the Zry sample is solved with non-linear boundary conditions determined by the Sieverts law.

The obtained system of equations is analysed qualitatively and quantitatively. It is analytically shown that the hydrogen uptake and release can occur in different ways. Under conditions of

the FZK separate-effects tests [33] with abrupt variation of the hydrogen gas pressure between zero and a finite value (0.5 bar) at various temperatures, the hydrogen release is described by a slow (hyperbolic) function of time, whereas the hydrogen uptake obeys a rapid (exponential) time law, in accordance with experimental observations. Under conditions of the hydrogen pressure variation between two finite values, the model predicts similar (exponential) kinetics in both cases of the hydrogen release and uptake. Later this conclusion was confirmed by the FZK observations.

The simplified qualitative consideration is completely confirmed by numerical calculations. Numerical solution of the problem provides a satisfactory agreement between measured kinetic curves [33] and calculations.

The other model developed for the description of hydrogen absorption kinetics by Zr-1%Nb cladding during oxidation in steam, is essentially based on the experimental results [40] performed in the temperature range from 900 to 1200 °C.

The model takes into account that hydrogen may intrude into the oxide as the result of H_2O dissolution process in the form of positively charged protons. Discharge of protons by electrons occurs at the oxide/metal interface (rather than at the gas/oxide interface as considered in the standard approach) after diffusion transporting of highly mobile protons through the oxide scale.

For quantitative description of hydrogen behaviour by this mechanism, mass transfer in the three layers: gas, oxide and metal, and at the corresponding interfaces: gas/oxide and oxide/metal, is considered.

The obtained system of equations is qualitatively analysed explaining the main features of the observed complicated kinetics of hydrogen uptake: (i) continuous increase of hydrogen concentration in the metal phase being roughly proportional to the oxidation mass gain, in the initial stage of the process; (ii) desorption of hydrogen to the gas phase accompanied by slow decrease of measured hydrogen concentration in the metal phase, in the late stage of the process; (iii) decrease of maximum hydrogen concentration in Zr attained at the absorption/desorption regime transformation, with temperature increase.

Numerical solution of the problem generally confirms the main conclusions of the simplified analytical treatment and furnishes a satisfactory fitting between measured kinetic curves [40] and calculations.

References

[1] Severe Accident Risks: An Assessment for Five U.S. Nuclear Power Plants. Final Summary Report. U.S. Nuclear Regulatory Commission. NUREG-1150, Vol.1. December 1990.

[2] Deutsche Risikostudie Kernkraftwerke, Phase B. Köln: Verl. TÜV Rheinland, 1990. ISBN: 3-88585-809-6.

[3] Gemeinsame Empfehlung von RSK und GPR vom 16.06.1993. Sicherheitsanforderungen an zukünftige Kernkraftwerke mit Druckwasserreaktor.

[4] P.Kuan, J.L.Anderson, and E.L.Tolman. Thermal Interactions During the Three Mile Island Unit 2 2-B Pump Transient. Nuclear Technology 87, p.977, 1989.

[5] R.R.Hobbins and G.D.McPherson. A Summary of Results from the LOFT LP-FP-2 Test and Their Relationship to Other Studies at the Power Burst Facility and of the Three Mile Island Unit 2 Accident. In "The OECD/LOFT Project: Achievements and Significant Results", ISBN 92-64-033339-4, OECD Paris, 1991.

[6] A.D.Knipe, S.A.Ploger and D.J.Osotek. PBF Severe Fuel Damage Scoping Test – Test Results Report. NUREG/CR-4683, March 1986.

[7] S.Hagen, P.Hofmann, G.Schanz, G.Schumacher, F.Seibert, L.Sepold. Effects of Quenching Observed in the CORA Severe Fuel Damage Experiments. Proc. of the American Nuclear Society Meeting on the Safety of Thermal Reactors, p.85-91, 21-25 July, 1991, ANS, 1991.

[8] S.Hagen, P.Hofmann, V.Noack, L.Sepold, G.Schanz. Comparison of the Quench Experiments CORA-12, CORA-13, CORA-17. FZKA 5769, 1996.

[9] C.Gonnier, G.Geoffroy and B.Adroguer. PHEBUS SFD Programme: Main Results. A.N.S. Int. Meeting on Safety of Thermal Reactors, Portland, USA, July 1991.

[10] G.Schanz, S.Leistikow. Experimental Results on the Hydrogen Pick-up and Storage Potential of Zircaloy-4. 1st Int. QUENCH Workshop, FZK Karlsruhe, 4-6 October, 1995.

[11] J.Frecska, G.Konczos, L.Maroti, L.Matus. Hydrogen Uptake during Steam Oxidation of Zr1%Nb. 1st Int. QUENCH Workshop, FZK Karlsruhe, 4-6 Oktober, 1995.

[12] M.Steinbrück. Hydrogen Absorption of Zircaloy at High Temperatures. 2nd Int. QUENCH Workshop, FZK Karlsruhe, 17-19 September, 1996.

[13] S.R.Kinnersly, J.N.Lillington, A.Porracchia, K.Soda, K.Trambauer, P.Hofmann, Y.Waarenpera, R.A.Bari, C.E.L.Hunt, J.A.Martinez. In-Vessel Core Degradation in LWR Severe Accidents: A State of the Art Report to CSNI, January 1991. NEA/CSNI/R(91)12, November 1991.

[14] P.Hofmann, V.Noack, M.S.Veshchunov, A.V.Berdyshev, A.V.Boldyrev, L.V.Matweev, A.V.Palagin, V.E.Shestak. Physico-chemical Behavior of Zircaloy Fuel Rod Cladding Tubes during LWR Severe Accident Reflood. FZKA 5846, May 1997.

[15] S.Hagen, P.Hofmann, V.Noack, G.Schanz, G.Schumacher and L.Sepold, "Results of SFD Experiment CORA-13 (OECD International Standard Problem 31)". KfK 5054, February 1993.

[16] C.M.Alison et. all., "MATPRO-A Library of Materials Properties for Light-Water-Reactor Accident Analysis", NUREG/CR-6150, 1994.

[17] P.Hofmann, W.Leiling, A.Miassoedov, D.Piel, L.Schmidt, L.Sepold, M.Steinbrück. QUENCH-01 Experimental Results. FZKA 6100, 1998.

[18] L.Steinbock, J.Stuckert. Determination of Crack Patterns of Quenched Zircaloy Tubes, FZKA 6013, 1997.

[19] D.R.Olander, "Materials Chemistry and Transport Modeling for Severe Accidents Analysis in Light Water Reactors I: External Cladding Oxidation", J.Nucl.Eng.Des., v.148, 1994, p.253-271.

[20] A.V.Berdyshev, A.V.Boldyrev, A.V.Palagin, V.E.Shestak, M.S.Veshchunov, "Modelling of LWR Core Quench Phenomena. Part II", Russian Academy of Sciences, Nuclear Safety Institute, Moscow, Russia, Interim report, May 1997. Prepared for Forschungszentrum Karlsruhe, under the conditions of the Research Agreement No. 315/20046178/IMF.

[21] A.Sawatzky, "A Proposed Criterion for the Oxygen Embrittlement of Zircaloy-4 Fuel Cladding", Zirconium in the Nuclear Industry (Fourth Conference), ASTM STP 681, American Society for Testing and Materials, 1979, pp. 479-496.

[22] H.M.Chung, T.F.Kassner, "Embrittlement Criteria for Zircaloy Fuel Cladding Applicable to Accident Situations in Light-Water Reactor: Summary Report", Argonne National Laboratory, Materials Science Division, NUREG/CR-1344, ANL-79-48, January 1980.

[23] SCDAP/RELAP5/MOD2 Code Manual, Volume 4: MATPRO-A Library of Materials Properties for Light-Water-Reactor Accident Analysis. NUREG/CR-5273 EGG-2555. Vol.4., 1990.

[24] NOTE TECHNIQUE DRS/SEMAR 92/24. ICARE2. Version 2.MOD 0 and MOD 0.1. Description of Physical Models. Institute de Protection et de Surete Nucleaire. CEA-France.

[25] A.M. Katz, "Theory of elasticity", Moscow, 1956 (in Russian).

[26] B.Burton, A.T.Donaldson and G.L.Reynolds, "Interaction of Oxidation and Creep in Zircaloy-2", Zirconium in the Nuclear Industry (Fourth Conference), ASTM STP 681, American Society for Testing and Materials, 1979, pp. 561-585.

[27] A.Boldyrev, N.Yamshchikov, V.Shestak, "Fuel Cladding Deformation Behavior Module (CROX)", Russian Academy of Sciences, Nuclear Safety Institute, Moscow, Russia, Report No. NSI-SARR-05-94 (1994).

[28] M.Moalem, D.R.Olander, J.Nucl.Mater., 178 (1991) 161.

[29] M.Tada, Y.C.Haung, Titanium-Zirconium, 19 (1971) 260.

[30] C.E.Ells, A.D.McQuillan, J.Inst.Met., 85 (1956) 89.

[31] K.Watanabe, J.Nucl.Mater., 136 (1985) 1.

[32] S.Yamanaka, K.Higuchi, M.Miyake, J.Alloy.Comp., 231 (1995) 503.

[33] P.Hofmann, V.Noack, M.Steinbrück, L.Schmidt, Cooperative Severe Accident Research Program Meeting, Bethesda, Maryland, May 5–8,1997.

[34] C.Katlinski, Inorg. Mater., 14 (1978) 1305.

[35] B.Cox, Advances in Corrosion Science and Technology, 5(1976)173.

[36] J.Boehmert, M.Dietrich, J.Linek, Nucl.Energy and Design, 174(1993)53.

[37] J.Boehmert, J.Linek, M.Dietrich, Untersuchungen zur Hochtemperatur-Dampfoxidation von Zr1%Nb, Zentralinstitut für Kernforschung Rossendorf bei Dresden, Report ZfK-743, 1991, p.1.

[38] V.Vrtilkova, L.Molin, K.Kloc, V.Gamouz, Voprosy Atomnoi Nauki I Tehniki, 27(1988)89 (in Russian).

[39] V.I.Dyachkov, Zhurnal Prikladnoi Chimii, 64(1991)2029 (in Russian).

[40] J.Freska, G.Konczos, L.Maroti, L.Matus, Oxidation and Hydriding of Zr1%Nb Alloys by Steam, Report KFKI-1995-17/G, 1995.

[41] K.Park, D.R.Olander, J.Am.Ceram.Soc.,74(1991)72.

[42] K.-N.Choo, S.-I.Pyun, Y.-S.Kim, J.Nucl.Mater., 226(1995)9.

[43] C.Wagner, Ber.Bunsen-Ges.Phys.Chem., 72(1968)778.

[44] V.G.Levich, Physico-Chemical Hydrodynamics, Moscow, 1959 (in Russian).

[45] D.R.Olander, Nucl.Engineering and Design, 148(1994)253.

[46] C.Katlinski, Inorg.Mater., 14(1978)1305.

[47] E.S.Shchetinnikov, Physics of Gas Combustion, Moscow, 1970 (in Russian).

[48] A.V.Berdyshev, L.V.Matveev, M.S.Veshchunov, Development of the Database for the Kinetic Model of the Zircaloy-4/Steam Oxidation at High Temperatures (1000 °C $\leq$ T $\leq$ 1825 °C), Preprint IBRAE-97-05, Moscow, 1997.

Appendix

In the present Appendix the derivation is presented of the H_2 and O_2 fluxes in the diffusion layer of the steam taking into account dissociation/association of the H_2O molecules in the gas mixture: $H_2O(g)=H_2(g)+(1/2)O2(g)$. In accordance with this chemical reaction there is a source for H_2 and O_2 molecules (and a corresponding sink for H_2O molecules) in each spatial point x of the gas phase. Mass transfer equations in the diffusion layer for the two components accordingly take form:

$$\partial c_1/\partial t = D_H \partial^2 c_1/\partial x^2 + Q(x,t), \tag{A.1}$$

$$\partial c_2/\partial t = D_O \partial^2 c_2/\partial x^2 + (1/2)Q(x,t), \tag{A.2}$$

where a value of the spatially distributed source $Q(x)$ is determined by the relation:

$$Q(x) = k_1 \left[c_3^2(x) - k c_1^2(x) c_2(x)\right], \tag{A.3}$$

the equilibrium constant $k = \exp(2\Delta G/RT)$ is determined by Eq. 3.69, the kinetic constant k_1 specifies the velocity of the H_2O dissociation reaction, c_i is the molar density of the i-th component in the mixture, $i = 1,2,3$ denote H_2, O_2, H_2O, respectively (see Eq. 3.63). Possible convection fluxes of the two components H_2 and O_2 are neglected in Eqs. A.1 and A.2 in accordance with estimations presented in section 3.4.2.1 (see derivation of Eq. 3.73).

Mass transfer in the gas phase is a very quick process in comparison with that in the solid oxide ($D_H \sim D_O \sim 10\,\mathrm{cm/s}$ at $T \approx 1000\,^\circ\mathrm{C}$), for this reason for the self-consistent solution of the Zr oxidation problem the quasistationary approximation for the gas phase is valid:

$$\partial c_1/\partial t \approx 0, \quad \partial c_2/\partial t \approx 0. \tag{A.4}$$

Substituting Eqs. A.3 and A.4 into Eqs. A.1 and A.2 and integrating them, one gets:

$$D_H \partial^2 c_1/\partial x^2 + R(x,t) = A = \mathrm{const}, \tag{A.5}$$

$$D_O \partial^2 c_2/\partial x^2 + (1/2)R(x,t) = B = \mathrm{const}, \tag{A.6}$$

where

$$R(x) = \int Q(x)dx.$$

Superposition of Eqs. A.5 and A.6 yields:

$$\partial c_2/\partial x = (D_H/2D_O)\partial c_1/\partial x + M, \tag{A.7}$$

where

$$M = (2B - A)/2D_O = \text{const.}$$

Integration of Eq. A.7 yields:

$$c_2 = (D_H/2D_O)c_1 + Mx + N, \tag{A.8}$$

where $N = \text{const.}$

By substitution of Eq. A.8 into initial Eq. A.1 taking into account Eqs. A.3 and A.4 one gets:

$$D_H\partial^2 c_1/\partial x^2 + k_1\left[c_3^2 - kc_1^2((D_H/2D_O)c_1 + Mx + N)\right] = 0, \tag{A.9}$$

Local equilibration of the H_2O dissociation reaction is a much more quick process than the diffusion in the gas layer, that means:

$$k_1 \gg D_H/L^2, \tag{A.10}$$

where L is the thickness of the diffusion boundary layer.

Indeed, at $T \sim 1000\,^{\circ}C$, $k_1 \sim 10^6 - 10^8\ s^{-1}$ [47], whereas $D_H/L^2 \sim 10^2\ s^{-1}$ when $L \sim 0.3$ cm. Hence, under this approximation the diffusion term in Eq. A.9 can be neglected, leading to:

$$k_1\left[c_3^2 - kc_1^2((D_H/2D_O)c_1 + Mx + N)\right] \approx 0, \tag{A.11}$$

or, after transformation of the molar concentrations to the specific values: $C_i = c_i/c_g$, i=1,2,3, with account of $C_3 \approx 1$ (since $c_1, c_2 \ll c_3$), finally one gets:

$$kc_gC_1^2\left[(D_H/2D_O)C_1 + mx + n\right] \approx 1, \tag{A.12}$$

where $m = M/c_g$, $n = N/c_g$, c_g is the molar concentration of the gas phase, $c_g = c_1 + c_2 + c_3$.

In order to determine the constants m and n, the obtained Eq. A.12 should be substituted into boundary conditions at the oxide/gas interface:

$$x = 0, \quad C_1 = C_1(s),$$

and at the outer boundary of the diffusion layer:

$$x = L, \quad C_1 = C_1(b).$$

Differentiating Eq. A.12:

$$\partial C_2/\partial x = -mC_1/(2mx + 1.5(D_H/D_O)C_2 + 2n),$$

and substituting the determined constants m and n, finally one gets:

$$\partial c_1/\partial x|_{x=0} = -c_1(s)/L, \tag{A.13}$$

$$\partial c_2/\partial x|_{x=0} = -((D_H/D_O) - 1)c_2(b)/L, \tag{A.14}$$

(for comparison, the value of one of the derivatives at the opposite boundary can be also presented: $-\partial c_1/\partial x|_{x=L} = c_1(b)/L \ll -\partial c_1/\partial x|_{x=0}$).

It should be noted that to deduce the final Eqs. A.13 and A.14 the following inequalities were used: $c_2(s) \gg c_2(b)$, $c_1(b) \gg c_1(s)$, which were discussed in section 3.4.2.1 (see derivation of Eq. 3.71), and also $kc_1^2(b)c_1(s)/c_3 \gg 1$, which results from the relations $kc_1^2(b)c_2(b)/c_3 \sim kc_1^3(b)/c_3 \sim 1$ and $c_2(s) \gg c_2(b)$.